Radiation Transmission Imaging Applications for Nuclear Reactor Systems

by

Julio Diaz

A dissertation submitted in partial fulfillment
of the requirements for the degree of
Doctor of Philosophy
(Nuclear Engineering and Radiological Sciences)
in The University of Michigan
2022

Doctoral Committee:

Professor Annalisa Manera, Co-Chair
Associate Research Scientist Victor Petrov, Co-Chair
Professor Jeffrey Fessler
Dr. Alan Kastengren, Argonne National Lab
Professor Xiaodong Sun

Julio Eduardo Diaz

juliod@umich.edu

ORCID iD: 0000-0001-9523-5571

DEDICATION

To my beloved mother and all those who have helped me get here.

ACKNOWLEDGEMENTS

To all of the people who have lent their hand for I would not be without you. To my mother Maria Gloria Gomez, who provides a fountain of insurmountable love. To my father Ernesto Diaz whose thoughtfulness and encouragement brings inner peace. To Dane and Ines Shepherd who helped raise me. To the friends with whom we build memories, share adventures, but more importantly support each other in the hardest times: Patrick Russell, Daniel Nunez, Jake Williams, Justin Weber, Vanesa Gutierrez, Natalie Georges, Siddhant Garg, Stephanie Miller, Joseph Groele, Abhijit Jassem, Drew Packard, and Marlon Ramos. To the parent figures who are not obligated but choose to treat me as family: Andrea Williams, Doug Williams, Patrick Russell (senior), and Candie Russell. To all my lab mates and colleagues, for the road is long but we push each other to the finish line: John Downing, Nicholas Adamowicz, Summing Qin, Aaron Huxford, Jiaxin Mao, Zachary Welker, Pei-Hsun Huang. A special mention to Dr. Qingqing Liu with whom I had the privilege to share many days and nights working in the lab, collaborating, and figuring it all out. To the post-doctorate researchers who mentored and provided guidance: Benedict Krohn, Robert Adams, Taehwan Ahn, and Juan Jose Serrano-Aguilera (aka el Tio). A special thanks to Victor Petrov who is a fearless leader, a source of knowledge, a thoughtful mentor, and a great friend, truly thank you. Last but not least, to Annalisa Manera, who chose to see and bring out the best in me, who is one of the most compassionate human beings, and whose brightness is admirable and intimidating. It has been a true privilege to walk alongside all of you, this was a humbling experience, and feel truly fortunate to have undertaken such interesting research topics; primarily the fact that I have radiation vision.

A special show of gratitude to the Bridge to Doctorate program, the Rackham Merit Fellowship (RMF) program, and the Nuclear Regulatory Commission (NRC) for providing fellowship and project funding. To the Nuclear Engineering and Radiological Sciences (NERS) department as I had the privilege of growing academically through my bachelors, masters, and doctorate. The faculty and staff that constitute the department build the sense of cohesion and family, after all we are in this together.

TABLE OF CONTENTS

LIST OF TABLES

LIST OF FIGURES

LIST OF APPENDICES

LIST OF ABBREVIATIONS

ABWR	Advanced boiling water reactor
ANL	Argonne National Laboratory
BWR	Boiling water reactor
CANDU	CANadian Deuterium Uranium
CBCT	Cone beam computed tomography
CdTe	Cadmium-Telluride
CDF	Cumulative distribution function
CFD	Computational fluid dynamics
CHF	Critical heat flux
CHROMA	Michigan High Resolution Tomographic Imaging
CPR	Critical power ratio
CT	Computed tomography
DBA	Design basis accident
DFFB	Dispersed flow film boiling
DNB	Departure from nucleate boiling
DNBR	Departure from nucleate boiling ratio
ECCS	Emergency core cooling system
ECMFL	Experimental and computational multiphase flow laboratory
ESF	Edge spread function
FBP	Filter back projection
FCI	Fuel coolant interactions
FDK	Feldkamp, Davis, and Kress
FOV	Field of view
FWHM	Full-width half max
GE	General Electric
HRGTS	High-resolution gamma tomography system
HWR	Heavy water reactor
IAFB	Inverted annular film boiling
IB	Incidence of Boiling
ISFB	Inverted slug film boiling
LMR	Liquid metal reactor
LOCA	Loss of coolant accident
LSF	Line spread function
LWR	Light water reactor
LYSO	$Lu_{1.8}Y_{0.2}SiO_5$
MARBLE	Michigan Adiabatic Rod Bundle Experiment
MFB	Minimum film boiling
MTF	Modulation transfer function
MUSE	Metallic uranium safety experiment
NRC	Nuclear Regulatory Commission
PBR	Pin bundle metallic fuel relocation
PCHT	Post-CHF heat transfer
PGSFR	Prototype generation-IV sodium cooled fast reactor
PWR	Pressurized water reactor
RCIR	Reactor core recirculation
RCP	Reactor coolant pump
RMSE	Root mean square error
RPM	Revolutions per minute
RPV	Reactor pressure vessel
RSD	Relative standard deviation

SFR	Sodium fast reactor	TC	Thermocouple
SG	Steam generator	UM	University of Michigan
SiPM	Silicon photomultiplier	WMS	Wire mesh sensor
STD	Standard deviation		

ABSTRACT

Computational advancements in the past couple of decades have propelled the capabilities to design, model, and benchmark nuclear reactor systems. However, the lack of high-resolution two-phase flow data has hampered the development and validation of high-fidelity models for computational fluid dynamics (CFD) and subchannel codes, in particular pertaining to Light Water Reactor (LWR) systems. Radiation based methods have gained traction and are being widely deployed for the study of two-phase flows. These methods present inherit advantages over conventional instrumentation due to their non-intrusiveness as well as the capability to perform measurements through complex and opaque geometries. The present dissertation is focused on the development of in-house gamma tomography and high-speed x-ray radiography systems and their application to high-resolution two-phase flow measurements. The two measurement systems were also applied to non-destructive measurements of sodium fast reactor mock-up fuel assemblies under severe accident scenarios.

A major contribution of this dissertation consisted in supporting the development and testing of the High-Resolution Gamma Tomography System (HRGTS). This is a computed tomography (CT) imaging device designed and assembled in-house at the Experimental and Computational Multiphase Flow Laboratory (ECMFL) with the purpose of performing high-spatial resolution void fraction measurements. This CT system is deployed at the Michigan Adiabatic Rod Bundle Flow Experiment (MARBLE) facility which consists of an 8 x 8 modular assembly designed to simulate scaled PWR and BWR assemblies. The present work discusses the design, construction, and operation of the MARBLE facility. This facility has been instrumented to establish a high-spatial resolution experimental database of two-phase flows inside reactor assembly geometries and investigate the effect of spacer grids and mixing vanes on void drift across subchannels. The present work discusses the design, construction, modeling, and initial measurements performed with the HRGTS at the MARBLE facility.

Additionally, the high-speed x-ray radiography imaging system was assembled and deployed at the post-CHF Heat Transfer (PCHT) facility. This experiment is designed to achieve post Critical Heat Flux (CHF) conditions to investigate the following two-phase flow regimes: Inverted Annular Film Boiling

(IAFB), Inverted Slug Film Boiling (ISFB) ranging to Dispersed Flow Film Boiling (DFFB). However, radiation-based measurements of boiling experiments bear several challenges due to the high temperature conditions which result in the following: mismatch of calibration to experimental conditions, x-ray beam hardening, thermal expansion, material and working fluid density. The present research focuses on developing methods to overcome these challenges and obtain meaningful quantitative results. These were validated through rigorous modeling and testing in which the aforementioned challenges are recreated. Preliminary pool boiling measurements are analyzed with the developed post-processing strategies at hand.

Lastly, in collaboration with Argonne National Laboratory (ANL), 3D-CT imaging measurements of the Pin Bundle Metallic Fuel Relocation (PBR) assemblies are carried out. The PBR assemblies were manufactured following the Prototype Generation-IV Sodium-cooled Fast Reactor (PGSFR) with the intent to investigate the relocation behavior of the metallic fuel in case of severe accidents in sodium fast reactors. The tested accident conditions include initial core disruption in which the molten fuel breaks through the cladding, the second mode involves severe core meltdown conditions in which a large amount of corium is suddenly dropped into the test assembly. High-resolution CT imaging of the PBR assemblies was performed using x-rays as well as a nominal 15 Ci ^{192}Ir radioisotopic source in conjunction with a high-resolution CdTe detector panel. The x-ray results show adequate qualitative reconstruction features wherever the molten uranium was not present, otherwise, photon starvation artifacts appear in the form of streaks around the fuel regions. The gamma-ray results properly resolved regions with moderate molten fuel material, these where then used to estimate the assembly flow blockage.

CHAPTER I

Introduction

1.1. Motivation

The current nuclear reactor fleet in the U.S. is comprised entirely of Light Water Reactors (LWRs), that supply 20% of the commercial baseload electricity around the country. The construction of the nuclear power plants fell stagnate during the late 1980s due to the escalating capital cost, lengthy construction process, loss of popular support, and the growth of competing forms of energy such as natural gas. The promise of a new generation of smaller reactor designs is fast approaching, with inherently safer systems, and economic viability. However, the prospect of deploying these reactors for commercial electricity production is pending, contingent to the rigorous licensing process. As long as LWRs are operational, essential research of these systems further strengthens the safe operation of these reactors and reinforces the safety culture of the nuclear sector as a whole.

Nuclear reactors are multi-physics systems whose operational foundations lie upon the interplay of nuclear physics, heat transfer, fluid dynamics, and chemistry. Early reactor research heavily relied on analytical modeling and experimental undertakings. Since, the experimental instrumentations has evolved due to technological advancements, achieving higher temporal and spatial resolutions. In parallel, computational breakthroughs over the past decades have facilitated the rapid design and analysis of the various aspects of these nuclear reactor systems. However, one of the areas which requires further understanding is the production of steam-gas and transport mechanisms of liquid-steam mixtures inside nuclear reactors; this topic is referred as two-phase flows and will be a central focus of the current research. In the case of LWR systems, the presence of steam affects the reactor power as well as the ability to remove heat during operation and accident scenarios.

Despite research efforts, there exists a lack of high-resolution two-phase flow data, which has hampered the development and validation of high-fidelity models for computational fluid dynamics (CFD) and subchannel codes, in particular pertaining to LWR rod bundle geometries. The present research aims to

provide tools to bridge this gap through the development of radiation transmission instrumentation and methods for the analysis of two-phase flow phenomena that occur inside nuclear reactor systems; the applied modalities include high-speed radiography and computed tomography (CT). Prior to diving into the premise of the present research, it is important to lay the foundations behind nuclear reactor systems to understand what the main challenges are. This chapter intends to systematically connect the fundamental concepts behind LWR systems and two-phase flow studies.

1.2. Thesis Outline

The present dissertation covers a wide range of topics focusing on the fields of radiation imaging intermingled with two-phase flow; for this reason, each chapter contains its own nomenclature given that there are several repeating Greek-variables that overlap within said fields, and these are adapted in accordance with the evolution of the dialogue. The references are arranged in alphabetical order. This work is organized to first introduce the principles behind LWR systems and the role of two-phase flows. We must then cover the theory behind the radiation detection to build the inner workings of the radiation imaging instrumentation that are deployed in the present research. Afterwards, the discussion shifts to describe the radiation measurement process of two-phase flows. This lays the ground for the extensive discussion covering the two separate experimental facilities designed for the study of two-phase flow in LWRs. Lastly, we perform non-destructive testing of test assemblies designed after up-and-coming advanced reactor systems. The dissertation is organized in the following chapters:

- **Chapter I** – This chapter introduces the basic concepts behind LWR systems, covering nuclear fission, heat transfer and two-phase flows. This then proceeds to review the types of LWRs deployed in the U.S., namely Pressurized Water Reactors (PWRs) and Boiling Water Reactors (BWRs). Lastly, it compiles a literature review of two-phase flow experiments pertaining to LWR systems and need for high-resolution data.
- **Chapter II -** Theoretical foundations of radiation transmission imaging covering the radiation transmission process and pertinent detection methodologies. This then segues into the working principles behind computed tomography imaging and allows us to introduce the developed imaging systems deployed in the present research; namely the High-Resolution Gamma-Tomography System (HRGTS) and the Michigan High Resolution Tomographic Imaging (CHROMA) system. Lastly, this chapter introduces the basics behind a custom ray-tracing modeling approach used in the

analysis of the measurements performed at the various experimental facilities considered throughout this research.

- **Chapter III -** Theory behind temporal varying void fraction signals measured with radiation transmission-based methods. Previous research theorized the concern of a phenomena called the dynamic bias which arises from the wrongful averaging of transient signals that occurs during radiation transmission measurements. This chapter emphasizes the development of a more accurate dynamic bias model and tests it with experimental signals of two-phase flow regimes.
- **Chapter IV -** Application of high-speed x-ray radiography to the measurement of steam-liquid flows at a post-CHF experimental facility. This chapter emphasizes on characterizing the identified radiation-transmission challenges that arise from high temperature effects such as thermal expansion, change in material density, phase changes of the working fluid, as well as x-ray beam hardening. This work provides a modeling framework to properly map low temperature calibration conditions to high temperature measurement conditions. In addition, it develops methods to evaluate the cross-sectional average void fraction along the axial direction of the test section; the method is validated by simulating the radiation detection system paired with bubbly and film boiling regimes. Lastly, it analyzes preliminary high-speed x-ray measurements performed for pool boiling.
- **Chapter V -** Design and construction of the Michigan Adiabatic Rod Bundle Experimental (MARBLE) facility consisting of an 8 x 8 rod bundle modeled after LWR systems. The objective is to perform high resolution CT measurements of two-phase flows in complex geometries representative of LWRs reactor cores. Prior to achieving set goals, extensive modeling of the CT system and the MARBLE facility is carried out to determine the imaging limitations, radiation noise analysis, and subchannel void fraction accuracy. This is then proceeded by preliminary void fraction CT measurements performed for two different rod-bundle gas distributions, including: uniform distribution and assembly centered distribution.
- **Chapter VI -** The final chapter focuses on non-destructive measurements of Sodium Fast Reactor (SFR) assemblies used to simulate hypothetical fuel relocation behavior under severe accident conditions. This involved 3D CT measurements using gamma-rays and x-rays. The gamma CT results are used to determine assembly flow blockage throughout the measured sections. This work was performed in collaboration with Argonne National Laboratory (ANL).

Nomenclature

Roman Variables

A	Area
A_v	Avogadro's number
a	Atomic fraction
C	Precursor concentration, or constant
C_p	Specific heat capacity
D	Diameter
d	Chordal-length
E	Energy
H	Enthalpy
h	Heat transfer coefficient
j	Superficial phase velocity
k	Thermal conductivity or neutron multiplication factor
L	Length
M	Molar mass
$\dot{m}$	Mass flow rate
$\vec{\boldsymbol{n}}$	Directional unit vector
N	Atomic density
P	Pressure or scattering probability distribution
p	Pitch
Q^{235}	Energy released per fission
$\dot{Q}$	Heat rate
$\dot{q}$	Pin power
R	Radius
r	Radial variable
RR	Reaction rate
S	Slip ratio or surface area
T	Temperature
t	Time
V	Volume
v	Velocity
$\dot{W}$	Pump power
X	Quality
$\boldsymbol{x}$	Spatial coordinates

Greek Variables

α	Void fraction or target atom mass coefficient
β	Delayed neutron fraction
Δ	Change in condition
δ	Delta function
ε	Fuel enrichment
η	Recovery factor
θ	Angle
λ	decay constant
μ_s	Scattering cosine
ν	Produced neutrons
ρ	Density
τ	Thickness
Σ	Macroscopic cross-section
σ	Microscopic cross-section
χ	Neutron emission spectrum
ψ	Angular flux
Ω	Thermal resistance

Subscripts & Superscripts

235	Uranium 235 isotope
238	Uranium 238 isotope
2φ	Two-phase flow
φ	Single phase
B	boundary

clad	Cladding	L	Liquid
cm	Center of mass	p	Prompt
cool	Coolant	O	Oxygen
core	Reactor core	o	origin or base value
d	Delayed	*out*	Outer boundary
Fl	Flow	s	Scattering
f	Final condition or fission	*sat*	Saturation
fuel	Fuel	*sc*	Subchannel
G	Gas	*source*	Source
gap	Fuel-cladding gap	T	Total
h	Hydraulic	*Th*	Thermal
i	Initial condition, or indexing variable	U	Uranium
in	Inner boundary	UO_2	Uranium Oxide

1.3. Background

1.3.1. History of Nuclear Power

The discovery of nuclear fission took place in 1938 by two German scientists, Otto Hahn and Fritz Strassmann, who were the first to measure the split of the Uranium atom caused by a thermal neutron, for which the theoretical background was developed shortly after by Otto Frisch and Lise Meitner, as narrated by Salvetti [158]; two impactful publications both in *Nature* titled *"Disintegration of uranium by neutrons: a new type of nuclear reaction"* by Meitner and Frisch, as well as *"Physical evidence for the division of heavy nuclei under neutron bombardment"* by Frisch would follow soon after. The exciting scientific discovery was eclipsed by the geopolitical scenery that was foreshadowing World War II. In light of the political tensions brewing in Europe, many renown scientists flew into exile, amongst these was Enrico Fermi who would go onto join the physics department at Columbia University. Soon after arriving at Columbia University, Enrico Fermi learned about the prospect of nuclear fission, which would become his life-long obsession. Through experiments, Fermi and his team would go on to show that at least two neutrons would be emitted following a fission reaction; this process can be summarized as $(n, 2n)$. Leo Szilard, one of Fermi's collaborators, saw the potential that the $(n, 2n)$ reaction could have, a multiplicative effect which would become the basis to sustain or unleash a chain reaction. Mindful of the ongoing discoveries, this

information was handled with outmost secrecy to avoid tipping off the German counterparts. Soon after, President Roosevelt was informed by Albert Einstein about the potential implications of Fermi's and Szilard's fission reaction research, with anguish that the Germans could be conducting similar research. Without hesitancy, Roosevelt instated the Advisory Committee on Uranium to coordinate the research effort throughout the various U.S. laboratories. As the scientific effort made headway, Louisa Bonolis [20] notes Fermi's initial remarks of utilizing this chain reaction for energy production:

> *"Until the summer of 1941, research focused on the possibility of using the chain reaction for production of power rather than for explosion in a bomb. Fermi, because of this, wrote a report in which he mainly discussed some general points of view as to the methods that could be employed for using a chain reaction in uranium as a source of energy, and submitted it to the Uranium Committee on June 30, 1941"* (pp. 359).

By the end of that year, Japan attacked Pearl Harbor, an event which would accelerate the research effort to attain nuclear weapons. The Metallurgical Laboratory was established at the University of Chicago to carry-out top-secret experiments which would be known as *the exponential pile experiments*, a research effort in which Fermi would play a crucial role. The efforts would focus on converging into a system which could yield a multiplication factor $k = 1$. This multiplication factor essentially describes the ratio between the new generation of neutrons produced in comparison to the previous generation that caused the fission events; thus $k < 1$ occurs when there are more losses than new neutrons which describes a subcritical system, $k = 1$ occurs as the new and old population remains constant which describes a critical system, and $k > 1$ occurs when the population becomes successively larger which describes a supercritical system. On December 2$^{\text{nd}}$, 1942, Enrico Fermi along with the greatest scientific and engineering minds of the time proved that energy could be produced as a result of stable self-sustaining fission chain reactions in the Chicago Pile-1 (CP-1) experiment [50]. This moment in time marked the birth of nuclear reactors as CP-1 became critical for 28 minutes with an output power of 0.5 watt. The secretive scientific foundation for reactor systems would not be shared with the world until the first Geneva Summit in 1955 [50].

1.3.2. Basic Principles of Nuclear Reactor Systems

The present discussion will focus on a small overview behind the principles of nuclear reactor systems, a topic covered in extensive detail by Duderstadt and Hamilton [37] (neutronics), Larsen and Kiedrowski (neutronics) [103], Ott and Neuhold [137] (reactor kinetics), Todreas and Kazimi [180] (thermal-hydraulics),

and lastly Masterson [117] (thermal-hydraulics). This intends to highlight the various levels of complexity of the multi-physics coupled system that constitutes a nuclear reactor, focusing primarily on LWRs. We shall begin by laying the basics starting from nuclear fission, then heat transfer, fluid mechanics, and lastly a discussion about two-phase flow phenomena.

1.3.2.1. Neutrons and Fission Reactions

The fission reaction can be induced for many heavy isotopes, amongst these ^{232}Th, ^{233}U, ^{235}U, ^{238}U, ^{239}Pu, ^{240}Pu, and ^{241}Pu to name a few. The primary focus of this discussion will center around the ^{235}U fission reaction because it is the primary isotope used in the current fleet of civil purposed nuclear reactors around the United States. The reactor fuel is fabricated in UO_2 ceramic pallets containing 2 - 4% ^{235}U enrichment, while the remainder is ^{238}U. The relative abundance of Uranium found in nature is composed 99.28% by ^{238}U, while its less abundant sibling ^{235}U corresponds to 0.72% [117], hence the need to extract and enrich the composition of the nuclear fuel. Let us now imagine for a moment an ensemble of neutron particles flying towards a thin layer of heavy Uranium atoms; some might pass through the interstitial gaps, others will scatter off the target nuclei, some may be captured, and others may produce fission reactions. The likelihood that a neutron will interact by one of these mechanisms is dictated by the neutron's energy as well as the cross-sectional area σ of interaction of the target atom. These interaction cross sectional areas are depicted as a function of incident neutron energy in Fig. 1.1 for ^{235}U and ^{238}U, given that these are the primary isotopes found in the fuel; these cross sections are defined in units of barns [b] which are equivalent to b=10^{-24} cm^2. In the case of the ^{235}U isotope the cross section is dominated by elastic scattering at high neutron energies, however, the fission cross section becomes the dominant mechanism at lower or *thermal* neutron energies.

The absorption cross-section remains consistently lower than that for fission, therefore playing a secondary less likely neutron removal role. Another important feature that needs to be highlighted is the resonance region, this arises from the constructive wavefunction overlap between the target nuclei and the passing neutron which as a result enhances the probability of interaction; the origins of resonance between particles is best explained by Krane et al. [99]. Now let's contrast ^{238}U, which is fissile only at high neutron energies, or for so called *fast neutrons*, and the fission cross section is significantly reduced at low energies. The predominant cross section corresponds to elastic scattering, yet the absorption cross section becomes greatly enhanced for a large part of the resonance region with peaks well above those of ^{235}U. For these

reasons ^{238}U is primarily fertile, meaning that it absorbs neutrons and breeds heavier isotopes. This characteristic makes ^{238}U and interesting fuel for fast breeder reactors.

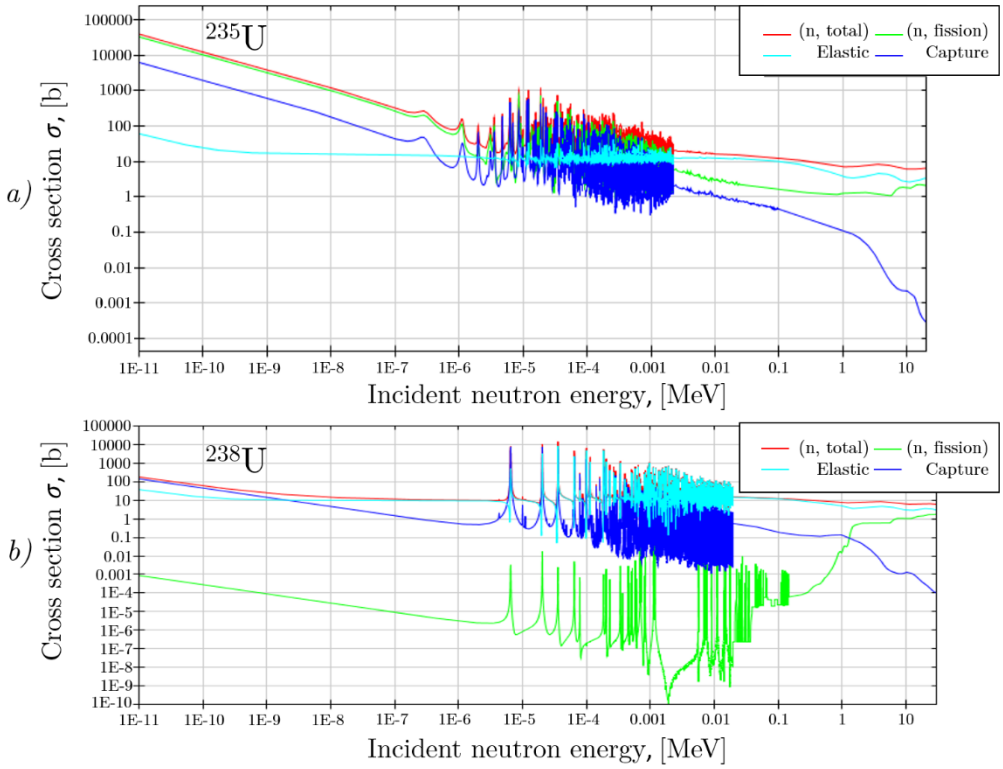

Fig. 1.1. Neutron and uranium interaction cross sections; *a)* ^{235}U and *b)* ^{238}U. The data was obtained from ENDF B-VII.1 library [25].

We now dive into the spreading the ^{235}U nuclei throughout the fuel to ultimately describe the reaction rates between the nuclei and the neutrons. First, one must formulate the molecular or atomic density of a material, which can be defined as

$$N = \frac{\rho\, A_v}{M}$$
$$\left[\frac{\text{atoms}}{\text{cm}^3}\right] = \left[\frac{\text{kg}}{\text{cm}^3}\right]\left[\frac{\text{mol}}{\text{kg}}\right]\left[\frac{\text{atoms}}{\text{mol}}\right] \qquad \text{Eq.(1-1)}$$

where A_v is Avogadro's number (0.60225 x 10^{24}), ρ is the material density and M is the molar mass or atomic mass (depending if it is a compound or a pure element, respectively). Now if we consider UO_2 fuel, we can define the molecular mass as

$$M_{UO_2} = aM_{235} + (1-a)M_{238} + 2M_O. \qquad \text{Eq.(1-2)}$$

in which a is the atomic fraction, as well as the corresponding atomic masses of ^{235}U is $M_{235} = 235.0439$ and for ^{238}U is $M_{235} = 238.0508$. Todreas and Kazimi [180] shows that the enrichment can then be defined as

$$r = \frac{aM_{235}}{aM_{235} + (1-a)M_{238}}. \qquad \text{Eq.(1-3)}$$

The atomic fraction of ^{235}U in the fuel can then be defined based on a specific enrichment ε as

$$a = \frac{\varepsilon}{\varepsilon + \frac{M_{235}}{M_{238}}(1-\varepsilon)} \qquad \text{Eq.(1-4)}$$

Lastly, we consider the density of the fuel ρ_{UO_2}= 10.97 g/cm^3 as provided by Masterson [117]. With all this in hand we can estimate the ^{235}U atom density in the fuel as

$$N_{235} = a \frac{\rho_{UO_2} A_v}{M_{\mathrm{UO_2}}}. \qquad \text{Eq.(1-5)}$$

The atomic density is used to estimate the macroscopic cross section of the material

$$\begin{gathered} \Sigma(E) = N \sigma(E) \\ \left[\frac{\text{atoms}}{\text{cm}} \right] = \left[\frac{\text{atoms}}{\text{cm}^3} \right] [\ \text{cm}^2\ ]. \end{gathered} \qquad \text{Eq.(1-6)}$$

The macroscopic cross sections are dependent on the neutron energy and can be defined for scattering, capture, fission as well as the total sum of interactions. This property is useful in describing many of the processes occurring inside the reactor; these are also analogous to the linear attenuation coefficient that is used to describe photon interactions with matter, a topic that will be discussed in the next chapter. The reaction rate for a given interaction can be described using the macroscopic cross section and the angular neutron flux

$$RR(\boldsymbol{x}, E, t) = \int_{4\pi} \Sigma(\boldsymbol{x}, E)\ \psi(\boldsymbol{x}, \vec{\boldsymbol{n}}, E, t)\ d\vec{\boldsymbol{n}}. \qquad \text{Eq.(1-7)}$$

Here ψ is the angular neutron flux which describes the number of photons located at $\boldsymbol{x}$, traveling in direction $\vec{\boldsymbol{n}}$ (unit vector), at time t, with energy E; this has units of [neutrons/(cm^2 s MeV sr)] in which sr is the unit steradian. The reaction rate is considered for neutrons traveling over all directions resulting in the integration over the surface area of the unit sphere and therefore over 4π.

The ^{235}U fission reactions induced by thermal neutrons release roughly 200 MeV in the form of particle kinetic energy, we will refer to this energy release as Q^{235}. As Fermi had measured, more neutrons are expelled from the fission reaction, these are referred as prompt neutrons ν_p, and on average 2.6 neutrons are emitted from the fission of ^{235}U; these neutrons are released according to the fission emission spectrum $\chi_p(E)$ where E is the energy of the emitted neutrons. Todreas and Kazimi [180] highlights that roughly 95% of the released energy is recoverable inside a nuclear reactor system; losses include leakage of particles outside of the system as well as production of elusive neutrinos. The released energy is then deposited within

the surrounding materials as the fission fragments, gamma-rays, alpha particles, and released neutrons collide with atoms along their path. The aforementioned fission chain reaction process is depicted in Fig. 1.2. The neutrons produced from the fission reactions can then be described as

$$\chi_p(E)\ \nu_p\ RR_f(\boldsymbol{x},E,t)\ =\ \chi_p(E)\nu_p\int_{4\pi}\Sigma_f(\boldsymbol{x},E)\ \psi(\boldsymbol{x},\vec{\boldsymbol{n}},E,t)\ d\vec{\boldsymbol{n}}. \qquad \text{Eq.(1-8)}$$

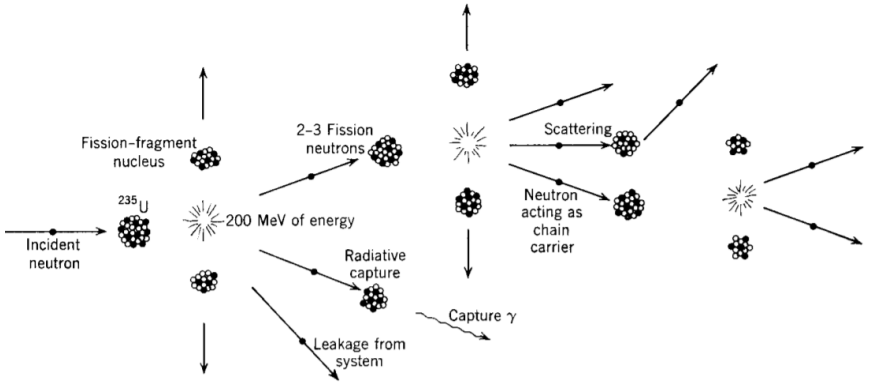

Fig. 1.2. ^{235}U fission reaction process republished from Duderstadt and Hamilton [37].

A large part of the fission fragments (daughter nuclei) are unstable, thus resulting in more nuclear decay reactions which further supply neutrons into the reaction chain, these are often referred as *delayed neutron precursors*. On average, in thermal reactors, 0.016 ± 0.005 delayed neutrons ν_d are emitted with a corresponding emission spectrum $\chi_d(E)$ as a result of the ^{235}U fission reaction [137]. The time scale at which these precursors atoms decay is relatively large in comparison to the prompt fission reactions; the decay constants for the precursor atoms are λ and their concentration is C. The delayed neutron emissions are typically lumped into six different groups ranging in time emission time scales from the shortest 0.26 s to the longest 78.7 s. The existence of delayed neutrons is vital to the kinetic control of the reactor system during startup, normal operation and shut down for a reactor cannot shutdown faster than the slowest decaying group. These precursor emitters are responsible for the remaining neutron generation and fission events after shut down, which are a source of fission products resulting in the release of decay heat. The production and loss of precursor atoms can be described by

$$\frac{dC_i}{dt}(\boldsymbol{x},t) = \underbrace{-\lambda_i C_i(\boldsymbol{x},t)}_{\text{Loss from decay}} + \underbrace{\int_0^\infty\int_{4\pi}\beta_i(\nu_p+\nu_d)\Sigma_f(\boldsymbol{x},E)\ \psi(\boldsymbol{x},\vec{\boldsymbol{n}},E,t)\ d\vec{\boldsymbol{n}}\ dE}_{\text{Precursor production from fission reactions}}; \qquad \text{Eq.(1-9)}$$

here, i is the precursor group index, $\nu_p+\nu_d$ is the total number of fission neutrons, and β is the corresponding fractional yield for the precursor group.

The focus now shifts to the neutron thermalization mechanism which is fundamental to the sustainability of the chain reaction, although this will be a superficial discussion of the process. In principle, the high-energy prompt neutrons lose and transfer energy through a series of scattering events. One could visualize this process as a billiard ball that decelerates and changes direction as it collides with other balls along its path. Following the derivation by Duderstadt and Hamilton [37], the final neutron energy of a scattered neutron can be described as

$$E_f = \left[\frac{(1+\alpha)+(1-\alpha)\cos\theta_{cm}}{2}\right] E_i, \qquad \text{Eq.(1-10)}$$

where E_i is the initial energy, E_f is the final neutron energy, θ_{cm} is the scattering angle in the center of mass perspective and α is

$$\alpha = \left[\frac{A-1}{A+1}\right]^2, \qquad \text{Eq.(1-11)}$$

in which A is the atomic mass of the target nuclei. The expression of Eq.(1-9) shows that when the scattering angle $\theta_{cm} = 0$, then $E_f = E_i$ symbolizing that a collision did not occur. Now, in the case when $\theta_{cm} = 180°$, then $E_f = \alpha E_i$ meaning that this is the maximum loss of energy or down scattering a neutron can experience through a collision event. The resulting elastic scattering probability distribution is

$$P(E_i \to E_f) = \begin{cases} \dfrac{1}{(1-\alpha)E_i}, & \alpha E_i \le E_f \le E_i \\ 0, & otherwise \end{cases}. \qquad \text{Eq.(1-12)}$$

The average final energy of the neutron can then be estimated as

$$\overline{E}_f = \int_{\alpha E_i}^{E_i} P(E_i \to E_f)\ E_f\ dE_f = \int_{\alpha E_i}^{E_i} \frac{1}{(1-\alpha)E_i} E_f\ dE_f \qquad \text{Eq.(1-13.}a\text{)}$$

$$= \frac{1}{(1-\alpha)E_i}\ \frac{{E_f}^2}{2}\Bigg|_{\alpha E_i}^{E_i} = \frac{(1+\alpha)}{2} E_i. \qquad \text{Eq.(1-13.}b\text{)}$$

And the average fractional energy loss

$$\frac{\overline{\Delta E}}{E_i} = \frac{E_i - \overline{E}_f}{E_i} = \frac{(1-\alpha)}{2} \qquad \text{Eq.(1-14)}$$

This consequential loss of energy is obtained by using a moderator material, which allows "thermalizing" the neutrons such that they can cause a fission reaction with the ^{235}U atom. Table 1.1 compares some of the common elements found in nuclear reactors, such as coolant (water, helium), moderator (water or graphite), cladding (zircoloy compound) and fuel (UO_2). It is worth highlighting the fact that lighter atoms such as hydrogen are more efficient at down scattering the neutron energy, while the heavier elements as those found in the cladding and fuel are emphatically inefficient. For this reason, the moderator material is selected with a characteristically low atomic mass, and a low absorption cross section to minimize parasitic

neutron losses in the moderator itself.

The scattering event also results in a change in direction from $\vec{\boldsymbol{n}}_{\boldsymbol{i}}$ to $\vec{\boldsymbol{n}}_{\boldsymbol{f}}$, this creates a scattering cone of equal probability as a result of the dot product of the two directional vectors $\vec{\boldsymbol{n}}_{\boldsymbol{i}} \cdot \vec{\boldsymbol{n}}_{\boldsymbol{f}}$. Therefore, if the final energy is known, then the scattering cosine μ_s of the event can be described as

$$\mu_s(E_i \to E_f) \;=\; \left(\frac{A+1}{2}\right)\sqrt{\frac{E_f}{E_i}} \;-\left(\frac{A-1}{2}\right)\sqrt{\frac{E_i}{E_f}}. \qquad \text{Eq.(1-15)}$$

Ultimately, we can define the differential macroscopic scattering cross section as

$$\Sigma_s(\vec{\boldsymbol{n}}_{\boldsymbol{i}} \cdot \vec{\boldsymbol{n}}_{\boldsymbol{f}}, E_i \to E_f) \;=\; \Sigma_s(E_i) P(E_i \to E_f) \frac{\delta(\vec{\boldsymbol{n}}_{\boldsymbol{i}} \cdot \vec{\boldsymbol{n}}_{\boldsymbol{f}} \;-\; \mu_s(E_i \to E_f))}{2\pi}; \qquad \text{Eq.(1-16)}$$

here, δ is represents the delta function which sifts the scattering cosine of the interaction. From here onward the initial energy will be changed from E_i to E', and the resulting scattered energy will be switched form E_f to simply E; similar changes are also applied to the directional unit vectors.

Table 1.1. Comparison of neutron average fractional energy loss for common reactor elements

Element	**Atomic Mass [amu]**	α	$\overline{\Delta E}/E_i$
Hydrogen [H]	1.008	0	0.500
Helium [He]	4.003	0.360	0.320
Carbon [C]	12.011	0.7162	0.142
Oxygen [O]	15.999	0.779	0.111
Zirconium [Zr]	91.224	0.957	0.022
Uranium [^{235}U]	235.044	0.983	0.008

The time dependent neutron transport equation best describes the processes occurring inside nuclear reactors. A proper derivation and explanation of the neutron transport equation is shown by Larsen and Kiedrowsky [103]. For the time being, this equation can be formulated based on the various different mechanisms that have been previously discussed:

$$\underbrace{\left(\frac{1}{v(E)}\frac{\partial}{\partial t} + \vec{\boldsymbol{n}} \cdot \boldsymbol{\nabla} + \Sigma_T(\boldsymbol{x}, E)\right)\psi}_{\substack{\text{Time change} \\ \text{+ Leakage out of the system} \\ \text{+ Losses from interaction}}} \;=\; \underbrace{\int_0^{\infty}\int_{4\pi} \Sigma_s(\vec{\boldsymbol{n}}' \cdot \vec{\boldsymbol{n}}, E' \to E)\; \psi(\boldsymbol{x}, \vec{\boldsymbol{n}}', E', t)\, d\vec{\boldsymbol{n}}'\; dE'}_{\text{Scattering from } E' \text{ to } E, \;\; \text{and } \vec{\boldsymbol{n}}' \text{ to } \vec{\boldsymbol{n}}}$$

$$+ \;\underbrace{\sum_i \frac{\chi_{d,i}(E)}{4\pi}\lambda_i C_i(\boldsymbol{x}, E)}_{\text{Delayed Neutrons from Precursors}} \;+\; \underbrace{\frac{\chi_p(E)}{4\pi}\int_{4\pi} \nu_p \Sigma_f(\boldsymbol{x}, E)\; \psi(\boldsymbol{x}, \vec{\boldsymbol{n}}', E', t)\; d\vec{\boldsymbol{n}}'\; dE'}_{\substack{\text{Prompt neutrons from fission caused by} \\ \text{neutrons with energy } E' \text{ from direction } \vec{\boldsymbol{n}}'}}. \qquad \text{Eq.(1-17)}$$

where v is the neutron velocity and Σ_T is the total macroscopic cross section which considers all interactions (neutron capture is embedded in this term); we drop the angular flux phase space dependencies unless it explicitly requires calling the dependence such as the incident energy E' and direction $\vec{\boldsymbol{n}}'$. The expression above describes the balance between neutron productions and losses. The objective is to maintain the population of neutrons in steady state and thus removing the time dependencies. However, this is not necessarily always the case, for instance in the case in which a neutron absorber/poison is suddenly removed will incur a change in rate of the population, or what is called a reactivity insertion. This topic relates to the dynamics of the reactor system. The neutron transport equation is difficult to solve, often times requiring vast simplifications, otherwise deploying numerical methods in order to solve it. However, this is not the topic of this thesis, the present discussion merely serves to lay the foundation behind nuclear reactor systems, as one can imagine these are complex machines that require meticulous consideration.

1.3.2.2. Heat Transfer

The power production and heat removal of the system are the next fundamental principles, these topics are of great importance in regard to the operation and safety margins of the reactor. Light water reactor (LWR) systems, which will be the central focus of the present work, deploy cylindrical fuel pallets encased in zirconium cladding. Here, heat is generated within the fuel pallet, this is then dissipated through the cladding and onto the bulk coolant. Other fuel geometries could include planar and spherical (i.e., TRISO fuel) geometries, however these will not be considered in the current discussion. A simple overview of the heat transfer mechanisms will be discussed next. First, we must introduce the heat transfer equation which is derived from the energy balance equation, this is prescribed as:

$$\underbrace{\rho(\boldsymbol{x},t)C_p(\boldsymbol{x},t)\frac{\partial T(\boldsymbol{x},t)}{\partial t}}_{\text{Temporal Change}} = \underbrace{\nabla\cdot k(\boldsymbol{x},T)\nabla T(\boldsymbol{x},t)}_{\text{Heat Diffusion}} + \underbrace{q'''_{gen}(\boldsymbol{x},t)}_{\text{Heat Generation}} \quad , \qquad \text{Eq.(1-18)}$$

in which T is the temperature and the properties of the material including the specific heat capacity C_p, the density ρ, and the thermal conductivity k. It is important to note that the heat conductivity is also a function of the local temperature and spatial distribution, this increases the complexity of the equation, however it can be approximated as constant for simple calculations. The expression above allows one to estimate the temperature distribution within a component such as the fuel pallet.

The heat generated within the fuel can be estimate following the definition from Todreas and Kazimi [180], which formulates the volumetric heat rate generated from fission reactions as

$$
\begin{aligned}
q'''_{gen}(\boldsymbol{x},t) &= \int_0^{\infty}\int_{4\pi} \eta\ Q^{235}\Sigma_f(\boldsymbol{x},E)\ \psi(\boldsymbol{x},\vec{\boldsymbol{n}},E,t)\ d\vec{\boldsymbol{n}}\ dE\,, \\
&= \eta\ Q^{235}\ RR_f(\boldsymbol{x},t), \qquad \text{Eq.(1-19)} \\
&= \left[\frac{\text{MeV}}{\text{cm}^3\ \text{s}}\right] \text{or} \left[\frac{\text{J}}{\text{cm}^3\ \text{s}}\right]\ \text{or}\ \left[\frac{\text{W}}{\text{cm}^3}\right]
\end{aligned}
$$

mindful that Q^{235} is the energy released per fission event and η is the 95% recovery rate. This expression describes the total energy generated per unit volume per unit time, produced by fission reactions at location $\boldsymbol{x}$ and time t. This term becomes the source of heat in the heat conduction equation. To estimate the temperature profile within the fuel, one must solve Eq.(1-17) mindful that q'''_{gen} is a function of space and time unless otherwise stated constant. The left-hand side of Eq.(1-17) can be eliminated under steady state conditions, which also removes the time dependencies resulting in only spatial dependencies. The total heat rate (or power) generated and/or dissipated in the system must be conserved; the generated power has the following relations:

$$
\dot{q} = \int_L \underbrace{q'(z)}_{\substack{\text{Linear}\\ \text{Heat}\\ \text{Rate}}}\ dz\ = \int_S \underbrace{\vec{q}\,''(\boldsymbol{x})}_{\substack{\text{Heat}\\ \text{Flux}}} \cdot \overrightarrow{\boldsymbol{r}}\ dS = \int_V \underbrace{q'''(\boldsymbol{x})}_{\substack{\text{Volumetric}\\ \text{Heat}\\ \text{Rate}}}\ dV, \qquad \text{Eq.(1-20)}
$$

where $\dot{q}$ is the total power by a component (i.e. the fuel pin), q' $[W/cm]$ is the linear heat rate generation that is integrated along the axial direction (for cylindrical geometry), $\vec{q}\,''$ $[W/cm^2]$ is the heat flux whose dot product with $\overrightarrow{\boldsymbol{r}}$ describe the propagation along the radial direction and therefore is integrated over the surface area. Lastly, q''' $[W/cm^3]$ is the volumetric heat rate which must be integrated over the volume. Let us consider a steady-state cylindrical fuel pellet with constant $q'''(\boldsymbol{x}) = q'''_o$, in this case $\dot{q}$ is solved using the heat generated within the fuel,

$$
\dot{q} = 2\pi\ L \int_{R_{in}}^{R_{out}} q'''_o\ r\ dr\ = q'''_o \pi\ L\ (R^2_{out} - R^2_{in}). \qquad \text{Eq.(1-21.}a\text{)}
$$

$$
q'''_o = \frac{\dot{q}}{\pi\ L\ (R^2_{out} - R^2_{in})} \qquad \text{Eq.(1-21.}b\text{)}
$$

where R_i is the inner fuel radius, R_o is the outer fuel radius, and L is the height of the pallet/fuel-region. The heat equation for the fuel would be the following

$$
0 = \frac{1}{r}\frac{\partial}{\partial r}\left(k_{fuel}\ r\ \frac{\partial T}{\partial r}\right) + q'''_o \qquad \text{Eq.(1-22.}a\text{)}
$$

$$
\int \partial\left(k_{fuel}\ r\ \frac{\partial T}{\partial r}\right)\ = -\int q'''_o r\ \partial r \qquad \text{Eq.(1-22.}b\text{)}
$$

$$
k_{fuel}\ r\ \frac{\partial T}{\partial r} = -q'''_o \frac{r^2}{2}\ +\ C \qquad \text{Eq.(1-22.}c\text{)}
$$

Then, the boundary condition at $r = R_{in}$ is imposed such that $\frac{\partial T}{\partial r} = 0$, and we solve for C

$$C \;=\; q_o''' \frac{R_{in}^2}{2} \qquad \text{Eq.(1-22.}d\text{)}$$

Eq.(1-22.a) then becomes

$$\partial T = \frac{q_o'''}{2\ k_{fuel}} \left(\frac{R_{in}^2}{r} - r \right) \partial r, \qquad \text{Eq.(1-23.}a\text{)}$$

$$\int_{T_{fuel,out}}^{T(r)} \partial T = \frac{q_o'''}{2\ k_{fuel}} \int_{R_{out}}^{r} \frac{R_{in}^2}{r'} \;-\; r'\ \partial r', \qquad \text{Eq.(1-23.}b\text{)}$$

$$T(r) = \frac{q_o'''}{4\ k_{fuel}} \left[2\ R_{in}^2\, ln \left(\frac{r}{R_{out}} \right) + (R_{out}^2 - r^2) \right] + T_{fuel,out}, \qquad \text{Eq.(1-23.}c\text{)}$$

where $T_{f,o}$ is the outer surface temperature of the fuel, and by substituting Eq.(1-21.b) in terms of the total power results in

$$T(r) = \frac{\dot{q}}{4\pi\ L\ k_{fuel}\ (R_{out}^2 - R_{in}^2)} \left[2\ R_{in}^2\, ln \left(\frac{r}{R_{out}} \right) + (R_{out}^2 - r^2) \right] + T_{fuel,out}, \qquad \text{Eq.(1-23.}d\text{)}$$
$$where\ R_{in} \le r \le R_{out}.$$

This is a general equation for an annular fuel pellet with constant volumetric heat generation. The maximum temperature occurs at $r = R_i$, and can be expressed as

$$T_{max} = \frac{\dot{q}}{4\pi\ L\ k_{fuel}} \left[2\, ln \left(\frac{R_{in}}{R_o} \right) \left(\frac{R_o^2}{R_{in}^2} - 1 \right)^{-1} + 1 \right] + T_{f,o} \qquad \text{Eq.(1-24)}$$

The cylindrical pellet (non-annular) is then reduced in the case where the inner radius is equal to zero and thus the temperature profile becomes

$$\lim_{R_{in} \to 0} T(r) \;=\; \frac{\dot{q}}{4\pi\ L\ k_{fuel}} \left(1 - \frac{r^2}{R_{out}^2} \right) + T_{fuel,out}, \qquad \text{Eq.(1-25)}$$

and for which the maximum temperature is

$$T_{max} = \frac{\dot{q}}{4\pi\ L\ k_{fuel}} \;+ T_{fuel,out}\ . \qquad \text{Eq.(1-26)}$$

The present discussion intends to demonstrate the heat produced and conducted within the fuel. Although the examples are simple, the complexity of the solution becomes contingent to the spatial and temporal definition of $q_{gen}'''(\boldsymbol{x}, t)$.

The heat transport through the conductive mediums such as the cladding material is considered next. In the case of conductive mediums, it is appropriate to apply Fourier's Law which describes the heat flux in terms of the thermal conductivity and the temperature gradient

$$\vec{q}\,''(\boldsymbol{x}) \;=\; -k\ \nabla T(\boldsymbol{x}), \qquad \text{Eq.(1-27)}$$

and can be substituted into the heat diffusion term in Eq.(1-18) and dotted with $\overrightarrow{\boldsymbol{r}}$ will yield the component of the heat flux in the radial direction. The temperature profile in the absence of an internal heat source

within the material as would be the case for the cladding can be solved using Eq.(1-27) as:

$$q''(r) \;=\; \frac{\dot{q}}{2\pi L r} = -k_{clad}\frac{dT}{dr}, \qquad \text{Eq.(1-28.}a\text{)}$$

$$\int_{T_{clad,out}}^{T(r)} dT' = \frac{\dot{q}}{2\pi\ L\ k_{clad}}\int_{r}^{R_{clad,in}+\tau_c}\frac{dr'}{r'}, \qquad \text{Eq.(1-28.}b\text{)}$$

$$T(r) = \frac{\dot{q}}{2\pi\ L\ k_{clad}}\ln\left(\frac{R_{clad,in}+\tau_{clad}}{r}\right) + T_{clad,out}; \qquad \text{Eq.(1-28.}c\text{)}$$

$$\text{where} \qquad R_{clad,in} \le r \le R_{clad,in}+\tau_{clad},$$

where k_{clad} is the cladding conductivity, L is the axial length of the cladding, $R_{clad,in}$ is the cladding inner radius, τ_{clad} is the cladding thickness, and $T_{clad,out}$ is the temperature at the outer surface of the cladding. The temperature at the inner radius of the cladding is then

$$T_{clad,in} = \frac{\dot{q}}{2\pi\ L\ k_{clad}}\ln\left(1+\frac{\tau_{clad}}{R_{clad,in}}\right) + T_{clad,out}. \qquad \text{Eq.(1-29)}$$

The second form of heat removal is by means of convection obtained from Newton's law of cooling; this is representative of the heat transfer mechanism across the fuel-cladding gap as well as the cladding coolant interface. In this case the heat flux between a surface and liquid or gaseous (i.e., the coolant) interface must be defined differently since this becomes a convective boundary, in this case the heat flux is defined as

$$\begin{aligned} q''(\boldsymbol{x_B}) &= h\Delta T, \\ \left[\frac{W}{cm^2}\right] &= \left[\frac{W}{cm^2\ K}\right][K] \end{aligned} \qquad \text{Eq.(1-30)}$$

in which $\boldsymbol{x_B}$ is the boundary surface location (i.e., cladding surface-radius, $R_{clad,in}+\tau_{clad}$), ΔT is the change in temperature across the convective boundary (i.e. gas, fluid), h is the heat transfer coefficient. This latter parameter must be determined based on empirical correlations described for the fluid/gas composition (i.e., water, metallic fluids, organic fluids), flow conditions (i.e., free convection or forced circulation) and rod bundle lattice formation; these empirical correlations are typically described by the Reynolds (Re), Grashof (Gr) and Prandtl (Pr) numbers, these relations are covered in detail by Todreas and Kazimi [180]. Typically, the gap that exists between the fuel pellet and cladding is filled with a pressurized gas such as helium to improve the heat transfer across these components. The heat transfer through the existing gap between the fuel and cladding is then defined as

$$q''(R_{clad,in}) \;= \frac{\dot{q}}{2\pi\ L\ R_{clad,in}} = h_{gap}(T_{fuel,out} - T_{clad,in}), \qquad \text{Eq.(1-31)}$$

for which $T_{fuel,out}$ is the outer fuel temperature, and $T_{clad,in}$ is the cladding inner radius temperature. Similarly, the convective boundary between the cladding and coolant is define

$$q''(R_{clad,out}) \ = \frac{\dot{q}}{2\pi \ L \ R_{clad,out}} = h_{cool}(T_{clad,out} - T_{cool,\infty}), \qquad \text{Eq.(1-32)}$$

where h_{cool} is the coolant's heat transfer coefficient, $T_{c,out}$ is the cladding outer surface temperature, $T_{cool,\infty}$ is the average bulk coolant temperature. Lastly, the heat generated from an individual pin and transferred onto the flowing coolant can be described through the following relation, assuming for simplicity a constant coolant specific heat C_p

$$\begin{aligned} \dot{q} &= \dot{m} \ C_p \ \Delta T \\ [W] &= \left[\frac{kg}{s}\right] \left[\frac{J}{kg \ K}\right] [K] \end{aligned} \qquad \text{Eq.(1-33)}$$

for which $\dot{m}$ is the mass flow rate of the coolant. Therefore, we can rearrange the above equation and solve for the change in temperature along inlet to the outlet of the coolant channel

$$\Delta T = \frac{\dot{q}}{\dot{m} \ C_p} \qquad \text{Eq.(1-34)}$$

The temperature change is estimated between the inlet and outlet of the core; this is for single phase fluids (all-liquid or all-gas)

$$(T_{out} - T_{in})_{cool} = \frac{\dot{q}}{C_p \ \dot{m}_{cool}}. \qquad \text{Eq.(1-35)}$$

A simple graphical example of the heat transfer process through the nuclear fuel pellet is illustrated in Fig. 1.3. The various materials impose a resistance to the flow of heat through them; this is analogous to the resistance that the electric current experiences as it flows through components in series. Based on this analogy, the resistance of a system can be formulated as

$$\begin{aligned} \Delta T = & \ \dot{q} \quad \Omega \\ = & \ q' \quad \Omega' \\ = & \ q''(r) \ \Omega'' \\ = & \ q'''\Omega''', \end{aligned} \qquad \text{Eq.(1-36)}$$

where Ω^x is the corresponding resistance based on the formulated parameter (i.e., $\dot{q}, q', q''(r), q'''$). Therefore, the thermal resistance for the temperature drop from the maximum fuel temperature to the bulk coolant can be described

$$T_{max} - T_{in,cool} = \dot{q} \ \left[\Omega_{cool} + \Omega_{clad} + \Omega_{gap} + \Omega_{fuel}\right] . \qquad \text{Eq.(1-37.}a\text{)}$$

$$= \dot{q}\frac{1}{2\pi}\left[\frac{2\pi}{\dot{m}C_p} + \frac{1}{LR_{c,out}h_{cool}} + \frac{ln\left(1 + \dfrac{\tau_{clad}}{R_{clad,in}}\right)}{L \ k_{clad}} + \frac{1}{L \ R_{clad,in}h_{cool}} + \frac{1}{2Lk_{fuel}}\right] \qquad \text{Eq.(1-37.}b\text{)}$$

Although this discussion was lengthy, it serves as a simple pedagogical example of the heat transfer mechanisms present in a nuclear reactor system. In the special case of Boiling Water Reactors (BWR),

these are handled such that controlled boiling is accomplished within the reactor vessel and will be discussed in the next section. Particular consideration must be emphasized for the reactor system to operate bellow the maximum fuel temperature considered safe for operation; this is determined specifically for each reactor type. Heat removal is also a focal topic in case of reactor accidents in which time and resources are of the essence.

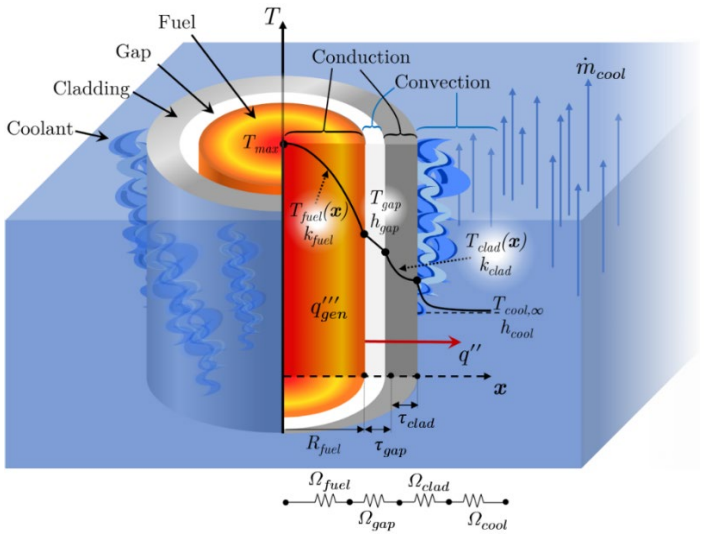

Fig. 1.3. Heat generation and conduction in nuclear fuel pallet.

1.3.2.3. Two-Phase Flow

The production of steam in the reactor arises when we consider the heat transfer effects as the coolant reaches saturation conditions and begins to boil; we shall refer to this as two-phase flow phenomena. This topic is of great importance in reactor studies for two reasons: first, the presence of steam in the reactor core reduces the effectiveness to remove heat, secondly, this leads to a decrement in neutron moderation from the effective decrease of coolant density, resulting in a reduction power. The latter effect is what is known as a negative void reactivity feedback. LWRs are specifically designed to have a negative void reactivity as an inherent safety feature, such that loss of coolant or sudden or excessive coolant evaporation would automatically yield a decrease in the reactor power. For these reasons it is of the utmost importance to understand the behavior of two-phase flow to best predict the coupled effects considering heat removal and the fuel neutronics.

The discussion now expands onto the various boiling regimes and the conditions at which these occur; a more in-depth and theoretical explanation is covered by Todreas and Kazimi [180]. To portray the evolution of boiling, we introduce the pool boiling curve depicted in Fig. 1.4. Although this considers a

stagnant liquid, unlike flowing reactor coolant, it serves as a representative foundation of the boiling processes of interest. The horizontal axis of the boiling curve represents the cladding wall temperature relative to the liquid saturation conditions, while the vertical axis represents the heat flux. Initially, the dominating heat removal mechanism is natural convection for modest relative temperature difference, and the heat transfer coefficient is characterized by the empirical relations with the Re, Gr and Pr numbers. As the heat-flux and relative temperature increase, bubbles begin to form at the cladding surface, an effect referred to as incidence of boiling (IB); the surface roughness of the material affects bubble formation Richenderfer et al. [154]. As the heat-flux increases, the bubble formation, growth and detachment intensify as the conditions approach the critical heat-flux (CHF) condition. At this point, the wall has relatively large patches of vapor which weakens the heat removal, and thus presenting more heat resistance. The CHF condition leads to a departure from nucleate boiling (DNB). If the cladding wall temperature is controlled, the heat-flux is reduced by the overall resistance increase of the surrounding vapor, until the conditions reach the minimum film boiling (MFB) point. At this point the liquid phase no longer is in contact with the cladding surface, the vapor-film continues to grow with increase in heat flux, and removes heat by means of vapor convection. The reverse process follows the same boiling curve path in the opposite direction. Now, in the case in which the heat-flux is controlled, the path transitions from the CHF point across to the film boiling condition. This results in a sudden increase in cladding surface temperature. However, the reverse process results in a quenching effect in which the film boiling reaches the MLB, and transitions directly across to the nucleate boiling condition. Therefore, a heat-flux controlled system experiences a hysteresis boiling path.

In conjunction to the boiling curve, we must consider the coolant flow conditions which affect the boiling process and associated flow regimes as depicted in Fig. 1.5. The left-hand side depicts low flow rates which most resemble the aforementioned pool boiling; the regimes progress in ascending order from nucleate boiling, slug, annular, and dispersed film boiling regimes. Examples of these regimes are captured with x-ray radiography measurements in section 4.6. As the mass flow is increased as shown on the right-hand side of Fig. 1.5, the nucleate boiling directly transitions onto a film boiling, thus resembling the hysteresis effect in the boiling curve. The regimes that proceed include inverted slug film boiling and dispersed film boiling. The high flooding case has a prevalent importance as it represents the conditions during potential accident scenarios in which large amounts of coolant are being pumped to quench the reactor and prevent core damage.

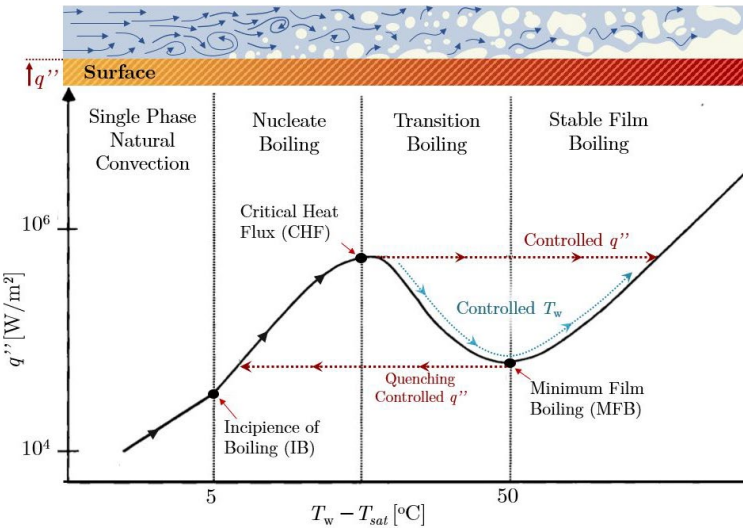

Fig. 1.4. Pool boiling curve, relation of heat flux to surface temperature past saturation conditions, Adapted from Todreas and Kazimi [180].

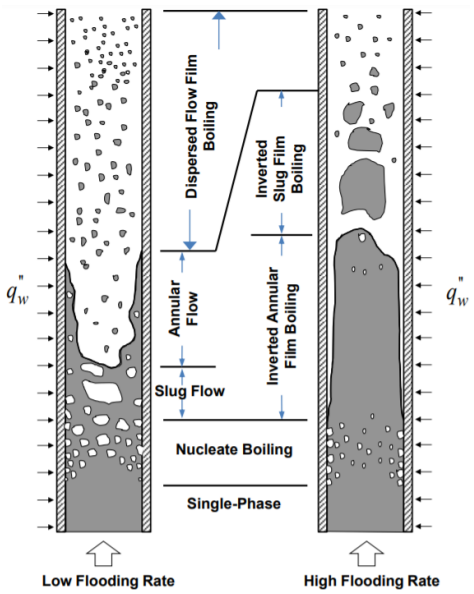

Fig. 1.5. Heat Transfer Regimes retrieved from Mohanta [123].

In practice, two-phase flows are described in terms of the *void fraction*. This parameter quantifies the fraction of gas in the gas-liquid mixture, the determination of this parameter will be the central theme of this research. Here we present the various definitions of the void fraction based on the hierarchical dimensional considerations in Eq.(1-37.*a*). The subscript G denotes the gas phase, L denotes the liquid phase, and T denotes the total mixture quantity in the system (gas-liquid). The individual chordal-segments d, areas A, or volumes V are identified with subscript n and are summed over the total number of regions N. Although the expressions bellow are expressed as sums of individual regions, these can be expressed more formally in integral forms.

- **1-D** - The chordal lengths of gas d_G are added and normalized over the total chordal length d_T; this relation in described in Eq.(1-38.*a*) and depicted in Fig. 1.6*a)*. This relation will be widely implemented throughout this work to describe the radiation transmission process through chordal lengths.

- **2-D** - The void fraction is defined as the sum of individual gas areas A_G normalized by the total area A_T; similarly, this relation in described in Eq.(1-38.*b*) and depicted in Fig. 1.6*b)*.

- **3-D** - Describes the volume average void fraction as the sum of the gas sub-volumes divided over the total control volume; this is typically referred to as the volume fraction, whose relation is expressed in Eq.(1-38.*c*) and depicted in Fig. 1.6*c)*.

1-D	2-D	3-D
$\alpha_{1-D} = \frac{\sum_N d_{G,n}}{d_T}$ Eq.(1-38.a)	$\alpha_{2-D} = \frac{\sum_N A_{G,n}}{A_T}$ Eq.(1-38.b)	$\alpha_{3-D} = \frac{\sum_N V_{G,n}}{V_T}$ Eq.(1-38.c)

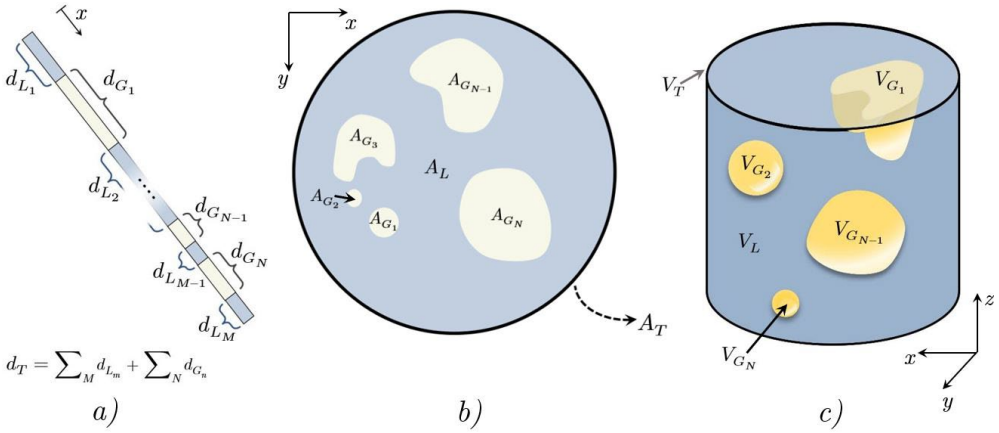

Fig. 1.6. Example of the different void fraction definitions for *a)* 1-D, *b)* 2-D, and *c)* 3-D.

The void fraction is a useful parameter to describe various aspects of the two-phase flow. For instance, the mixture's density can be defined as

$$\rho_{2\varphi} = \frac{\rho_L A_L + \rho_G A_G}{A_T} \quad , \quad \rho_{2\varphi} = \rho_L(1-\alpha) + \alpha\, \rho_G, \qquad \text{Eq.(1-39)}$$

where 2φ denotes the two-phase mixture, ρ_L is the liquid phase density, ρ_G is the gas phase density. here we denote that $(1-\alpha)$ analogously represents the liquid fraction. Another important parameter widely used in two-phase flow studies is the superficial phase velocity; the superficial gas velocity can be expressed as

$$j_G = \frac{A_G}{A_T}\, v_G, \quad j_G = \alpha\, v_G \qquad \text{Eq.(1-40)}$$

for which v_G is the true gas velocity. Similarly, the superficial liquid velocity can be expressed as

$$j_L = \frac{A_L}{A_T}\, v_L, \quad j_L = (1-\alpha) v_L. \qquad \text{Eq.(1-41)}$$

where v_L is the true liquid velocity. From the superficial phase velocity expressions above, it is worth noting how these quantities represent the relative velocity in comparison to a system that is fully occupied by the corresponding phase. In the case where $\alpha = 1$ then $j_G = v_G$ while $j_L = 0$, thus representative of an all-gas system. On the contrary $\alpha = 0$ then $j_G = 0$ while $j_L = v_L$, representing an all-liquid system. Throughout the literature, flow regime maps are commonly described in terms of the superficial phase velocities, namely comparing j_G vs. j_L. We must also consider the relative velocity between the phases described by the slip ratio defined as

$$S = \frac{v_G}{v_L} \quad , \quad S = \frac{j_G}{j_L}\frac{(1-\alpha)}{\alpha}. \qquad \text{Eq.(1-42)}$$

Lastly, the concept of two-phase flow quality must be introduced which considers the corresponding mass flow phases. First, we must define the mass flow of a phase φ as

$$\dot{m}_\varphi = [\rho\ v\ A]_\varphi, \qquad \text{Eq.(1-43)}$$

where A is the area occupied by the phase. The flow quality can then be defined as

$$X_{Fl} = \frac{\dot{m}_G}{\dot{m}_L + \dot{m}_G} \quad \text{or} \quad X = \frac{1}{1 + \frac{\rho_L}{\rho_G}\frac{(1-\alpha)}{S\ \alpha}}. \qquad \text{Eq.(1-44)}$$

In the case in which *S=1*, the flow quality becomes the static quality. Similarly, thermodynamic quality of the two-phase mixture is defined by the enthalpy (total energy stored) by each phase

$$X_{Th} = \frac{H_{2\varphi} - H_{L,sat}}{H_{G,sat} - H_{L,sat}}, \qquad \text{Eq.(1-45)}$$

in which $H_{L,sat}$ and $H_{G,sat}$ are the saturated liquid and vapor respective enthalpy, while $H_{2\varphi}$ is the two-phase mixture enthalpy.

Various two-phase flow predictive models have been formulated around the aforementioned parameters. Here we will only mention in passing two simple and renowned models applied in subchannel codes. These models vary in complexity, and often times have to be adapted to specific geometries of interest (i.e., vertical, horizontal, circular, rectangular, rod-bundle).

- **The Homogeneous Equilibrium Model (HEM)** – This model assumes that the liquid and gas are in mechanical equilibrium, therefore the phase velocities are equal $v_L = v_G$, which results in a slip ratio of $S = 1$. In addition, the model assumes that the gas and liquid phases are in thermal equilibrium which results in $X_{Fl} = X_{Th}$. This simplifies the conservation equations for mass, momentum, and energy which are then formulated for a single mixture species. This model was implemented in the early versions of the best-estimate system code RELAP as highlighted by Mesina [120] and is also available in U.S. NRC TRACE code. However, it must be stated that this is an approximate model, developments of a more complex 6-equation models which individually solve for mass, momentum and energy for each phase are currently implemented in the more current versions of the aforementioned system codes.
- **Drift-Flux Model** – This widely implemented model was first proposed by Zuber and Findlay [206] in 1965 with several contributions from Hibiki, Ishii, and other researchers [26, 27, 63, 64, 65,

139,140]; the latter presents a simple but pedagogical derivation of this model. The model does not assume mechanical equilibrium between the phases and considers the velocity differences between the phases $v_L \neq v_G$ by formulating the gas drift velocity. A new relation for the superficial gas velocity is described based on the mixture's volumetric flux and a modified distribution parameter; the latter is determined empirically for individual flow regimes from experimental results. This model is conveniently adaptable to a variety of flow conditions and geometries (i.e., co-current, countercurrent, vertical, and horizontal).

1.3.3. Light Water Reactors

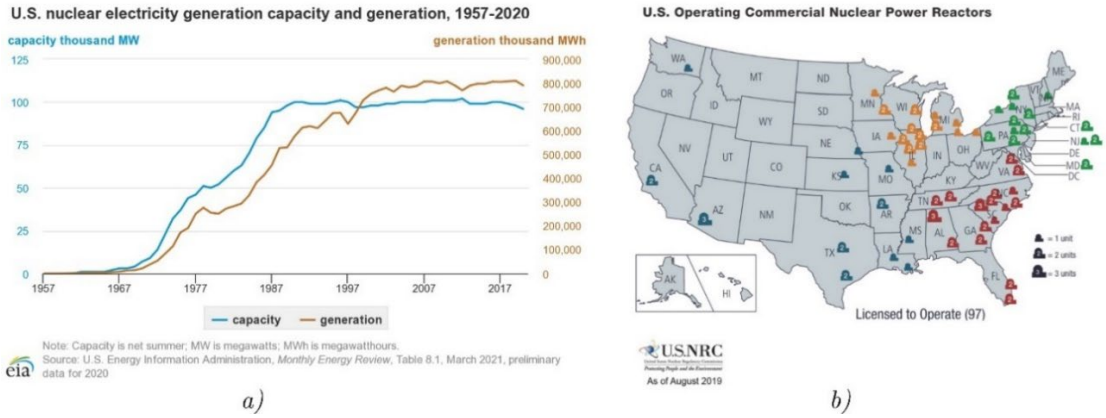

a) *b)*

Fig. 1.7. Overview of the U.S. nuclear sector; *a)* electricity capacity and generation [135], *b)* map of nuclear power plant units as of 2019 [133].

Historically, the growth of the nuclear sector geared towards the production of commercial electricity in the U.S. began in the 1960s and decelerated in the late 1980s. The sector began stagnating as the energy demand flattened, in addition to ever-growing capital and construction costs, as well as the increase in public opposition; these effects are reflected through the electricity capacity and generation depicted in Fig. 1.7*a)*. Only two nuclear reactors, Vogtle unit 3 and 4, will be the first units constructed in over three decades. The current commercial electricity nuclear reactor fleet in the U.S. is constituted entirely by LWR nuclear power plants as of 2021. The nuclear sector contributes about 19~20% of the baseload electricity in the U.S, a map of the commercial nuclear power plants is depicted in Fig. 1.7. As of 2019 there were 97 operational reactors, however this has decreased to 93 reactors in 2021. The short-term future of the nuclear fleet lies in the life-extension of individual reactors which is provided by the Nuclear Regulatory Commission (NRC); this agency oversees the nuclear sector and is charge of providing the license for reactor operation, originally granted for a period of 40 years. The life extension has been increased to 60 years contingent on

periodic inspections, it is unavoidable that the reactors will eventually need to retire. This will leave a foreseeable void in the electricity production that needs to be filled quickly by the up-and-coming next reactor generation.

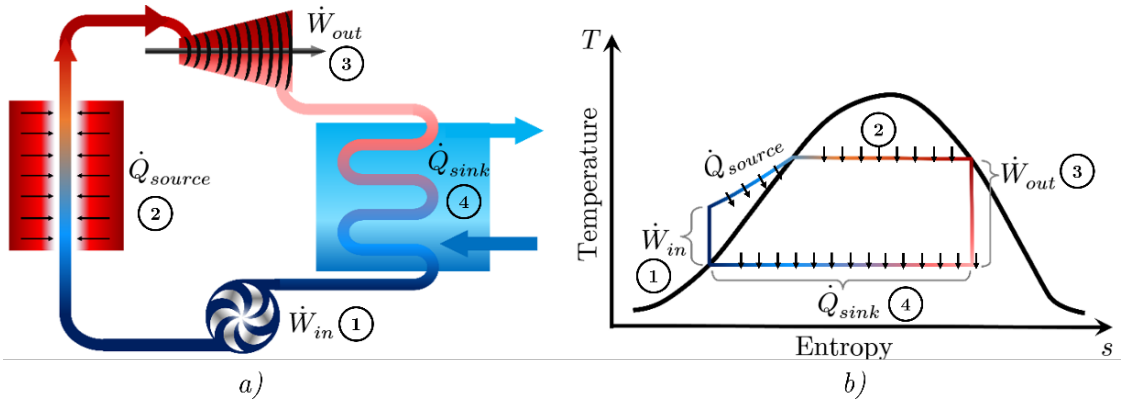

Fig. 1.8. Graphical representation of Rankine thermal cycle, *a)* component schematic, *b)* corresponding system s-T diagram.

LWRs, as many other types of electrical power plants (i.e., coal and oil) use the Rankine thermal cycle, with the underlying difference that the heat source in this particular case originates from fission reactions; the exception to the norm are gas cooled reactors which deploy the Brayton cycle, however these are not commercially implemented for electricity generation in the U.S. as of today. In principle the Rankine cycle is illustrated in Fig. 1.8, the process can be summarized through the following

- 1) The working fluid (typically water) is circulated by a pump through the system, this is an adiabatic process which requires input power $\dot{W}_{in}$; (constant entropy, increase in pressure and temperature).
- 2) The external heat source transfers energy $\dot{Q}_{source}$ onto the circulating working fluid which continues to increase in temperature until the fluid reaches saturation conditions, this then becomes a saturated liquid-steam mixture (increase in entropy and temperature).
- 3) The steam performs mechanical work as it spins a turbine to output power $\dot{W}_{out}$, (constant entropy, decrease in temperature).
- 4) The outcoming steam is then condensed by a heat sink (condenser), $\dot{Q}_{sink}$, this returns the working fluid to a subcooled state (decrease in entropy at constant pressure). The liquid is then pumped for circulation once again returning to step 1.

In the current discussion, the total reactor core power $\dot{Q}_{core} = \dot{Q}_{source}$, which can be described as the sum

of the heat rate generated by individual fuel pins,

$$\dot{Q}_{core} = \sum_{pin}^{core} \dot{q}_{pin}. \qquad \text{Eq.(1-46)}$$

Table 1.2. Comparison of LWR systems designs and operational parameters. Information retrieved from Masterson [117], Todreas and Kazimi [180].

Parameter	Units	PWR	BWR
Fuel ^{235}U Enrichment	%	4 - 5	3 - 4
Outer Cladding Diameter, D	[mm]	9.5	12.27
Rod Pitch, p	[mm]	12.6	16.2
Subchannel Hydraulic Diameter, $D_{sc,h}$	[mm]	11.78	14.96
Subchannel Flow Area	[mm^2]	87.88	144.2
Assembly Rod Arrangement	-	17 x 17	8 x 8 10 x 10 (ABWR)
Total # Assemblies	-	175 - 225	600 - 800
Operational Pressure, P	[MPa]	15.5	7.15
Operational Temperature, T	[^{o}C]	330	293
Core Mass Flow Rate	[kg/s]	594.34	737.31
Coolant Mass Flow Rate per Assembly, $\dot{m}_L$	[kg/s]	90	15.5
Avg. Core Linear Heat Rate, $\bar{q}'_{core}$	[kW/m]	17.8	19
Active Fuel Height	[m]	3.37	3.81
Thermal Power, $\dot{Q}_{core}$	[MW]$_{\text{th}}$	3400 - 3800	3580
Thermal Efficiency (Therm.→ Electric)	%	33 – 34	32 - 34

In practice, power plant thermodynamic cycles are modified variations of the Rankine cycle given that more intricate subsystems are added in order to improve, safeguard, and optimize certain processes; a careful thermodynamic analysis must be applied to each component and assess how the system performs as a whole. Examples of LWR nuclear power plants are depicted in Fig. 1.9*a)* and Fig. 1.11*a)*.

The term LWR is used as a generalized reference for reactors characterized by the use of water as a neutron moderator as well as cooling fluid, and whose fuel pins are arranged vertically in a square lattice formation; other reactor types such as the Heavy Water Reactors (HWR) have deuterium in their water (twice the mass of hydrogen), the assemblies for these reactors can be directed horizontally direction and arranged in a hexagonal lattice formation, primarily referencing the design of the CANadian Deuterium Uranium (CANDU) pressurized water reactors. Within the LWR are two types of reactors, the first is the Pressurized Water Reactor (PWR), the second is the Boiling Water Reactor (BWR). Fundamental differences exist between the two types of reactors as their names suggest, the design and operational parameters of these two reactors are highlighted in Table 1.2 and are the highlighted in the next subsections. The information detailed behind the design of the LWR reactors is referenced from [117, 179, 180].

1.3.3.1.Pressurized Water Reactors (PWR)

This section briefly describes PWRs, the information will follow the design from [179] as well as [97, 117, 180] to detail the principles behind this type of reactors. These types of reactors operate at 330 ^{o}C and 15.5 MPa. The relatively high pressure is used to maintain the coolant under subcooled conditions and thus ensuring an all-liquid phase. The reactor inlet is referred to as the *cold leg*. The coolant entering the cold leg picks up heat as it flows through the core, and then leaves the reactor pressure vessel though the outlet, referred to as the *hot leg*. The pressurizer is tasked of maintain the pressure in the system, this component consists of a large vessel (connected to one of the hot legs) which maintains a pocket of steam on the top in order to regulate the pressure in the system by increasing or decreasing the volume of the steam pocket. The PWR units are characterized by two flow loops, the primary loop corresponds to the coolant flow through the reactor pressure vessel (RPV), steam generator (SG), and the reactor coolant pump (RCP); the primary loop isolates the irradiated coolant from the rest of the system. The secondary loop extracts energy from the primary loop using SG as a heat exchanger (Hex) to extract the heat from the reactor. The number of SGs can range from two to four, depending on the size of the reactor, the corresponding heat removal leg has an RCP located at the cold leg. The SG is a large vessel comprised of thousands of u-shape tubes that pass the water coming from the *hot leg* and transfer heat and boil the water in the outer side of the tube; this ensures isolation of the reactor pressure boundary or so-called primary loop in relation to the remainder of the system. The produced steam is then used to spin the turbine following the concept from Fig. 1.8 with the exception that the SG is the intermediary heat source. The SG are placed above the

reactor height so that if the main recirculation pumps of the primary loop fails, natural circulation of the coolant through the core can establish. The excess reactivity introduced in the reactor core by fresh fuel is regulated by using soluble neutron poison (i.e. boric acid or solbor) whose concentration is slowly reduced based on the reactor burnup (i.e. fuel consumption). The schematic of the PWR system is shown in Fig. 1.9.

The number of fuel assemblies in the reactor core can range from 175 to 225 depending on the vendor and design. The fuel assemblies are commonly arranged in 17 x 17 square lattice formation as depicted in Fig. 1.10*a)*. The fuel rod diameter is 9.5 mm, with a rod pitch of 12.6 mm, resulting in a subchannel hydraulic diameter of 11.78 mm. A selected number of rods in the assembly are used as control rod guide thimbles to reserve the space for when the neutron absorber rod is enacted. The control rod system of these reactors is arranged in clusters (spider-web like) as depicted in Fig. 1.10*b)* as well as Fig. 1.9*b)*, the mechanical drive mechanism is located at the top of the reactor pressure vessel. The control rods are used primarily for reactor startup, shutdown, and scram scenario. In addition, the fuel assemblies are equipped with spacer grids which provide structural support and enhance turbulent mixing to homogenize the coolant temperature and avoid relative high temperature regions.

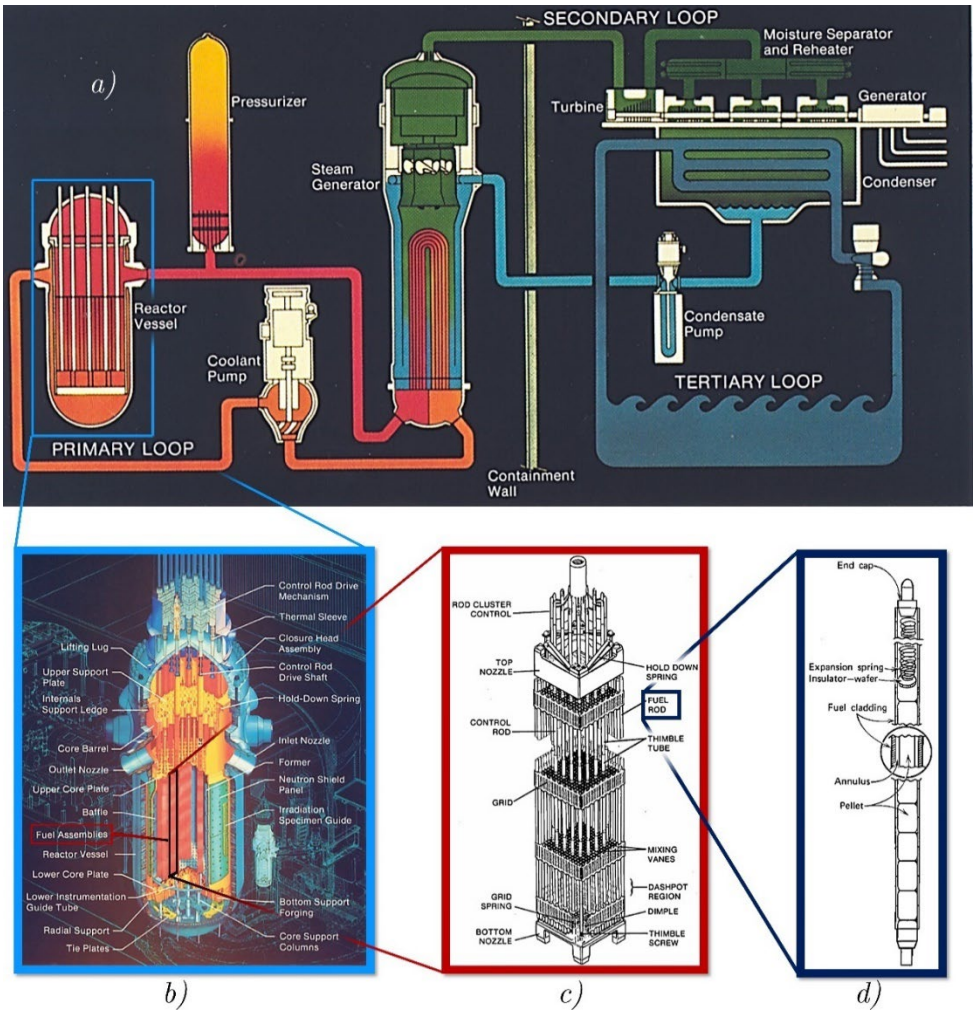

Fig. 1.9. Example overview PWR system; *a)* nuclear power plant schematic, *b)* reactor schematic, *c)* fuel assembly with control rod system, *d)* fuel rod. Republished and adapted from Westinghouse design [179].

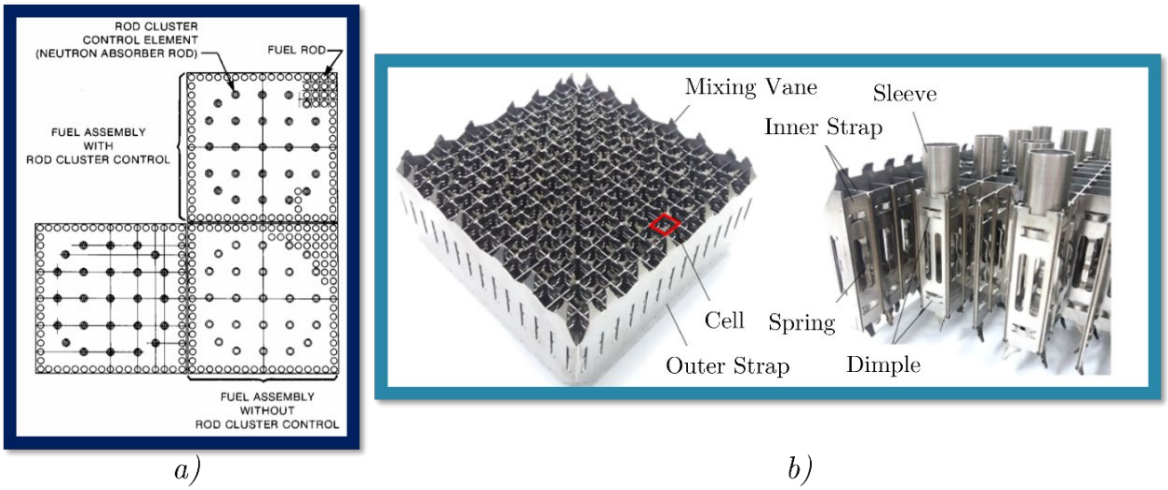

Fig. 1.10. Example of PWR assembly and control rod layout republished from Westinghouse design [179], *b)* spacer grid components [199].

1.3.3.2.Boiling Water Reactors (BWR)

BWRs operate under saturation conditions at 293 ^{o}C and 7.15 MPa, which is lower pressure in comparison to its PWR counterpart; a schematic example of this reactor system is presented in Fig. 1.11 for General Electric's (GE) - Hitachi Advanced BWR (ABWR). The RPV in this case is an annular barrel, the reactor core is located in the inner region, and the outer annular region corresponds to the downcomer to which the inlet discharges. The premise of this reactor type is to maintain a constant supply of coolant in the core to equilibrate the amount of steam generated. Here, boiling begins at 1 m from the bottom of the reactor core and the quality two phase mixture is on the order of 15 % towards the top of the reactor core according to Todreas and Kazimi [180] and Masterson [117]. This system is single loop given that the steam is directly produced within the reactor, removing the need for the SG. The two-phase mixture passes through cyclone separators, and a steam dryer system located towards the upper region of the RPV in order to remove liquid droplets and obtain the dry steam, this is then directed towards the turbine. The excess liquid from the dryer is separated towards the downcomer and redirected through the reactor core recirculation (RCIR) system which controls the flow of coolant through the core; the coolant recirculation process is best depicted in Fig. 1.12*a)*. From principle, low flow rate result in an increase in the boiling rate (voiding), which in turn decreases neutron moderation and reactor power; this occurs because the steam is significantly less dense than liquid, therefore neutrons do not interact with the same frequency. On the contrary, increase in flow rate, increases neutron moderation and reactor power.

The number of assemblies in the core can range from 600 to 800, said assemblies are typically arranged in an 8x8 square bundle lattice and are encased in a zircaloy sleeve; the ABWR design is arranged in a 10 x 10 formation as shown in Fig. 1.12*b)*. The assembly fuel rod diameter is 12.6 mm, with a lattice pitch of 16.2 mm, resulting in a subchannel hydraulic diameter of 14.96 mm. The assemblies incorporate tie rods in charge of holding the assembly together [40], water rods located towards the center region for increased moderation, partial length rods are used to increase the flow area and reduce two-phase flow frictional pressure drops; these features are reflected in Fig. 1.11*c)* and Fig. 1.12*b)*. Spacer grids are axially distributed to provide structural support to the assembly. The control rods consist of blades arrange in a cruciform geometry as shown in Fig. 1.11*d)* and Fig. 1.12*b)*; these occupy the space between four square neighboring assemblies whenever they are actuated, this grouping is typically referred as a *fuel module* by Kok [97]. The mechanical drive for the control rod system is located at the bottom of the reactor because of the lack of

space near the top of the RPV (due to the steam dryers), therefore the control rods are actuated in the upward direction.

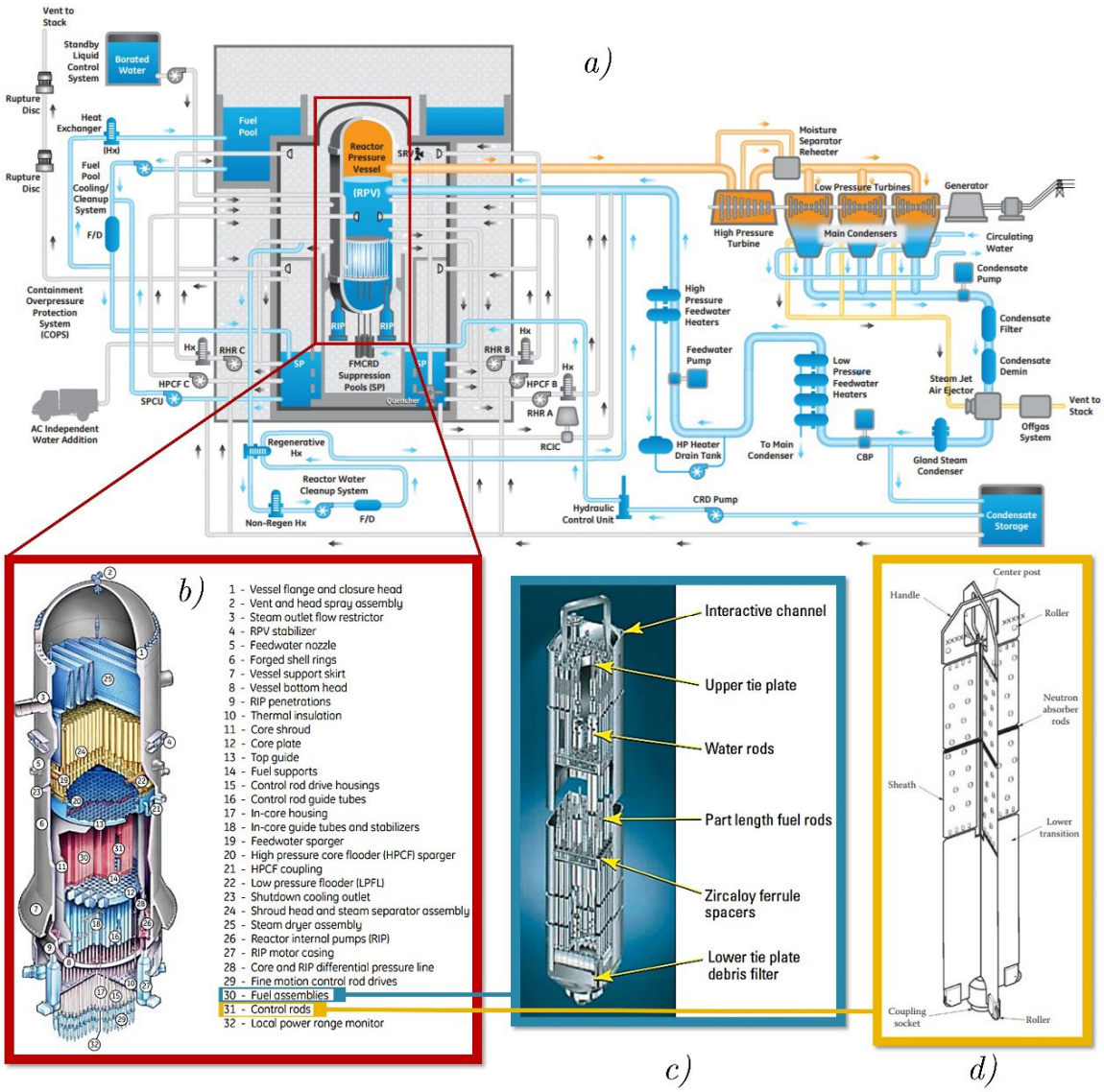

Fig. 1.11. Example overview BWR system; *a)* nuclear power plant schematic, *b)* reactor schematic, *c)* fuel assembly, *d)* control rod blade. Republished and adapted from GE-Hitachi ABWR design [40].

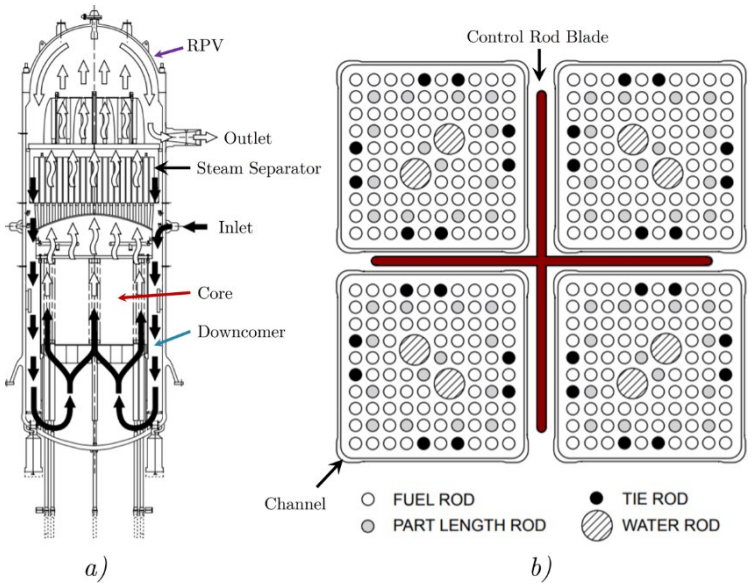

Fig. 1.12. ***a)*** **Steam separation and recirculation reprinted from [40], and** ***b)*** **fuel module schematic reprinted from [97].**

1.4. Need for High-Resolution Data

Strict design regulations of nuclear reactors such as PWRs and BWRs are imposed to ensure nominal operation and maintain ample safety margins; these regulations define the thermal, structural, and oxidation design limits as highlighted by Masterson [117]. In alignment with the previous discussions, the concern is emphasized in the thermal design limits which seek to ensure that the centerline fuel-pin temperature stays bellow 1600°C and the cladding temperature stays bellow 700°C during nominal operation. To maintain these safety margins in the case of PWRs, the heat flux must be maintained well below the necessary conditions that lead to DNB; the heat flux relation to different boiling conditions was previously depicted in Fig. 1.4, where the CHF point foments DNB conditions. The imposed safety margin requires the CHF to operational heat flux ratio to remain above 1.3 [117, 180]; this is formally referred to as the departure from nucleate boiling ratio (DNBR). These requirements change in the case of BWRs given that the operational basis of these lies in the controlled boiling of water and in which the rods are cooled by a liquid film as denoted by Todreas and Kazimi [180] and depicted by annular regime shown in Fig. 1.5. In this case, it is important to determine the critical power at which dryout conditions will be met based on operational parameters. The safety margin requires the critical power ratio (CPR) to be maintained above 1.2 [180]; the CPR is defined as the ratio of critical power to actual power. Said design and operational requirements aim to decrease the probability of design basis accidents (DBA) that may occur in a nuclear reactor. The

most serious form of DBA is the loss of coolant accident (LOCA) defined by the Nuclear Regulatory Commission (NRC) as:

> *"Those postulated accidents that result in a loss of reactor coolant at a rate in excess of the capability of the reactor makeup system from breaks in the reactor coolant pressure boundary, up to and including a break equivalent in size to the double-ended rupture of the largest pipe of the reactor coolant system."*

In essence, any leakage of coolant event that results in a rate of loss above what can be supplied safely into the system is considered a LOCA. In the worst-case scenario, the largest primary coolant supply pipe to the reactor breaks, resulting in a large break LOCA. The initial blowdown stage depressurizes the reactor vessel quickly as the coolant escapes. Instantly, the concern derived from these accident conditions is the reactor's cooling degradation due to the reduction of thermal removal capacity that if not promptly assessed leads to cladding and fuel failure. The emergency core cooling system (ECCS) instantly deploys and begins to supply the core with coolant. Several other support systems are brought online in the refill stage to begin the quenching process and fill the reactor. During this stage, the reactor is initially being cooled by means of convection from the generated steam. Although the coolant level of the reactor rises, the rods continue to boil wrapped in a film boiling layer until the quenching front can progress axially as the boiling crisis transitions to the nucleate boiling regime. The reflooding process of the reactor is completed once the reactor has been fully filled with coolant and has been successfully quenched; the possible reflooding regimes during LOCA conditions are depicted on the right-hand side of Fig. 1.5. Set conditions are difficult to recreate under lab conditions due to the elevated temperatures, and high-resolution experimental data is still required to formulate robust predictive models.

In addition, much emphasis of the preceding research has focused on identifying and establishing the transition conditions between flow regimes for rod-bundle geometries. The research objectives centralize in establishing predictive flow regime maps in relation to the conditions at which these regimes occur; these regime maps are often described in terms of the mixture's superficial velocities or superficial momentum mass-flux. The primary basic regimes that were identified by Hewitt and Roberts [62] in 1969 for vertical pipe flows were bubbly, slug, churn, and annular. In 1980, Taitel et al. [176] then proceeded to derive analytical expressions to describe flow regime transitions in vertical pipes. Contemporarily, Williams et al. [191] and Venkateswararao et al. [187] performed two-phase flow experiments of rod bundle geometries.

Based on his findings, Venkateswararao modified the flow regime maps theorized by Taitel to consider rod bundle geometries, this then became the established flow regime model. Until more recently Julia [80], Paranjape et al. [138, 139], as well as Liu and Hibiki [107] have progressively elaborated further refinements to the drift flux model and predictive flow regime maps. The improvement of these models provides higher fidelity relations implemented in computational reactor modeling programs; in turn, this enhances the thermal hydraulics coupling to the neutronics codes in the modeling process. This ultimately translates to further strengthening nuclear reactor safety and operation economics. For the reasons stated above, it is of crucial importance to continuously improve the two-phase flow models implemented in subchannel and best-estimate thermal-hydraulic system codes, specifically U.S. NRC TRACE code.

1.5. Advanced Instrumentation for Two-Phase Flow in Rod Bundles

An extensive literature review of previous experiments pertaining to two-phase flows in rod bundle geometries has been compiled in the Table 1.3.*a-c)*; it is important to note here that the reactor type was denominated as LWR in the cases in which the authors do not specify the reactor design of interest. The information is organized by publication year which serves to highlight the implemented instrumentation and its advancements. From the presented tables it emphasizes how early on in the research campaigns taking place from 1960 through early 2000s, the primary form of instrumentation deployed for two-phase flow applications relied on high-speed imaging (optical), implementation of pressure sensors (transducer), as well as radiation-based measurements. Conductivity based techniques began to appear in the 1990s, as Katoak et al. [84] developed needle-probes and Prasser et al. [148] developed wire-mesh sensors (WMS), however, these would not be implemented for rod bundle applications until the 2000s onward.

- **Optical methods** - From the chronological progression it is evident that optical base methods were the pioneering method early on and are still widely used in modern research. Technological advancements have allowed high-speed cameras to improve their acquisition rate and resolution. However, two-phase flows present several challenges with optical-based methods due to the index of refraction mismatch between the gas, liquid, and the translucent acrylic rods which impede the assessment of any quantitative data. For these reasons optical methods are most commonly utilized in a supportive role to assert qualitative aspects of the flow and are occasionally used for quantitative measurements when distinct or isolated features can be distinguished as is the case for bubbly flows. Nevertheless, optical based methods are preferably deployed to study single-phase

flow, in which modalities such as Particle Image Velocimetry (PIV) [134, 150] and Laser Doppler Velocimetry (LDV) are deployed for the study of turbulence. The applications have been extended to the study of two-phase flow, with a few examples presented in [159, 204]. These methods are limited to low system pressures and require transparent experimental housing as well as simple geometric arrangements.

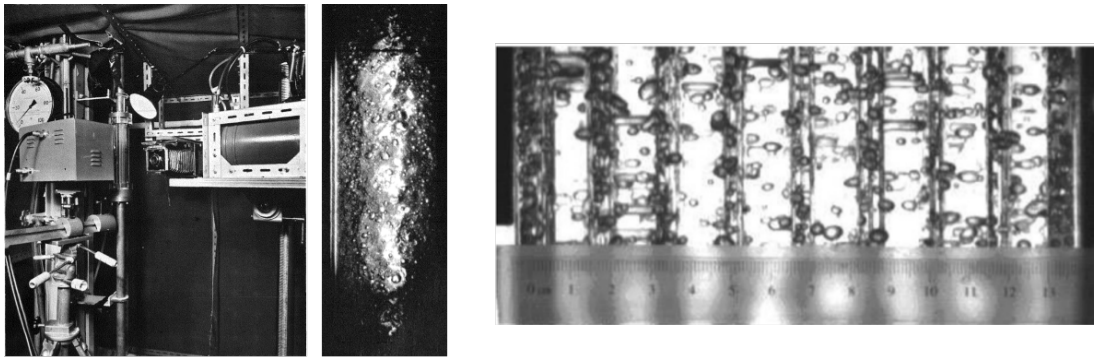

a) *b)*

Fig. 1.13. Example of applications of optical methods: *a)* imaging equipment used by Hewitt and Roberts [62] in 1969 to study two-phase flows in vertical pipes, *b)* high-speed imaging of bubbly flow reprinted from Paranjape [138].

- **Differential Pressure Sensors** – this method was essential at the onset of reactor studies and continues to be widely implemented throughout the research. This type of instrumentation measures the difference in pressure from two locations, with emphasis in the axial direction for reactor applications. These were used early on to develop empirical models linking the void fraction and the pressure effects, these now play a supportive role for more advanced acquisition methods. The pitfalls of the sole reliance on this type of instrumentation to estimate the void fraction requires the implementation of simplified models such as HEM or the drift-flux correlations which are limited in scope.

- **Radiation based** – this modality is the central pillar of the present research; this method relies on the interactions between radiation and matter. Derbyshire et al. [32] and Hewitt et al. [62] implemented x-ray radiography in the 1960s for studies of two-phase flows. However, advancements in new modalities such as computed tomography were later implemented towards the end of 1980 and mid 1990s for reactor applications in Japan[1]; here they would go on to use x-ray CT [74, 121,

[1] Historical context reveals Japan's commitment to nuclear energy strengthens after the oil shock of 1973.

125, 126], gamma-ray CT [7], and densitometry [74, 102]. The technology and CT methods were beginning to advance; however, the resolution was coarse due to cumbersome detectors systems. Advancements have allowed the detector elements to decrease in size thus improving spatial resolution, as well as enhance energy resolution. Although radiation-based methods have been around for some time, these have gained interest in the scientific community in the study of two-phase flows. These methods present inherit advantages over conventional instrumentation due to their non-intrusiveness as well as the capability to perform measurements through complex and opaque geometries.

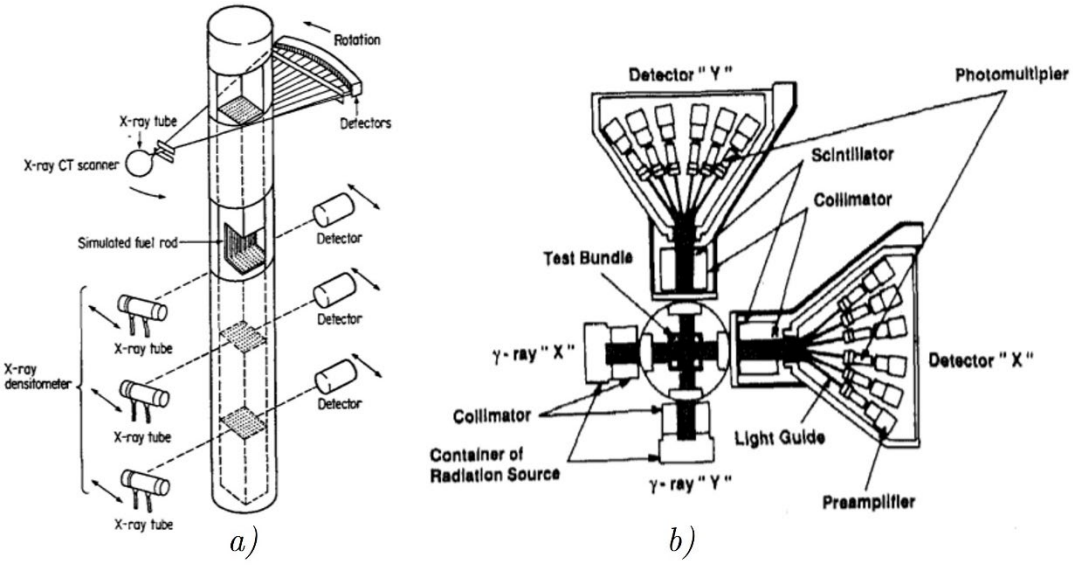

Fig. 1.14. Examples of radiation-based instrumentation: a) X-ray CT and densitometry reprinted from Inoue et al. [74], b) Gamma-ray CT scanning device reprinted from Akiyama et al. [7].

- **Conductivity Sensors** – these techniques exploit the difference in dielectric properties between coolant mixtures as a quantitative mechanism. The first type of instrumentation is the 4-sensor conductivity probe (also known as needle probes), which performs local measurements as the bubbles (voids) cross through the electrodes thus sensing a change in dielectric properties. This type of instrument requires a sufficiently high number of bubbles passing through the probe tip in order to obtain adequate average, in addition to extended measurement times. The second type of instrumentation is the Wire Mesh Sensor (WMS) which are arranged in a grid-like formation between transmitter and receiver wires. These have gained popularity in two-phase flow studies due to their high temporal resolution. WMS foster the capability to estimate the phase-velocity whenever multiple sensors are deployed in nearby proximity. Alternative instrumentation that has

been implemented include liquid film sensors and subchannel void sensor (SCVS). The drawbacks of these type of advanced instrumentations lie in the intrusive presence of the hardware which has the potential of perturbing the flow, and it is constrained to a single cross-section.

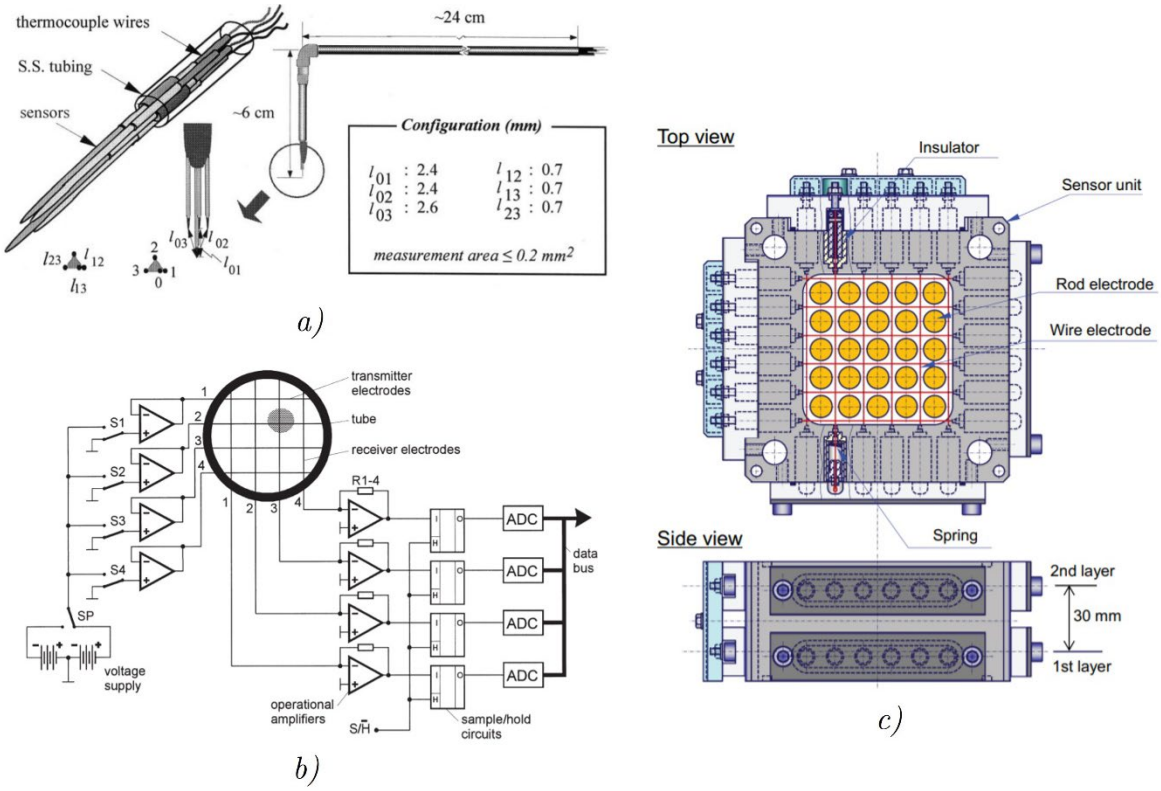

Fig. 1.15. Examples of conduction-based instrumentation: a) 4-sensor conductivity probe reprinted from Kim et al. [87], *b)* wire-mesh sensor schematic reprinted from Prasser et al. [148], and *c)* subchannel void sensor (SCVS) reprinted from Arai et al.[11].

Table 1.3.a. Literature review of two-phase flow rod-bundle experiments.

Literature Ref.	Year	Reactor Model	Working Fluids	Pressure [kPa]	Bundle Arrangement	Housing Geometry	D_h [mm]	Rod Diameter [mm]	Pitch [mm]	Measurement Methods
Williams et al. [191]	1978	LWR	Steam-Water	2700 - 13790	1x4	Rectangular	5.2	6.35	8.64	High Speed Camera (Shadowgraphy)
Venkateswararao et al. [187]	1981	PWR	Air-Water	101.3	24	Circular	~	12.7	17.5	Optical Observation
Iguchi et al. [73]	1981	PWR	Steam-Water	101.3 - 400	4x4	Rectangular	11.5	10.5	13.8	Differential Pressure
Anklam et al. [10]	1982	PWR	Steam-Water	4000 - 7000	8x8	Rectangular	10.8	9.5-10.2	12.7	Differential Pressure
Murao et al. [127]	1982	PWR	Steam-Water	98 - 392	4x4	Rectangular	11.5	10.5	13.8	Differential Pressure
Osakabe et al. [136]	1984	PWR	Air-Water	101.3	6x22	Rectangular	12	10.7	14.3	Differential Pressure
Morooka et al. [125, 126]	1988 1989	BWR	Steam-Water	500 - 1000	4x4	Rectangular	~	12.3	16.2	X-ray CT
Mitsutake et al. [121]	1990	BWR	Steam-Water	490 - 980	4x4	Rectangular	~	12.3	16.2	X-ray CT
Kumamaru et al. [102]	1993	PWR	Steam-Water	3000-12000	32	Circular	~	9.5	12.6	Differential Pressure, Gamma-Densitometer, Optical Probe
Qazi et al. [149]	1994	~	Steam-Water	1000	2x2	Circular	15.9	9.5	17	Gamma-Densometer
Akiyama et al. [7]	1995	PWR	Steam-Water	4900 - 16.6	5x5	Circular	~	~	~	Gamma CT, Differential Pressure
Inoue et al. [74]	1995	BWR	Steam-Water	1000 - 8600	8x8	Rectangular	~	12.3 - 15.0	16.2	X-ray CT & Densitometer, Diaphragm Transducer
Kok et al. [95, 96]	2001	BWR	Steam-Water	1100	6x6	Rectangular	~	6.35	8.8	Gamma CT

Table 1.3.b. Literature review of two-phase flow rod-bundle experiments.

Literature Ref.	Year	Reactor Model	Working Fluids	Pressure [kPa]	Bundle Arrangement	Housing Geometry	D_h [mm]	Rod Diameter [mm]	Pitch [mm]	Measurement Methods
Sadatomi et al. [155, 156]	2004 2005	BWR	Air-Water	101.3	2x3	Rectangular	12.3	16	20	Differential Pressure
Mizutani et al. [122]	2007	BWR	Air-Water	101.3	4x4	Rectangular	12.7	12	16	High Speed Camera
Yun et al. [200]	2008	BWR	Steam-Water	101.3 - 120	3x3	Rectangular	18.6	8.2	16.6	Conductivity Probe, High Speed Camera, Differential Pressure
Paranjape et al. [140, 138]	2008 2011	BWR	Air-Water	101.3	8x8	Rectangular	14.8	12.7	16.7	High Speed Camera, 4-Sensor Conductivity Differential Pressure
Damsohn et al. [30]	2010	BWR	Air-Water	101.3	2x3	Rectangular	~	20	23.25	Liquid Film Sensor
Kamei et al [81]	2010	PWR	Air-Water	101.3	4x4	Rectangular	9	10	12.3	Differential Pressure
Arai et al. [12]	2012	BWR	Air-Water	~	10x10	Rectangular	10.6	10	13	Subchannel Void Sensor (SCVS)
Chen et al. [26]	2012	BWR	Air-Water	101.3	8x8	Rectangular	14.8	12.7	16.7	Impedance Meter, High Speed Camera, Pressure Gauge, Differential Pressure,
Yang et al. [196]	2013	BWR	Air-Water	101.3 - 300 (1000 max)	8x8	Rectangular	21.7	10.3	16.7	4-Sensor Conductivity Probe, Pressure Sensors

Table 1.3.c. Literature review of two-phase flow rod-bundle experiments.

Literature Ref.	Year	Reactor Model	Working Fluids	Pressure [kPa]	Bundle Arrangement	Housing Geometry	D_h [mm]	Rod Diameter [mm]	Pitch [mm]	Measurement Methods
Ylönen et al. [198]	2013	LWR	Air-Water	101.3	4x4	Rectangular	33.9	25	34	Wire Mesh Sensor, High Speed Camera
Hosokawa et al. [70]	2014	LWR	Air-Water	101.3	4x4	Rectangular	9.1	10	12.5	Conductivity Probe, LDV
Zboray et al. [202]	2013	BWR	Air-Water	101.3	2x3	Rectangular	~	20	23.25	Neutron Tomography
Zhou et al. [204]	2015	LWR	Steam-Water	101.3	3x3	Circular	11.4	10	15	High Speed Camera, Differential Pressure
Ren et al.[153]	2018	LWR	Air-Water	101.3	5x5	Rectangular	8.8	9.5	12.6	4-Sensor Conductivity Probe
Takiguchi et al [176]	2018	PWR	Cold & Hot Water Mixing	101.3	5x5	Rectangular	10.1	10	13	Wire Mesh Sensor, Thermal Sensor
Arai et al. [13, 11]	2019, 2021	BWR	Steam-Water	101.3 - 7200	5x5	Rectangular	10.1	10	13	Differential Pressure, X-ray CT, Subchannel Void Sensor (SCVS)
Han et al.[56]	2019	BWR	Air-Water	101.3	6x6	Rectangular	18.7	10	16.7	Four-sensor Optical Probe
Shen et al. [166]	2019	BWR	Air-Water	101.3	6x6	Rectangular	18.7	10	16.7	Optical Probe, Differential Pressure
Ye et al. [197] & Ma et al. [114]	2019, 2020	LWR	Air-Water	101.3	5x5	Rectangular	10.3	9.5	12.6	Impedance meter, Differential Pressure
Chen et al.[27]	2020	BWR	Air-Water	101.3	3x3	Rectangular	13.3	11.5	15.4	Conductivity Probe, High Speed Camera, Gauge Pressure

CHAPTER II

Radiation Transmission Imaging

Nomenclature

Roman Variables

A	Atomic number or area
a	Specific activity
B	Blur
c	Speed of light
D	Diameter
d	Distance
E	Energy/ exponential integral
$\hat{\boldsymbol{e}}$	Unit vector
$\boldsymbol{e}^{-/+}$	Electron (-), positron (+)
$\mathcal{F}$	Fourier transform operator
f	Focal spot
h	Planck's constant
I	Source intensity/activity
KE	Kinetic energy
L	Traversing length
M	Object Fourier transform
Mag	Magnification
$m_e c^2$	Electron rest mass
N	Neutrons/Number of counts per projections
$\overline{\boldsymbol{n}}$	Directional or normal unit vector
P_θ	Sinogram's Fourier transform
p_θ	Sinogram
R	Radius
R_b	Relative blur
r	radial variable
S	Magnitude of ray-trace or total distance
s	Path length
$\overrightarrow{\boldsymbol{s}}$	Ray-casting vector
T	Detector recording time or total time
t	Time
u	Fourier variable of x
V	Volume, voltage, or vertices
v	Fourier variable of y
W	Number of readouts
w	Fractional elemental weight
X	Atom
$\boldsymbol{x}$	Spatial coordinates
Z	Proton number
z	Axial location

Greek Variables

$\overrightarrow{\beta}$	Particle speed relative to the speed of light
β	Relative source-detector size
Γ	Photoelectric scaling
γ	Photon or dilation factor
δ	Detector depth, or delta function
η	Absorption efficiency
θ	Angle
λ	decay constant
μ	Linear attenuation coefficient
μ/ρ	Mass attenuation coefficient
ν	Photon frequency, neutrino, or Fourier variable of r
ρ	Density
τ	temporal sifting variable
$\tau_{1/2}$	Half-life
σ_x^2	Variance of variable x
χ	Relative distance

Subscripts & Superscripts

■	Square or rectangular region
γ	Photon
$\boldsymbol{\phi}$	rotation
air	Air
b	back projection
CT	Computed tomography
cyl	Cylindrical region
d	Detector spatial location
det	Detector
$\boldsymbol{e}^-$	Electron
f	Plane face
i	indexing variable, iteration
j	indexing variable
in	Incoming
M	Measurement
max	Maximum value
min	Maximum value
o	Origin, object, or initial value
od	Object-detector distance
out	Outgoing
$proj$	projection
$read$	Readout
rev	Revolution
s	Source spatial location
sd	Source-detector distance
so	Source-object distance
sph	Spherical region
src	Source

2.1. Principles of Radiation Transmission & Detection

Radiation transmission imaging is a powerful tool that can be used to survey systems that are opaque, and which may involve complex geometries. Radiation imaging can be performed with neutrons [4], gamma-rays [2, 160] and x-rays [18 - 16]; the latter being the conventional form of radiation used in the medical field due to its low energy that helps regulate patient dose. The proper form of radiation required to measure a system depends on a series of factors such as, material compositions, required spatial resolution, size and

configuration of the test section to be scanned, and in some cases temporal constraints. This chapter will lay the groundwork of radiation imaging systems including the nature of radiation, interactions with matter, particle detection, to ultimately describe the imaging systems developed and implemented in the present work.

2.1.1. Radiation Sources and Interactions with Matter

The basis of any transmission imaging systems relies on the transport and detection of radiation particles; a relatable example of a common-day device is the camera, which captures the ambient light that is reflected from objects; this light has to be generated somewhere, a source, such as the sun, a light bulb, a campfire to name a few examples. However, there is a realm of particles that we humans cannot see, where special "cameras" are required to detect them. The types of particles can be categorized into four groups: electromagnetic radiation, heavy charged particles, neutrons, and fast electrons. Electromagnetic radiation, also known as photon particles, are characterized as energy wave packets with a corresponding frequency; the electromagnetic spectrum describes the wide range of energies and length-scale denominations encompassed by the electromagnetic radiation. Unfortunately, humans can only register a narrow band of the electromagnetic spectrum. The main particles of interests in this research are gamma-rays and x-rays which lie in the high-energy and high-frequency region of the spectrum.

2.1.1.1. Radioactive Decay and Gamma-ray Sources

The primary particle emission mechanisms that are of importance in this research are radioactive decay, this is a nuclear processes[2] that occurs when an unstable atom emits one or more particles carrying the excess energy. Some of the basic radiation emission via decay processes include:

- Beta decay in which a neutron inside the nucleus changes to proton and in the process a beta particle (e^- symbolizing a fast electron) and a nearly massless antineutrino are emitted, this process tends to occur in heavy neutron rich atoms.

$$ {}^{A}_{Z}X \rightarrow {}_{Z-1}{}^{A}X + e^- + \bar{\nu} $$

- Positron (e^+) decay in which a proton changes into a neutron and in the process a positron and a

[2] Other interesting nuclear interactions include nuclear fusion, spontaneous fission, and compound nucleus interactions explained in depth by Krane [99]

nearly massless neutrino are emitted, this process tends to occur in heavy proton rich atoms.

$$ {}^{A}_{Z}X \rightarrow {}^{A}_{Z+1}X + e^{+} + \nu. $$

- Alpha decay is the emission of a charged helium particle from a supermassive atom containing a large amount of nucleons (protons and neutrons); the atom tends to undergo several other decay processes after the expulsion of the helium particle.

$$ {}^{A}_{Z}X \rightarrow {}^{A-4}_{Z-2}X_{N-2} \; + \; {}^{4}_{2}He. $$

- Electron capture occurs when a proton inside the nucleus absorbs an electron and converts to a neutron, emitting a neutrino in the process.

$$ e^{-} + {}^{A}_{Z}X_{N} \rightarrow {}^{A}_{Z-1}X_{N+1} \; + \nu. $$

- Gamma-ray emission occurs when the nucleus is in an excited state denoted by the asterisk and releases this excess energy by emitting a gamma-ray photon thus transitioning to a lower energy state; the resulting gamma-ray's energy is equivalent to the discrete transition energy. This can sometimes result in several transition steps until the nucleus arrives to a stable ground state, resulting in the emission of several corresponding gamma-rays. All atoms above a nuclear mass A>5 have gamma-ray transitions.

$$ {}^{A}_{Z}X^{*} \rightarrow {}^{A}_{Z}X \; + \gamma. $$

Atoms can undergo multiple stages of decay whereby several of these nuclear processes occur, these are commonly known as a decay chains, where the end goal is to arrive at a stable nuclear arrangement. The aforementioned processes above often times leave the nucleus in an excited state. The atom releases a gamma-ray photon in order to release this excess energy and arrive to a ground state. Common gamma-ray emission examples of radioisotopes are ^{137}Cs and ^{60}Cs depicted in Fig. 2.1; this intends to highlight the decay and de-excitation process which an atom undergoes to arrive at a stable arrangement. A more complex radioisotope and the primary source of gamma-ray photons in the present research is ^{192}Ir, the decay schemes of this isotope are shown in Fig. 2.2, as characterized by Gehrke [51] in 1972. A thorough catalogue of isotopic gamma-ray emissions was first compiled by Heath[3] [59] and has been continuously updated since.

The process of radioactive decay depletes the atomic population of these unstable radioactive isotopes.

[3] The reader can find the gamma-ray spectroscopy catalogue at https://gammaray.inl.gov/Shared%20Documents/gecat.pdf

However, the rate at which this process occurs is dependent on the isotope's characteristic decay constant which dictates the probability that the decay event will occur per unit time. Radioactive decay over time can be expressed as

$$I(t) \;=\; I_o e^{-\lambda t}, \qquad \text{Eq.(2-1)}$$

where λ is the characteristic decay constant in units of [s^{-1}], and I_o is the isotopes initial activity symbolizing the disintegrations per second, and whose units are in becquerels [Bq] or curies [Ci]. Typically, the decay process is expressed in terms of the isotopes half-life which is the amount of time it takes the isotope to deplete to 50% of its original isotopic content. The half-life can be estimated from the decay constant as

$$\tau_{1/2} = \frac{1}{\lambda}\ln(2). \qquad \text{Eq.(2-2)}$$

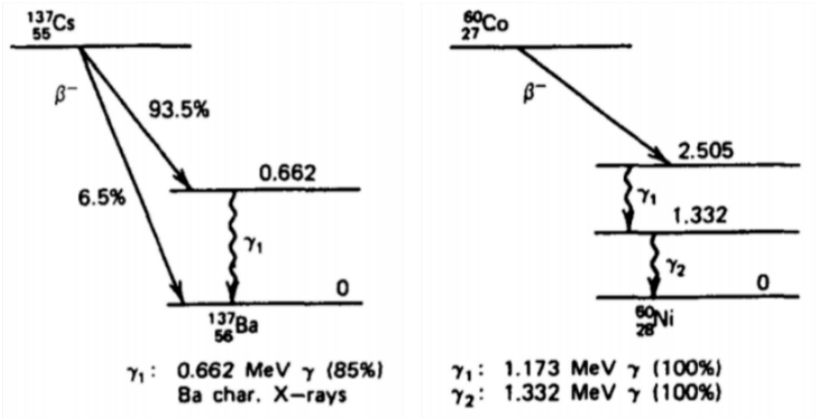

Fig. 2.1. Radioactive decay of ^{137}Cs and ^{60}Co taken from Knoll [94].

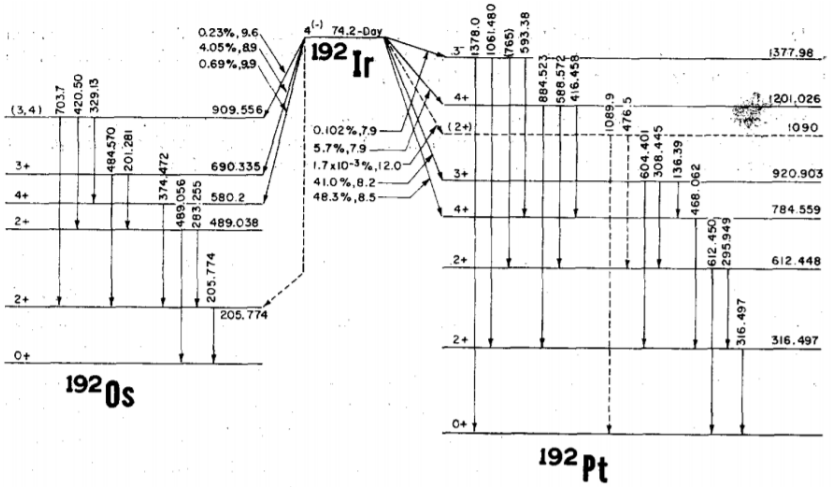

Fig. 2.2. Radioactive decay modes of ^{192}Ir from Gehrke [51].

Radioisotope decay length scale is dependent on the instability of the nucleus, highly unstable atoms decay in short time scales, while mildly unstable atoms decay in relatively long-time scales. To put it into perspective based on the isotope example from Fig. 2.1 and Fig. 2.2, the ^{137}Cs has a half-life of 30.17 years,

^{60}Co half-life is 5.3 years, and ^{192}Ir has a half-life of about 73.8 days. The given examples show the time scales at which radioactive decay can occur, there are isotopes whose half-lives are in the microsecond range and are perceived to decay instantaneously, while radioisotopes from nuclear waste have half-lives spanning in the scale of millions of years[4]. Another important factor that comes into play when selecting a radioisotope is the specific activity defined as the activity per unit mass in units of [Ci/g]; ideally the source should be selected to be as small as possible to imitate a point source. The isotope's specific activity, density and source volume can be used to estimate the source's activity

$$\begin{aligned} I &= a \quad \rho \quad V, \\ &= \left[\frac{\text{Ci}}{\text{g}}\right] \left[\frac{\text{g}}{\text{cm}^3}\right] [\text{cm}^3]. \end{aligned} \qquad \text{Eq.(2-3)}$$

The specific activity is dependent on the synthesis process of the radioisotopic source; often times compounds are doped with radioactive isotopes to produce a source. Following the example of ^{137}Cs, these types of radioactive sources can be manufactured in the form of Pollucite ceramics which can achieve a specific activity of 12 [Ci/g] and a density of 2.4 [g/cm^3] as reported by Enomoto et al. [41]. In comparison, ^{192}Ir is manufactured by neutron bombardment of a natural iridium target inside research reactors, the specific activity of this radioisotope is dependent on the amount of radiation exposure of the target; alternative, the radioisotopes can be produced in cyclotron as highlighted by Hilgers et al. [66]. The reported specific activity of ^{192}Ir is 9.22 [kCi/g] by Delacroix et al. [31], and the density of natural iridium is 22.56 [g/cm^3]. Now to put into perspective, comparing the two isotopic sources containing the same volume, the ^{192}Ir source emits about 7.22E3 more radiation per unit mass than the ^{137}Cs Pollucite source. Therefore, the selection of an ^{192}Ir isotope greatly reduces the size of the source used for imaging, however, the disadvantage is the quick disintegration and loss of activity from this type of isotope.

2.1.1.2. X-ray Sources

The most commonly applied form of radiation is in the forms of x-rays; these are widely used in medical settings, industrial non-destructive evaluation, material science, physics, and other fields. Medical x-ray tubes generate x-rays by accelerating an electron beam from the cathode onto a high-Z anode target. Now let us single out a highly energized electron from the beam, which experiences a change in acceleration as

[4] Although the topic of nuclear waste is not developed in this research, dealing with these long-lived isotopes in the form of nuclear residues from reactor operation is a controversial issue primarily due to geological storage and waste processing.

it approaches the positively charged target-nucleus, and in the process, an x-ray photon is emitted containing the electron's change in energy; this means that the closer the electron gets to the nucleus, the more energy it will lose resulting in a relatively higher energy x-ray photon emission. This is known as Bremsstrahlung radiation, where the emitted x-ray radiation from the decelerated electrons result in a continuum of energies. This radiation generation method imparts high quantities of thermal energy onto the target and only a very small fraction of energy results in x-ray photon emission. For this reason, tungsten is used widely as a target material due to its high-Z properties and good thermal conductivity which can enhance heat removal. Other mechanisms used to generate x-ray photons include synchrotron [131] and free electron laser [39] methods to name a few. In the present work, the x-ray photons radiation is generated using a standard medical x-ray tube.

2.1.1.3. Photon Interactions with Matter

The interactions between photon radiation and matter are dictated by the energy of the photon and the elemental composition of matter. Here, the focus will be photoelectric-absorption and Compton scattering. It is important to note that additional interactions include coherent scattering and pair-production [94] which shall be briefly discussed first, but which are pertinent to the present research. Coherent scattering is an elastic process in which the photon does not lose energy, nor the interacting atom is ionized or excited, however, the direction of the photon is changed. This interaction is most prominent for low energy photons and high-Z absorbing materials. This type of interaction is important to mention however, it will not be considered throughout the present research. The next interaction is pair production which occurs at high photon energies which are greater than twice the rest mass of the electron, $h\nu > 1.022\ MeV$. Here, the photon interacts with the nucleus, an electron and a positron are created traveling in opposite directions; the kinetic energy carried by the particles is distributed between the positron, electron, and recoiled nucleus, although the latter might be nearly negligible. The positron will then annihilate when it collides with another electron along its path, resulting in the emission of two more photons traveling in opposite directions. This interaction will not be of concern for the remainder of this research given that the radiation energies utilized do not surpass the minimum energy threshold required for this interaction to occur, nevertheless, it should be considered when applying high energy radiation.

Photoelectric absorption[5] occurs when a photon with an energy equivalent or higher to an electron's binding energy is fully absorbed, in turn the electron is freed and ejected out of the atom's valance shell. The kinetic energy of the electron can be described as

$$KE_{e^-} = h\nu \; - \; E_b \qquad \text{Eq.(2-4)}$$

where h is Planck's constant, ν is the photon frequency and E_b is the electron's binding energy. The liberated electron can scatter onto another electron in the process. The atom is then left in an excited state, given that there is now a vacancy in the K or L shell. An electron from an outer shell transitions to fill the vacancy, however there is still excess energy that needs to be released, this leads to two separate forms of relaxation. The first is the emission of an x-ray photon during the electron transitions, this process is described as fluorescence emission. The second relaxation mechanism is by emitting an Auger electron which ejects an outer shell electron during the transition. The photoelectric interaction proportionally scales with the number of protons in the target atom, and inversely scales with the photon energy through the following power relation obtained from Knoll (p.49),

$$\Gamma \propto \frac{Z^n}{(h\nu)^{3.5}}. \qquad \text{Eq.(2-5)}$$

where n ranges between 4 to 5 depending of the energy region of the photon. This means that photoelectric absorption will be increasingly relevant for proton rich atoms; this relation has a great influence in the radiation detection process which will be discussed later.

Lastly, the Compton scattering process is one of the most common forms of interactions; this was first derived by Arthur H. Compton in 1923 [29] for which he later won a Nobel prize. Here, the photon collides with an electron, in the process the photon changes direction and the part of its energy is transferred to the recoiled electron as shown in Fig. 2.3. Given that the interaction can result in a scattering angle ranging from 0^o to 180^o, this creates a continuum of plausible down scattering energy. The kinematics of this interaction can be obtained from the conservation of energy

$$h\nu + m_e c^2 \; = \; h\nu' + m_e c^2 \gamma \qquad \text{Eq.(2-6)}$$

and the conservation of momentum

$$\frac{h\nu}{c}\vec{\boldsymbol{n}} \; = \; \frac{h\nu'}{c}\vec{\boldsymbol{n}}' + m_e c \; \gamma\overrightarrow{\boldsymbol{\beta}} \qquad \text{Eq.(2-7)}$$

[5] The photoelectric absorption effect was explained by Albert Einstein in 1905 and received a Nobel Prize in 1921 for his work.

where θ is the scattering angle of the photon, $\vec{n}$ is unit vector describing the photon direction, $m_e c^2$ is the electron's rest mass this being 511. keV, γ is the relativistic energy factor describing the rest and kinetic energy, and $\overrightarrow{\beta}$ is the electron fractional velocity in terms of the speed of light. The resulting scattered photon energy can be described as

$$h\nu' = \frac{h\nu}{1 + \left(\frac{h\nu}{m_e c^2}\right)(1 - cos\,\theta)}, \qquad \text{Eq.(2-8)}$$

where $h\nu$ is the incoming photon energy, $h\nu$' is the scattered photon energy, θ is the photon's scattering angle, and $m_e c^2$ is the electron's rest mass. The kinetic energy of the recoil electron can be expressed as

$$\begin{aligned} KE_e &= m_e c^2(\gamma - 1) \\ &= h\nu - h\nu' \\ &= h\nu \left(1 - \frac{1}{1 + \frac{h\nu}{m_e c^2}(1 - cos\,\theta)}\right). \end{aligned} \qquad \text{Eq.(2-9)}$$

The maximum energy loss of the scattered photon energy occurs when the photon fully backscatters at 180°, the resulting photon energy is

$$h\nu'_{min} = \frac{h\nu}{1 + 2\frac{h\nu}{m_e c^2}}, \qquad \text{Eq.(2-10)}$$

and equivalently the maximum energy transferred to the electron is

$$KE_{e,max} = h\nu \left(1 - \frac{1}{1 + 2\frac{h\nu}{m_e c^2}}\right). \qquad \text{Eq.(2-11)}$$

This maximum transfer of energy describes the Compton edge of the continuum that is associated with a photon's photopeak; this will be revisited in the next subsection pertaining to radiation detectors, how the Compton scatter is embedded in measurements and contributes to radiation noise.

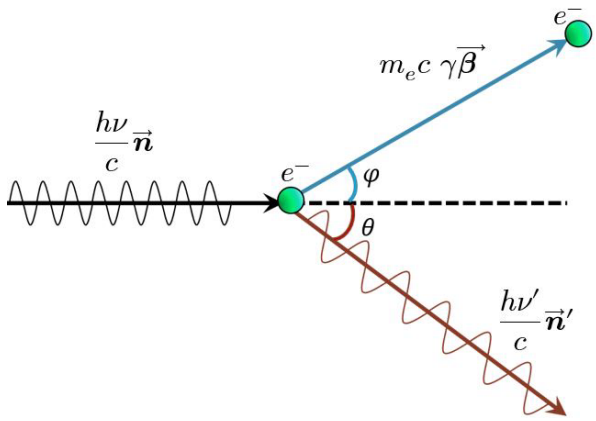

Fig. 2.3. Kinematics diagram of Compton scattering process.

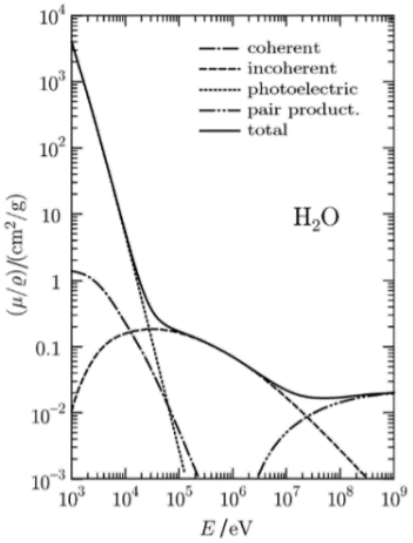

Fig. 2.4. Different photon interaction cross-sections as a function of energy for water, reprinted from Salvat et al. [157].

Typically, the aforementioned interactions are conglomerated into a single term known as the mass attenuation coefficient $\mu(E_\gamma)/\rho$, in which ρ is the density of the material and μ is the linear attenuation coefficient. This relationship describes the probability of interaction per unit mass per unit area, therefore, if the density of a material is halved, then the material needs to in the twice as thick to preserve the same mass and equivalent attenuation. The present work will use the linear attenuation coefficient primarily and the photon energy $h\nu$ will be replaced with E_γ. The mass attenuation coefficient is dependent on the energy of the photon given that it dictates the type of interaction the photon will have as it traverses through; and example of the contributions of the different interactions and the total mass attenuation is shown in Fig. 2.4 for water molecules. The mass attenuation coefficient of compounds made of various elements can be estimated as

$$\frac{\mu(E_\gamma)}{\rho} = \sum_i w_i \left(\frac{\mu(E_\gamma)}{\rho}\right)_i, \qquad \text{Eq.(2-12)}$$

where i denotes the individual element components, and w_i is the fractional weight of these element for each material compound; this formula is a simple but powerful tool that will be used to estimate the mass attenuation for various materials throughout the modeling process. An example of water and iron mass attenuation coefficients are presented in Fig. 2.5, these materials will be commonly present throughout the presented experiments. Although, they might appear comparable at energies higher than the x-ray range, the mass attenuation needs to be scaled by the density, which results in iron being a significantly more attenuating medium in comparison to water. The example intends to highlight how high-Z materials have

larger mass attenuation coefficients at low photon energies. This effect leads to a phenomenon known as beam hardening for poly-energetic x-ray beams, in which the lower-energy photons are preferentially absorbed, therefore the remaining ensemble of particles that are more likely to make it through the material are in the higher energy range. In the presence of high-Z materials, gamma-rays or neutrons are more suitable for imaging purposes. Alternatively, neutrons are highly penetrative through dense materials, while highly interactive with lighter elements; this can result in a favorable light-material contrast, however this can lead to the undesirable neutron activation of materials though other nuclear processes. Additional limitations arise from the lack of commercial availability of neutron source used for imaging. The advantages of gamma-ray radiation lie in the discrete energies of the photons emitted.

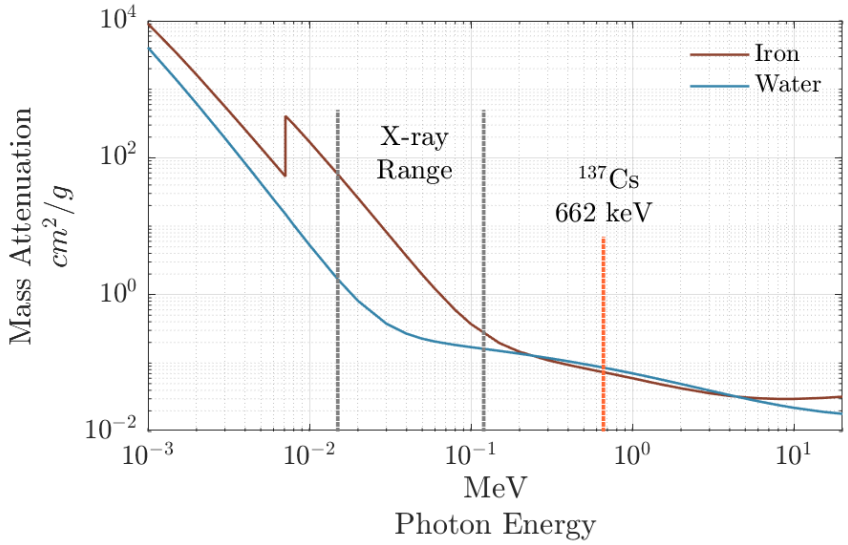

Fig. 2.5. Mass attenuation coefficient for iron and water, comparison between standard x-ray medical tube and ^{137}Cs radioisotope, data obtained from NIST[6].

2.1.1.4. Radiation Transmission

The transmission of particles through matter follows an exponential attenuation behavior. This is analogous to shining a light through an opaque glass, where the intensity of the light observed at the opposite side is dimmed in comparison. Radiation acts in this very same way, here we can describe the radiation intensity or number of particles that cross through a material using the Beers-Lambert Law [24],

$$N = \int_0^T \int_0^\infty I_o(E_\gamma) e^{-\int_0^d \mu(s,E_\gamma) ds} \, dE_\gamma \; d\tau, \qquad \text{Eq.(2-13)}$$

[6] The National Institute of Standards and Technology (NIST) provides an ample mass attenuation database for individual elements and for determined compound materials.

where τ is the time integration variable, E_γ is the photon energies, s is the path length that the photon is traversing, d is the total distance traversed, μ is the energy dependent linear attenuation coefficient, and I_o is the source activity as a function of energy; this expression is generalized to consider poly-energetic sources such as x-rays, therefore the intensity is perceived as an integral over all the photon energies. In the case of gamma-rays, Eq.(2-13) reduces its dependency over energy where the source and the linear attenuation coefficient become constants. It is also worth pointing out that the linear attenuation coefficient is space dependent, a dependency that is encapsulated in the variable s, given that the photons can cross through various materials along its path. The resulting expression describes the radiation intensity crossing a slab in a 1-D geometry.

2.1.2. Radiation Detection

Radiation detectors are sensors which interact and quantify the intensity of the measured radiation, and in some cases depending on the detector type can characterize the energy spectrum associated to the radiation field. So far, the radiation interactions with matter described the mechanisms by which the radiation particle ionizes the atoms along its path, knocking off the electrons, and unleashing chains of events. This section will describe the fundamentals behind counting-based detectors. The detector's function is to translate the total deposited energy into useful signals. The generation of these signals is dependent on the characteristics of the detector as follows: material composition, density, size, and geometry. Nevertheless, the basic task of radiation detector is to keep track of the events that took place inside the detector volume and output an analog signal. This is then amplified, digitized, and discriminated based on an input reference comparison; the latter serves as an energy discriminator in which the events that surpass the reference value then tallied. This counting process is best depicted in Fig. 2.6.

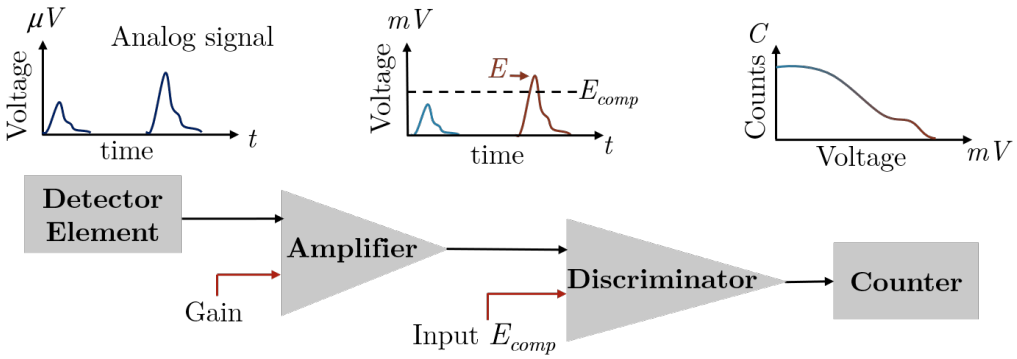

Fig. 2.6. Radiation detection process diagram.

The energy spectrum of the radiation field can be measured by performing subsequent measurements in which the energy threshold is systematically increased. The outcome of the measurement is a counting curve which represents the number of events recorded as a function of threshold voltage; this curve is also referred to as the integral pulse spectrum. Advanced detector systems deploy multichannel analyzers in order to perform this energy discriminating function. This counting curve can then be differentiated resulting in the differential pulse spectrum which is widely used throughout the literature. The integral pulse spectrum is characterized by large drops and counting plateaus. The latter feature represents the transition between two different features in the differential pulse spectrum; this could be different photon peaks for instance. A graphical example of the relations between the integral pulse spectrum and the differential pulse spectrum is shown in Fig. 2.7.

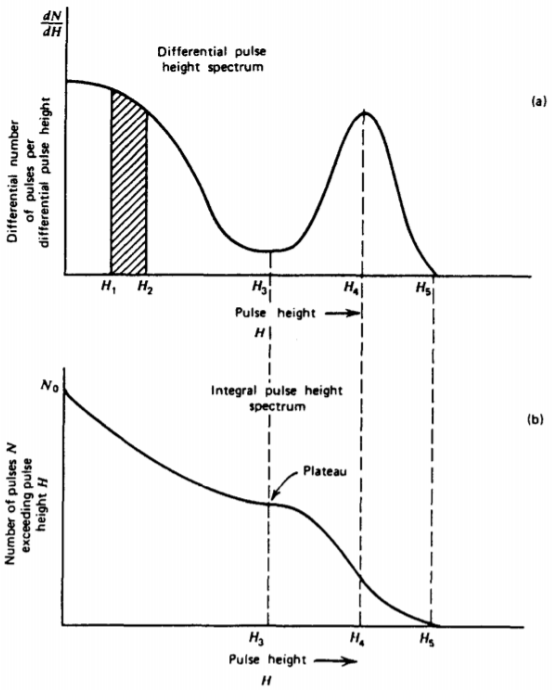

Fig. 2.7. Example of differential and integral pulse height spectra, published in Knoll [94].

The energy resolution of the detector can be determined for a particular detector with the differential spectrum at hand. The energy resolution is defined as the ratio between the width of the photopeak and the centroid of the photopeak as follows

$$Res \; = \; \frac{FWHM}{V}. \qquad \text{Eq.(2-14)}$$

The units of the FWHM and centroid are in terms of the voltage. However, the voltage can be converted into electron volts [eV] by using well known radioisotopes such as ^{137}Cs to determine the energy scaling factor, assuming that this scales predominantly linearly. Additionally, the thickness or depth of the detector along the normal direction of the dictates how efficient the detector is at interacting with the radiation field. This absorption efficiency as a function of photon-energy can be described as

$$\eta(E, \delta) = \; 1 - e^{-\mu(E)\delta} \qquad \text{Eq.(2-15)}$$

where δ is the detector depth. It is evident that if the sufficiently long detectors enhance the probability of interaction for high energy photons which translates to increase in counts correspondent for these energies. However, it must be also noted that this also enhances the ability of the detector to absorb scattered photons which will increase the counts corresponding to lower-energy photons.

It is important to determine the intended application to select the detector accordingly and in an affordable manner. In the present research the detectors are tasked to perform high-spatial resolution measurements, therefore these will be constrained in size to small detector elements. The selected detector materials are LYSO ($Lu_{1.8}Y_{0.2}SiO_5$) scintillation crystals and CdTe crystals. It stands out that these materials have prudent number of Z-rich atoms, which increases the photoelectric response. The qualities and characteristics of these detector materials will be further elaborated in the following sections.

2.1.2.1. LYSO Scintillators

Inorganic scintillation materials are doped with activation atoms that act as scintillation centers [175] which emit visible light in response to radiation interactions. The scintillation process is fairly complex, the reader can find a concise explanation articulated by Knoll [94]. To summarize, this response occurs when the radiation particles interacts through the mechanisms previously described, the scattered energetic electrons further collide with other electrons and ionize atoms along their path, creating a chain of events which generate electron-hole pairs; these events are ionization avalanches that are unchained as the primary scattered electron collides with secondary electrons along its path, similarly the secondary electrons undergo the same process and so on until the energy has been fully deposited. The holes quickly combine with the activation atom thus ionizing it and leaving it in an excited state. The activator atoms are quickly neutralized with electrons emitted from valance shells in the avalanche, the neutralized atom relaxes via electronic transitions, emitting visible light photons in the process. The relaxation and emission of light are characterized by a decay constant which symbolizes how fast the process occurs in a specific scintillation material; preferably this constant should be small for an efficient distinction between subsequent events and avoid build up. Additionally, it is important that the emitted light is not absorbed by the material, therefore, the material remains translucent to the emitted wavelength; this requires that the light absorption/excitation and emission spectrums of a material do not overlap. The light output efficiency of a material is characterized by the number of photons generated per unit of deposited energy. Ultimately, the light output can then be used to generate an analog output by pairing it onto a photomultiplier component.

The detection process of scintillation crystals is graphically depicted in Fig. 2.8 which highlights the conversion from radiation energy deposition into light emissions.

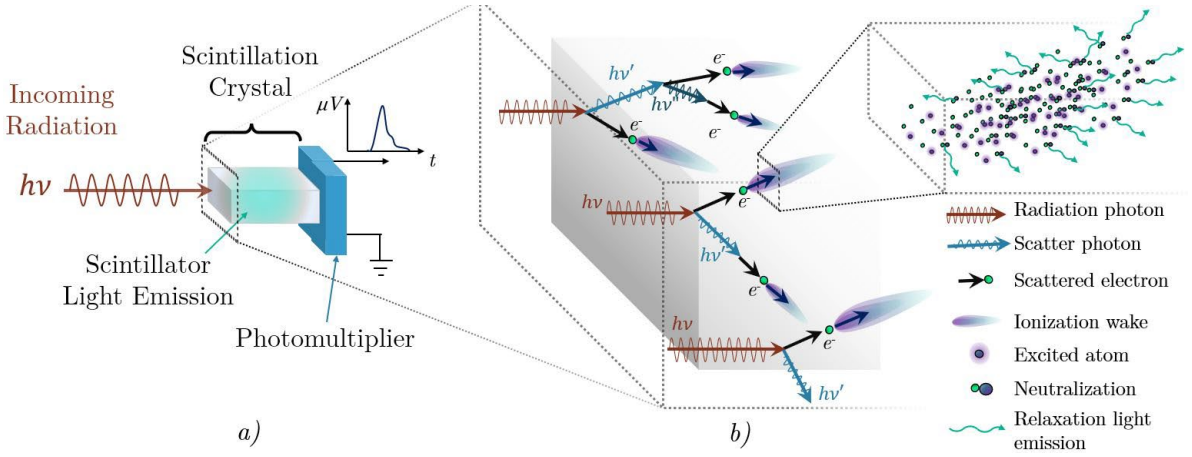

Fig. 2.8. ***a)*** **Scintillation detector element and** ***b)*** **visual representation of interactions occurring inside the crystal structure and the scintillation process.**

Conveniently, LYSO is characterized by a fast relaxation time of about 50 ns and output light yield of about 33k photons/MeV reported by Pidol et al. [143], which highly enhances the counting rate capabilities and energy conversion in comparison to other scintillator crystal such as BGO. Furthermore, it has a moderate density of ranging from 7.1 g/cm^3 to 7.4 g/cm^3 and an effective Z of 66 also reported in [143], this enhances the probability of interaction and favorability of photoelectric interactions. The absorption and emission spectrum of the LYSO scintillation materials are sufficiently separated which reduces the self-absorption of the emission light, demonstrated by Pepin et al. [141]. The reported composition of LYSO varies slightly throughout the literature, however, the composition reported by Dominguez et al. [35] will be used as reference to estimate the absorption efficiencies of the LYSO material, these are tabulated in Table 2.1. The absorption efficiency of LYSO crystal can be obtained by first calculating the mass attenuation coefficient using Eq.(2-12) with the corresponding element mass fraction from Table 2.1, then multiplying by the LYSO density to convert into the linear attenuation coefficient, and finally plugging these into Eq.(2-15) for the thickness $\delta \in [1, 5, 10, 15, 20]$ mm. The absorption efficiency shown in Fig. 2.9 demonstrates that the LYSO material is proficient in detecting x-ray photons for crystal depths of 5 mm and above. Typical γ-rays are above the x-ray range, the efficiency consistently decreases with increase in energy. The increase in crystal depth shifts the absorption probability towards higher energies and increases the probability of interaction.

Table 2.1. LYSO elemental composition reported from Dominguez et al. [35].

Element	Atomic Number	Struct. # of atoms	Mass Fraction
Lu	71	1.8	0.7145
Y	39	0.2	0.0403
Si	14	1	0.0637
O	8	5	0.1815

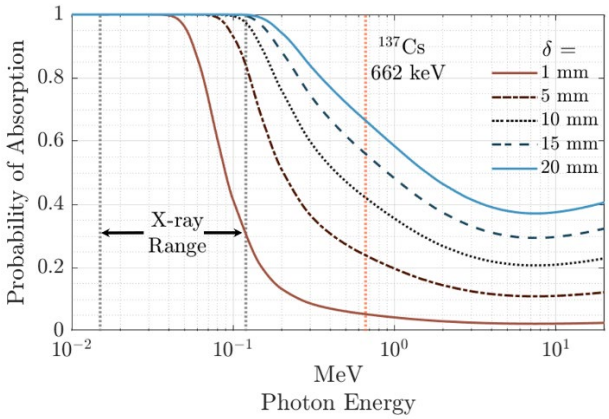

Fig. 2.9. LYSO absorption efficiency as a function of photon energy for various crystal depths.

The LYSO crystal utilized in the present research have dimensions of 2x6x15 mm^3; the absorption efficiency of these crystals follow the dashed line corresponding to a 15 mm depth shown in Fig. 2.9. A prototype detector element was assembled with a sample LYSO crystal. The LYSO crystal was enclosed in a reflective material leaving one face open. The light emission from the crystal is measured utilizing a Silicon-Photomultiplier (SiPM) diode. The LYSO and the SiPM were coupled with optical grease, this practice has been shown by Turtos et al. [182] and Gramuglia et al. [52] to improve the light transmittance from the LYSO crystal to the photomultiplier medium. Two different SiPM diodes with crystal depths of 15µm and 25µm were tested; the respective SiPM models are Kretek PM3315 and PM3325. The bias of the PM3315 SiPM was varied from 28.5V to 31.5V in incremental steps of 1V. Similarly, the PM3325 SiPM bias voltage was varied from 26.5V to 29.5V in incremental steps of 1V. Spectral measurements were performed using a ^{137}Cs source with an activity of 22 µCi at the time the measurements were performed. The prototype detector element was placed in a dark box along with the radioisotopic source; the prototype detector and source are shown in Fig. 2.10. The readout of the detector was carried out with a DRS4 evaluation board. The measured differential spectrums for the two SiPMs are shown in Fig. 2.11. The 15µm SiPM captures the associated spectrum with bias voltages above 29.5V. The 25µm SiPM captures the spectrums for all applied bias, however, at the lowest setting the spectrum is compact. Overall, the SiPM bias has the effect of scaling the measured spectrum, thus refining the deposited energy scale to output signal unit. The measured spectrums of the 137Cs source show the 662 keV characteristic photopeak, and behind it is the Compton continuum. The origin of this continuum is briefly explained in Section 2.1.1.3, most importantly, this low energy region is a source of radiation noise in imaging applications, unless the

objective is to perform Compton scatter imaging. The peak energy resolution at the associated photopeak for both detector arrangements is shown to improve with increased bias, achieving an energy resolution of 14.1% for the 15µm thick SiPM and 12.8% for the 25µm SiPM. The estimated resolution with the 25µm SiPM matches the photopeak energy resolution reported by Pepin for LYSO scintillators; differences with the reported values in [141] also arise from the difference in crystal dimensions. Other studies report energy resolution of LYSO crystals as low as 8.1% by Pidol et al. [143]. This small prototype serves to highlight the performance of LYSO scintillation crystals utilized in the present research with further elaboration in later sections, it also emphasizes the importance of carefully selecting a light-to-signal convertor component in the design process of a detector element, thus best optimizing the performance of the detector.

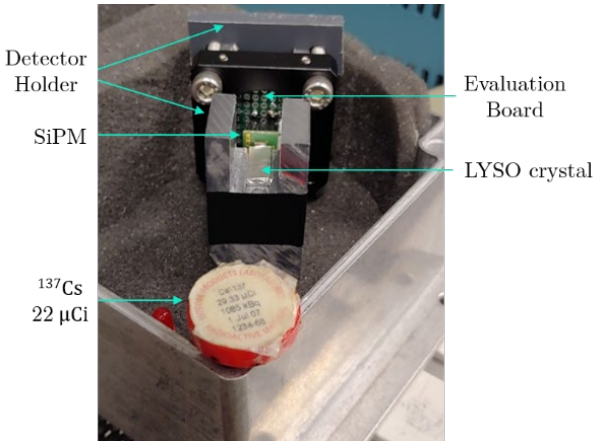

Fig. 2.10. Detector prototype and 22µCi ^{137}Cs source.

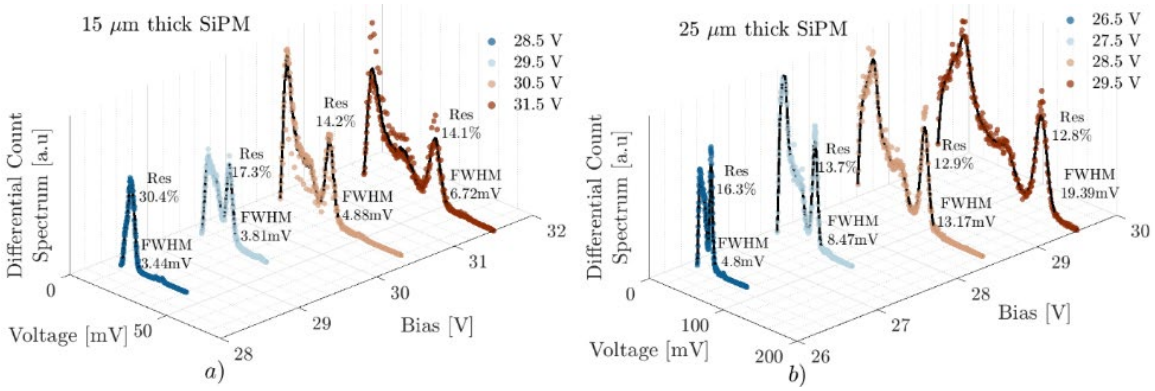

Fig. 2.11. Measured ^{137}Cs differential spectrum with a prototype LYSO crystal paired with a) 15µm thick and b) 25µm thick SiPM component.

2.1.2.2. CdTe Semiconductors

The second type of detectors implemented in the present research are CdTe semiconductors; first the discussion will briefly focus on the functionality of semiconductor detectors, and then the characteristics of the CdTe material will be discussed. Semiconductor materials are characterized by their narrow bandgap which facilitates the ascension of electrons from the valance band and onto the conduction band; typical bandgaps energies are of less than 2 eV. The mobility of this ascended electron implies that a vacancy is

generated. This produces a net positive charge (or absence of negative charge) that can drift in the same manner as an electron but in the opposite direction under the presence of an electric field, this vacancy is referred to as a hole. An applied electric field facilitates the transport and collection of these freed electrons and their corresponding hole pairs; semiconductor detectors are typically arranged in planar geometry as shown in Fig. 2.12, a simple geometry which applies an electric field across the semiconductor material from the anode to the cathode. In the presence of radiation field, ionization trails create various of the electron-hole pair sites. Therefore, the energy deposited inside the material volume is proportional to the charge collected from the generated electron-hole pairs. Fig. 2.12 depicts the ionization process and the drift of electrons and holes towards the respective electrode. These semiconductor materials are often doped with impurities to increase their conductivity by virtually reducing the crystal structure's bandgap between the valance band and the conductive band with forbidden bands that lie in between. These dopants can be in the form of *n*-type dopants which are atoms that act as electron donors or *p*-type dopants which contribute to the overall hole bulk. These types of detectors intrinsically generate leakage currents which are proportional to the applied bias [94, 168-171], it is important to minimize these such that the signals generated by ionization events are not overwhelmed by the leakage current; this is particularly the case in ohmic electrode contacts. Other known issues include recombination in which the charge carrier is neutralized as an electron fills an available hole, this leads to a decrement of charge associated with an ionization event. Additional charge removal mechanisms occur due to hole trapping arising from low hole mobility and short lifetime.

CdTe detectors are attractive because they are relatively high-Z materials which enhances the interaction probability with radiation, yielding higher detection efficiency. In recent decades production methods [49, 85, 174] have advanced significantly to reduce the size of the crystal along with the compact detector readout electronics thoughtfully developed by Spartiotis et al. [168-171] in conjunction with Schulman [164], thus making them ideal for high spatial resolution measurements. This material type has a bandgap of 1.54 eV which enables detector operation at room temperature [174] and improved performance with modest cooling. The CdTe crystals utilized in the present research have range dimensions of $100\times100\times500$ μm^3 and $100\times100\times750$ μm^3, representing different detector systems. The absorption efficiency of CdTe for crystal depths of $\delta \in [0.5, 0.75, 1.0, 2.0]$ mm is shown in Fig. 2.13 based on the composition presented in Table 2.2. The absorption efficiency depicts how these crystals are optimal for low energy x-ray and γ-rays However, at increased energies, these are less likely to interact, therefore it is increasingly

difficult to have full energy deposition as scattered photons escape the detector volume. In addition, fluorescent x-rays emitted from Cd and Te generated from after photoelectric processes can also escape, which further extends the loss of energy from the detector element volume. In tightly packed detector panels composed of multiple detector elements, creates an environment in which scattered photon or emitted x-ray originating in one detector element interacts in an adjacent detector element-pixels. This results in double counting an ionizing radiation event due to the signals generated in these detector elements. A clever solution was elaborated by Ullberg et al. [183, 184] in which temporally matching charge signals from neighboring detector pixels are added and assigned to the pixel which registered the largest charge. The results presented by Ullberg significantly improved spatial resolution and decreased the associated noise for measurements performed with the panel geometry.

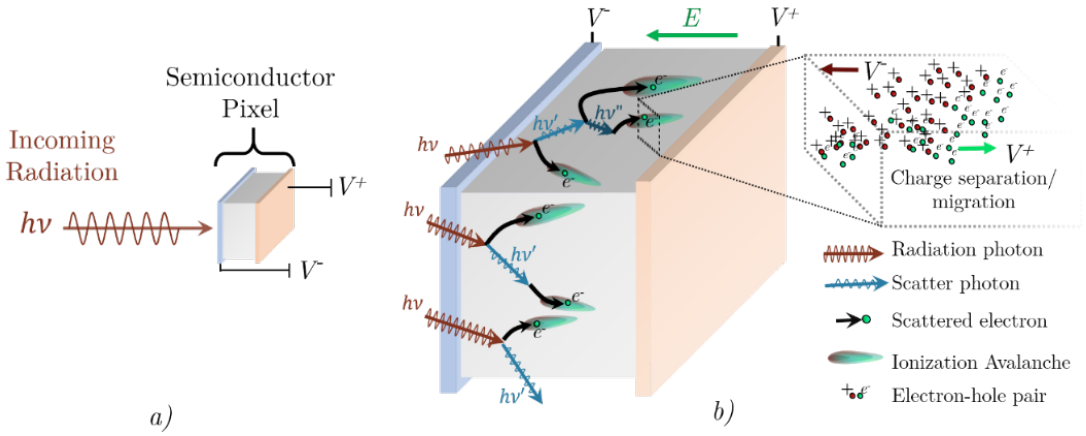

Fig. 2.12. ***a)*** **Semiconductor detector element and** ***b)*** **visual representation of interactions occurring inside the semiconductor pixel.**

Table 2.2. CdTe elemental composition.

Element	Atomic Number	Struct. # of atoms	Mass Fraction
Cd	48	1	0.4684
Te	52	1	0.5316

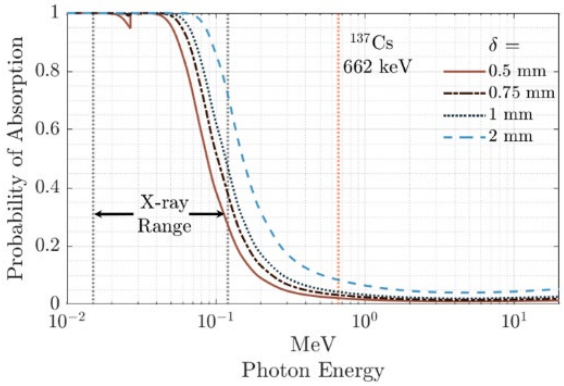

Fig. 2.13. CdTe absorption efficiency as a function of photon energy for various crystal depths.

2.2. Computed Tomography Imaging

So far, the discussion has been centralized in the principles behind particle interactions with matter and radiation detection. These mechanisms are the fundamental basis behind radiation-based imaging to survey objects that are otherwise optically thick. The focus is now shifted to imaging methods where the objective is to obtain qualitative and quantitative information of the material composition, and map the spatial distribution in the measured region of interest. The present discussion will be a brief overview on the topic of Computed Tomography (CT) methods used to reconstruct cross-sectional or volume regions of an object; however, a more enriching and thorough explanation is provided by Fessler in his book [45]. Various reconstruction algorithms have been developed with a wide range of complexities; however, this research will implement primarily Filter-Back Projection (FBP) which is practical for the present applications.

The measurement process is carried out with CT scanners, these are large imaging devices that deploy arrays or panels composed of hundreds of detector elements. The device includes a radiation source which is placed at a determined distance across from the detector, where the field of view (FOV) is the space between the source and the detector. Calibration of the imaging device requires the measurement of the radiation intensity crossing the FOV without an object, also known as the *flat field*; this is used as a reference signal for the actual measurement. Next, we will describe the scanning and reconstruction process of the object following the derivations prescribed by Fessler's book [45] and Noll's notes [130] on tomography.

2.2.1. Forward Projection

The object is placed in the FOV at a determined distance away from the radiation source. The detector is tasked with measuring the radiation intensity variation in the transverse direction as it crosses the present material, this is the resulting projection of the object. Sequential measurements are performed by rotating the imaging system (source-detector) in small incremental angular steps around the object, thus recording the intensity variation as a function of angular position as well, this process is best depicted in Fig. 2.14.*a)* for three simple cylindrical objects; here two angular measurements are depicted. Sufficient information of the object is acquired as a function of radial position and angle. The measurement needs to be transformed based on the radiation transmission relations from Eq.(2-13) to retrieve the material attenuation information, this can be done in the following:

$$p_\theta(r) = -\ln\left(\frac{N_M(r,\theta)}{N_o}\right), \qquad \text{Eq.(2-16.}a\text{)}$$

where N_o is the flat field calibration, N_M is the recorded count measurement with the object present. Here, $p_\theta(r)$ is known as the sinogram; an example of this object is shown in Fig. 2.14.*b)*. It is worth noting the sinusoidal characteristic of the sinogram which becomes more prominent with an object's increased distance away from the center of rotation. This forward projection process is known as the Radon transform [151], the properties of this transformation are listed in Fessler's book [45]. The notation used by Fessler is adapted here to describe a formal definition of the Radon transform for the case of a parallel radiation beam,

$$p_\theta(r) = \int\int \mu(x,y)\ \delta(x\cos\theta\ +\ y\sin\theta\ -r)\ dx\ dy. \qquad \text{Eq.(2-16.}b\text{)}$$

The expressions Eq.(2-16.a) and Eq.(2-16.b) are equivalent, it becomes evident that the projections are line integrals belonging to the cumulative attenuation coefficient values along the ray paths traversing the object that are incident on the detector elements. Additionally, the sinogram for the case of a parallel beam has symmetric and periodic property

$$p_\theta(r)\ =\ p_{\theta+\pi}(-r), \qquad \text{Eq.(2-17)}$$

therefore, for this specific case, measurements of $\theta \in [0, \pi]$ yield sufficient angular information. The sinogram below is extended for angles up to $\theta = 2\pi$ to highlight the periodicity of the Radon transform. In the example bellow, the cumulative attenuation is represented by the magnitude in the resulting projection space, some objects present higher attenuation due to their material composition and size.

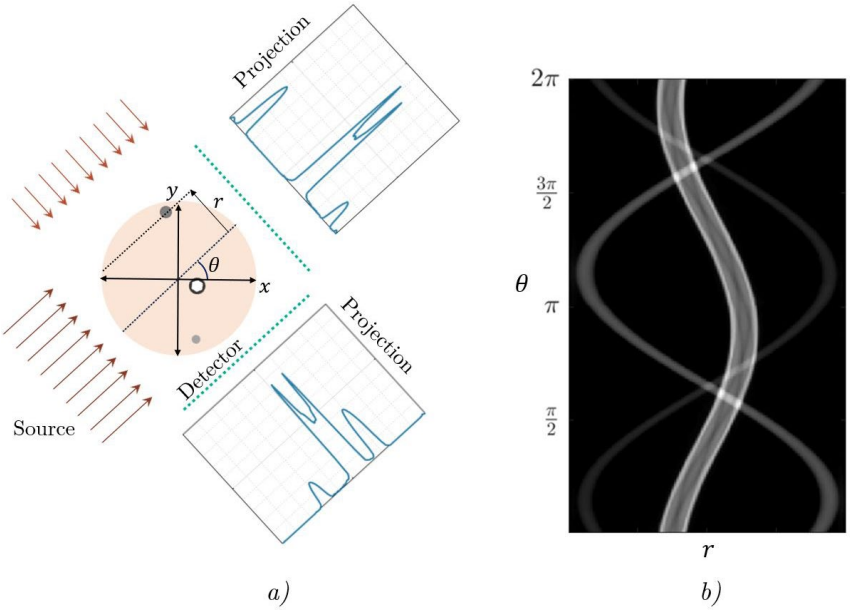

a) *b)*

Fig. 2.14. *a)* Example of forward projection of three simplified objects, and *b)* resulting sinogram.

The pillar behind CT is the Fourier-slice theorem also known as the central-slice theorem. This describes the relation of the radon transform of an object $p_\theta(r)$ and how its 1D Fourier transform is a slice spanning along the angle θ in the Fourier space, whereby multiple slices are used to sample the 2D Fourier space of the object. Let us define the 1D Fourier transform of the projected space $p_\theta(r)$ as

$$P_\theta(\nu) \;=\; \int_{-\infty}^{\infty} p_\theta(r)\; e^{-i\;2\pi\;\nu\;r}\; dr. \qquad \text{Eq.(2-18)}$$

The 2D Fourier transform of the object can then be described as

$$M(u,v) \;=\; \int_{-\infty}^{\infty}\int_{-\infty}^{\infty} \mu(x,y)\; e^{-i\;2\pi[ux\;+\;vy]}\; dx\; dy. \qquad \text{Eq.(2-19)}$$

Then, the Fourier spaces variable (u,v) can be defined by their polar form

$$u \;=\; \nu\cos\theta, \qquad \text{Eq.(2-20.}a\text{)}$$

$$v \;=\; \nu\sin\theta. \qquad \text{Eq.(2-20.}b\text{)}$$

The Fourier-slice theorem can be used to relate the corresponding Fourier-projection to the object's transform as

$$P_\theta(\nu) \;=\; M(u,v)\;|_{\,v\;=\;\nu\sin\theta}^{\,u\;=\;\nu\cos\theta}, \qquad \text{Eq.(2-21.}a\text{)}$$

$$P_\theta(\nu) \;=\; M(\nu,\theta) \qquad \text{Eq.(2-21.}b\text{)}$$

or more explicitly related

$$P_\theta(\nu) \;=\; \mathcal{F}_{\,2D}\{f(x,y)\}\;|_{\,v\;=\;\nu\sin\theta}^{\,u\;=\;\nu\cos\theta}. \qquad \text{Eq.(2-22)}$$

An example of the Fourier-slices are depicted in Fig. 2.15 correspondent to some of the collected projections in the example above, this serves to show the sampling relations in the Fourier space.

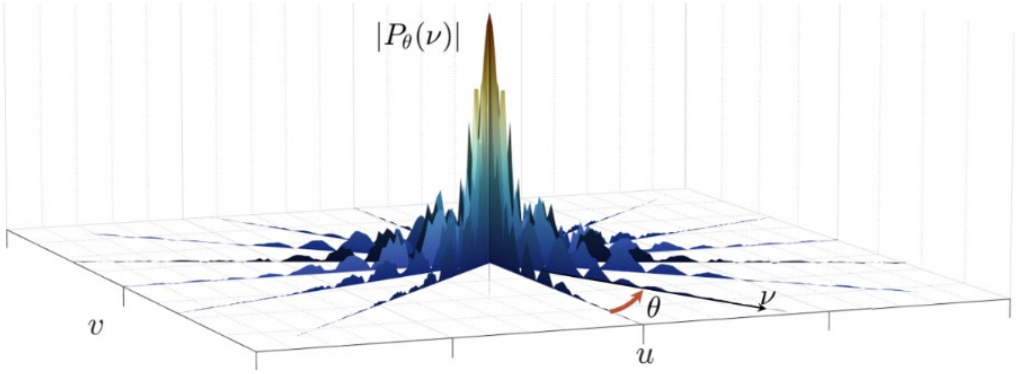

Fig. 2.15. Example of Fourier slices corresponding to 1D Fourier transform of the collected projections.

2.2.2. Object Reconstruction

Once the forward projection measurement of the object has been obtained, the reconstruction is performed in the data post processing step. The end goal of the reconstruction process is to map the spatial distribution of the of the linear attenuation $\mu(x, y)$ properties of the measured object. Here, the reconstruction is left open-ended given that different methods and algorithms can be used to perform this task, these include conjugate gradient least square (CGLS), simultaneous algebraic reconstruction technique (SART),simultaneous iterative reconstruction technique (SIRT), and filter-back projection (FBP); the latter will be the focus of the brief discussion in this section.

Intuition would first tell us to use the projected data and superimpose back into the spatial domain; this process is defined as the inverse Radon transform [45, 100] also referred to as backprojection. This can be defined as

$$\mu_b(x, y) = \int_0^{\pi} \int_{-\infty}^{\infty} p_\theta(r)\ \delta(x\cos\theta\ +\ y\sin\theta\ -r)\ dr\, d\theta, \qquad \text{Eq.(2-23)}$$

where the subscript b denotes the backprojection process. This can also be described with the Fourier transformed projections relations from Eq.(2-21.b),

$$\begin{aligned} \mu_b(x, y) &= \int_{-\infty}^{\infty} \int_0^{\pi} \int_{-\infty}^{\infty} M(\nu, \theta)\ \delta(x\cos\theta\ +\ y\sin\theta\ -r)\ e^{i2\pi\nu r} dr\, d\theta\, d\nu \\ &= \int_0^{\pi} \int_{-\infty}^{\infty} M(\nu, \theta)\ \ e^{i2\pi\nu[x\cos\theta\, +\, y\sin\theta]}\ d\nu\ d\theta \end{aligned} \qquad \text{Eq.(2-24)}$$

This form highly resembles the inverse Fourier transform form in polar coordinates; however, the respective limits of integration need to change to $(0, \infty)$ and $(0, 2\pi)$, along with a missing ν factor for it to be complete; this is easily implemented by including $\frac{1}{\nu} \times \nu$,

$$\begin{aligned} \mu_b(x, y) &= \int_0^{2\pi} \int_0^{\infty} \frac{M(\nu, \theta)}{\nu}\ \ e^{i\ 2\pi\ \nu\ [x\cos\theta\, +\, y\sin\theta]}\ \nu\ d\nu\ d\theta\,, \\ &= \mathcal{F}_{2D}^{-1}\left\{\frac{M(\nu, \theta)}{\nu}\right\}, \\ &= \mu_b(x, y) \ast\ast\, \mathcal{F}_{2D}^{-1}\left\{\ \frac{1}{\nu}\ \right\}, \\ &= \mu(x, y) \ast\ast \frac{1}{r}. \end{aligned} \qquad \text{Eq.(2-25)}$$

Here, ** symbolizes a 2-D convolution between the present functions. This derivation highlighted in Noll [130] denotes the fact that simple backprojection reconstruction is the result of a convolution of the object with a degrading blur relation of $1/r$. The backprojection reconstruction of the example sinogram is shown

in Fig. 2.16.*a)*, where the objects are spatially mapped with different intensities associated to each of them, however, there is a glow emanating from the objects which is the result of the $1/r$ convolution. This can also be thought as the residual tails from the superposition of consecutive projections on to the reconstruction space in the backprojection process.

The results from the backprojection highlight the need to filter out and counteract these undesired residual effects. This can be performed by adding one extra step to the post processing prior to performing the backprojection in which a ramp filter (or other type of filter) is applied to the collected projections. The implementation of the ramp filter takes place once the Fourier transform of the projection is carried out,

$$\begin{aligned} \hat{p}_\theta(r) &= \mathcal{F}_{1D}^{-1}\{\ \mathcal{F}_{1D}\{p_\theta(r)\} \cdot\ |\nu|\ \}, \\ &= \mathcal{F}_{1D}^{-1}\{\ P_\theta(\nu)\ \cdot\ |\nu|\ \}, \\ &= \mathcal{F}_{1D}^{-1}\{\ \widehat{P_\theta}(\nu)\ \}, \end{aligned} \qquad \text{Eq.(2-26)}$$

where $\hat{p}_\theta$ is the newly filtered projection. This exploits the convolution property in which the convolution of two functions in the spatial domain results in the product of the Fourier transformed functions in the frequency domain. Otherwise, the equivalent spatial ramp filter must be convolved onto the projection space. The filtered projections can then be backprojected onto the reconstruction space,

$$\hat{\mu}(x,y) = \int_0^\pi \int_{-\infty}^{\infty} \hat{p}_\theta(r)\ \delta(x\cos\theta\ +\ y\sin\theta\ -r)\ dr\, d\theta. \qquad \text{Eq.(2-27)}$$

Equivalent to the previous derivation of Eq.(2-24) with slight change that accounts for the missing factor of ν, is now provided by the filter. Similarly, applying the change of integration bounds, the resulting reconstruction can be described as

$$\begin{aligned} \hat{\mu}(x,y) &= \int_0^\pi \int_{-\infty}^{\infty} |\nu|\ M(\nu,\theta)\ \ e^{i2\pi\nu[x\cos\theta\ +\ y\sin\theta]}\ d\nu\ d\theta \\ &= \int_0^{2\pi} \int_0^{\infty} \nu\ M(\nu,\theta)\ e^{i2\pi\nu[x\cos\theta\ +\ y\sin\theta]}\ d\nu\ d\theta\,, \\ &= \mathcal{F}_{2D}^{-1}\{M(\nu,\theta)\}, \\ &= \mu(x,y). \end{aligned} \qquad \text{Eq.(2-28)}$$

The result of the filtered backprojection (FBP) of the example sinogram is depicted in Fig. 2.16.*b)* which shows a significant improvement in the imaging reconstruction quality with the applied filter. Additional methods highlighted by Fessler [45] include direct Fourier reconstruction which requires interpolation from the polar coordinate system (ν,θ) in the Fourier domain to the gridded Cartesian-like coordinate system (u,v), and from this, perform the inverse 2D Fourier transform to retrieve the object; without proper

treatment, this can embed undesired interpolation artifacts. The relations between the object and the resulting projections and transforms are presented in Fig. 2.17 adapted from Fessler [45].

The present discussion serves to provide the theoretical background of the FBP method that is widely used in this research. Although, the derivation is provided for the simple case of the parallel-beam, the methods are slightly modified for different geometries such as flat-fan and arc-fan geometries [45], as well as its 3D analogue, the FDK (Feldkamp, Davis, and Kress) [43] algorithm for detector panels.

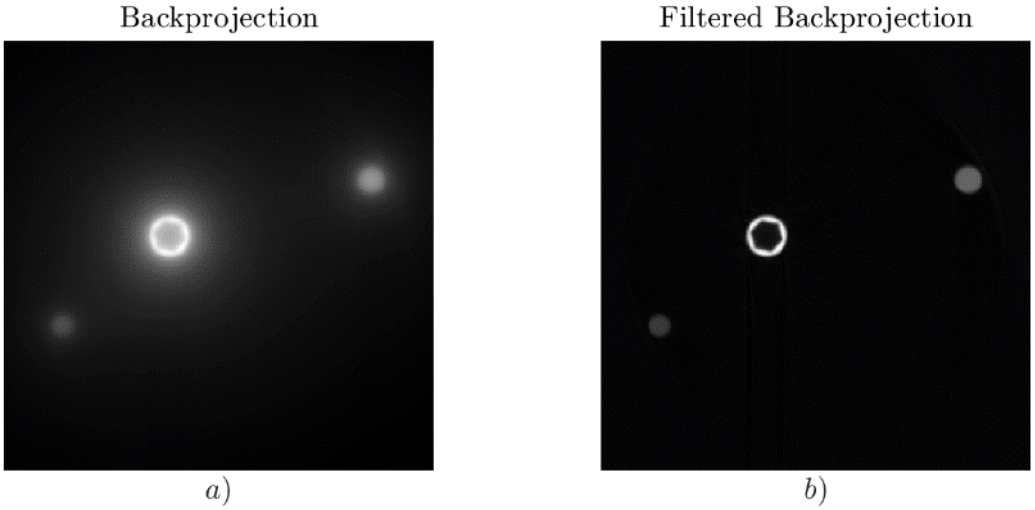

Fig. 2.16. Object reconstruction performed with *a)* backprojection, and *b)* Filter-backprojection.

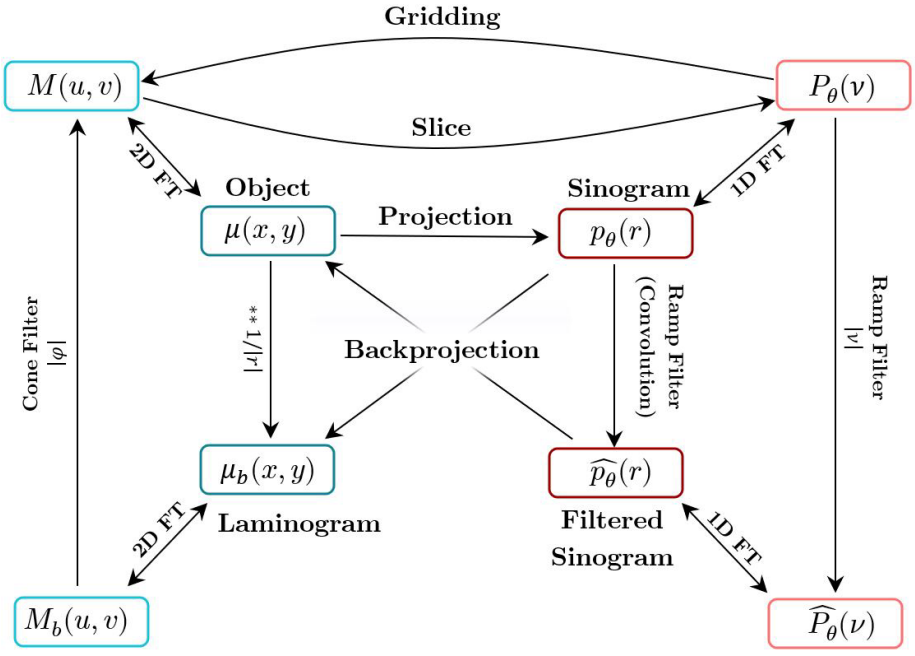

Fig. 2.17. Relationships between object and projection domain, along with their associated Fourier transforms. Reprinted and adapted from Fessler [45].

2.2.3. Imaging System Geometries

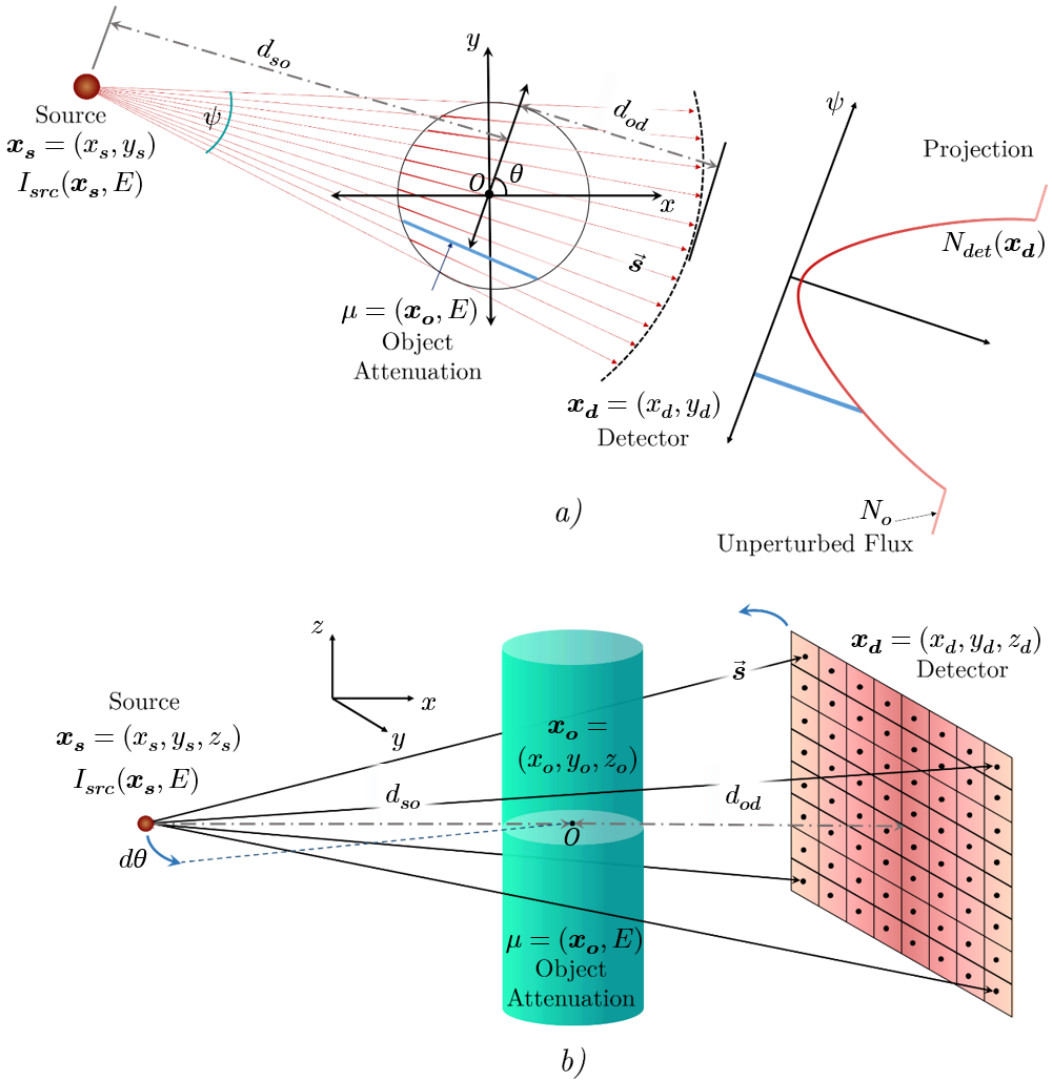

Fig. 2.18. Relations for *a)* fan-arc imaging system, and *b)* cone beam detector-panel imaging system.

The primary imaging system geometries utilized in the present research include arc-fan and cone beam CT; these are graphically represented in Fig. 2.18. Here, the object location is defined with coordinates $\boldsymbol{x_o}$ centered at the origin O and containing spatially distributed linear attenuation coefficients $\mu(\boldsymbol{x_o}, E)$. The radiation source is described by coordinates $\boldsymbol{x_s}$, and detector system with coordinates $\boldsymbol{x_d}$; the object-source distance is defined as d_{so} and the object-detector distance is defined as d_{od}. The generic vector $\vec{s}$, describes the path-length that connects source location, $\boldsymbol{x_s}$ and a given detector location, $\boldsymbol{x_d}$. The source and detector synchronously move around the object with incremental angular step $d\theta$, performing measurements over 360°.

The Beers-Lambert Law in Eq.(2-13) is adapted to describe any arbitrary system and incorporate the vector definitions of the source, object, and detectors; this will be useful to describe the modeling process in later sections. Let $I_{src}(\boldsymbol{x_s}, E)$ denote the activity or photon-rate emitted by the source with energy E. The linear attenuation coefficient is then sifted along the path of $\vec{\boldsymbol{s}}$. The recorded counts by the detector are denoted as

$$N_{det}(\boldsymbol{x_d}) = \int_0^T \int_0^\infty \frac{I_{src}(\boldsymbol{x_s}, E)\ C(E)}{4\pi\ \|\overrightarrow{\boldsymbol{s}}\|^2}\ e^{-\int_0^{\vec{\boldsymbol{s}}} \mu(\overrightarrow{\boldsymbol{s}}', E) d\overrightarrow{\boldsymbol{s}}'}\, dE\ d\tau, \qquad \text{Eq.(2-29)}$$

where, T is the detector recording time, $d\overrightarrow{\boldsymbol{s}}'$ is a differential length along the dummy vector $\overrightarrow{\boldsymbol{s}}'$ that is used to sift the linear attenuation values along the total path length $\overrightarrow{\boldsymbol{s}}$. In addition, a factor of $1/(4\pi\ \overrightarrow{\boldsymbol{s}}^2)$ is included to account for the geometric drop in radiation intensity with increase in distance. The constant C combines various source and detector and geometric constants; these include the detector absorption efficiency $\eta(E, \delta)$, source photon-yield, and detector area. The expression in Eq.(2-29) is further simplified for the case of mono-energetic gamma rays: in this case, the linear attenuation coefficient μ is constant for any given material.

2.2.4. Projection Error Propagation

Extending the analysis to the error propagation of the measured projection, the variance associated to the measured counts is obtained through the following steps:

$$\sigma_{p_\theta}^2 = \sigma_{N_{M,\theta}}^2 \left(\frac{\partial p_\theta}{\partial N_{M,\theta}}\right)^2 + \sigma_{N_0}^2 \left(\frac{\partial p_\theta}{\partial N_0}\right)^2, \qquad \text{Eq.(2-30)}$$

$$\frac{\partial p_\theta}{\partial N_{M,\theta}} = -\frac{1}{N_{M,\theta}}, \qquad \text{Eq.(2-31)}$$

$$\frac{\partial p_\theta}{\partial N_0} = \frac{1}{N_0}, \qquad \text{Eq.(2-32)}$$

$$\sigma_{p_\theta}^2 = \frac{\sigma_{N_{M,\theta}}^2}{N_{M,\theta}^2} + \frac{\sigma_{N_0}^2}{N_0^2}, \qquad \text{Eq.(2-33)}$$

where $\sigma_{N_0}^2$ and $\sigma_{N_{obj}}^2$ are the respective measured count variances for the flat field and with object present. It can be seen from Eq.(2-33) that the variance of the measured photon field when the test section is present between source and detector decreases inversely with the square of the measured counts, meaning that large radiation fluxes and increased measurement times can drastically reduce the attenuation variance. If the flat field is measured for a long period of time, the variance of the second term becomes negligible, further reducing the variance to

$$\sigma_{p_\theta}^2 \approx \frac{\sigma_{N_{M,\theta}}^2}{N_{M,\theta}^2}, \qquad \text{Eq.(2-34)}$$

which is only dependent on the measurement performed with the object present. The variance of the projections can be obtained by performing several measurements at the same location. However, in the case where several measurements cannot be carried out, the Poisson statistical behavior of radiation dictates that the variance is equivalent to the recorded counts as

$$\sigma_N^2 = N. \qquad \text{Eq.(2-35)}$$

Therefore, utilizing this assumption further simplifies Eq.(2-34) to

$$\sigma_{p_\theta}^2 \approx \frac{1}{N_{M,\theta}}. \qquad \text{Eq.(2-36)}$$

Methods to estimate the variance of the reconstructed images were proposed as early as 1984 by Huesman [71]. Since, several research efforts have continued to refine this analysis for FBP method [192, 193] and expanded to iterative algorithms proposed by Fessler [44] and Schmitt [163]. Although, this is not further elaborated in the present research, it can be implemented in future work to further enhance the analysis of the results presented in later chapters.

2.2.5. Blur Considerations

Ideally, a perfect imaging system would be composed of a point-source and point-detector as these would allow to perfectly sift the object's spatial information. However, this system is not realistic since conventional detectors and sources have finite dimensions. Therefore, the resulting imaging system requires the convolution of the source, object, and detector functions in the consideration of the system response; this results in blurring effects of sharp interfaces, and small details to be lost. The achievable resolution of an imaging system is dictated by several geometric factors. Fig. 2.19 shows an example of a simplified imaging system composed of a detector array, a radioactive source and an object placed in between the two. The focal spot, f, is defined as the diameter (or characteristic width) of the radiation source. The blur of the detector, B_d, is defined by the width of the detector crystal. The system magnification is defined as

$$Mag = \frac{d_{sd}}{d_{so}}. \qquad \text{Eq.(2-37)}$$

The blur of the detector at the object plane is

$$B_{do} = \frac{B_d}{Mag}, \qquad \text{Eq.(2-38)}$$

similarly, the blur of the focal spot at the object plane is

$$B_{fo} = f\left(1 - \frac{1}{Mag}\right). \qquad \text{Eq.(2-39)}$$

The object blur can then be defined as the root mean square of the detector blur and focal-spot blur at the object plane

$$B_o = \sqrt{{B_{do}}^2 + {B_{fo}}^2} \qquad \text{Eq.(2-40.}a\text{)}$$

$$B_o = \sqrt{\left[\frac{B_d\, d_{so}}{d_{sd}}\right]^2 + \left[f\left(1 - \frac{d_{so}}{d_{sd}}\right)\right]^2}. \qquad \text{Eq.(2-40.}b\text{)}$$

We can further simplify the expression by parametrizing this relation based on the relative blurring $R_b = B_o/B_d$ in respect to the detector size, we then use the relative distances $\chi = d_{so}/d_{sd}$ form the source for which d_{so} can freely be ranged, and the relative focal-spot to detector size is defined by the variable $\beta = f/B_d$; it is worth noting that $\beta < 1$ represents a relative small source focal-spot in comparison to the detector size, while $\beta > 1$ represents the opposite case. The expression above can then be redefined as the relative blur by normalizing the expression in terms of the detector size

$$R_b(\chi\ ,\beta) = \sqrt{\chi^2 + [(1-\chi)\beta]^2}. \qquad \text{Eq.(2-40.}c\text{)}$$

Let us take the partial derivative of the object blur with respect to the source–object distance

$$\frac{\partial B_o}{\partial d_{so}} = \frac{\frac{{B_d}^2\, d_{so}}{{d_{sd}}^2} + \frac{f^2}{d_{sd}}\left(1 - \frac{d_{so}}{d_{sd}}\right)}{\sqrt{\left[\frac{B_d\, d_{so}}{d_{sd}}\right]^2 + \left[f\left(1 - \frac{d_{so}}{d_{sd}}\right)\right]^2}}. \qquad \text{Eq.(2-41.}a\text{)}$$

And can also be algebraically defined in terms of the relative values as

$$\frac{\partial R_b}{\partial \chi} = \frac{\chi + (1-\chi)\beta^2}{\sqrt{\chi^2 + [(1-\chi)\beta]^2}}\,. \qquad \text{Eq.(2-41.}b\text{)}$$

Now, we can find the optimized source–object distance by setting the derivative in Eq.(2-41.a) to zero and solving the source-object distance as

$$d_{so-opt} = \frac{d_{sd}\ f^2}{{B_d}^2 + f^2}. \qquad \text{Eq.(2-42.}a\text{)}$$

Or the relative equivalence

$$\chi_{opt} = \frac{\beta^2}{1+\beta^2}. \qquad \text{Eq.(2-42.}b\text{)}$$

These expressions can help minimize the blur of an imaging system from a geometric standpoint. The relative blur is depicted in Fig. 2.20 as a function of the relative distance $\chi \in [0,1]$ and the relative source-detector sizes β. The results are a family of curves which skew either towards the detector or the source depending on their sizes. The optimal distance is closer to the source whenever $\beta < 1$, in this case the source

is the smaller component therefore it becomes the driver of decreasing the geometric blur. On the contrary, when the detector is relatively smaller sized than the source, $\beta > 1$, then the detector becomes the driving component that decreases the geometric blur. The case in which the detector and the source have the same sizes, $\beta = 1$, then the optimal location is half of the source-detector distance, and the curve becomes a symmetric parabola. The source-detector distance d_{sd} has the effect of broadening or constraining the family of curves, therefore large distances would cause the blur to be more gradual within the space the object occupies, however this comes at the cost as the radiation flux is reduced due to the increased distance.

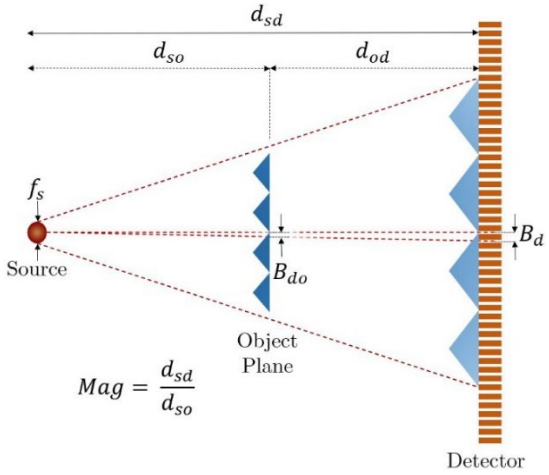

Fig. 2.19. Geometric relations to determine the blur at the object plane.

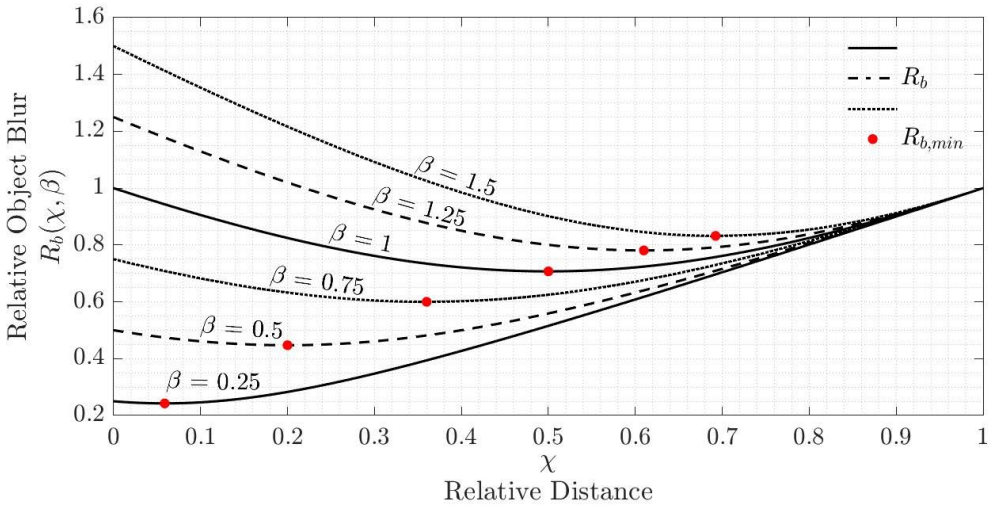

Fig. 2.20. Relative blur as a function of relative distance for various source-detector size ratios.

2.3. Radiation Imaging Systems

The discussion now will shift to the systems developed in the present research tasked with performing computed tomography measurements. These systems have been developed and/or assembled by the team at the Experimental Multi-Phase Flow Lab (ECMFL) at the University of Michigan (UM). Similar applications have been performed for x-ray imaging [74, 121, 125, 126], and gamma-ray imaging [96, 147].

2.3.1. High-Resolution Gamma-Tomography System (HRGTS)

The first imaging system is the High-Resolution Gamma-Tomography System (HRGTS) designed primarily by Dr. Robert Adams during his appointment at UM with research support of the present author; the design and characterization of the detector system has been reported in Adams et al. [1, 2] and Diaz et al. [33, 34]. The HRGTS consists of an array of 240 LYSO crystal detectors arranged in fan-arc geometry as shown in Fig. 2.18.*a)* with a pitch of 2.5 mm between adjacent detector elements. Each of the LYSO crystals is coupled to two SiPM components to maximize the conversion of scintillation light to signal output. The radiation source paired with the detector system is a nominal 15 Ci ^{192}Ir cylindrical source with a diameter of 1.5 mm and length of 0.75mm. The source to detector-arc distance is 800 mm and source to object is nominally 400 mm.

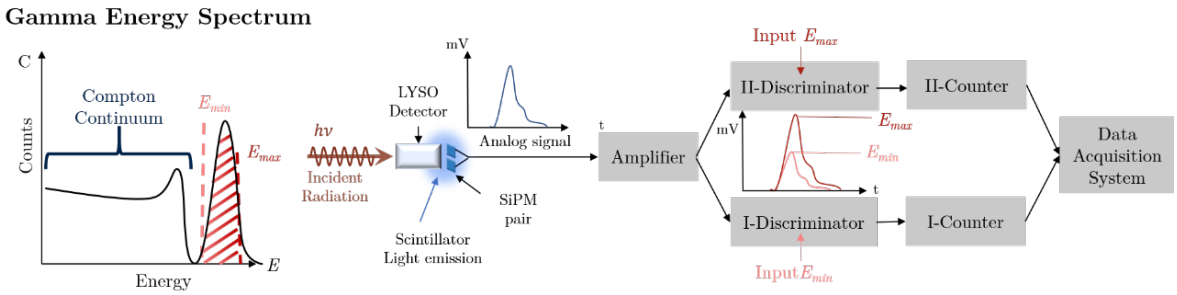

Fig. 2.21. Photopeak discrimination process deployed during data acquisition of the HRGTS.

The HRGTS employs the energy discrimination methods previously discussed in Section 2.1.2. This process is slightly modified by including an upper and lower energy threshold for each detector element. The purpose is to isolate the counting events associated with the photopeak photons of the gamma-emitter. This in effect removes the counting contributions from photons which have scattered on their way from source to detector, thus filtering the Compton continuum from the measurement. The implemented energy thresholds are determined at an individual basis by measuring the differential energy spectrum with all 240 detector elements. The energy discrimination process implemented in the HRGTS is highlighted in Fig. 2.21. Here, the objective is to reduce the associate radiation-based noise from the measurements and ultimately improve the quality of the reconstructed cross-section.

The imaging system is composed of four separate electronic systems, three of which were designed in-house, primarily the signal post-processing electronics. These delegate different functions in the radiation detection and data acquisition process highlighted in Fig. 2.21; the components include the SiPM board,

amplifier/discriminator board, counter board, and a microcontroller. Together, these components comprise a detector module, each detector module is in charge of 8 individual detectors, this results in 30 detector modules in total; the schematic of a single detector module is shown in Fig. 2.22. The detector electronics are described as follows:

- **SiPM Board -** designed to accommodate 2 rows of 8 SiPM diodes. The SiPM diodes are biased at 30 V during operation; this voltage was found to be suitable for operation, however, the voltage can be ranged between 26V to 31V. The SiPM PCB board includes push-in female RF connector jacks as well as two mounting holes. Custom SiPM holders were designed to house these boards. The holders and the SiPM boards are shown in Fig. 2.23.
- **Amplifier/Discriminator Board -** was designed to process 8 detector channel outputs coming from the SiPM board; this includes multi-channel amplifier/comparator. The pulses that pass through the thresholds are then digitized and sent to the next processing electronic circuitry (the counter board). Each detector channel is therefore split into two separate discriminators whose difference is intended to isolate the radiation counting events corresponding to the photopeak, the total output from the amplifier board are 16 digitized signals. Additionally, a pulse-width-modulator (PWM) driver is paired to the amplifier board circuitry with the purpose of setting and controlling individual channel thresholds (high and low). Communication with the PWM driver board is performed with i2c communication protocols. The PWM board also incorporates individual address identifier such that each detector module is unique and easily identifiable. The amplifier-discriminator board component is shown in Fig. 2.24.*b).*
- **Counter Board -** The digitized outputs from the amplifier board are directed by a circuit bridge on to the inputs of the counter board shown in. The purpose of this electronic component, as its name states, is to tally the digitized pulses representing pertinent radiation detection events. This task is delegated to a 16-bit counter per channel which stores the data in memory; this is activated by sending the record signal. A second signal dictates when the data needs to be stored, and a third signal erases the counter memory. The counter board component is shown in Fig. 2.24.*b).*
- **Microcontroller** – this device is paired to the counter board (one per module) to pull the data from the counters and write it into a file when the store signal is received, this is then transmitted wirelessly over Wi-Fi to the user-computer controlling the system.

The layout of the HRGTS design is depicted in Fig. 2.25. This shows the detector array, radiation source, and how the detector modules are split into two groups located on both sides of the array.

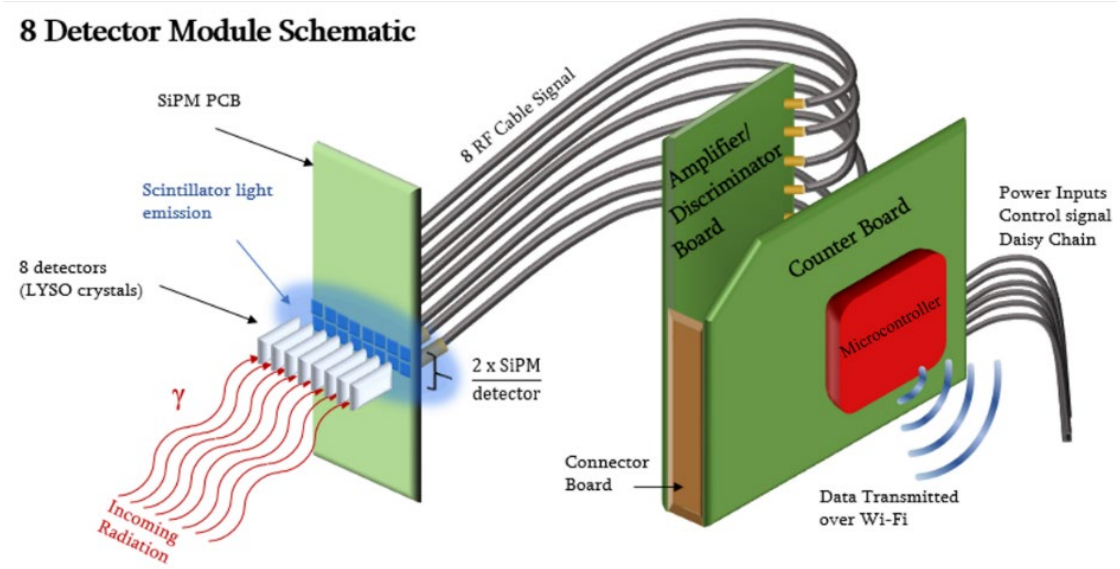

Fig. 2.22. Schematic of detector module electronic components, presented in Adams et al. [2].

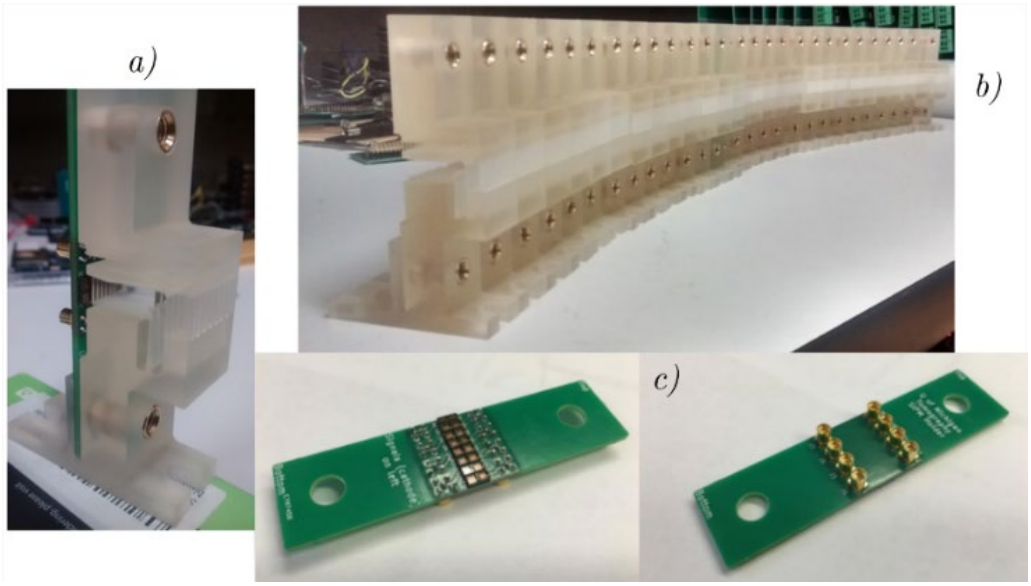

Fig. 2.23. ***a)*** **SiPM mounting example,** ***b)*** **Holder array, and** ***c)*** **SiPM board.**

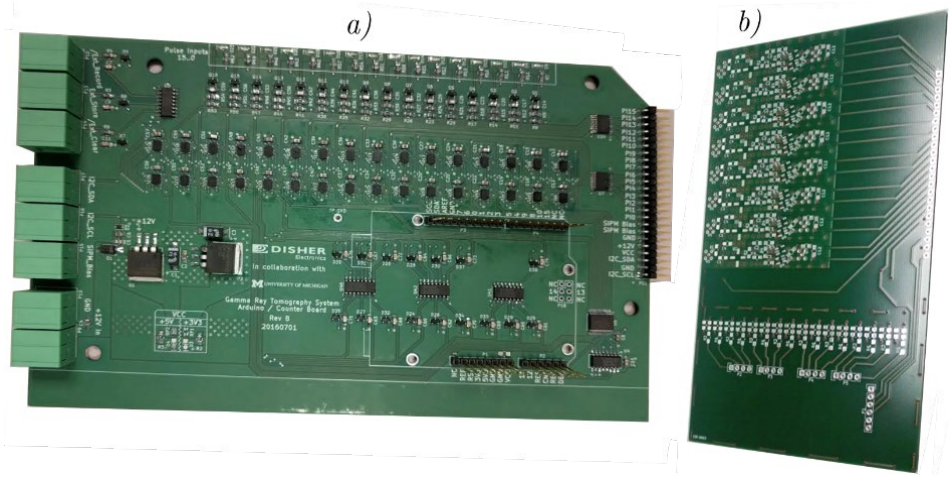

Fig. 2.24. ***a)*** **Counter board and** ***b)*** **Amplifier-discriminator board.**

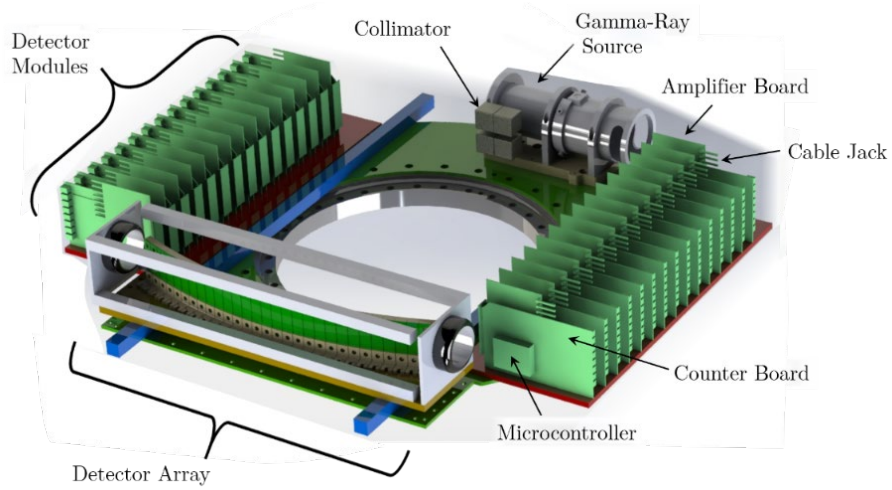

Fig. 2.25. Layout and design of the HRGTS.

2.3.1.1. Radiation Spectrum

Energy spectrum measurements were performed with the HRGTS system electronics. An example of the ^{137}Cs radioisotope spectrum measured with the multi-channel amplifier system deployed in the HRGTS is shown in Fig. 2.26 (the counting curve is not depicted). The 662keV photopeak is distinguishable here at the 240mV threshold location, behind the photopeak is the Compton continuum. A second example shown in Fig. 2.27 involves the measurement of the ^{192}Ir gamma-ray source performed with a detector module of the fully assembled HRGTS. The measured counting curves are shown on the left, and the associated radiation spectrum is presented on the right. The spectrum exhibits two distinguishable photopeak associated with the 475 keV and 604 keV energies; the 310 keV falls in the Compton scattering region of the other photopeak and is difficult to observe.

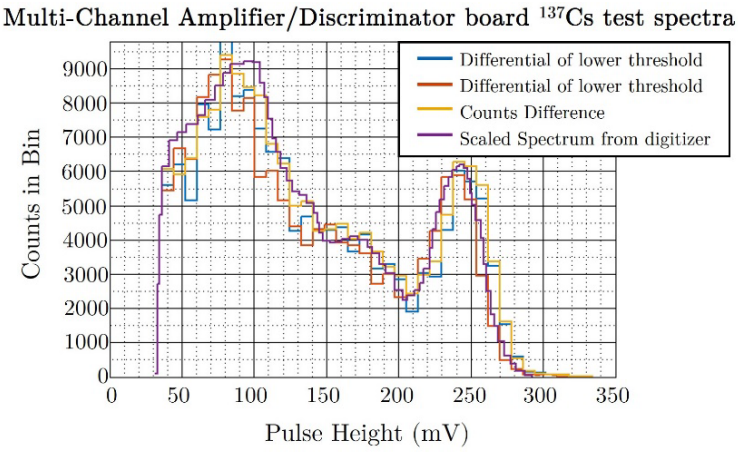

Fig. 2.26. Measured ^{137}Cs pulse height spectra from multi-channel amplifier/discriminator board courtesy of Dr. Robert Adams et al. [1,2].

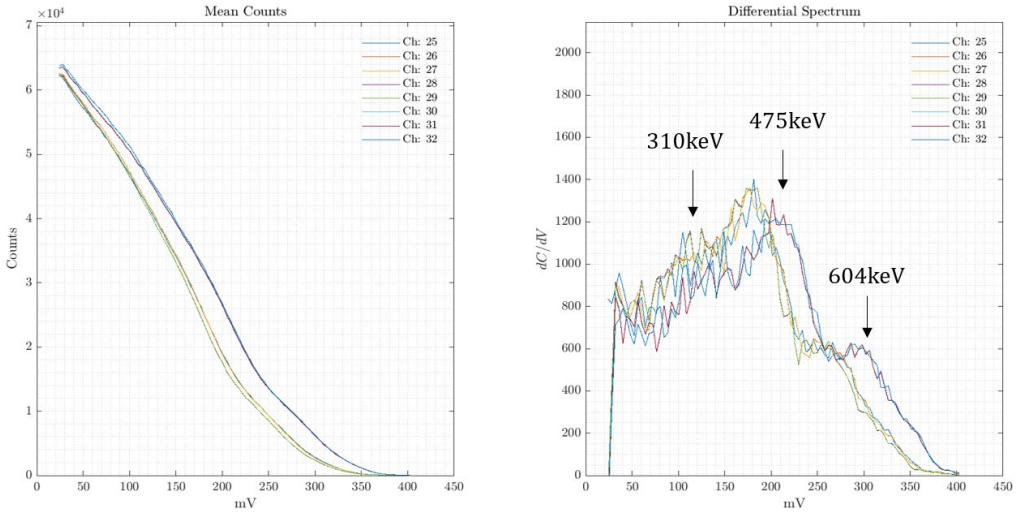

Fig. 2.27. ^{192}Ir spectrum measured with a detector module (8-detector) count spectrum (left), differential spectrum (right)

2.3.1.2. Imaging Resolution

The achievable resolution of the HRGTS was determined by performing a CT measurement of a Siemens star shown in Fig. 2.28.*a)*. The Siemens star consists of wedges pointing inward, periodically repeating every 36°, with an outer diameter of 50.0 mm, and a smaller inner diameter of 3.8 mm. The ideal cross section of the Siemens star is illustrated in Fig. 2.28.*b*. The results of the tomographic measurements obtained with the HRGTS paired to the 15 Ci ^{192}Ir source for a short and long measurement time respectively are depicted in Fig. 2.28.*c)* and *d)* respectively. The long measurement was performed by counting photons for one minute per degree, while the short measurement was obtained by counting photons for 6 seconds per degree. The flat field counts taken for an iteration of 100 ms time period were on the order of 9600 low threshold

and 6200 for the high threshold. Similarly, the measured counts with the object present for the same iteration time were in the order of 7200 counts in the low threshold and 2800 for the high threshold. As expected, measuring for longer time reduces the measurement uncertainty associated to the stochastic nature (Poisson distribution) of gamma radiation and results in a clearer image.

Analysis of the tomographic images results in a demonstrated achievable spatial resolution of about 1 mm demonstrated by Adams et al. [2]. This was determined by estimating the modulation transfer function (MTF). To achieve this one must first use the edge spread function (ESF) defined as the profile of an arbitrary wedge; this is fitted using an error function to approximate the ideal behavior. The line spread function (LSF) is then determined by taking the spatial derivative of the ESF. Next, MTF is determined by calculating the Fourier transform of the LSF. The ESF and LSF are plotted in Fig. 2.29.*a)*, and the MTF is shown Fig. 2.29.*b)*. The MTF depicts the contrast variation as a function of spatial frequency; from the MTF, measuring between 10% to 30% contrast, the spatial resolution of the system is estimated to be 0.71 mm and 1.0 mm respectively.

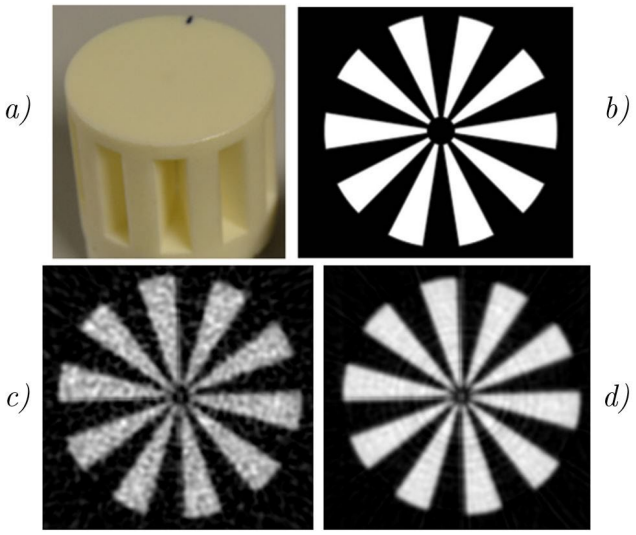

Fig. 2.28. Siemens star *a)* object used for to determine imaging resolution, *b)* ideal object cross-section, *c)* measurement for long time, and *d)* measurement for short time. Retrieved from Adams et al. [2].

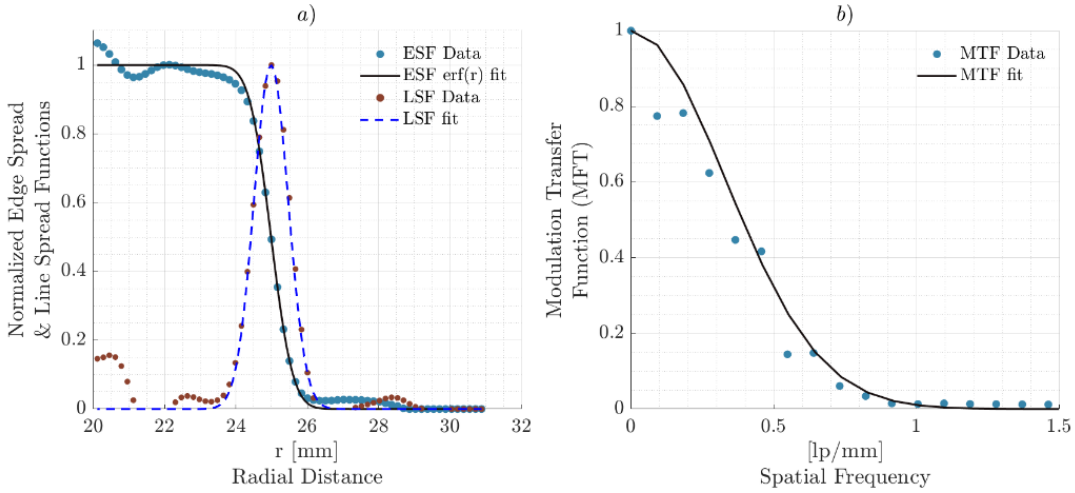

Fig. 2.29. Spatial resolution of measurement of the Siemens Star performed with the HRGTS; *a)* ESF and LSF, *b)* MTF.

2.3.1.3. Area Estimation

The area occupied by a material is defined by the population of voxels corresponding to that material in the tomogram. This statistical problem is an analogous process to measuring the energy dependent event counting curves described previously and shown from Knoll [94]. Taking inspiration from this procedure provides a simple way to determine the cumulative area occupied by pixels above a certain threshold, and incrementally increasing the threshold as follows:

$$A(\mu_{th}) = \int_{\mu_{th}}^{\infty} \frac{dA(\mu')}{d\mu'} d\mu', \qquad \text{Eq.(2-43)}$$

where μ_{th} is the imposed threshold attenuation. The equation above also describes the corresponding CDF of the tomogram voxel values. The voxel differential attenuation distribution can then be determined by taking the derivative of the cumulative area previously established; the obtained distribution is equivalent to binning (with a histogram) the linear attenuation values from the tomogram, achieved by different means. Fig. 2.30 presents the voxel counting curve in units of area (on the left) and the respective differential voxel distribution (on the right) for the Siemens star tomogram. The counting curve is characterized by large drops and counting plateaus. The latter feature represents the transitional attenuation voxel values between two different materials; for instance, the transition described by the ESF lies in the plateau region of the counting curve. These regions contain the highest fluctuation sensitivity where a small decrease in the plateau symbolizes a sharp increase in the attenuation. The results of the differential spectrum present two distinct material peaks, the first is the air (void space) located in the low attenuation range, the second corresponds to the Siemens star (PLA material) centered at a higher attenuation. The transitional region between the two adjacent peaks needs to be minimized in order to formulate an accurate method of estimating the cross-sectional area of the Siemens star,

$$\underset{\mu \in [\bar{\mu}_{pk_1}\ ,\ \ \bar{\mu}_{pk_2}]}{\operatorname{argmin}} \; -\frac{dA(\mu)}{d\mu}. \qquad \text{Eq.(2-44)}$$

The minimization bounds can be determined by locating the respective material peaks with gaussian fits or finding the local maxima of the distribution denoted as $\bar{\mu}_{pk_1}$ and $\bar{\mu}_{pk_2}$. The minimization procedure accurately estimates the attenuation threshold representing the Siemens star object, referred as the red line in the counting curve and red area in the differential spectrum. The ideal area of the Siemens star is 977.26 mm^2, while the area estimated using this procedure is 989.8 mm^2 which corresponds to 2.3% error in the area estimation. To assess the sensitivity of this estimation, bounded attenuation thresholds are obtained from the differential distribution corresponding to two times the minimized distribution quantity. The area

corresponding to the left bound overestimates by 7.54% and the right bound underestimated by 12.33% in comparison to the ideal, these correspond to the blue-dotted lines on the left figure, and the blue and purple area on the differential spectrum shown on the right of Fig. 2.30.. This method shows that by minimizing the region between two peaks, one can determine the transitional threshold value optimized to calculate the material area. The analysis above is performed for a tomogram containing two materials, air, and PLA; however, this can be extended to a tomogram containing various materials with identifiable corresponding peaks in the voxel distribution.

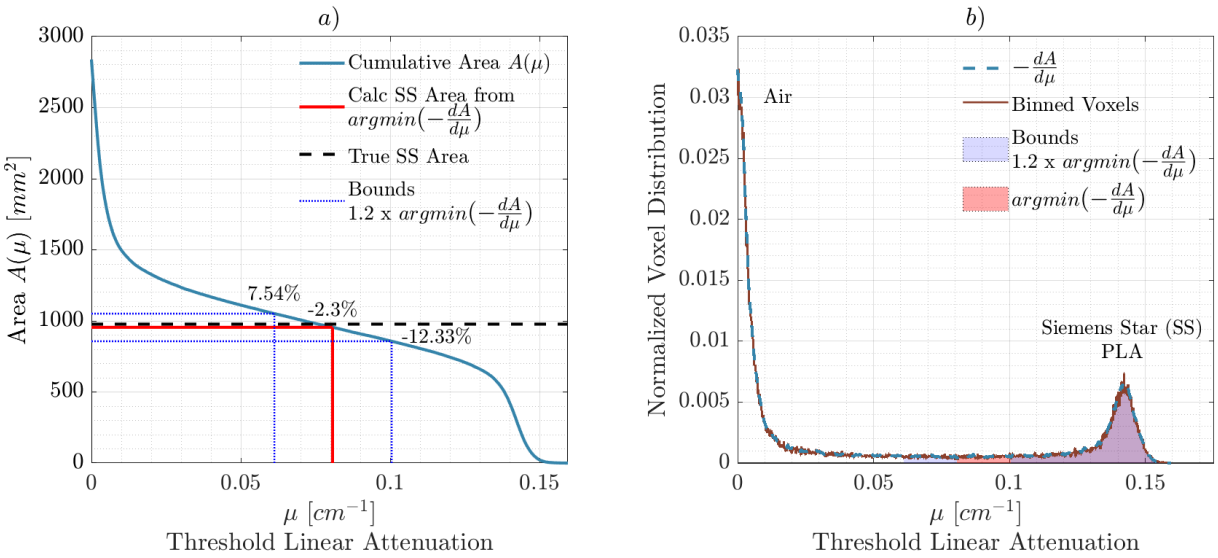

Fig. 2.30. Area assessment of Siemens star performed with HRGTS; *a)* Cumulative area counting curve, and *b)* normalized voxel distribution.

The stoichiometric composition of PLA is $C_3H_4O_2$ and is characterized by a density of about 1.24 g/cc, based on the energy of 475keV photons emitted from ^{192}Ir results in a linear attenuation coefficient of 0.144 cm^{-1} for the material. The estimated linear attenuation coefficient from the material pixel distribution is 0.142 cm^{-1}, this represents an underestimation of 1.6% thus demonstrating good agreement.

2.3.1.4. Field of View

Tomographic measurements of three cylindrical objects spatially distanced were performed to test the range of the wide field of view of the detector arc; these objects are composed of plastic, aluminum and carbon-steel rods respectively, as illustrated in Fig. 2.31.*c)*. The wide field reconstruction is shown in Fig. 2.31.*a)*, this demonstrates how the system is capable of resolving the inner cross-section of the hexagonal carbon steel hex. In addition, different brightness are associated to the different material compositions,

demonstrating that the tomographic image gray level can be used to discriminate different material densities. A second imaging test was performed by measuring a 3D-printed lab logo; the object is shown in Fig. 2.31.*b)*, and the tomographic reconstruction is presented in Fig. 2.31.*d)*. The resulting reconstructed cross-section resolves the inner support structure of the 3D-printed object.

Fig. 2.31. ***a)*** **Measurement of wide field measurement and** ***b)*** **respective object (bottom-left);** ***c)*** **3D printed lab logo and** ***d)*** **measurement.**

2.3.1.5. Volume Imaging

Imaging a volume can be performed by stacking several cross-sectional sliced measurements. To show this proof of concept, measurements of a propeller were performed with an incremental height Δz of 1.0 mm, and an exposure time of 50 ms per degree. Examples of cross-sectional slice measurements are shown in Fig. 2.32, and the rendered volume is shown in Fig. 2.33. The cross-sectional images show a blurring effect at the blades, this is due to the thinness in addition to the helical characteristic of these.

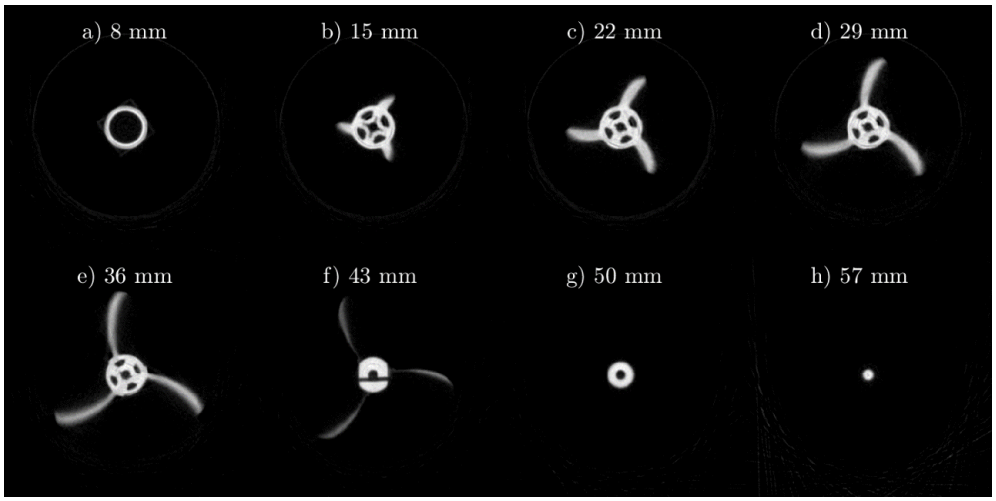

Fig. 2.32. Cross sectional images of propeller.

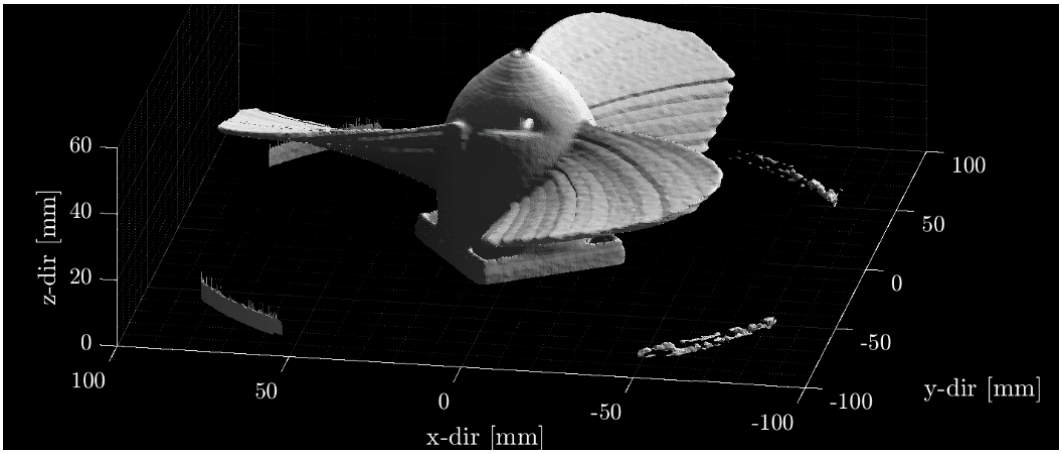

Fig. 2.33. Volume rendering of measured propeller.

2.3.1.6. Phase Locking

Lastly, a phase locking algorithm was developed which synchronizes the HRGTS system to perform measurements of a rotating object. Example of such methods were shown by Prasser et al. [147] in which CT measurements of a rotating impeller were performed with the aim of studying the presence of gas that occurs in petrol-chemical industrial settings. In the present research a Hall-effect sensor to the imaging system, a small magnet is attached to the object (or shaft), the system is triggered whenever the magnet comes near the hall sensor. The phase-locking algorithm uses the magnets timing as a 0° position, based on the rotation of the object, the phase-delay is applied to the trigger. Therefore, the object can be surveyed by systematically increasing the triggering delay with which allows us to collect sufficient angular data to perform CT reconstruction.

Careful considerations of the total measurement time needs to be kept in mind, given that this increases significantly based on the required exposure time and the angular velocity of the object. Prior to estimating the total measurement time, let us define the influencing parameters:

$$\tau_\phi = \frac{\tau_{rev}}{N_{proj}}; \qquad i = \frac{T_{exp}}{\tau_\phi}; \qquad W = \frac{\tau_{rev}}{\tau_\phi + \tau_{read}} \qquad \text{Eq.(2-45)}$$

- T_{exp} - Total exposure time per degree.
- τ_{rev} - The time it takes for the object to perform a revolution.
- N_{proj} - Number of angular locations to measure.
- τ_{read} - Readout time or system dead time.
- τ_ϕ - Exposure time per rotation.

- i - Number of iterative measurements required to fulfill the total exposure time.
- W - Number of readouts that can be performed per revolution.

The total measurement time can be estimated with the following

$$\begin{aligned} \text{Ideal} \quad t_{CT} &= \frac{i\ N_{proj}\ \tau_{rev}}{W}, \\ \text{Actual} \quad t_{CT} &= \frac{\lceil i \rceil\ N_{proj}\ \tau_{rev}}{\lfloor W \rfloor}. \end{aligned} \qquad \text{Eq.(2-46)}$$

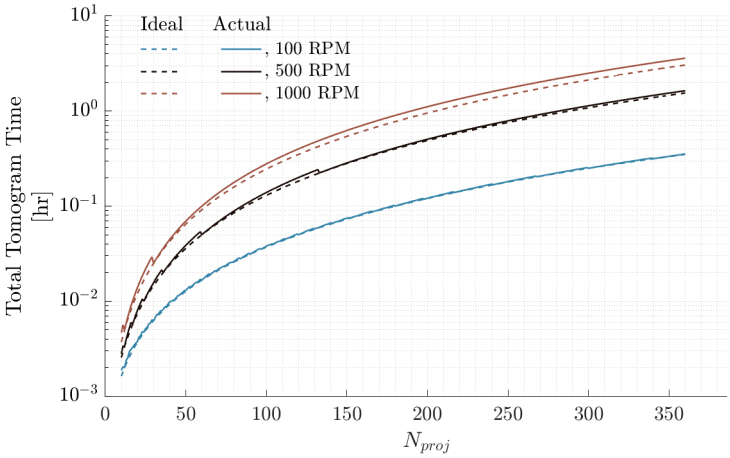

Fig. 2.34. Estimated CT measurement times for phase-locking arrangement.

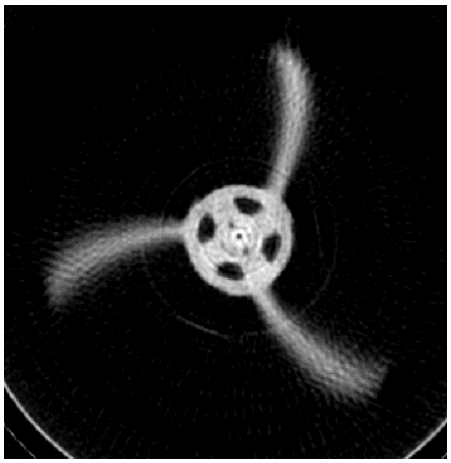

Fig. 2.35. CT reconstruction of propeller spinning at 600 RPM with an exposure time of 0.25 seconds per degree.

The system's actual time accounts for integer values of the number of readouts and iterative measurements. An example of the CT measuring time is shown in Fig. 2.34 for an exposure time of 0.5 s per degree, and for different object speeds. The actual time results in a larger measurement time than the idealized time, particularly for high revolutions per minute (RPM). Phase-locking measurements were performed of the propeller spinning at 600 RPM with an exposure time of 0.25 seconds per degree and 120 projection locations, the CT reconstruction is shown in Fig. 2.35. The reconstruction is noisier in comparison to the results presented in Fig. 2.32 dues to its reduced radiation exposure time.

2.3.2. Michigan High Resolution Tomographic Imaging System

The second imaging system utilized in the present research is the Michigan High Resolution Tomographic Imaging (CHROMA) system designed and assembled by the team at ECMFL. This system is

characterized by a 1.0 m bore-diameter rotary table with a mounted linear stage that capable of adjusting the distances between the source, object, and the detector. The CHROMA facility can accommodate different radiation sources, including radioisotopic sources and x-ray tubes. The x-ray system used in the present study is a standard medical x-ray tube rated at 150 kV with a max current of 500 mA and a minimum focal spot of 0.6 mm. The ^{192}Ir radioisotopic source implemented in the HRGTS can also be paired for imagining with the present facility. The CHROMA facility can also accommodate large detectors such as image intensifiers, detector panels, or linear detectors. The detector utilized in the present work is composed of cadmium telluride (CdTe) crystals arranged in a 256 x 2048 detector panel, with each voxel having an effective area of 100 x 100 μm^2; the characteristics of these detector elements are described in Section 2.1.2.2. The source-detector distance is 1000.0 mm, the source-object distance is 710.0 mm, resulting in an object-detector distance of 290 mm; however, these distances can be adjusted. Based on the geometric constrains, the resulting object magnification is 1.4 for the mentioned geometric constraints. The cone beam geometry of the CHROMA facility is described by the relations shown Fig. 2.18.*b)*. The FDK [43] algorithm from the ASTRA Toolbox [185] was used to reconstruct the 3-D tomograms resulting from measurements performed with the CHROMA facility. Experimental studies performed with this facility are presented in Chapter-6. Future research activities involving this facility includes the measurement of sodium heat-pipes as passive heat removal systems in special purpose nuclear reactors, a work presently carried out and described in Ahn et al. [5].

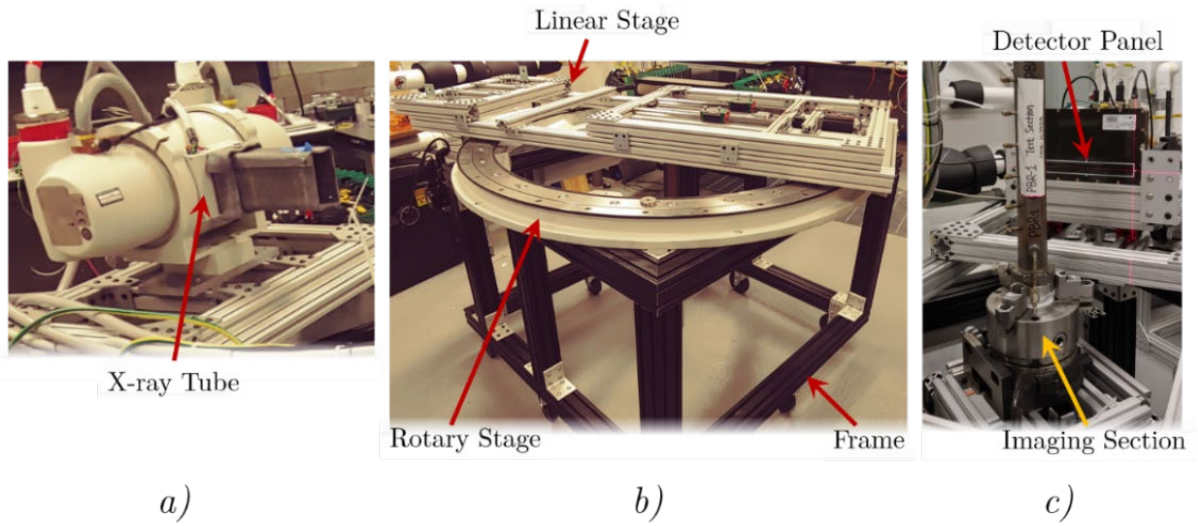

Fig. 2.36. CHROMA facility; *a)* X-ray tube, *b)* rotary stage, support frame, and linear stage, *c)* detector panel, and imaging section.

2.3.2.1. Imaging Resolution and Area Estimation Assessment

The resolution of the CHROMA facility was also assessed by performing measurements of the Siemens star object previously described in Section 2.3.1.2. The object was measured with incremental step of 1° along a 36°arc, with one minute measurement per degree; the ideal and measured object are presented in Fig. 2.37. The tomogram was reconstructed using a voxel side length of 0.144 mm. The imaging resolution was determined with the same procedure that was carried out for the HRGTS. The estimated ESF and LSF are shown in Fig. 2.38.*a)* while the MTF is shown in Fig. 2.38.*b)*; by measuring the MTF between 10% to 30% contrast, the spatial resolution of the system is estimated to be approximately 0.42 – 0.63 mm respectively. The spatial resolution is affected by the focal spot size of the source, which for the gamma-ray source was 1.5 mm. Therefore, a better spatial resolution is expected when using the x-ray tube, which has a nominal focal spot of 0.6mm.

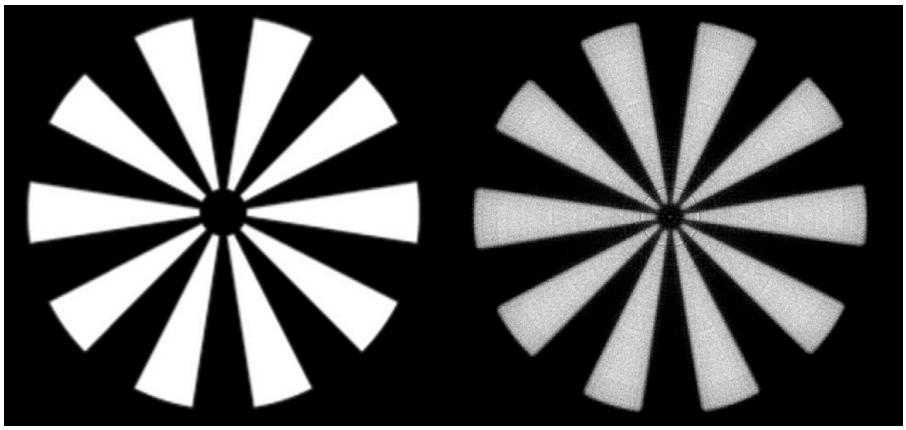

Fig. 2.37. Example of ideal (left), and reconstructed tomogram (right) of the Siemens star.

The area of the Siemens Star was determined from the measurement performed with the CHROMA facility, similar to the analysis carried out for the HRGTS. The estimated area was 989.8 mm^2 which corresponds to 1.17% error in the area estimation. To sensitivity of the bounded attenuation thresholds overestimates by 10.73% and the right bound underestimated by 11.06% in comparison to the ideal; these correspond to the blue-dotted lines on the left figure, and the blue and purple area on the differential spectrum shown on the right of Fig. 2.39. This method will be used later on in Chapter 6 to estimate the area corresponding to molten uranium inside reactor test assemblies. The estimated linear attenuation from the material pixel distribution is 0.1275 cm^{-1}, this results in an underestimation of the linear attenuation coefficient of 11.34% in comparison to the PLA property referenced in section 2.3.1.3.

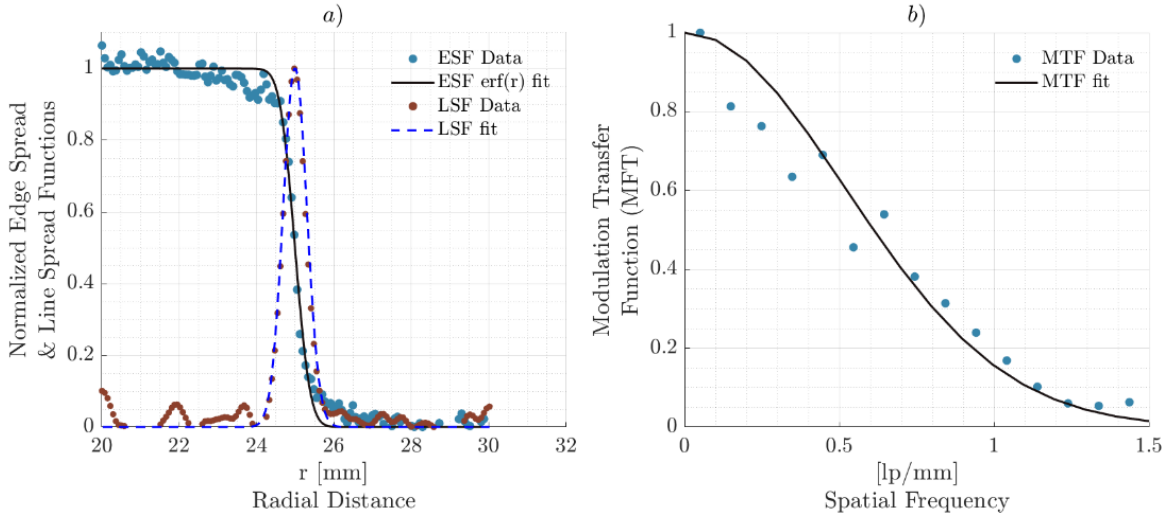

Fig. 2.38. Siemens Star resolution analysis; *a)* ESF, and LSF from measurement and fitted function, *b)* MTF.

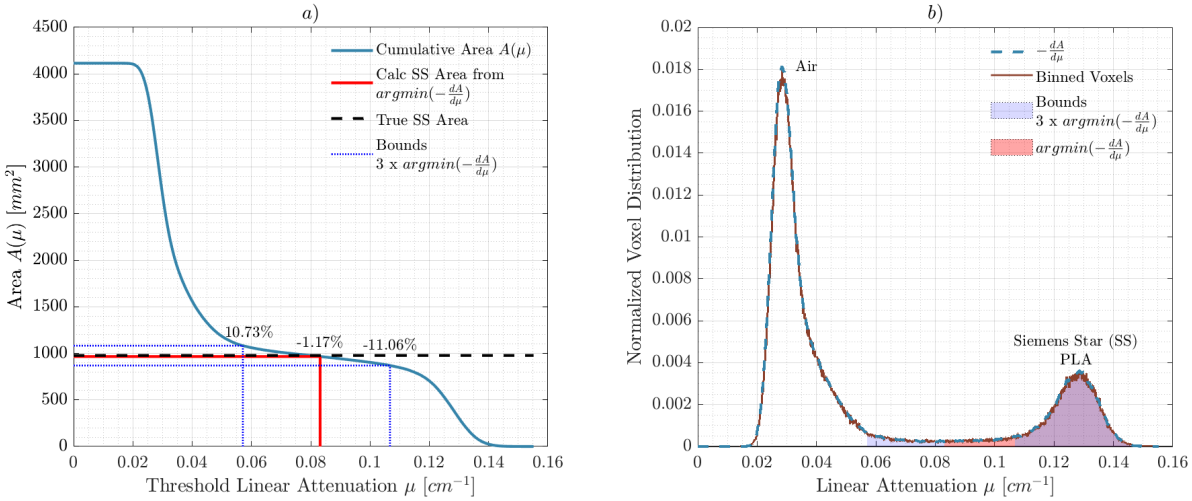

Fig. 2.39. Area assessment of Siemens star performed with CHROMA; *a)* Cumulative area counting curve, and *b)* normalized voxel distribution.

2.4. Radiation Modeling with Ray Tracing

Prior to setting up any experimental facility, it is a common practice to perform preliminary studies, hereby modeling the intended system to estimate the expected outcome; within reason, this can help give perception of experimental feasibility and design requirements. Various radiation transport and other codes which have been developed can be utilized to model radiation-transmission imaging. The methods and degrees to which they adhere to the physics principles can vary, depending on the level of priorities. Typically, CT simulation programs model systems using point-source and point-detectors, discretized cross-sectional images are passed as inputs to perform the forward projection and generate the resulting sinogram,

and lastly perform reconstruction; these are idealized systems which emphasize in the reconstruction process. Oftentimes these neglect the blurring effects resulting from the volume or area of the source and the detector size.

To increase the fidelity of the imaging process with emphasis of the forward projection aspect, a ray-tracing based program has been developed as a toolset to model the experimental facilities described in Chapters 4 and Chapter 5 which intend to study two-phase flows inside nuclear reactor assemblies. Ray-tracing exploits simple yet powerful geometric relations of ray-casting, and by embedding physics principles results in an ideal tool to describe radiation transmission. Advances in ray-tracing methods have greatly propelled computed animation industries due to increased computational improvements of graphics processing units (GPU) that have resulted in high resolution graphics rendering; these allow to improve the physics models implemented in the rendering process of light interactions with objects. The mathematical relations derived in this section are based on the derivations expressed by Buss [23] and Shirley [167], which have been adapted to the notation of the present research. The custom-built program serves to quantify the pertinent compounding effects for an imaging setup based on geometry, material composition, thermal effects such as density changes and expansion, as well as beam-hardening in the case of x-ray systems.

2.4.1. Ray-Casting and Intersections

This section will focus in describing the process of ray-casting, intersections, and crossing distance of through simple objects such as spheres, cylinders, and cube prisms; although these geometries are simple, we can use them to model reactor assemblies and idealized bubbles. These can then be used to estimate the attenuation contribution of a number of arbitrary regions along a ray-trace; it is assumed here that the trace emanates from point source. For convenience, the coordinate system will be defined in Cartesian form. Prior to achieving set goal, the ray trace needs to be characterized, we can describe the ray-tracing vector $\overrightarrow{\boldsymbol{s}}$ as

$$\overrightarrow{\boldsymbol{s}} \;=\; \boldsymbol{x_d} - \boldsymbol{x_s}, \qquad \text{Eq.(2-47)}$$

and whose magnitude is

$$\begin{aligned} S \;&= \|\boldsymbol{x_d} - \boldsymbol{x_s}\| \\ &= \sqrt{(x_d - \; x_s)^2 + \; (y_d - \; y_s)^2 + \; (z_d - \; z_s)^2}. \end{aligned} \qquad \text{Eq.(2-48)}$$

The unit-vector $\hat{\boldsymbol{e}}$ associated with the ray-trace $\overrightarrow{\boldsymbol{s}}$ is described by its respective components

$$\hat{\boldsymbol{e}} = \; \langle e_x, e_y, e_z \rangle: \qquad \text{Eq.(2-49)}$$

$$e_x = \frac{x_d - x_s}{S} \quad , \qquad x - \text{direction}, \qquad \text{Eq.(2-49.}a\text{)}$$

$$e_y = \frac{y_d - y_s}{S} \quad , \qquad y - \text{direction}, \qquad \text{Eq.(2-49.}b\text{)}$$

$$e_z = \frac{z_d - z_s}{S} \quad , \qquad z - \text{direction}. \qquad \text{Eq.(2-49.}c\text{)}$$

The parametric description of the line along the ray-trace is

$$\boldsymbol{x_\gamma} = \boldsymbol{x_s} + d\,\hat{\boldsymbol{e}} \quad for \quad 0 \le d \le S. \qquad \text{Eq.(2-50)}$$

where d represents the distance away from the emission origin $\boldsymbol{x_s}$; this allows us to describe any point along the ray path.

2.4.1.1. Planes

Simple objects such as cubes, rectangular prisms, or rectangular ducts can be built using planes to describe their faces as shown in Fig. 2.40.*a)*. The description of a plane is

$$\begin{aligned} 0 &= (\boldsymbol{x} - \boldsymbol{x_0}) \cdot \vec{\boldsymbol{n}}_{\boldsymbol{f}}, \\ &= a(x - x_o) + b(y - y_o) + c(z - z_o), \end{aligned} \qquad \text{Eq.(2-51)}$$

where $\boldsymbol{x}$ and $\boldsymbol{x_0}$ are two arbitrary points on the plane. The plane normal can be described using three different points, conveniently in this case the vertices of the prism are used,

$$\begin{aligned} \vec{\boldsymbol{n}}_{\boldsymbol{f}} &= \langle a, b, c \rangle \\ &= (\boldsymbol{V_{f1}} - \boldsymbol{V_{f2}}) \times (\boldsymbol{V_{f2}} - \boldsymbol{V_{f3}}) \end{aligned} \qquad \text{Eq.(2-52)}$$

here, the subscript f denotes an arbitrary face, and $\boldsymbol{V}$ is a vertex as those shown in Fig. 2.40.*a)*; the second definition can help us retrieve the components of the normal vector. Now by substituting the parametric description of the ray in Eq.(2-50) into the definition of the plane Eq.(2-51) and using an arbitrary point in the plane, allows us to solve for the distance from the source to the plane with the following

$$0 = (\boldsymbol{x_s} + d\,\hat{\boldsymbol{e}} - \boldsymbol{V_f}) \cdot \vec{\boldsymbol{n}}_{\boldsymbol{f}} \,, \qquad \text{Eq.(2-53)}$$

re-arranging the expression and solving for the distance as

$$d = \frac{(\boldsymbol{V_f} - \boldsymbol{x_s}) \cdot \vec{\boldsymbol{n}}_{\boldsymbol{f}}}{\hat{\boldsymbol{e}} \cdot \vec{\boldsymbol{n}}_{\boldsymbol{f}}} \,. \qquad \text{Eq.(2-54)}$$

It is worth noting that if $\hat{\boldsymbol{e}} \cdot \vec{\boldsymbol{n}}_{\boldsymbol{f}} = 0$, then the ray travels parallel to the plane and does not intersect. Lastly, if $d < 0$, then the intersection occurs in the opposite direction of travel and therefore is considered to not intercept the plane. Although an intersection between the casted ray and the plane may exist, criterions of the entrance and exit locations needs to be formulated; Fig. 2.40.*b)* depicts how some of these rays intersect the planes outside of the object-region. This can be done by evaluating the intersection point with the plane

and ensuring that it lies inside the region defined by its respective vertices. The traversed length that the ray travels through the object is then defined as

$$L_{\blacksquare} = d_{out} - d_{in}. \qquad \text{Eq.(2-55)}$$

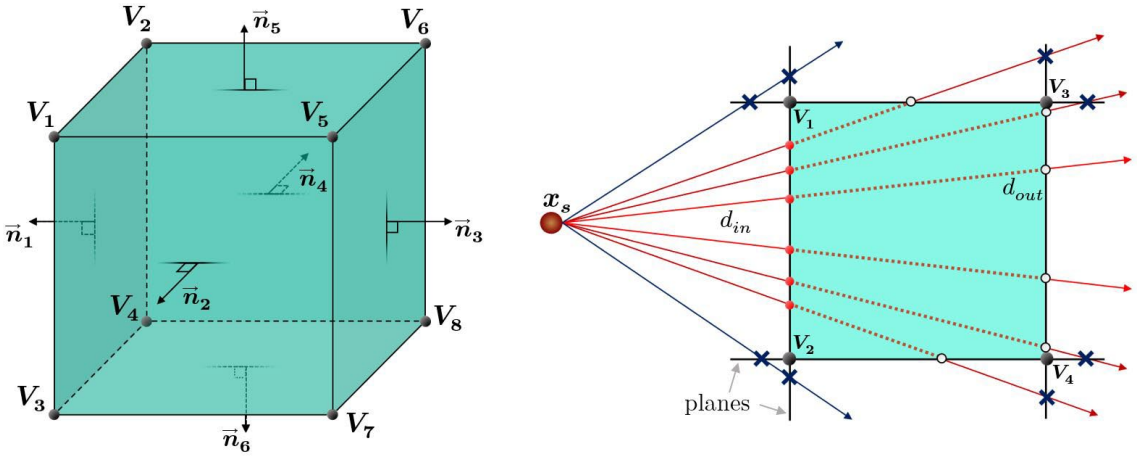

Fig. 2.40. ***a)*** **Cube prism defined by its vertices and face normal vectors.** ***b)*** **Example of 2D view of intersections between rays and planes: ● entrance and ○ exits of plane-defined object, and × intersection with planes but not with object.**

2.4.1.2. Spheres

Spherical objects can be used to represent radiation sources and bubbles. The spherical object can be described by its radius R and its center $\boldsymbol{x_o}$. The equation of a sphere intersected by a ray can be defined using the parametric expression defined in Eq.(2-50),

$$\begin{aligned} R^2 &= \|\boldsymbol{x_\gamma} - \boldsymbol{x_o}\|^2 \\ &= \|(\boldsymbol{x_s} - \boldsymbol{x_o}) \; + \; d \; \hat{\boldsymbol{e}} \; \|^2. \end{aligned} \qquad \text{Eq.(2-56)}$$

By expanding and rearranging the equation we obtain

$$0 = (\boldsymbol{x_s} - \boldsymbol{x_o})^2 - R^2 \; + \; 2d(\boldsymbol{x_s} - \boldsymbol{x_o}) \cdot \hat{\boldsymbol{e}} \; + \; d^2 \; \hat{\boldsymbol{e}}^2. \qquad \text{Eq.(2-57)}$$

The resulting expression has a quadratic form where the quadratic constants are

$$a = \; e_x^2 + \; e_y^2 + \; e_z^2, \qquad \text{Eq.(2-58.}a\text{)}$$

$$b = \; 2[(x_s - \; x_o) \; e_x + \; (y_s - \; y_o) \; e_y \; + \; (z_s - \; z_o) \; e_z], \qquad \text{Eq.(2-58.}b\text{)}$$

$$c = \; x_s^2 + \; y_s^2 + \; z_s^2 + x_o^2 + \; y_o^2 + \; z_o^2 - \; R^2 - 2(x_s x_o + \; y_s y_o + z_s z_o). \qquad \text{Eq.(2-58.}c\text{)}$$

The distances from the source to the entrance and exit of the sphere along the ray-traces can be described using the quadratic formulas respectively as

$$d_{in} = \frac{-\,b\; -\; \sqrt{b^2 - 4\;a\;c}}{2\;a}, \qquad \text{Eq.(2-59)}$$

and

$$d_{out} = \frac{-\,b + \sqrt{b^2 - 4\;a\;c}}{2\;a}. \qquad \text{Eq.(2-60)}$$

The resulting traversing length through the spherical region is

$$L_{sph} = d_{out} - d_{in}. \qquad \text{Eq.(2-61)}$$

2.4.1.3. Cylinders

Cylinders are used to represent objects such as pipes, fuel rods, and fuel pellets. The intersection of the ray trace to the surface of the cylinder is analogous to the spherical derivation expressed in Eq.(2-57). A significant simplification is made by ignoring the terms related to the extruding axis, thus reducing the relations to a line intersecting a circle; here it is assumed that the cylinder extrudes in the z-direction, thus neglecting the z-component of the ray as well. The relations derived for a cylinder characterized by radius R and centered at $\boldsymbol{x_o}$ are

$$0 = (x_s - x_o)^2 + (y_s - y_o)^2 - R^2 \;+\; 2d\big[(x_s - x_o)e_x + (y_s - y_o)e_y\big] \;+\; d^2({e_x}^2 + {e_y}^2), \qquad \text{Eq.(2-62)}$$

and the quadratic constants are then defined as

$$a = \; e_x^2 + \; e_y^2, \qquad \text{Eq.(2-63.}a\text{)}$$

$$b = \; 2\big[(x_s - \; x_o)\; e_x + \; (y_s - \; y_o)\; e_y\big], \qquad \text{Eq.(2-63.}b\text{)}$$

$$c = \; x_s^2 + \; y_s^2 + x_o^2 + \; y_o^2 - \; R^2 - 2(x_s x_o + \; y_s y_o). \qquad \text{Eq.(2-63.}c\text{)}$$

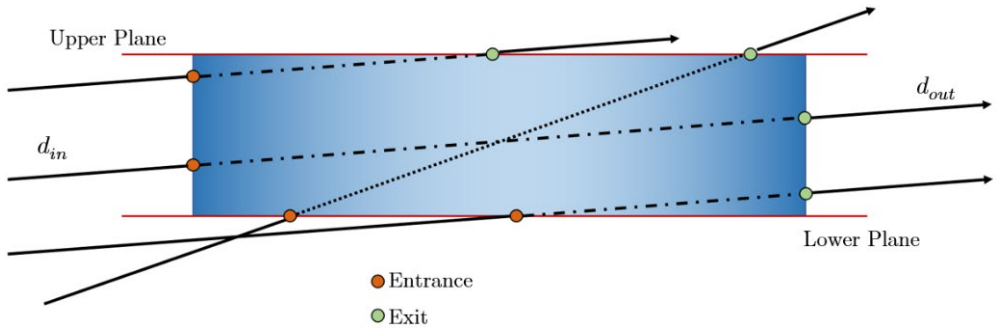

Fig. 2.41. Entrance and exit mechanisms of a ray-trace intersecting a finite cylinder.

The equations do not contain any z-direction components in this case, nevertheless, the ray still preserves this component as expressed in its parametric description. The entrance and exit points are then solved by the quadratic equations defined in Eq.(2-59) and Eq.(2-60). For an infinite cylinder, the z-intersection locations can be evaluated by inserting the resulting distances into the parametric equation Eq.(2-50). On the other hand, for the finite cylinder case, the end caps must be described using planes following the

relations prescribed in Section 2.4.1.1. The possible entrance and exit mechanisms of the ray are depicted in Fig. 2.41. Therefore, it is important to assess which surfaces are encountered by the ray and treat them accordingly.

$$L_{cyl} = d_{out} - d_{in}. \qquad \text{Eq.(2-64)}$$

2.4.1.4. Crossing Multiple Regions

Now that the crossing lengths have been defined for various simple objects, the linear attenuation is assigned to each region based on the corresponding material. The attenuation for a ray that crosses through multiple regions is then described by modifying the exponent from the Beers-Lambert Law,

$$I_{det}(\boldsymbol{x_d}) = \int_0^\infty \frac{I_{src}(\boldsymbol{x_s}, E)\ C(E)}{4\ \pi\ S^2}\ e^{-\sum_j L_j \mu_j(E)}\, dE. \qquad \text{Eq.(2-65)}$$

The subscript j is used to index the object or region. The next step is to rotate the source and detector synchronously around the center of rotation while casting rays and solving for their crossing lengths through the field of view. As an example, Fig. 2.42 is a rendering of a nuclear assembly geometry, ray-tracing is used to perform the forward projection; this is a depiction of the experimental setup explained in Chapter 5.

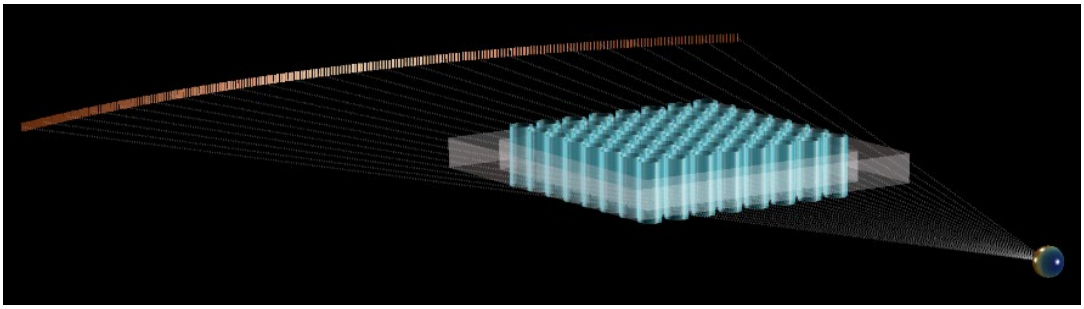

Fig. 2.42. Ray casting example of rod bundle geometry found inside nuclear reactors (teal), outer housing (gray), detector arc, and spherical source.

2.4.2. Source and Detector Modeling

Conventional radiation detectors and sources have a finite size which lead to blurring effects in the imaging process. Isotopic sources often have cylindrical or spherical geometries, while x-ray focal spots can be modeled as disks representing an emission area. Naturally, a volume source will experience self-shielding or self-attenuation, in addition to the blur that is caused by the emission of photons throughout its volume; an approximation of the blur was formulated in Section 2.2.5 from a simple geometric perspective. To model these types of sources, we describe the volume or area in a discretized mesh with point sources $\boldsymbol{x_s}$ located

in the middle of the cells with differential volume dV or area dA; the definitions of these must match the type of source geometry. Similarly, this blueprint can also be applied to the detector element either as a detection surface or volume. The present ray-tracing method numerically evaluates complex transport geometries that are otherwise difficult to solve analytically.

2.4.2.1. Disk Source and Benchmark

Let us first use the case of a disk source and a point detector to demonstrate and validate the ray-tracing method, this case is simple enough that an analytical expression can be derived; in this case the detector is treated as an observer that perceives the emission of photons emitted from the disk with radius R (with diameter D) and are incident on the detector point as shown in Fig. 2.43. Additionally, the emission will be assumed to be monoenergetic, thus treating the attenuation coefficient as a constant. The source-detector distance is described by z_{sd}, the attenuation medium is assumed to be air, however the medium can be arbitrary if it is not changing. To remain consistent with the previously described expressions, S denotes the distance traveled by the photons from the source to the detector; following the relations the presented graphic, the distance traveled is

$$S \;=\; \sqrt{r^2 + {z_{sd}}^2}. \qquad \text{Eq.(2-66)}$$

Differentiating S in terms of r results in the following

$$\begin{aligned} dS \;&=\; \frac{r}{\sqrt{r^2 + {z_{sd}}^2}} dr, \\ dS \;&=\; \frac{r}{S} dr, \\ S\; dS \;&=\; r\; dr. \end{aligned} \qquad \text{Eq.(2-67)}$$

The intensity perceived by the detector can be described as

$$I_{det} = a \int_0^{2\pi} \int_0^{R} \frac{e^{-(\mu_{air}\sqrt{r^2+{z_{sd}}^2})}}{4\pi(r^2 + {z_{sd}}^2)}\; r\; dr\; d\theta\,, \qquad \text{Eq.(2-68)}$$

where the constant a is analogous to the specific activity, with units of emitted photons per unit area; this factor scales the photon flux, in this case it will be assumed to be 1. By performing a change of variables with the relations from Eq.(2-67), the expression is transformed to

$$I_{det} = \frac{a}{4\pi} \int_0^{2\pi} \int_{z_{sd}}^{\sqrt{R^2+{z_{sd}}^2}} \frac{e^{-\mu_{air} S}}{S}\; dS\; d\theta\,. \qquad \text{Eq.(2-69)}$$

The transmission nearly resembles the form of the exponential integral function, whose definition is

$$E_1(x) \;=\; \int_x^{\infty} \frac{e^{-t}}{t}\; dt. \qquad \text{Eq.(2-70)}$$

To fulfill the form, an additional change of variables is performed,

$$\begin{aligned} t &= \mu_{air}\, S, \\ dt &= \mu_{air}\, dS. \end{aligned} \qquad \text{Eq.(2-71)}$$

We can now carry out the following steps

$$\begin{aligned} I_{det} &= \frac{\mu_{air}\, a}{2} \int_{z_{ds}}^{\sqrt{R^2+{z_{sd}}^2}} \frac{e^{-(\mu_a S)}}{\mu_a S}\, dS\,, \\ &= \frac{a}{2} \int_{\mu_{air}\, z_{ds}}^{\mu_{air}\sqrt{R^2+{z_{sd}}^2}} \frac{e^{-t}}{t}\, dt\,, \\ &= \frac{a}{2} \left(\int_{\mu_{air}\, z_{sd}}^{\infty} \frac{e^{-t}}{t}\, dt - \int_{\mu_{air}\sqrt{R^2+{z_{sd}}^2}}^{\infty} \frac{e^{-t}}{t}\, dt \right), \\ &= a \left[\frac{E_1(\mu_{air}\, z_{sd}) - E_1(\mu_{air}\sqrt{R^2+{z_{sd}}^2})}{2} \right]. \end{aligned} \qquad \text{Eq.(2-72)}$$

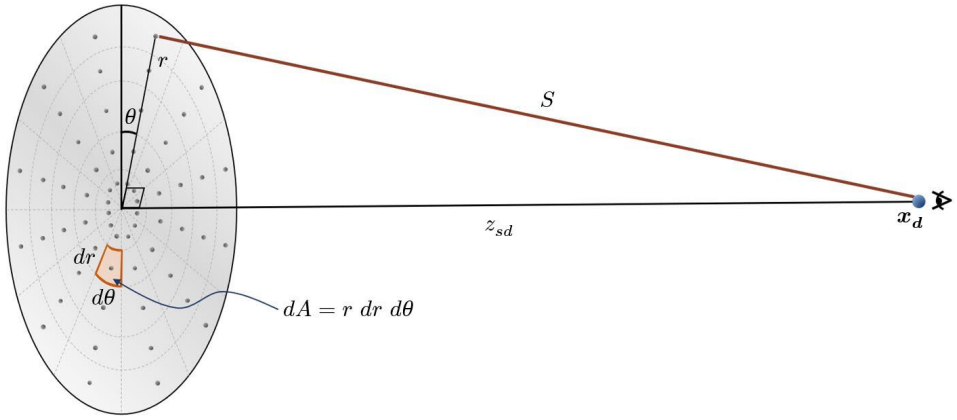

Fig. 2.43. Representation of discretized disk source and point source.

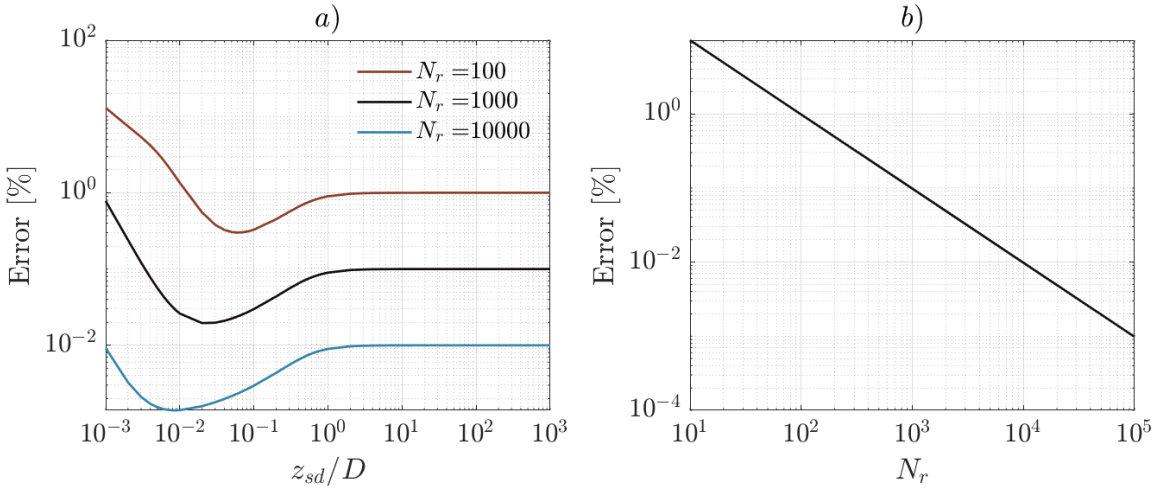

Fig. 2.44. ***a)*** **Percentage error as a function of normalized distance between disk source and point detector.** ***b)*** **Percentage error as a function of number of radial cells.**

The numerical evaluation of the system was carried out for a range of relative distances $10^{-3} \leq z_{sd}/D \leq 10^{3}$ between the source and the detector element, as well as a range of cells in the radial direction $10^{1} \leq N_r \leq 10^{5}$ and the angular discretization was $d\theta = 2°$ representing 180 cells in the angular direction. The value of interest in this case is the percent error between the analytical solution and the numerical evaluation; this can give us perception of the accuracy of the numerical method. Fig. 2.44.*a)* shows the percentage error as a function of relative distance, it is observed how the error starts high, dips, then increases and reaches an asymptotic behavior for $z_{sd}/D > 10^{1}$. The increase of radial cells further decreases the error; this was evaluated for $N_r \in$ [100,1000,10000]. Lastly, the relation between the percent error and the number of radial cells in the asymptotic region is depicted in Fig. 2.44.*b),* the error decreases with $1/N_r$.

2.4.2.2. Other Volume Sources

Other conventional forms of source geometries include spheres, and cylinders. Expressions for these were not derived in the present work. Examples of the relative intensity distribution throughout the volume sources perceived by a distant point-detector are shown in Fig. 2.45 for a sphere, Fig. 2.46 for a cylinder with its axis pointing along the direction of the detector, and Fig. 2.47 for a perpendicular cylinder. The depicted sources have a diameter of 1.0 mm and were modeled following the attenuation of ^{192}Ir at 475 keV; this is a high-density material which in effect highly attenuates of photons. The depictions intend to emphasize the self-shielding that a volume source experiences, and visually depict the regions of the source that wield the highest influence in the imaging process. This is best shown by the spherical source in which the regions nearest to the surface facing the detector have the highest relative intensity while the backside has the lowest relative intensity, as it would be expected.

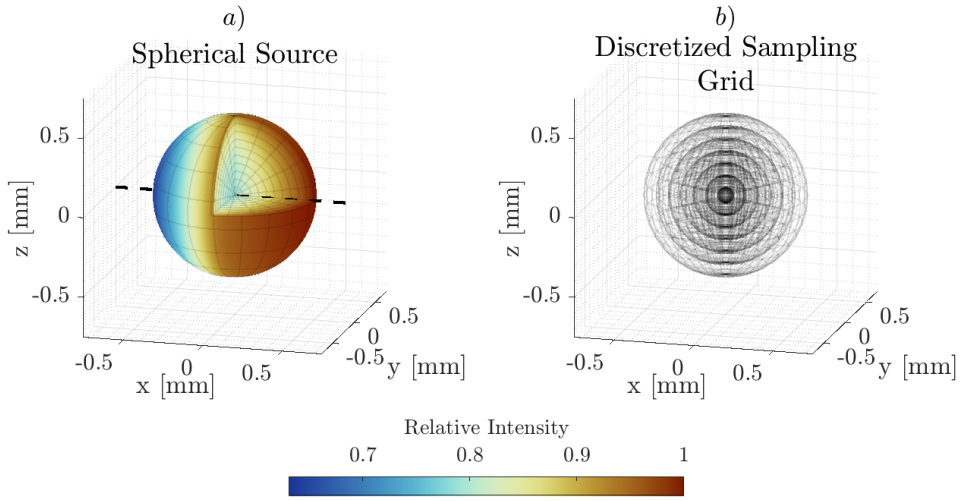

Fig. 2.45. Spherical source, *a)* relative intensity from volume perceived by a point detector. *b)* Discretized mesh of spherical source.

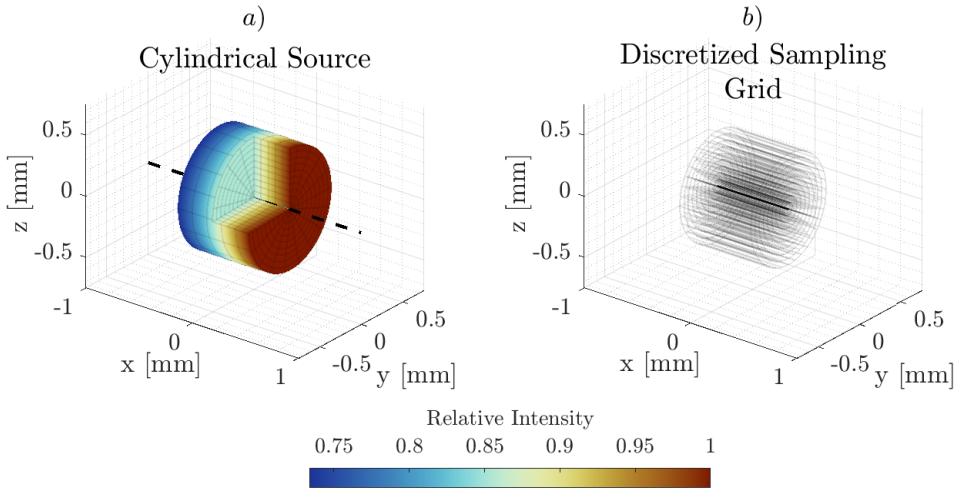

Fig. 2.46. Cylindrical source with axis along detector direction. *a)* relative intensity from volume perceived by a point detector. *b)* Discretized mesh of cylindrical source.

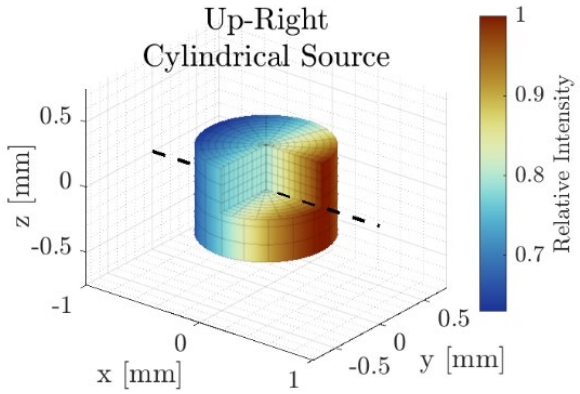

Fig. 2.47. Cylindrical source with axis perpendicular to detector direction. Relative intensity from volume perceived by a point detector.

2.5. Summary of Findings

The presented discussion of this chapter lays the basis behind radiation imaging methods which will be the concurrent theme for future chapters; this progressively evolves from radiation sources and basics of radiation detection to an overview of CT imaging focusing on Filter-Back Projection reconstruction. These fundamentals set the stage to describe the development of the deployed imaging systems and the methods utilized to quantify their performance.

The first system of interest is the High-Resolution Gamma Tomography System. This CT scanning system was designed in-house by the team at the ECMF lab with contributing development support of the present author. The system is designed in arc-geometry with a source-detector distance of 800 mm. The arc is composed of 240 LYSO detector crystals with a detector pitch of 2.5 mm, a crystal detection area of 2x6 mm^2 and a crystal depth of 15 mm. The radioactive source is an ^{192}Ir pellet with dimensions of 1.5 mm diameter and a 0.75 mm thickness; the choice to use Iridium as a photon source stems from the high activity per unit volume that this isotope can achieve, this reduces the source size therefore reducing the source blur while maintaining a large photon flux. Preliminary testing with a 662keV ^{137}Cs source of the LYSO crystals paired with the SiPM demonstrated a photopeak energy resolution of a between 12.8% and 14.1% depending on SiPM crystal depth and applied bias. The LYSO scintillating crystals are coupled to SiPMs which convert the scintillated light into an electric signal. The analog signal is then fed into an Amplifier Board which amplifies the signal and applies two pulse-height discriminators; the latter allows the isolation of events associated with the source-photopeak photons thus filtering events related to the Compton continuum. The discriminated signals are digitized and transmitted onto the Counter Board which tallies the events of interest. The data stored in the counter board memory is then extracted by an Arduino Yun which is written on a file and transmitted to the user computer. The SiPM, amplifier, counter and Arduino boards are in charge of processing the signals of 8 LYSO crystals at a time, requiring 30 boards of each type. The system is controlled by a microcontroller which signals the timing to begin recording events, data-download, and clearing the counter board's memory. The imaging resolution of the HRGTS was assessed by measuring a Siemens star, from which the resolution was determined to be between 0.71mm and 1.0 mm based on analysis of the MTF (modular transfer functions) with respective 10% and 30% contrast cutoffs. The detector was used to perform volumetric imaging of an aluminum propeller as well as phase-locking reconstruction; the latter images a rotating object, in this case a fast-moving propeller, while the detector remains stationary. Ultimately, the objective of the HRGTS is to perform measurements of

liquid-gas phase mixtures inside nuclear reactor representative geometries, this will be demonstrated in Chapter 5.

The second imaging system designed in the present research is the Michigan High Resolution Tomographic Imaging System (CHROMA). This system utilizes a CdTe detector panel with an active detection area of 25.6 x 204.8 mm^2 and contains crystal pixels with an effective area of 100 x 100 μm^2. The system is designed to fit the ^{192}Ir source or a standard medical x-ray tube. The source sits on a linear stage that allows variable adjustment of the source detector distance. The imaging resolution of the system was determined to be approximately 0.42-0.63 mm based on the analysis of the MTF; these results were obtained with the ^{192}Ir source and are expected to improve with the x-ray tube using a focal spot of 0.6 mm.

Lastly, parallel efforts were focused on the development of a ray-tracing forward-projection modeling toolset meant to compliment the experimental endeavors of this research. The final section of the chapter details the geometric formulations between ray-traces and different objects such as planes, cylinders, and spheres. These descriptions although idealized, can simulate a reference case for the expected outcome of an experimental setup paired with an imaging system; these capabilities are exploited in particular in Chapters 4 and 5. The toolset is designed to consider volume objects which increases the fidelity of the radiation transport, this treatment naturally embeds the detector and source blur as well as the source's self-shielding in the case of a volume source.

CHAPTER III

The Void Fraction and the Dynamic Bias Error in Temporal Two-Phase Flow Measurements Performed with Radiation Transmission

Nomenclature

Roman Variables

A	Component area
a	Lower integration limit
b	Upper integration limit
D	Total flow chord length
d	Chord length
f	Frequency
I	Radiation count-rate/flux
j	Superficial velocity
M	Number of recorded measurements
T	Signal period/Integration period
t	Time
u	Conductivity

Greek Variables

α	Void fraction
β	Sampling to phenomena period ratio
$\Delta\alpha$	Dynamic bias
δ	Pipe thickness
ε	Phase amplitude component
Θ	Centroid value
λ	Contrast attenuation factor
μ	Linear attenuation coefficient
ξ	Peak-to-peak amplitude
σ	Standard deviation
τ	Signal integration time
ω	Phase temporal-distribution/duty-cycle

Subscripts & Superscripts

2φ	Two-phase flow
cent	Centroid
CL	Center line
cr	Critical duty cycle
d	Detector subscript
G	Gas phase
i	Indexing variable
ideal	Reference
k	Indexing variable
L	Liquid phase
m	Discrete time variable
max	Maximum
model	Derived model

n	Discrete sampling variable	Tri	Triangular signal
o	Source subscript	$+$	Active or positive portion
$Rect$	Rectangular signal	$-$	Passive or negative portion
$Sine$	Sinusoidal signal	$\sim$	Implemented model
s	Sampled	α	Void fraction

3.1. Motivation

Radiation based measurements have become an essential tool in the study of multi-phase flow phenomena due to its non-intrusive nature. These phenomena present various levels of complexity due to the turbulent nature of flows, phase changes and multiphase flow interactions. The primary parameter of interest which is measured in two-phase flow phenomena is the void fraction which describes the percent of gas-phase content in the system. The determination of this parameter is of particular importance in nuclear reactor systems in which the presence of the gas phase affects the reactor performance and operational safety margins [95, 117, 161, 180].

Reported void fraction measurements using radiation transmission were performed as early as 1958 by Hooker et al. [69] and Petrick et al. [142]. Further measurements focused on nuclear reactor system applications were performed in 1965 when Sha et al. [165] utilized a neutron-beam to estimate the void fraction of inserts in a nuclear test section. Since, applied radiation measurement techniques have been widely implemented in the forms of densitometry [102, 173], radiography [22, 203], and computed tomography [17, 125]; these increase in spatial complexity respectively, from 1D up to 3D fields.

The accuracy of the radiation transmission measurement of two-phase flow relies on several factors including but not limited to the detector system performance, radiation source type and strength, geometry of the experimental setup, and the transient nature of the flow; the latter is often neglected. Radiation transmission measurements of two-phase flows contain an intrinsic measurement bias which deviates the measured void fraction from the true void fraction, this is referred to as the dynamic bias. This phenomenon was first investigated by Harms et al. [57, 58], deriving expressions for simple temporal void fraction signals, exposing the magnitude that this type of bias can have on the measurement's accuracy. Andersson et al. [9], Hampel et al. [54, 55] and Wagner et al. [188] have performed additional studies using simplified temporal signals to address void fraction corrections.

In this chapter, we first establish the applied relations between radiation transmission measurements and the estimation of the void fraction. The discussion is then expanded to the analytical derivation of the dynamic bias for evenly distributed and duty cycle modulated rectangular signals; a new and more encompassing analytical expression is obtained from the relations derived from the latter. The purpose of the present study is to fully characterize the dynamic bias, benchmark previous research using numerical methods, transform measured experimental data recorded with a wire-mesh sensor (WMS) into hypothetical radiation transmission signals to analyze the bias magnitude for realistic two-phase flows over various flow regimes, and assess the effects that the bias may introduce on the measurement accuracy.

3.2. Void Fraction

Previously, we described the transmission of radiation through a medium using the Beer-Lambert law elaborated in Section 2.1.1.4, in which an ensemble of radiation particles is exponentially attenuated due to interactions with matter; the present analysis will drop the temporal dependency of Eq.(2-13) that yields particle counts and instead will describe the transmission in terms of intensity/activity or counts per second. The following relation is adapted for radiation transmission passing through a two-phase flow system, which is analogous to the one proposed by Andersson et al. [9] and is expressed by the function

$$I_{2\varphi} = I_0 \, e^{-(d_L \, \mu_L + d_G \, \mu_G) - \sum_i \mu_i \delta_i}, \qquad \text{Eq.(3-1)}$$

where I_0 is the *flat field* radiation count rate (s^{-1}), d_G is the gas chord-length (m), d_L is the liquid chord-length along the radiation beam line, μ_G is the gas linear attenuation, μ_L is the liquid linear attenuation, and $\sum_i \mu_i \delta_i$ are the remainder linear attenuations and chord-lengths of additional materials in the system (i.e. pipes, insulators, etc.). The linear attenuation coefficient for any given material is dependent on its atomic composition, as well as the type and energy of the crossing radiation particles; these material properties are described in Section 2.1.1.3. This requires mindful consideration in the treatment of x-rays and neutrons which are emitted in a spectrum of energies and where the low energy particles are preferentially attenuated, thus beam hardening the particle energy spectrum; this effect is further elaborated in Chapter 4. The corresponding calibration measurement for the test section completely filled with water (all-liquid system) is

$$I_L = I_0 \, e^{-D\mu_L - \sum_i \mu_i \delta_i}, \qquad \text{Eq.(3-2)}$$

and for the test section completely filled with gas (all-gas system) is

$$I_G \;=\; I_0\, e^{-D\mu_G - \sum_i \mu_i \delta_i}, \qquad \text{Eq.(3-3)}$$

where D is the pipe's inner diameter (or the flow region's total chord length). During temporal two-phase flow measurements, the gas phase chord length d_G, can be described using the remainder liquid phase chord length d_L, as

$$d_G\,(t) = D - d_L(t). \qquad \text{Eq.(3-4)}$$

The void fraction along the chordal length is defined as

$$\alpha(t) = \frac{d_G(t)}{D}. \qquad \text{Eq.(3-5)}$$

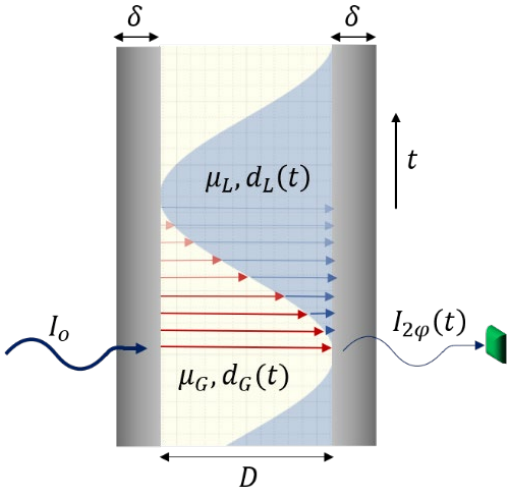

Fig. 3.1. Radiation transmission process of a simplified time dependent two-phase flow.

The temporal void fraction $\alpha(t)$ can be any arbitrary time dependent continuous function. Based on the relations in Eq.(3-4) and Eq.(3-5), the two-phase flow radiation transmission function can be expressed in terms of the temporal void fraction as

$$I_{2\varphi}(t) = I_0 e^{-(D[(1-\alpha(t))\mu_L + \alpha(t)\mu_G] + \sum_i \mu_i \delta_i)} \qquad \text{Eq.(3-6)}$$

This is the ideal transmission response where the attenuated intensity fluctuates based on the time dependent two-phase flow, the process is best depicted in Fig. 3.1.

Real detector systems cannot perfectly sift the radiation transmission function due to several limiting factors. Such systems require a finite integration time window in order to count radiation events. Since the detector can only sample in discretized steps, this leads to a treatment of time as a discrete sequence t_m, where the subscript m denotes the frame number in the sampling process. For convenience, time will be centered in the middle of the frame. Next, the measured detector count rate is described as a function of discrete time and detector integration period.

$$\bar{I}_{2\varphi,m}(t_m,T) = \frac{I_0\ e^{-\sum_i \mu_i \delta_i}}{T_d} \int_{a_m}^{b_m} e^{-D[(1-\alpha(\tau))\mu_L + \alpha(\tau)\mu_G]}\ d\tau. \qquad \text{Eq.(3-7.}a\text{)}$$

$$a_m = t_m - \frac{T_d}{2} \qquad \text{Eq.(3-7.}b\text{)}$$

$$b_m = t_m + \frac{T_d}{2} \qquad \text{Eq.(3-7.}c\text{)}$$

Here, a_m and b_m are the lower and upper time bounds of the frame, T_d is the detector frame integration period and τ is the time integration variable of the frame. The response of the detector is described here as the time average of the transmission function over a given integration window. In the case where the detector samples increasingly fast, the detector response will become the same as the ideal transmission function through the first fundamental theorem of calculus

$$\lim_{T_d \to 0} \bar{I}_{2\varphi,m}\,(t_m, T_d) \ = \ I_{2\varphi}(t) \qquad \text{Eq.(3-8)}$$

For convenience, the flow attenuation terms are consolidated into a contrast attenuation factor using the all-gas and all-liquid calibration measurements as

$$\lambda = \ (\mu_L - \mu_G)D \ = \ \ln\left(\frac{I_G}{I_L}\right). \qquad \text{Eq.(3-9)}$$

This dimensionless quantity is a property of the radiation type, geometry, and two-phase flow composition which expresses the maximum contrast attenuation ranges plausible between the present phases of interest; it can represent different attenuation chord-lengths crossing the available flow geometry region (i.e. chordal paths along a circular pipe), and different types of liquid-gas mixtures described by the linear attenuation coefficients (i.e. water coolant, molten salt coolant). To give the reader some perspective, for a water-air mixture system at 20°C with a thickness D of 1 cm, paired with a standard x-ray tube at 150keV represents a $\lambda = 0.260$, and for a ^{137}Cs gamma-emitting source $\lambda = 0.086$; similarly, for a system with a thickness D of 10 cm increases the contrast attenuation factor to $\lambda = 2.165$, and $\lambda = 0.856$ respectively. It is important to highlight that the x-ray spectra experiences beam hardening, this is noted from the corresponding 10 cm value of λ being less than ten times the value of the 1 cm value, on the other hand, the monoenergetic gamma-ray values maintain linearity. It is also worth noting how x-rays are preferentially attenuated in comparison to gamma-rays; typically, gamma-ray photons are higher energy which are less likely to interact with matter than the lower energy medical x-ray photons.

After the two-phase flow measurement is performed, the signal is post processed by transforming the measurement from recorded transmission counts to void fraction; this requires dividing the measurement in Eq.(3-7.a) by the liquid calibration in Eq.(3-2), taking the natural logarithm and dividing by Eq.(3-9) as

$$\alpha_s(t_m, T_d, \lambda) = \frac{1}{\lambda} \ln \left(\frac{I_0 e^{-(D\mu_L + \sum_i \mu_i \delta_i)}}{I_L \; T_d} \int_{a_m}^{b_m} e^{\,\lambda \alpha(\tau)} \, d\tau \right); \qquad \text{Eq.(3-10)}$$

the subscript s is used here to denote the sampling process of the void fraction. The division by the all-liquid calibration measurement eliminates the liquid and external material attenuation terms which are also found in the two-phase flow transmission function. With further simplifications of Eq.(3-10) allows us to estimate the sample average void fraction from the temporally collected frames

$$\bar{\alpha}_s(T_d, \lambda) = \frac{1}{M} \sum_{m=1}^{M} \left[\frac{1}{\lambda} \ln \left(\frac{1}{T_d} \int_{a_m}^{b_m} e^{\,\lambda \alpha(\tau)} \, d\tau \right) \right], \qquad \text{Eq.(3-11)}$$

where M is the total number of frames or recorded measurements. The sample average void fraction shows that the averaging procedure should be performed after the logarithmic conversion in Eq.(3-11), Hampel [54] refers to this as the correct averaging method, supported in the limit where the detector integration period becomes significantly small, as described in Eq.(3-8). On the contrary, when the detector integration window becomes increasingly large, temporal averaging occurs during the actual measurement integration period, thus happening inside the logarithmic function in Eq.(3-11); this results in an erroneous averaging procedure.

3.3. The Dynamic Bias

The dynamic bias emerges as a result of the inexact averaging procedure previously discussed; the bias is defined as the deviation or absolute error of the sampled void fraction in comparison to the true void fraction. Let us first define the instantaneous frame bias as

$$\Delta\alpha(t_m, T_d, \lambda) = \frac{1}{\lambda} \ln \left(\frac{1}{T_d} \int_{a_m}^{b_m} e^{\,\lambda \alpha(\tau)} \; d\tau \right) - \frac{1}{T_d} \int_{a_m}^{b_m} \alpha(\tau) \; d\tau. \qquad \text{Eq.(3-12)}$$

The dynamic bias becomes the average accumulation of error over the range of the instantaneous frames throughout the measurement; this is expressed as

$$\Delta\alpha(T_d, \lambda) = \frac{1}{M} \sum_{m=1}^{M} \left[\frac{1}{\lambda} \ln \left(\frac{1}{T_d} \int_{a_m}^{b_m} e^{\,\lambda \alpha(\tau)} \; d\tau \right) - \frac{1}{T_d} \int_{a_m}^{b_m} \alpha(\tau) \; d\tau \right]. \qquad \text{Eq.(3-13)}$$

This type of error arises from the fact that the natural log of the measurement is a non-linear transformation that is applied on the outside of the integral operation, therefore it occurs as the acquisition window is

extended which results in a deviation from the behavior of the sampled function. Now, changing variables allows the sampling integration period to be defined relative to the two-phase flow phenomena period, removing the need to stipulate a specific period, but conveniently describing how one scales relative to the other:

$$T_d = \beta\, T_\alpha, \qquad \text{Eq.(3-14.}a\text{)}$$

$$f_d = \frac{f_\alpha}{\beta}, \qquad \text{Eq.(3-14.}b\text{)}$$

$$\beta = \frac{T_d}{T_\alpha} = \frac{f_\alpha}{f_d}. \qquad \text{Eq.(3-14.}c\text{)}$$

Here, T_α is the ideal void fraction phenomena period, f_α is the corresponding ideal phenomena frequency, T_d is the detector sampling time period and f_d is the corresponding detector sampling frequency. The parameter β can characterize the transition from the proper to the wrongful averaging implementation. When $\beta < 1$, the sampling is occurring faster than the phenomena frequency, nevertheless, one should sample at $\beta < 0.5$ following the Nyquist criterion to capture time resolved information of the phenomena. When $\beta > 0.5$ results in a time average beyond the Shannon-Nyquist criterion, thus failing to capture temporal information, instead becoming a measure of the average behavior of the flow. The dynamic bias buildup from Eq.(3-13) can then be rewritten using the new relations as

$$\Delta\alpha(\beta,\lambda) = \frac{1}{M}\ \sum_{m=1}^{M}\left[\frac{1}{\lambda}\ \ln\left(\frac{1}{\beta\ T_\alpha}\ \int_{a_m}^{b_m} e^{\ \lambda\alpha(\tau)}\ d\tau\right) - \frac{1}{\beta\ T_\alpha}\int_{a_m}^{b_m}\alpha(\tau)\ d\tau\right]. \qquad \text{Eq.(3-15)}$$

This expression will be used to numerically evaluate the dynamic bias associated to arbitrary temporal two-phase flow functions being measured by a hypothetical radiation detection system.

3.4. Variance Effects on the Dynamic Bias

The dynamic bias is also strongly dependent on the gas fraction fluctuations of the true void fraction $\alpha(t)$ function, this will be referred as the void fraction amplitude throughout the text; as one can imagine, abrupt and irregular behavior could heavily influence the buildup of this error. If a time-resolved experimental signal is analyzed in steady-state conditions, it basically consists of a fluctuation around the true mean value $\bar{\alpha}$, which can be obtained by means of time averaging given a time frame T_α. However, the characteristic amplitude of such random-like oscillation influences the dynamic bias. Square-like signals can be taken as a reference so that a general approximation can be obtained to estimate the dynamic bias. Let us first derive a generalized expression based on rectangular pulse signals whose void fraction is composed

of an active and passive phase components, as shown in the examples of Fig. 3.2. Throughout the text the active portion is considered as the components of the signal that are above the average, similarly, the passive portion is considered as those below the average and represent a void fraction baseline, or lack thereof. The temporal distribution or in this case the duty cycle ω represents the portion of time for which the void fraction is active over the phenomena cycle T_α, this can be expressed as

$$\omega = \frac{\tau^+}{T_\alpha}, \qquad \text{Eq.(3-16.}a\text{)}$$

and the passive portion of the time is described as

$$(1-\omega) = \frac{\tau^-}{T_\alpha}. \qquad \text{Eq.(3-16.}b\text{)}$$

Here τ^+ and τ^- represent the signal's active and passive duration. The active and passive amplitudinal displacements away from the mean void fraction are $\varepsilon^+$and ε^- respectively. The signal variance is an important parameter of interest which characterizes the signal fluctuation, however, this parameter is obtained with time resolved measurements. The variance of the square signal is defined as

$${\sigma_\alpha}^2 = \omega(\varepsilon^+)^2 + (1-\omega)(\varepsilon^-)^2. \qquad \text{Eq.(3-17)}$$

This involves respectively weighting the squared active and passive amplitudes by the corresponding temporal portion described respectively in Eq.(3-16.a). The dynamic bias can be modified from Eq.(3-15) for a square signal with a single measurement cycle assuming $M = 1$ and an acquisition to phenomena period ratio of $\beta = 1$, the expression is then simplified through the following steps:

$$\Delta\alpha(T_\alpha, \tau^\pm, \varepsilon^\pm, \lambda) = \frac{1}{\lambda} \ln\left(\frac{1}{T_\alpha}\int_0^{\tau_i^+} e^{\lambda(\bar{\alpha}+\varepsilon^+)}\, d\tau + \frac{1}{T_\alpha}\int_0^{\tau_i^-} e^{\lambda(\bar{\alpha}-\varepsilon^-)} d\tau\right) - \bar{\alpha}, \qquad \text{Eq.(3-18.}a\text{)}$$

with some algebraic manipulation and using the substituting in the relations from Eq.(3-16.a), the dynamic bias becomes

$$\Delta\alpha(\omega, \varepsilon^\pm, \lambda) = \frac{1}{\lambda}\ln(\omega e^{\lambda\varepsilon^+} + (1-\omega)e^{-\lambda\varepsilon^-}). \qquad \text{Eq.(3-18.}b\text{)}$$

This final expression describes the dynamic bias for any parametrized square signal. It is worth pointing out that Eq.(3-18.a) reveals that the dynamic bias is dependent on the temporal distribution and amplitude displacements between the active and passive components of the signal and is independent on the average void fraction of the signal; this implies that the dynamic bias is shift invariant.

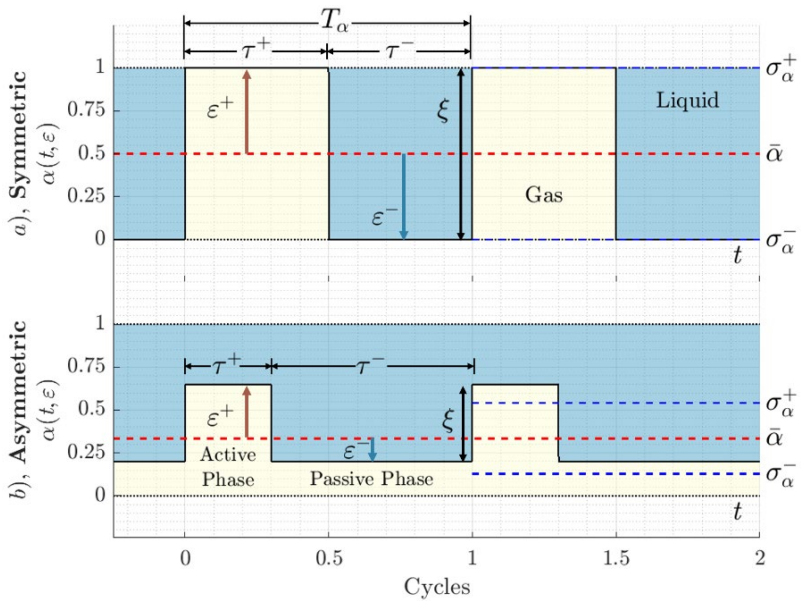

Fig. 3.2. Example of a) symmetric and b) asymmetric square signals.

Now let us consider a symmetric square signal as shown in Fig. 3.2.*a*; for reference, symmetric in this case describes equal temporal and amplitudinal distributions between the active and passive components of the signal; the assumptions for this particular case then implies:

$$\omega = (1-\omega) = \frac{1}{2}, \qquad \text{Eq.(3-19)}$$

$$\varepsilon^+ = \varepsilon^- = \varepsilon\ . \qquad \text{Eq.(3-20)}$$

It can then be easily proven that the standard deviation σ_α is equivalent to the amplitudinal components by replacing the relations of Eq.(3-19) and Eq.(3-21) into the expression in Eq.(3-17) which simplifies to.

$$\sigma_\alpha = \varepsilon \qquad \text{Eq.(3-21)}$$

The dynamic bias from Eq.(3-18.*b*) can now be expressed in terms of the signal's standard deviation

$$\Delta\alpha(\sigma,\lambda) = \frac{1}{\lambda}\ln\left(\frac{e^{\lambda\sigma_\alpha} + e^{-\lambda\sigma_\alpha}}{2}\right) = \frac{1}{\lambda}\ln[\cosh(\lambda\sigma_\alpha)], \qquad \text{Eq.(3-22)}$$

which is the same expression proposed by Harms et al. [58] following an analogous derivation. In addition, the expression in Eq.(3-22) is expanded with the Maclaurin series based on $\lambda\sigma_\alpha$ as the independent variable,

$$\frac{1}{\lambda}\ln[\cosh(\lambda\sigma_\alpha)] = \frac{\lambda}{2}\sigma_\alpha^2 - \frac{\lambda^3}{12}[\sigma_\alpha^2]^2 + \cdots \qquad \text{Eq.(3-23)}$$

where it can be observed that if the value of σ_α is small enough, the linear term is the only relevant portion. Therefore, the dependence of the dynamic bias and the signal's variance σ_α^2 is virtually linear.

Now let us consider an asymmetric periodic square signal with unbalanced temporal and amplitudinal distributions between the active and the passive phases with an arbitrary example shown in Fig. 3.2.b. The active and passive amplitudinal displacements of the signal can now be defined in terms of the signal variance and the temporal distribution

$$\varepsilon^{+} = \sqrt{\frac{\sigma_{\alpha}^{2}(1-\omega)}{\omega}}, \qquad \text{Eq.(3-24.}a\text{)}$$

$$\varepsilon^{-} = \sqrt{\frac{\sigma_{\alpha}^{2}\ \omega}{1-\omega}}. \qquad \text{Eq.(3-24.}b\text{)}$$

The peak-to-peak amplitude of the signal is described as the sum of the active and passive amplitude displacements of the signal

$$\xi \ = \ \varepsilon^{+} \ + \varepsilon^{-}, \qquad \text{Eq.(3-25.}a\text{)}$$

$$\xi = \sqrt{\frac{\sigma_{\alpha}^{2}}{(1-\omega)\omega}}. \qquad \text{Eq.(3-25.}b\text{)}$$

The peak-to-peak amplitude ξ has a plausible range between 0 and 1; the expression in Eq.(3-25.b) allows us to substitute between the signal variance and the peak-to-peak amplitude depending on which one is more convenient. The dynamic bias can alternatively be expressed in terms of ξ or σ_{α}^{2} by algebraically rearranging Eq.(3-18.b) as

$$\Delta\alpha(\omega,\xi,\lambda) = \frac{1}{\lambda}\ln(\ \omega + (1-\omega)e^{-\lambda\xi})\ +\ \xi(1-\omega) \qquad \text{Eq.(3-26.}a\text{)}$$

$$\Delta\alpha(\omega,\sigma_{\alpha}^{2},\lambda) = \frac{1}{\lambda}\ln\left(\ \omega + (1-\omega)e^{-\lambda\sqrt{\frac{\sigma_{\alpha}^{2}}{(1-\omega)\omega}}}\right) + \sqrt{\frac{\sigma_{\alpha}^{2}(1-\omega)}{\omega}}. \qquad \text{Eq.(3-26.}b\text{)}$$

These expressions are equivalent and describe the corresponding dynamic bias of a system characterized by λ, a temporal distribution ω, the peak-to-peak amplitude ξ, and whose variance is σ_{α}^{2}; which estimates the bias for the set of conditions which describe the signal. The most direct way to see the advantages of this proposed model Eq.(3-26.b) is to compare it with the expression proposed by Harms in Eq.(3-22). The latter has only two parameters to characterize the signal. However, when studying signals from two-phase flow, the different flow patterns have a non-symmetrical time distribution between the two phases as will be shown in Fig. 3.21.c in section 3.6.5; the experimental results will depict that ω is significantly dependent on the flow regime. In reality, the condition $\omega = 0.5$ to which Harms's model is constrained cannot be guaranteed. Alternatively, the proposed expression in Eq.(3-26.b) incorporates the third parameter ω that accounts for the temporal asymmetry information that was previously missing. By having this additional third parameter, the prediction becomes more accurate, however, this third parameter implies greater

complexity in the prediction since ω value must be approximated.

The 3D diagram of the dynamic bias is depicted in Fig. 3.3.*a* as a function of the possible values of ω and λ, and where the condition of ξ =1 defines the outermost boundary of the volume; the superimposed color corresponds to the duty cycle and the planes are examples of a 1cm thick water-air system at 20°C paired with 150 keV x-ray and ^{137}Cs radiation sources. The cross-sectional slice shown in Fig. 3.3.*b* corresponds to the example plane for $\lambda = 2$. This highlights the inner region of the volume in which the grid denotes the parabolic isolines corresponding to constant peak-to-peak amplitude ξ and the vertical isolines corresponding to constant duty cycle ω. The cross-section exhibits a skewing behavior towards low void fraction range, in particular with the increase of λ.

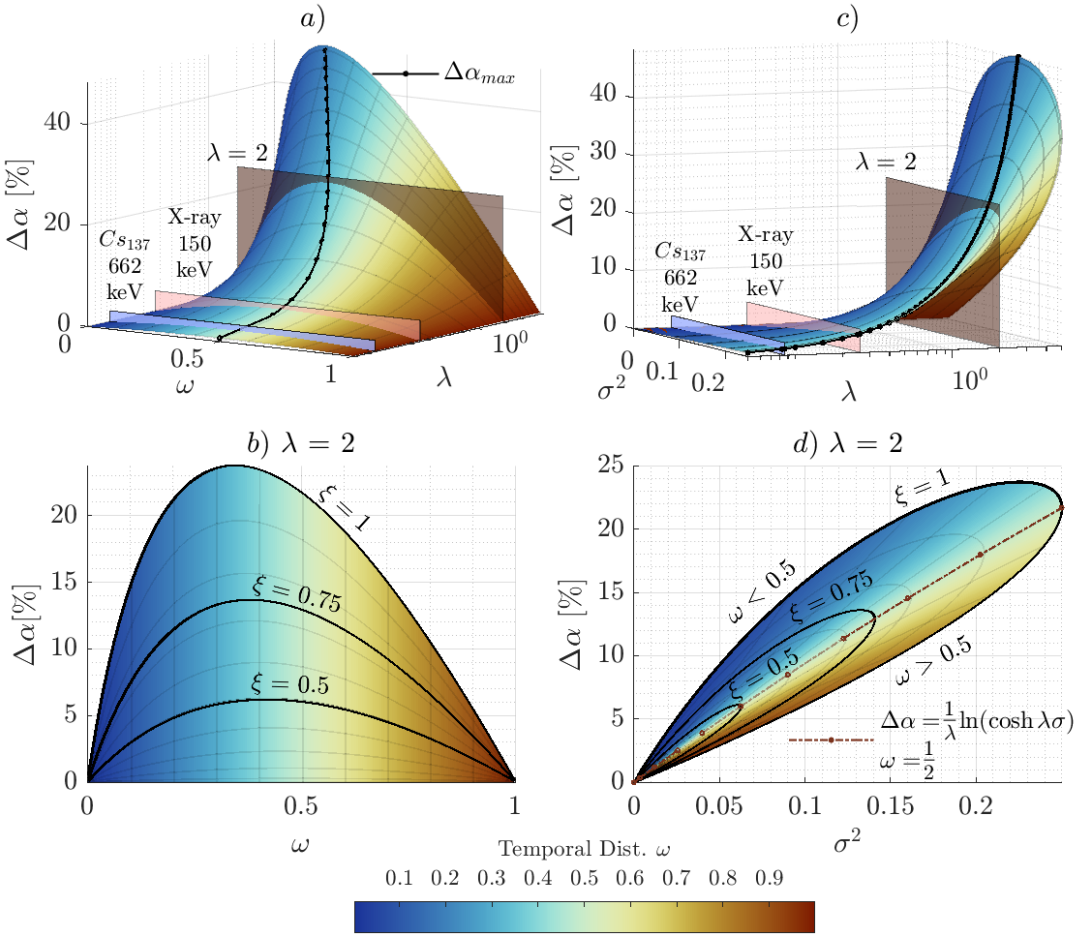

Fig. 3.3. Dynamic bias of rect function *a)* as a function of $\bar{\alpha}$ and λ top with planes representing x-ray and gamma-ray system for 1 cm thickness, *b)* cross-sectional slice as a function of $\bar{\alpha}$ for $\lambda = 2$. *c)* as a function of σ_α^2 and λ, *d)* cross-sectional slice as a function of σ_α^2 for $\lambda = 2$.

Similarly, the 3D diagram of the dynamic bias as a function of the possible values of ${\sigma_\alpha}^2$ and λ is presented in Fig. 3.3.*c*. The dynamic bias grows in a predominantly linearly fashion for small values of λ and can be best predicted following the expression Eq.(3-23) in this region, however, the error unfolds to an elliptical shape with increased λ; the latter is best depicted by the cross-sectional slice corresponding to $\lambda = 2$ shown in Fig. 3.3.*d*. The elliptical slice can be described as a series of concentric shells corresponding to the peak-to-peak isolines ξ. The upper portion of the shell correlates to $0 \leq \ \omega < \frac{1}{2}$, the bottom correlates to $\frac{1}{2} < \omega \leq 1$, and these converge to Eq.(3-22) when $\omega = \frac{1}{2}$. The physical connotation implies that a short burst signal has a larger embedded error than a signal of longer duration, for signals characterized by the same variance. This also entails that for the prior case, the passive phase is dominant, which contains the largest amount of liquid, representing a higher attenuation medium. In the latter case, the active phase is dominant, which contains a significantly larger amount of gaseous phase constituting a lower attenuation medium that yields a lower dynamic error.

The parabolic shape of the dynamic bias shown in Fig. 3.3.*a* indicates that there is a maximum value which corresponds to a critical duty cycle. This can be solved by differentiating Eq.(2-26) in terms of the duty cycle ω as

$$\frac{\partial \Delta\alpha}{\partial \omega} = \frac{e^{\lambda\xi} - 1}{\lambda + (e^{\lambda\xi} - 1)\lambda\omega} - \xi \ . \qquad \text{Eq.(3-27)}$$

Setting the derivative to zero allows us to solve for the critical duty cycle corresponding to the maximum dynamic bias for a given contrast attenuation factor and peak-to-peak amplitude,

$$\omega_{cr} = \frac{e^{\lambda\xi} - \lambda\xi - 1}{\lambda\xi(e^{\lambda\xi} - 1)} \ . \qquad \text{Eq.(3-28)}$$

The evolution of the maximum dynamic bias as a function of λ is obtained by inputting the critical duty cycle ω_c from Eq.(3-28) into Eq.(3-26.*a*) for $\xi = 1$; this is depicted by the superimposed black line of Fig. 3.3.*a*, and the evolution of the maximum value is shown in Fig. 3.4.*a*. The results reinforces the linear behavior of the error for small values of λ, as well as its deviation from linearity with increased λ. The critical duty cycle ω_{cr} starts at 0.5 and rapidly decreases, which symbolizes the tendency of the bias to be preferentially larger for short duration signals with a dominant passive-phase; when $\xi = 1$ represents an all-liquid passive phase.

The critical variance is obtained by solving Eq.(3-25.*b*) in terms of the variance and plugging in the critical duty cycle,

$$\sigma^2_{\alpha_{cr}} = \xi^2(\omega_{cr} - {\omega_{cr}}^2). \qquad \text{Eq.(3-29)}$$

The evolution of the critical variance corresponding to the maximum dynamic bias is shown Fig. 3.4.*b*; it presents an initially slow decline which becomes linear with increased λ. The black line following the maximum bias in Fig. 3.3.*a* shows that the critical variance is influenced by values where $\omega_{cr} < 1/2$ which is consistent with what has been observed. The analytical expression derived of the dynamic bias from the rectangular pulsed signal serves as a framework for the improved modeling and understanding of said phenomenon.

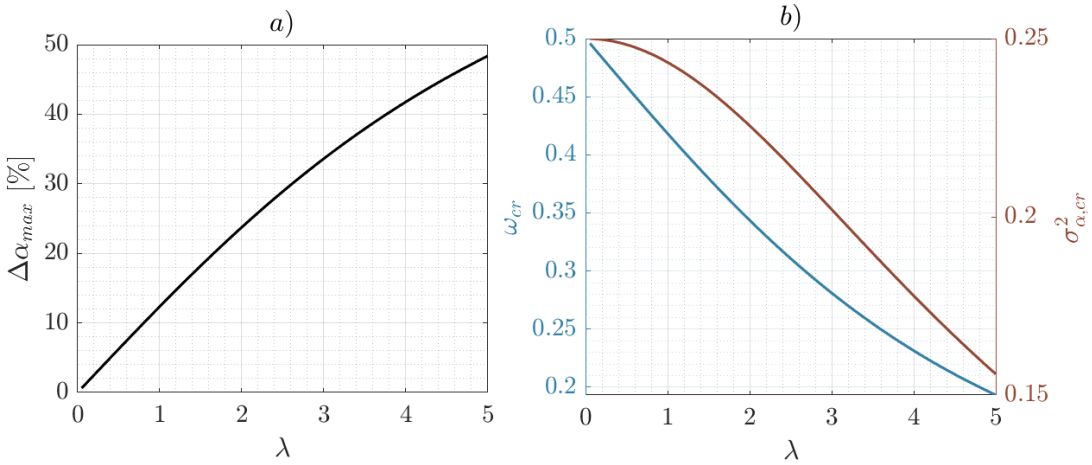

Fig. 3.4. *a)* evolution of maximum dynamic bias as a function of λ. *b)* critical duty cycle (blue) and corresponding critical variance (red) as a function of λ.

3.5. Simplified Signals

The dynamic bias is an unavoidable effect intrinsic to radiation measurements of temporal signals. This section will focus on the numerical modeling of the dynamic bias for simplified void fraction signals to gain intuition of its behavior. Simplified signals can give insight into how the dynamic bias varies as a function of integration window, contrast attenuation factor, and imposed void fraction. These parameters are influenced by several experimental conditions including but not limited to:

- Frame rate limitation of the detector.
- Operation below the counting saturation limit of the detector counters.
- Radiation source strength: weak radiation sources require long integration periods of time to obtain statistically significant results.
- Experiments with high-attenuation materials (i.e. insulators, pipe walls) effectively reduce the radiation flux available which can also result in longer integration periods of time.

- Type of radiation and atomic composition of the liquid and gas phases which determine the contrast attenuation factor.

3.5.1. Numerical Modeling

The present study aims to validate the dynamic bias model based on well-behaved void fraction signals, in this section we will use rectangular, sinusoidal, and triangular pulses for these purposes; these signals are ordered in descending temporal gradient complexity and will be respectively referred to as Rect, Sine, and Tri functions throughout the text. These signals serve as ideal models used to first understand the dynamic bias; however, real life signals are random in nature resulting in an erratic behavior in comparison to the ones that will be utilized. The signals are built by manipulating the duty cycle ω or full width half max (FWHM) of the pulsed shape, the imposed peak-to-peak amplitude ξ has a value of 1 given that this defines the outer limit of the dynamic bias volume as was observed in the previous section. The generated signals serve as inputs to a custom-built script that numerically evaluates Eq.(3-13); the data analysis scripts, and other functions were developed in MATLAB® 2019b.

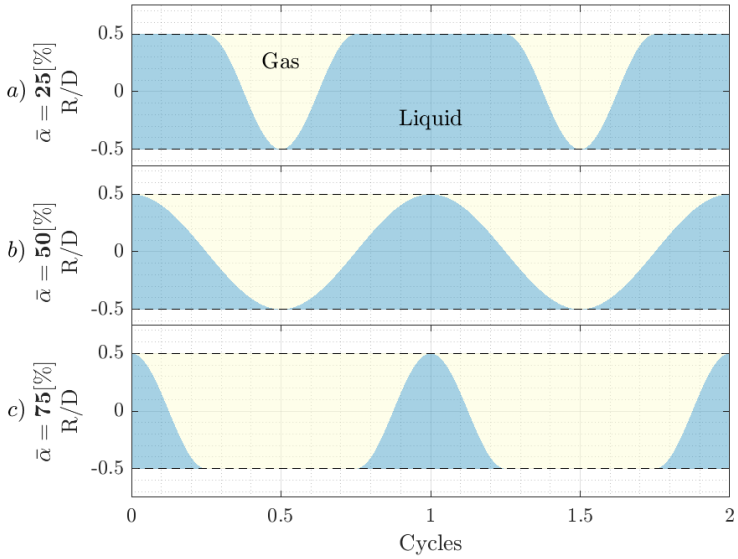

Fig. 3.5. Example of sinusoidal with modified duty cycle modulation for *a)* 25%), *b)* 50%, *c)* and 75% average void fraction.

The Rect function was characterized in the previous section, this function represents the most extreme case in which the phase changes occur abruptly, while the triangular function steadily shifts the balance between the phases. The sinusoidal function represents an intermediate behavior between the prior two other functions. The temporal duration of the pulse is fitted to yield the desired average void fraction in a cycle; this will be referred as the pulse duty cycle modulation method. The implemented definitions of the

Tri and Sine functions can be found in the Appendices A and B. An illustrative example of the modified Sine signal is shown in Fig. 3.5 for 25%, 50%, and 75% imposed average void fraction; the 25% and the 75% void fraction signals contain equivalent variance. The 50% void fraction signal will be first used to compare the dynamic bias model with the literature.

The geometric and material parameters such as pipe diameter, liquid, and gas linear attenuations used in this subsection are based on the study performed by Andersson et al. [9] which modeled a neutron radiation system with two-phase flow at 80 bars of pressure. The reported pipe diameter is 25 mm, the liquid attenuation is 7.2E-3 mm^{-1}, and the gas attenuation is 3.6E-4 mm^{-1}; this is equivalent to a contrast attenuation factor of $\lambda = 0.173$. For this study, the signals had an imposed average void fraction of 50% and were carried out over 50 phenomena cycles. The standard deviation of the true void fraction is expressed with the following

$$\sigma_\alpha = \sqrt{\frac{1}{M} \sum_{m=1}^{M} (\alpha_m - \overline{\alpha})^2} \qquad \text{Eq.(3-30)}$$

where α_m is the ideal void fraction sampled over the frame m, and $\overline{\alpha}$ is the true average void fraction. The standard deviation of the dynamic bias is defined with the following

$$\sigma_{\Delta\alpha} = \sqrt{\frac{1}{M} \sum_{m=1}^{M} (\Delta\alpha_m - \Delta\overline{\alpha})^2}, \qquad \text{Eq.(3-31)}$$

which describes the spread of the instantaneous frame errors in comparison to the average error build-up. The dynamic bias results for the three modeled functions are shown in Fig. 3.6.*a*. The instantaneous realizations of the dynamic bias described by Eq.(3-12) are depicted as scatter dots; these illustrate the aliasing lobes that arise from the mismatched sampling frequencies and the phenomena frequency, with nodes located where the phenomena frequency is divisible by the sampling frequency. The build-up curves described by Eq.(3-15) increase in the region where $\beta < 1$, these then stabilize in the region where $\beta > 1$ with dampening oscillations and asymptotically converging due to the increased average integration window. For this case, the asymptotic value of the Rect function is 2.14%, the Sine function is 1.07%, and for the triangular function is 0.71%. These results match the values reported by Andersson et al. [9] for the Rect with a difference of 0.04% and the Sine function with negligible difference; the small sources of difference may arise due to noise incorporation in the referenced study. The results also show that the Rect function has the largest dynamic bias, the Sine has the second largest and the Tri function has the smallest. This occurs because the Rect function has the most abrupt transitions between phases as previously mentioned.

The instantaneous realizations also show the variation of dynamic bias which is best described by its standard deviation expressed in Eq.(3-31) and shown in Fig. 3.6.*b*. The dynamic-bias standard deviation is depicted as a series of lobes that are damped due to the increased averaging that occurs with increase in β, with the largest lobe occurring where $0 < \beta < 1$. The standard deviation of the true window averaged void fraction described by Eq.(3-30) is plotted in Fig. 3.6.*c* as a function of β. This also exhibits a dampening lobe behavior. As β approaches zero representing an ideally fast sampling system, the true void fraction's standard deviation converges on to the function's analytical standard deviation, with values of 50% for the Rect function, 35.6% for the Sine function, and 28.9% for the Tri function; the latter two results can be verified using Eq.(B.3.*b*) and Eq.(A.3.*b*) respectively. When performing time resolved measurements, one should maintain the sampling rate below the Nyquist criterion as previously postulated, therefore sample at least at twice the phenomena frequency, nevertheless it becomes clear that there is an inherit bias error from the measurements which is decreased but not entirely eliminated at high sampling rates, unless the flow appears completely stationary during the measurement period.

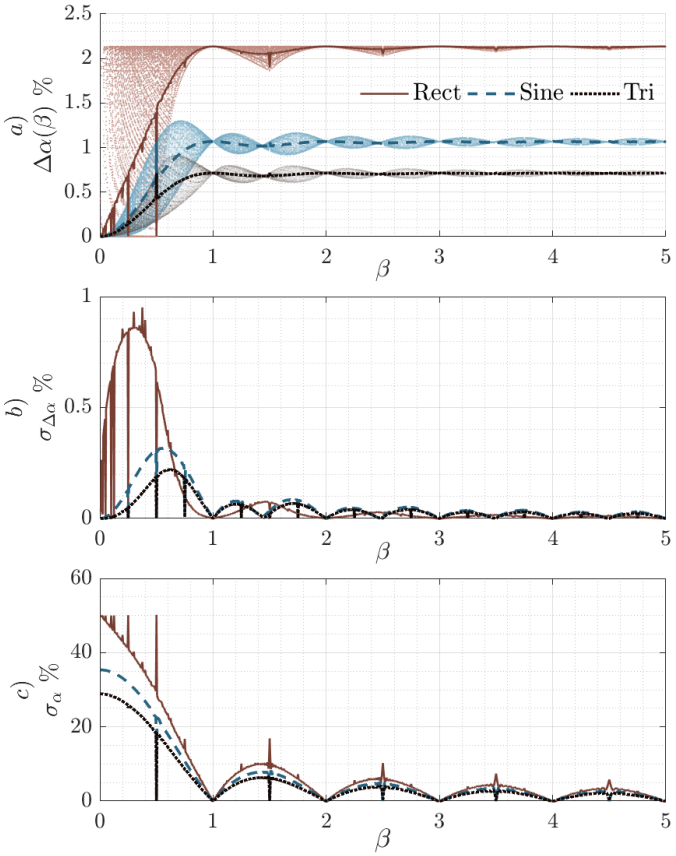

Fig. 3.6. *a)* Dynamic bias curve build-up, *b)* dynamic bias standard deviation, and *c)* true void fraction standard deviation for 50% imposed void fraction.

3.5.2. Radiation Noise

In this subsection we will branch-off momentarily to discuss the mixed effects between the radiation noise and the dynamic bias. Radiation based measurements can be performed with different sources whose radiation flux is either fixed, as is the case for radioisotopic sources, or whose flux can be adjusted which is the case for many x-ray systems. This gives rise to two separate ways to incorporate noise, which will be used in this analysis. The first involves a fixed count rate with a varying integration window (i.e.

radioisotopic source case) depicted as the blue lines in Fig. 3.7. The second adapts the radiation strength such that the detected counting event in the sampling window are held constant (i.e. x-ray systems) depicted as the red lines in Fig. 3.7; alternatively, this can also be interpreted as a stationary flow in respect to the sampling window range. The noise incorporation was performed for the Rect, Sine and Tri signals analyzed in the previous section.

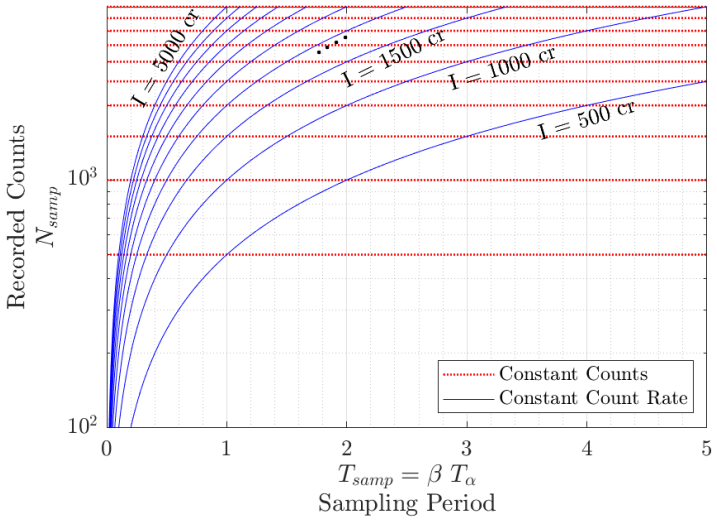

Fig. 3.7. Visualization of fixed counts (red) and fixed count rates (blue).

3.5.2.1. Differential Count Rate

The first case models a radioisotope with a fixed activity and whose radioactive decay is negligible in comparison to the measurement time. The differential count rate describes the difference in count rate between the liquid and gas phases, this is denoted with subscript *dcr*, and will be defined as

$$\begin{aligned} I_{dcr} &= I_G - I_L, \\ &= \epsilon\, I_0 (e^{-\mu_G D} - e^{-\mu_L D}) e^{-\sum_i \mu_i \delta_i}, \end{aligned} \qquad \text{Eq.(3-32)}$$

where the term ϵ represents the detectors intrinsic and geometric efficiencies. Solving for the corresponding flat field results in the expression

$$I_0 = \frac{I_{dcr}}{\epsilon\, (e^{-\mu_G D} - e^{-\mu_L D}) e^{-\sum_i \mu_i \delta_i}}. \qquad \text{Eq.(3-33)}$$

The source flux is scaled based on all the input factors, for this study the ϵ will be assumed as 100% and the outside materials are assumed to be negligible $\mu_i \delta_i = 0$, (but need to be consider in any physical system). The considered differential count rates I_{dcr} used are [100, 500, 1000, 5000], representing a range of source activities.

The radiation detection process follows the Poisson distribution, where the standard deviation of the

measurement is characterized as the square-root of the recorded counts. The expected number of counts in each integration window is defined as

$$N_{2\varphi}(t_m, \lambda) = \int_{a_m}^{b_m} I_{2\varphi_s}(I_0, \tau, \lambda)\ d\tau. \qquad \text{Eq.(3-34)}$$

Random noise representing the stochastic nature of the process is added by drawing Poisson-random samples from the expected counts in Eq.(3-34) during the measurement window

$$\tilde{N}_{2\varphi}(t_m, \lambda)\ \in\ Poiss(N_{2\varphi}(t_m, \lambda)), \qquad \text{Eq.(3-35)}$$

where $\tilde{N}_{2\varphi}$ is the noise incorporated counts. The dynamic bias formula can then be expressed in terms of the number of counts instead of the count rate as

$$\Delta\overline{\alpha}(\beta, \lambda) = \frac{1}{M} \sum_{m=1}^{M} \left[\frac{1}{\lambda} \ln \left(\frac{\tilde{N}_{2\varphi}(t_m, \beta, \lambda)}{N_L} \right) - \int_{a_m}^{b_m} \alpha(\tau)\ d\tau \right]. \qquad \text{Eq.(3-36)}$$

Noise was incorporated for 250 case-replicas of the signals; Fig. 3.8 depicts the results of the noisy cases for the Rect, Sine, and Tri functions. The results follow closely to the ideal build-up curves Fig. 3.6.*a* with a noisy fluctuating behavior, as the differential count rate increases, the noise-based dynamic bias approaches the ideal behavior for all functions. At small values of $\beta < 1$, the dynamic bias becomes negative and abruptly decreasing in particular for the low count rates, thus underestimating the void fraction for all three functions. This is a result of the low count bias described by Liang et al. [106] due to photon starvation and can be attributed to the small count expectation that occurs during fast sampling conditions. Additional trend shows that low differential count rates require longer integration periods to approach the corresponding asymptotic value with significant noise-spread in the process.

The standard deviation of the dynamic bias shown on the left-columns of Fig. 3.9, follows a $1/\beta$ relation, which implies that increasing the sampling time (and linear increase in counts) results in an effective decrease of the dynamic bias standard deviation due to the increase in the integration window of the function which reduces the true function-based fluctuations. The standard deviation of the sampled void fraction shown on the right-columns of Fig. 3.9, also follows the $1/\beta$ trend influenced by the aliasing lobes and resembling the ideal behavior shown in Fig. 3.6.*c*. Photon starvation causes a sharp increase as β approaches zero. The increase in differential count rate effectively lowers the standard deviation; at β= 5 and I_{dcr}= 5000, the void fraction standard deviation is about 1.5% for the three signals.

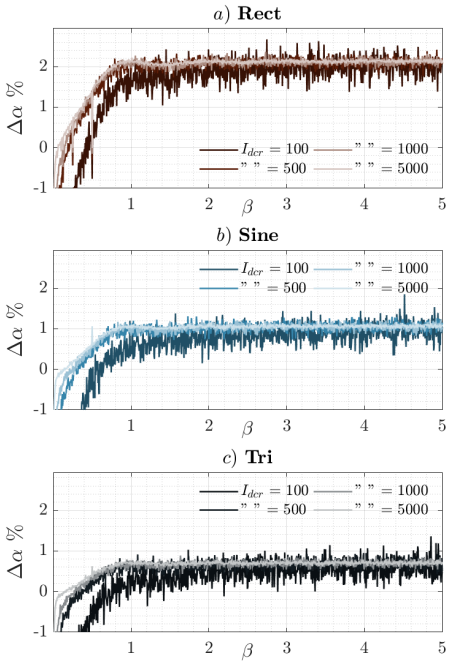

Fig. 3.8. Implemented noise using various differential count rates, *a)* Rect, *b)* Sine, and *c)* Tri function.

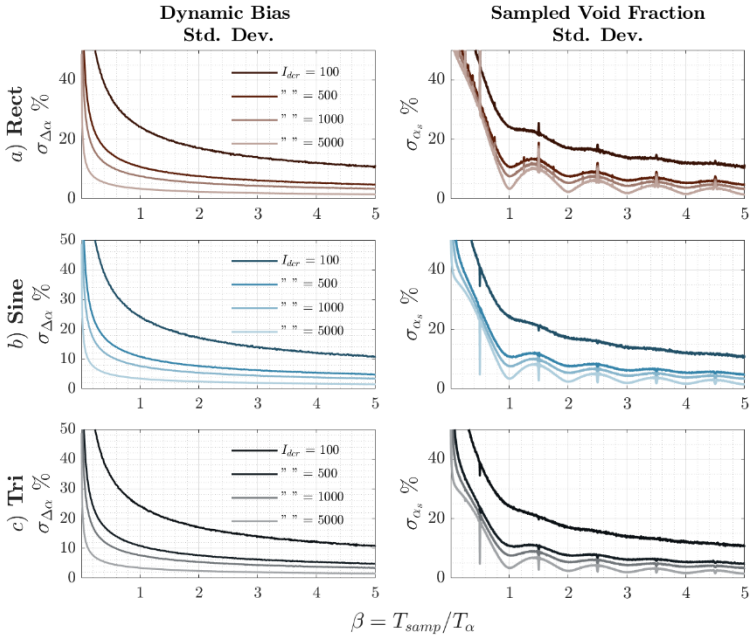

Fig. 3.9. Differential count rate standard deviation of the dynamic bias (left) and the sampled void fraction (right), for *a)* Rect, *b)* Sine, and *c)* Tri functions.

3.5.2.2. Differential Counts

The second case models a source whose radiation flux can be adjusted in a measurement frame; for example, this can be done by doubling the x-ray tube current and doubling the detector sampling frequency. Here we will define the differential counts as the difference in counts between the liquid and gas phases. In this case the counts in the interrogation window remains fixed while stretching the phenomena signal when $\beta < 1$ or compressing the signal when $\beta > 1$ relative to the measurement window. The differential counts can then be expressed as follows

$$N_{dc} \;=\; \epsilon\ \beta\ T_\alpha\ I_0(e^{-\mu_G D} - e^{-\mu_L D})e^{-\sum_i \mu_i \delta_i}. \qquad \text{Eq.(3-37)}$$

Solving for the corresponding flat field count rate results in

$$I_0 \;=\; \frac{N_{dc}}{\epsilon\ \beta\ T_\alpha\ (e^{-\mu_G D} - e^{-\mu_L D})e^{-\sum_i \mu_i \delta_i}}. \qquad \text{Eq.(3-38)}$$

The imposed differential counts N_{dc} implemented in this case are [100, 500, 1000, 5000]. The results shown in Fig. 3.10 follow the trends of the dynamic bias build-up curves plotted in Fig. 3.6.*a*. Low differential counts result in a down shift of the build-up curves as well as an increase in noise spread with increase in β. The increase in differential counts reduces the variation of the bias and converges on to the ideal build-up

curve. The standard deviation of the dynamic bias shown in the top row of Fig. 3.11, is constant throughout the sampling range. However, it becomes increasingly noisy with increase in β because it is measuring an increased amount of flow cycles during the detector integration period. The standard deviation of the noisy void fraction resembles the ideal behavior of true signals standard deviation previously shown in Fig. 3.6.*c*. The largest lobe is located at $\beta < 1$, approaching the ideal standard deviation as β approaches zero. Increasing values of $\beta > 1$ dampen the sequential aliasing lobes, however approaching an asymptotic behavior that is equal to the constant value of the dynamic bias standard deviation. Low differential counts result in an upward shift of the sampled void fraction standard deviation as well as an elevated asymptotic value due to the poor statistics. On the contrary, an increase in differential counts effectively down shifts to the ideal functions' standard deviation, and significantly improves the asymptotic behavior due to the increased radiation statistics.

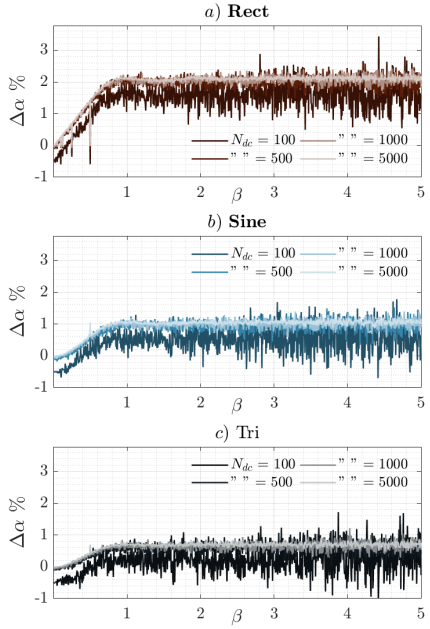

Fig. 3.10. Implemented noise using various differential counts for *a)* Rect, *b)* Sine, and *c)* Tri function.

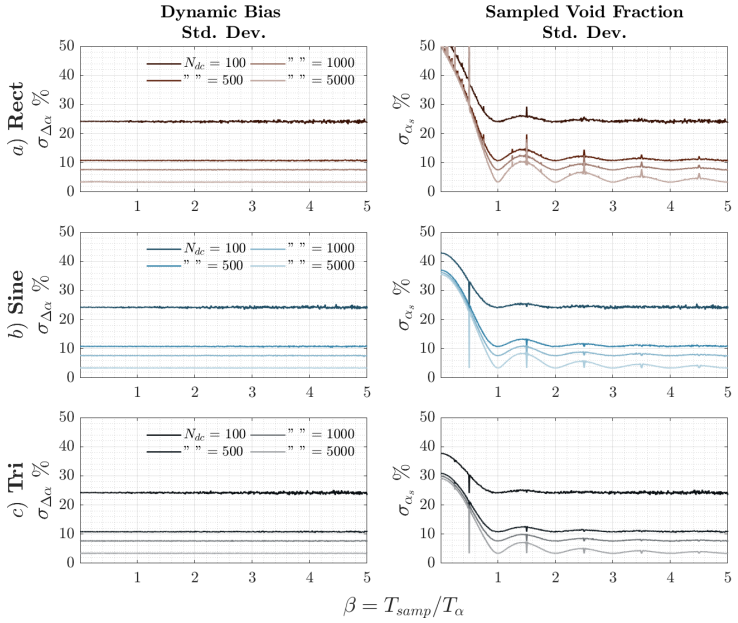

Fig. 3.11. Differential counts' standard deviation of the dynamic bias (left) and the sampled void fraction (right), for *a)* Rect, *b)* Sine, and *c)* Tri.

The results from both cases consistently show that high radiation fields improve the measurement statistics. The noise based dynamic bias was shown to follow the ideal build-up of error. The dynamic bias can be larger than the void fraction standard deviation in the case where high radiation flux and large sampling periods are used; these effectively reduce the standard deviation, but also increases the

measurement's dynamic bias. Therefore, one could have high precision with a strong source yielding a low standard deviation yet have low accuracy due to the dynamic bias.

3.5.3. Pulse Duty Cycle Modulation Study

Now, the discussion will transition to the characterization of the dynamic bias for a range of void fractions by applying the direct numerical method developed and using the three simplified signals as models. The dynamic bias parametric study was conducted by implementing the duty cycle modulation approach, the average void fraction $\bar{\alpha}$ was systematically increased from 0.2% to 99.8% in steps $\Delta\bar{\alpha}$ of 0.2%. The contrast attenuation factor λ values used were varied from 0.01 to 3 in incremental steps $\Delta\lambda$ of 0.01, the peak-to-peak amplitude was maintained as $\xi = 1$, and $\beta = 1$ was used to assume a detector integration period equivalent to the signals period. The results presented in Fig. 3.12 depict the dynamic bias as a function of the imposed average void fraction and contrast attenuation factor for the three functions. The dynamic bias of the Rect function exhibits a skewed behavior leaning towards the low void fraction range; this is supported in Sec. 3.4 and the analytical results validate the numerical model implemented in this study. The Sine and the Tri functions have two peaks with a cusp located along the void fraction value of 50%; this is due to the piecewise definition of the functions used to build the signals. The tendency shows that the low void fraction peak is larger for both functions.

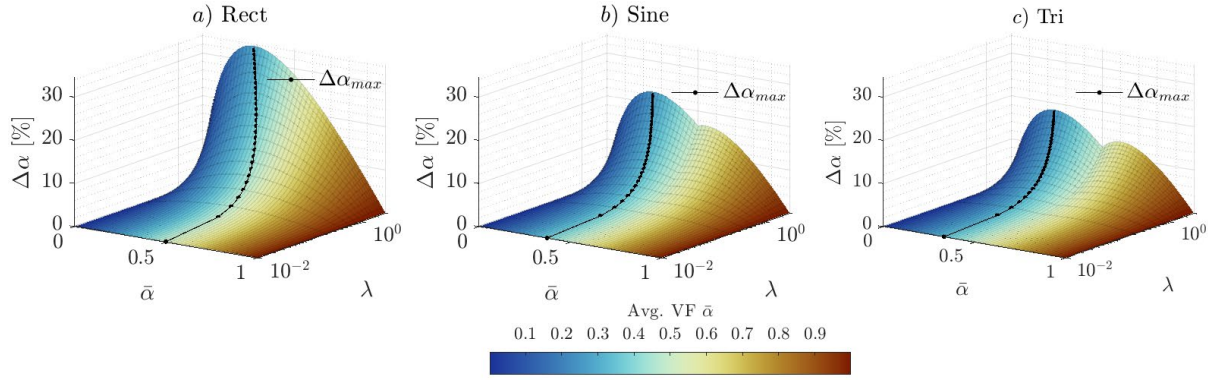

Fig. 3.12. Dynamic bias as a function of imposed average void fraction and contrast attenuation factor. *a)* Rect, *b)* Sine, and *c)* Tri functions.

The dynamic bias plotted against the variance of the original signal is shown in Fig. 3.13.*a)* for $\lambda = 1$, and *b*) for $\lambda = 2$. The results further confirm the analytical expression derived from the Rect function in Eq.(3-26.*b*). Although the Rect function exaggerates the abrupt phase change, it traces the boundary for the maximum possible error as a function of the true signal variance. The Sine and Tri functions present

similar elliptical behaviors overall contained within the Rect functions range. The results reaffirm that signals with equal variance but with dominant liquid phase, lead to higher accumulations of error. Experimental facilities with large contrast attenuation factors are more susceptible to these types of embedded errors, therefore it is important to estimate this factor to scale the dynamic bias appropriately. The Rect function can be used as a conservative and slightly exaggerated measure of the maximum dynamic bias error; this can be estimated for a given experimental setup by calculating the critical duty cycle as defined in Eq.(3-28) and plug it into Eq.(3-26.a) for a peak-to peak amplitude $\xi = 1$.

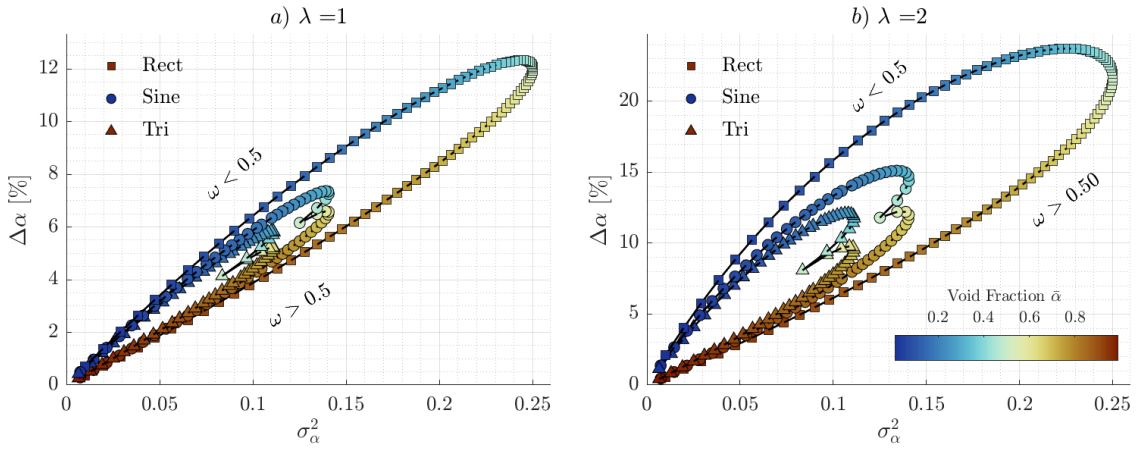

Fig. 3.13. Dynamic bias relation to the variance of the true void fraction for the three simplified signals. *a)* $\lambda = 1$, and *b)* $\lambda = 2$ contrast attenuation factor.

3.5.4. Temporal Distribution Model

The analytical expression of the dynamic bias derived from the rectangular pulse provides a framework which could be used to better predict the error for any arbitrary signal. To achieve this, we propose the temporal distribution model which aims to estimate the dynamic bias by simplifying an arbitrary signal into equivalent active and passive phase components from an approximated temporal distribution, while preserving the average void fraction and signal variance. In this study, we decided to calculate the amplitudinal centroids of the signal's active and passive components, and from these, estimate the temporal distribution ω. This requires the signal to be mean centered, therefore one must subtract the average value of the signal and split it into positive and negative parts as follows

$$\alpha(\tau)^{+} = \begin{cases} \alpha(\tau) - \bar{\alpha} & \text{if } \alpha(\tau) - \bar{\alpha} > 0 \\ 0 & \text{otherwise} \end{cases}, \qquad \text{Eq.(3-39.}a\text{)}$$

$$\alpha(\tau)^{-} = \begin{cases} \bar{\alpha} - \alpha(\tau) & \text{if } \alpha(\tau) - \bar{\alpha} < 0 \\ 0 & \text{otherwise} \end{cases}, \qquad \text{Eq.(3-39.}b\text{)}$$

where $\pm$ defines the polarity of the component. The positive and negative areas of the mean centered signal are respectively defined as

$$A^{+} = \int_{0}^{T_d} \alpha(\tau)^{+} \, d\tau, \qquad \text{Eq.(3-40.}a\text{)}$$

$$A^{-} = \int_{0}^{T_d} \alpha(\tau)^{-} \, d\tau. \qquad \text{Eq.(3-40.}b\text{)}$$

The centroids of the positive and negative portions of the signal are then estimated as

$$\Theta^{+} = \frac{1}{A^{+}} \int_{0}^{T_d} \frac{1}{2} [\alpha(\tau)^{+}]^2 \, d\tau, \qquad \text{Eq.(3-41.}a\text{)}$$

$$\Theta^{-} = \frac{1}{A^{-}} \int_{0}^{T_d} \frac{1}{2} [\alpha(\tau)^{-}]^2 \, d\tau. \qquad \text{Eq.(3-41.}b\text{)}$$

The amplitude centroids define the active and passive component's weight-like center and their separation with respect to the mean. The temporal distribution can then be estimated as a weighted quantity, in which the negative centroid Θ^{-} is divided by the sum of both centroids.

$$\omega_{cent} = \frac{\Theta^{-}}{\Theta^{+} + \Theta^{-}}. \qquad \text{Eq.(3-42)}$$

This estimates the balance that exists between the active and the passive phase of the signal, therefore if the signal is temporally asymmetric as shown in Fig. 3.2.b, in which one phase has a longer duration, then this will be reflected in the centroid separation with respect to the mean. In the opposite case where the signal is temporally symmetric as shown in Fig. 3.2.a, then the centroid separation will be equivalent and $\omega_{cent} = 1/2$. In addition, the amplitudinal components can be estimated with the relations presented in Eq.(3-24.a) through Eq.(3-25.b) which depend on σ_{α}^{2} and ω_{cent}. This model allows us to reduce an intricate signal into an equivalent rectangular distribution. As a proof of concept, it is important to verify that this method solves the case of the rectangular pulsed signal. The positive and negative parts of a mean centered rectangular signal can be defined as

$$\alpha(\tau)^{+}_{Rect} = \begin{cases} \varepsilon^{+} & \text{if } \alpha(\tau) - \bar{\alpha} > 0 \\ 0 & \text{otherwise} \end{cases}, \qquad \text{Eq.(3-43.}a\text{)}$$

$$\alpha(\tau)^{-}_{Rect} = \begin{cases} \varepsilon^{-} & \text{if } \alpha(\tau) - \bar{\alpha} < 0 \\ 0 & \text{otherwise} \end{cases}. \qquad \text{Eq.(3-43.}b\text{)}$$

These can then be used to evaluate the respective centroids defined in Eq.(3-41) which yield the following

$$\Theta^{+}_{Rect} = \frac{\varepsilon^{+}}{2}, \qquad \text{Eq.(3-44.}a\text{)}$$

$$\Theta^{-}_{Rect} = \frac{\varepsilon^{-}}{2} \, . \qquad \text{Eq.(3-44.}b\text{)}$$

These definitions can be plugged into Eq.(3-42), and the temporal distribution for a Rect function is then expressed as

$$\omega_{Rect} = \frac{\varepsilon^{-}}{\varepsilon^{+} + \varepsilon^{-}} \, . \qquad \text{Eq.(3-45)}$$

Alternatively and in a straightforward manner, the temporal distribution can be solved by equating the positive and negative areas respectively above and below the mean,

$$0 = \ \omega\varepsilon^{+} - \ (1-\omega)\varepsilon^{-}. \qquad \text{Eq.(3-46)}$$

and solving for the temporal distribution results in the same expression as in Eq.(3-45). Although the proof of concept is simple in nature, it shows that the centroid estimation method appropriately estimates the temporal distribution of a rectangular function. However, the goal is to approximate ω for any arbitrary function. The dynamic bias can then be estimated from Eq.(3-26.b) based on the signal variance σ_{α}^{2} and the obtained value of ω.

In practice, the dynamic bias was typically calculated using the expression in Eq.(3-22) originally derived by Harms [58] which only requires the signal's variance as an input. Nevertheless, this expression considered symmetry of the amplitudinal displacement in relation to the mean and neglects the influence that the temporal distribution has on the dynamic bias. In contrast, the proposed model now incorporates the temporal aspect to predict this error more accurately. The temporal distributions of the previously modulated signals were estimated using the centroid method, the dynamic bias was then calculated using Eq.(3-26.b). Next, we subject Harms's model and the proposed model to a 1:1 comparison in relation to the ideal error, this is assessed for the three types of signals using a contrast attenuation value of $\lambda = 2$. The results of Harms's model are plotted against the true dynamic bias in Fig. 3.14.a; ideally, the prediction should lie close to the identity line. Similarly, the 1:1 comparison of the ideal and the proposed model is depicted in Fig. 3.14.b. The results show that Harms's predictive model broadly deviates away from the identity line for all three signal types, while the proposed model closely maps the results of the triangular and sinusoidal signals along the identity line, and the results from the rectangular signals match perfectly as it would be expected. Moreover, the model's accuracy can be further evaluated by estimating the root mean square error (RMSE); this parameter quantifies the predictive power of a model in relation to the data samples. We will define the RMSE as

$$RMSE = \sqrt{\frac{1}{N}\sum_{n}^{N}(\Delta\tilde{\alpha}_n - \Delta\alpha_n)^2} \qquad \text{Eq.(3-47)}$$

where $\Delta\tilde{\alpha}$ denotes the implemented model, $\Delta\alpha$ is the ideal dynamic bias, and n denotes the data points in each signal type analyzed. The RMSE was evaluated for various values of λ given that the error increases with this parameter. The results of the three functions are depicted in Fig. 3.15, this reflect how the predictability of Harms's model degrades rapidly with increased λ, while the proposed model remains within 1% for values of λ as large as 3. It is worth mentioning that the proposed model yields an RMSE of zero for the Rect function, meaning that it perfectly estimates the bias for this signal type since it is the basis of the model.

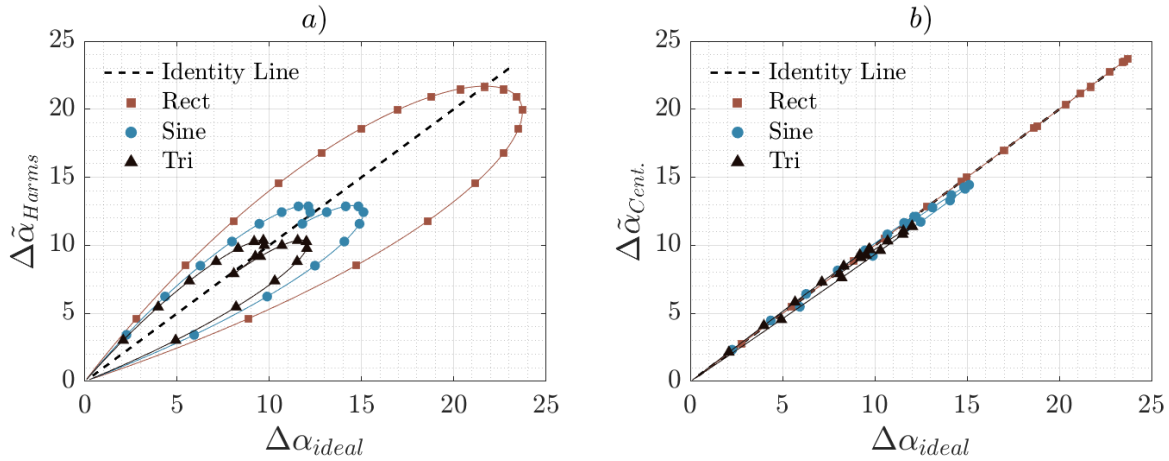

Fig. 3.14. One to one comparison of the ideal dynamic bias with value predicted for *a)* Harms model, and *b)* temporal distribution model.

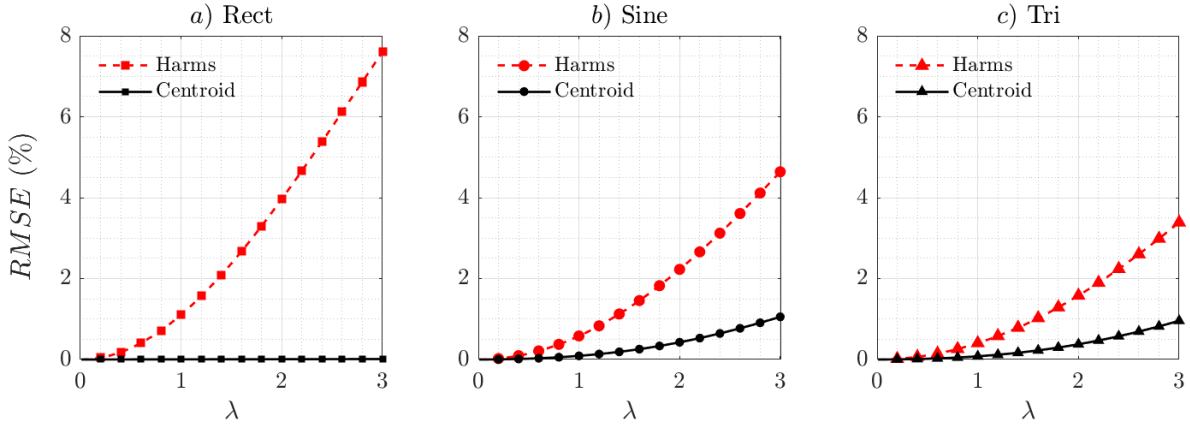

Fig. 3.15. RMSE estimation of Harms's model and proposed model for *a)* Rect, *b)* Sine, and *c)* Tri functions.

3.6. Experimental Signal Analysis

The previous sections describe the progression in which the dynamic bias is defined and tested using simplified temporal signals. However, real life two-phase flows are complex due to their random turbulent behavior. The dynamic bias of experimental two-phase flow signals is analyzed in this section to give an idea of how the radiation transmission function deviates from its ideal behavior for various flow regimes. This is accomplished by converting high-temporal resolution WMS signals along a hypothetical chord into a radiation transmission signal; this procedure was previously implemented by Manera [116] which showed proper agreement between the gamma densometer data and the converted WMS signal. It is important to clarify that WMS signals are used as the reference truth due to their high temporal resolution, on the other hand, actual radiation transmission measurements would have implicitly contained the dynamic bias that is being investigated.

The WMS measures the conductivity of the liquid and gas phases mapped over a plane. The temporal void fraction of the WMS data along the hypothetical chord direction is estimated as

$$\alpha(i,t) = \frac{1}{K}\sum_{k=1}^{K}\left(1-\frac{u_{2\varphi}[i,k,t]-\overline{u}_G[i,k]}{\overline{u}_L[i,k]-\overline{u}_G[i,k]}\right), \qquad \text{Eq.(3-48)}$$

where $\overline{u}_G$ is the average conductivity of the gas-phase , $\overline{u}_L$ is the average conductivity of the liquid-phase, $u_{2\varphi}$ is time dependent conductivity of the two-phase measurement, i and k are the spatially mapped voxels, and t is the measurement time. In the present study, we estimate the void fraction along the centerline where $i = CL$, and is averaged over the pixels along k. The temporal void fraction along the center line is then input into Eq.(3-12) to simulate radiation transmission measurement of the ideal function. The current study focuses on a 1-D arrangement for a point-source and point-detector system. Admittedly, advanced radiation-based systems such as computed tomography and radiography systems are spatially complex, these require expanding the modeling process of multiple individual detectors representative of these geometries, however this would be a topic for future investigations.

The present research deploys the WMS data belonging to the TOPFLOW facility benchmarked database obtained and reported by Lucas et al. [112, 113], the representative flow regimes for this database are highlighted in Fig. 3.16. To briefly summarize, the TOPFLOW facility consists of a nominally 195.3 mm diameter and 8.0 m in length vertical steel pipe. The facility contains 6 injection layers which are logarithmically spaced away from the WMS plane located in the upper plenum of the facility, each injection layer is composed of 32 evenly distributed orifices characterized by a 4.0 mm diameter; the corresponding

L/D relative injection distances away from the WMS are [1.4, 2.8, 7.7, 13, 22.9, 39.7]. The facility's operational (absolute) pressure is 0.25 MPa. The WMS is characterized by a 64x64 wire arrangement with a pitch of 3.0 mm between adjacent wires, and a gap distance of 2.0 mm between the transmission and the perpendicular-receptor layers. The WMS data acquisition was performed with a 2.5 kHz sampling frequency for a duration of 10 seconds. The data used in this study belongs to three flow regimes and one transitional flow; these are bubbly, bubbly to churn turbulent, churn turbulent, and wispy annular flow reported by Lucas. The selected datasets corresponds to those with a reported liquid superficial velocity of 1.017 m/s and with varying superficial gas velocity of [0.037, 0.14, 0.534, 2.038] m/s in respective order of ascending flow regimes; Table 3.1 summarizes the selected data sets used in the present study and these are highlighted in Fig. 3.16. The dynamic bias behavior for the hypothetical transmission system was estimated by using sampling periods divisible by the original experimental sampling period, this being 0.4 ms. The radiation transmission was simulated along the centerline of the pipe, therefore integrating the spatial void fraction data of the WMS along this chord-length. In this section, the dynamic bias will be normalized by the contrast attenuation factor λ, mindful that the maximum dynamic bias scales predominantly linearly in relation to $\lambda < 2$, nevertheless, at large values the behavior deviates from the linear growth. The contrast attenuation factor λ for this facility would correspond to a value of 1.71 for a ^{137}Cs isotopic-source, 1.91 for a ^{192}Ir isotopic-source, and 4.07 for an x-ray source. The integration period required to reach 90% of the asymptotic dynamic bias buildup value will also be reported for each flow regime in order to give perspective of the corresponding dynamic bias build time.

Table 3.1. WMS data sets matrix obtained from Lucas et al. [112, 113].

Case	Identifier	Regime	j_L [m/s]	j_G [m/s]	Sampling Frequency [kHz]
1	074	Bubbly	1.017	0.037	2.5
2	107	Bubbly to Churn Turbulent	1.017	0.14	2.5
3	140	Churn Turbulent	1.017	0.534	2.5
4	173	Wispy Annular	1.017	2.038	2.5

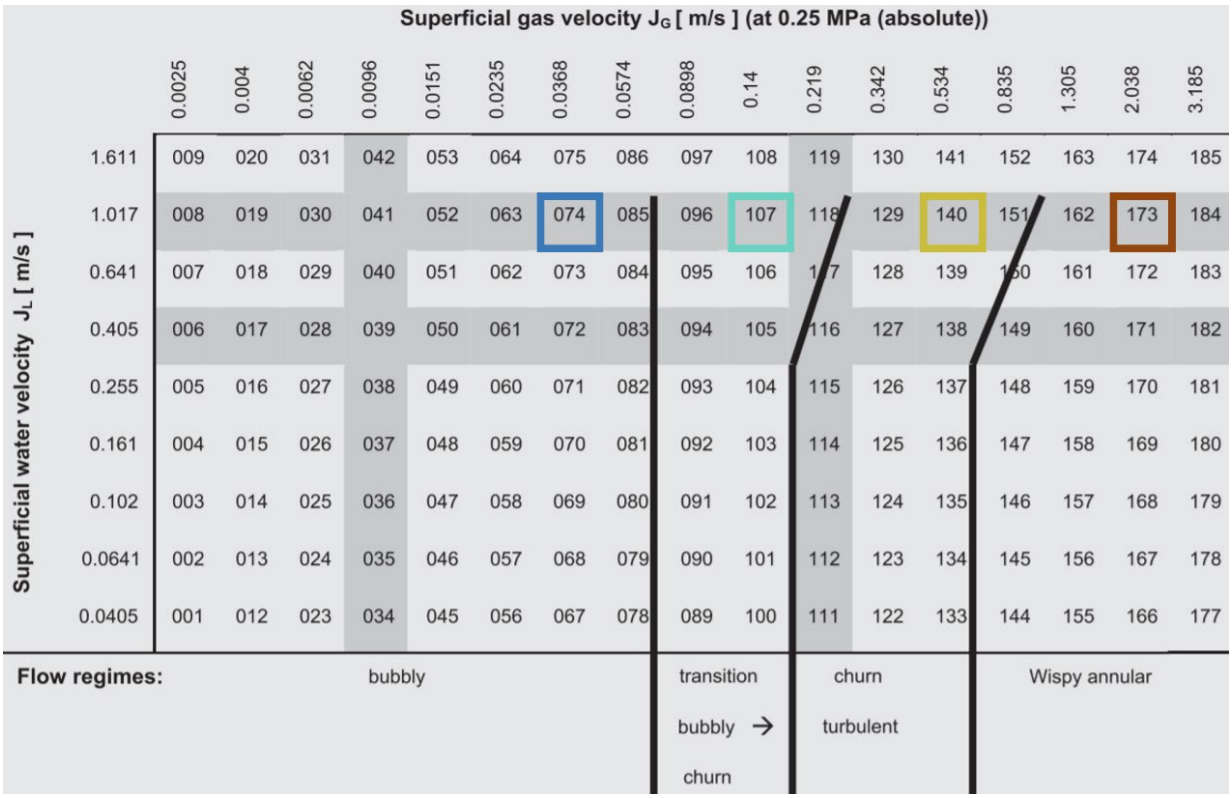

Fig. 3.16. TOPFLOW database obtained from and reported by Lucas et al. [112, 113]; highlighted are the selected datasets for bubbly, bubbly to churn turbulent, churn turbulent, and wispy annular.

3.6.1. Bubbly Flow

The first regime of interest is the bubbly flow, with a low superficial gas velocity of 0.037 m/s and a relatively low average void fraction. The parameters of interest are tabulated in Table 3.2, and are shown in Fig. 3.17; the time-average spatial void fraction with the black plane representing the transmission centerline are shown in plot *a*, the centerline temporal void fraction is plotted in *b*, and the dynamic bias build up curves is plotted in *c* for the various L/D. The spatial void fraction visualizes how the gas is injected and remains near the wall with a slow cross migration towards the center of the pipe; full migration is accomplished at the last measurement length $L/D = 39.7$. The temporal void fraction signals are characteristically noisy due to the bubble size and quantity, best depicted by the temporal centerline void fraction. The standard deviation has a gradual increase in relation to the injection length with a max value of 3.67% at L/D equal to 39.7. The normalized dynamic bias has a slight increase from the nearest to the furthest measurement length, however it is too small to attribute it to any effect. The values of $\Delta\alpha/\lambda$ are consistently small, below 0.1%, which can be considered negligible. The dynamic bias buildup period ranges

from 58 ms to 141 ms at most from the obtained results, these correspond to sampling frequencies of 17.24 Hz and 7.08 Hz respectively; The results show that the buildup of the bias is relatively fast, however it becomes slower at the injection lengths L/D of 7.7 and 13; this is perhaps aided as the gas migrates towards the center of the pipe and the flow evolves.

Table 3.2. Bubbly Flow

Parameters	L/D	**1.4**	**2.8**	**7.7**	**13**	**22.9**	**39.7**
Centerline Avg. Flow	**Avg. Void Fraction** $\overline{\alpha}_{CL}$ [%]	2.29	1.90	2.26	2.82	4.47	6.57
	STD. $\sigma_{\alpha,CL}$ [%]	3.04	2.90	3.07	3.15	3.59	3.67
Dynamic Bias	**Norm. Asymptotic** $\Delta\alpha/\lambda$ [%]	0.04	0.04	0.05	0.04	0.06	0.07
	90% Build-up Int. Period T [ms]	58	82	135.2	141.2	76	88
	Equivalent Sampling Freq. f [Hz]	17.24	12.2	7.4	7.08	13.16	11.36

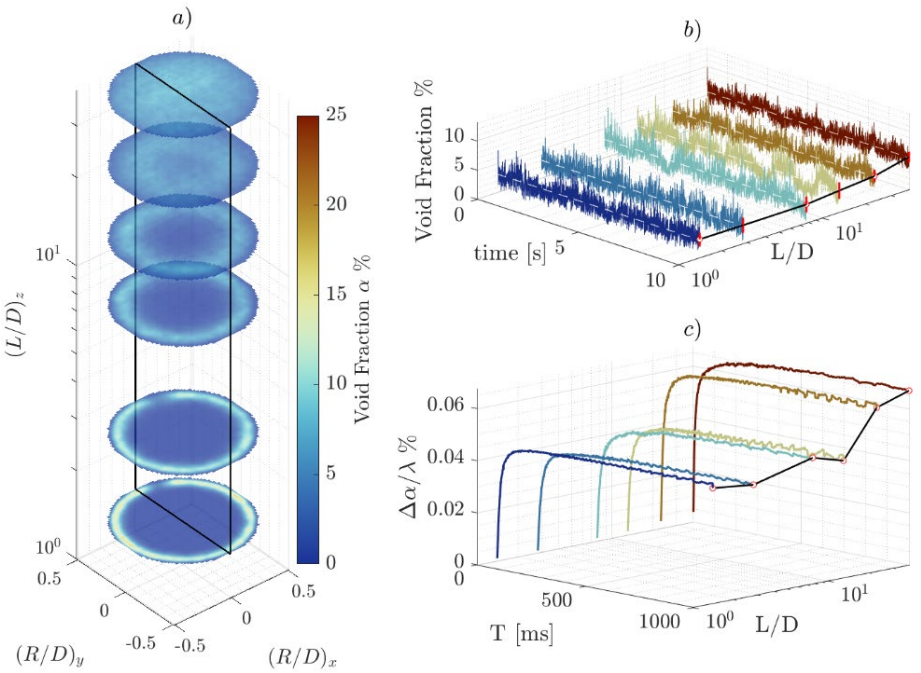

Fig. 3.17. Analysis of bubbly flow regime: *a)* time-average spatial void fraction, *b)* temporal centerline void fraction, and *c)* dynamic bias build-up curves.

3.6.2. Bubbly to Turbulent Churn Flow

The transitional regime from bubbly to turbulent churn has a gas superficial velocity of 0.14 m/s; the flow analysis is shown in Fig. 3.18 and reported in Table 3.3. The flow spatial progression shows a faster void fraction cross migration towards the center of the pipe, with a fully transitioned parabolic profile at L/D equal to 22.9. The centerline average void fraction shows an overall increase from 10.15% to 23.10%. The standard deviation increases from 5.06% for the nearest injection length to 7.89% for the furthest injection length, with the largest value located at L/D equal to 22.9. This effective increase in the standard deviation occurs as the sharp peaks depicted by the temporal centerline void fraction become more prominent at increased L/D. The normalized dynamic bias $\Delta\alpha/\lambda$ increases from 0.13% for the nearest length to 0.31% for the furthest length. The buildup integration period ranges from 88 ms to 221 ms, which correspond to sampling frequencies of 11.36 Hz to 4.52 Hz respectively. The results show that the buildup is the fastest at the smallest L/D, and the buildup of this error tends to get slower with increase in development length.

Table 3.3. Bubbly to Churn Turbulent

Parameters \ L/D		**1.4**	**2.8**	**7.7**	**13**	**22.9**	**39.7**
Centerline Avg. Flow	**Avg. Void Fraction** $\overline{\alpha}_{CL}$ [%]	10.05	12.90	17.79	17.56	20.74	23.10
	STD. $\sigma_{\alpha,CL}$ [%]	5.06	5.49	6.51	7.24	8.05	7.89
Dynamic Bias	**Norm. Asymptotic** $\Delta\alpha/\lambda$ [%]	0.13	0.15	0.21	0.27	0.34	0.31
	90% Build-up Int. Period T [ms]	88	178.8	159.2	182.8	187.2	221.2
	Equivalent Sampling Freq. f [Hz]	11.36	5.59	6.28	5.47	5.34	4.52

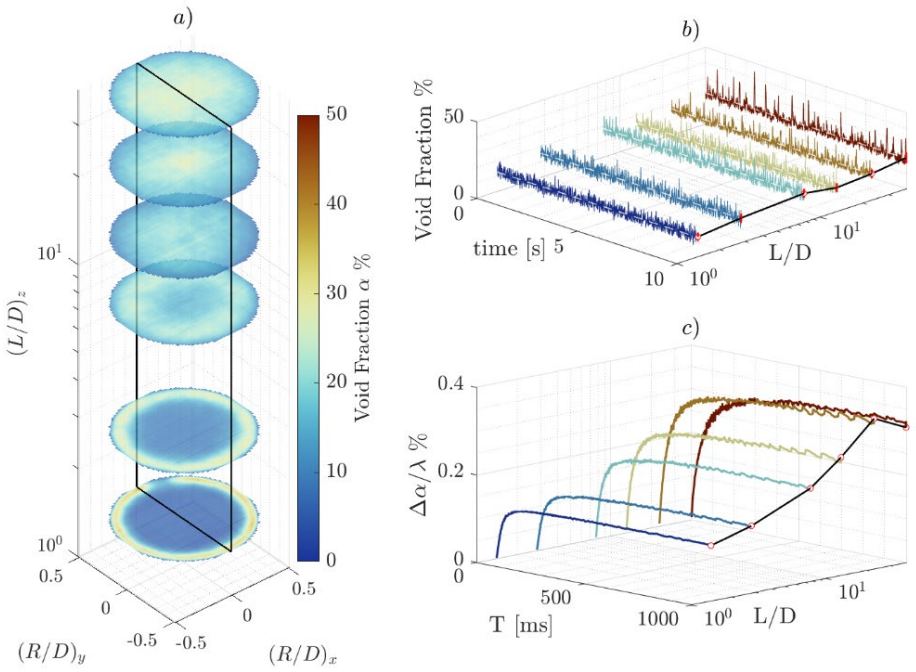

Fig. 3.18. Analysis of transition from bubbly to turbulent churn regime: *a)* time-average spatial void fraction, *b)* temporal centerline void fraction, and *c)* dynamic bias build-up curves.

3.6.3. Turbulent Churn Flow

The second regime of interest is the fully transitioned turbulent churn flow with a gas superficial velocity of 0.534 m/s; the analysis is shown in Fig. 3.19 and tabulated in Table 3.4. The time-average spatial void fraction shown in *a*) depicts how the gas phase has an increased cross migration at L/D of 7.7. The centerline void fraction steadily increases from 12.38% from the nearest length to 44.56% at the furthest length along the centerline, the standard deviation increases from 6.06% to 11.02% respectively representing a surge in fluctuations with increased distance, best depicted by the temporal centerline signal shown in Fig. 3.19.*b*. The value of $\Delta\alpha/\lambda$ increases from 0.19% for the nearest length to 0.61% for the furthest length, with its maximum value of 0.71% located at an L/D of 22.9. The dynamic bias buildup integration period ranges from 95 ms to 196 ms, corresponding to sampling frequencies of 10.5 Hz and 5.1 Hz. The buildup is faster near the closest injection length, and tends to get slower with increased injection length distance L/D.

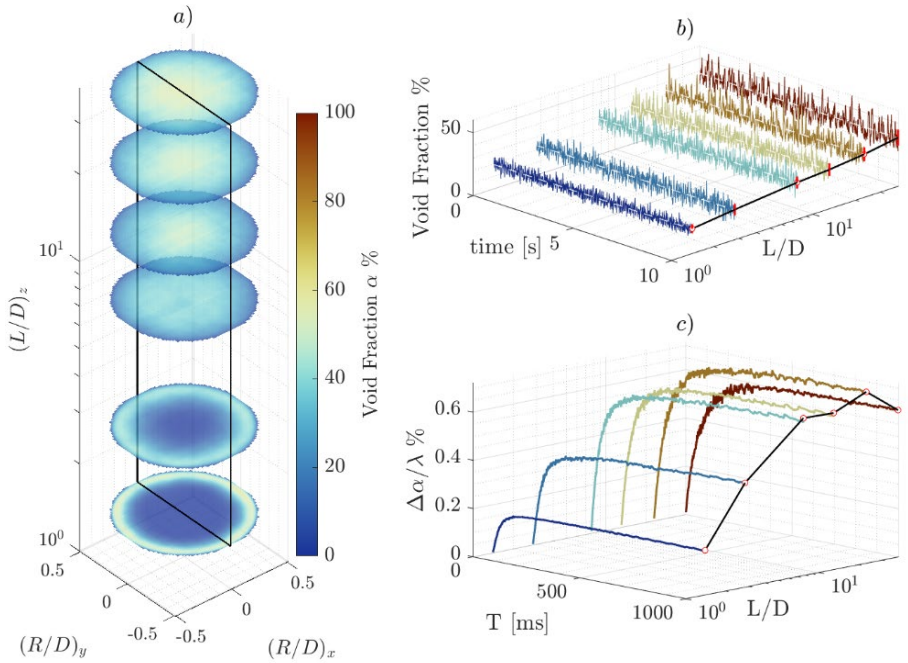

Fig. 3.19. Analysis of turbulent churn regime: a) time-average spatial void fraction, b) temporal centerline void fraction, and c) dynamic bias build-up curves.

Table 3.4. Churn Turbulent

Parameters \ *L/D*		**1.4**	**2.8**	**7.7**	**13**	**22.9**	**39.7**
Centerline Avg. Flow	**Avg. Void Fraction** $\overline{\alpha}_{CL}$ [%]	12.38	16.94	33.94	38.74	41.46	44.56
	STD. $\sigma_{\alpha,CL}$ [%]	6.06	9.22	11.20	11.27	11.77	11.02
Dynamic Bias	**Norm. Asymptotic** $\Delta\alpha/\lambda$ [%]	0.19	0.43	0.65	0.65	0.71	0.61
	90% Build-up Int. Period T [ms]	95.2	155.2	158	156	176	196
	Equivalent Sampling Freq. f [Hz]	10.5	6.44	6.33	6.41	5.68	5.1

3.6.4. Wispy Annular Flow

The last regime investigated was the annular flow with a gas superficial velocity of 2.038 m/s; the results are presented in Fig. 3.20 and tabulated in Table 3.5. The spatial void fraction shown in *a*) further demonstrate how the gas phase promptly migrates towards the center of the pipe at L/D equal to 7.7. The centerline average void fraction increases from 39.89% at the nearest length to 70.32% at the furthest length, and the standard deviation ranges from 6.70% to 8.24%. The normalized dynamic bias $\Delta\alpha/\lambda$ varies across the measurement lengths from 0.22% at the nearest length to 0.32% at the furthest length, with the largest value of 0.34% at L/D equal to 2.8. The buildup integration period is 145.2 ms for the nearest length and 235.2 ms for the furthest length, corresponding to sampling frequencies 6.9 Hz and 4.25 Hz respectively. Similar to the previous flow regimes, the buildup is the fastest at the nearest injection length and tends to become slower with increase in injection length. This flow regime has overall the slowest buildup in comparison to the other flow regimes.

Table 3.5. Wispy Annular Flow

Parameters \ L/D		**1.4**	**2.8**	**7.7**	**13**	**22.9**	**39.7**
Centerline Avg. Flow	**Avg. Void Fraction** $\overline{\alpha}_{CL}$ [%]	39.89	46.04	65.22	66.65	68.95	70.32
	STD. $\sigma_{\alpha,CL}$ [%]	6.70	8.26	7.62	7.81	7.55	8.24
Dynamic Bias	**Norm. Asymptotic** $\Delta\alpha/\lambda$ [%]	0.22	0.34	0.28	0.29	0.28	0.32
	90% Build-up Int. Period T [ms]	145.2	234	156	238	227.2	235.2
	Equivalent Sampling Freq. f [Hz]	6.89	4.27	6.41	4.2	4.4	4.25

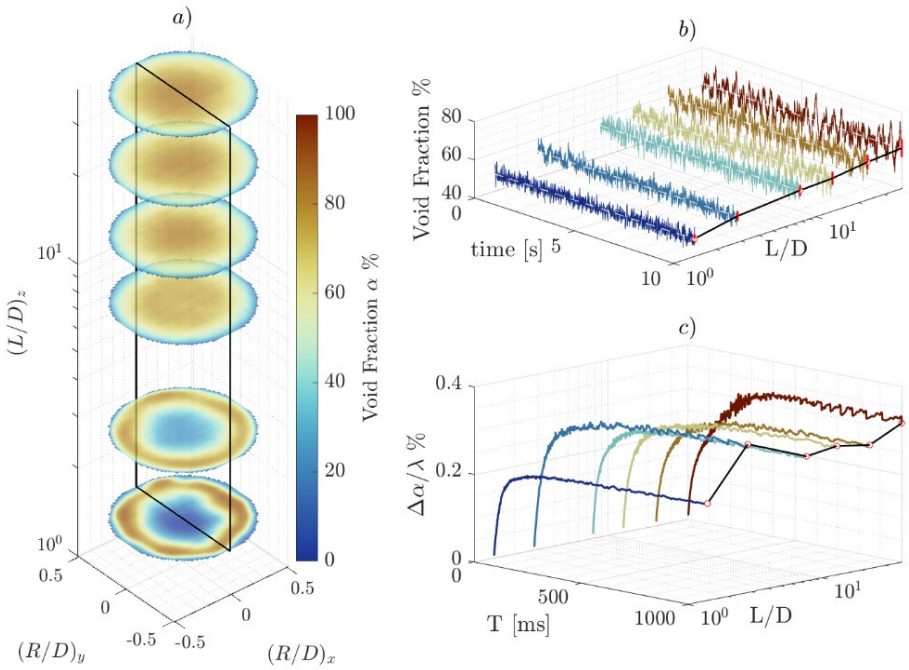

Fig. 3.20. Analysis of annular flow regime: *a)* time-average spatial void fraction, *b)* temporal centerline void fraction, and *c)* dynamic bias build-up curves.

3.6.5. Signal Characteristics

To develop a more accurate dynamic bias expression, a method was formulated in Section 3.5.4 to simplify complex signals into a two-component rectangular signal model which preserves the original signal's average void fraction and variance. Applying this simplification method, the active and passive amplitudinal displacement parameters can be derived which quantify how the active and passive phases deviate from the average; as a reminder to the reader, these are denoted as ε^+ and ε^- respectively. The temporal distribution ω describes the fraction of time in which the signal is active, while $(1-\omega)$ dictates the fraction of time the signal is in the passive phase. In this section we further analyze the results obtained for the WMS data across different flow regimes.

The relation between the signal variance and the average void fraction is shown in Fig. 3.21.*a)*. Here the general trend shows an increase in variance with increase in average void fraction for the regimes ranging from bubby to churn turbulent flow, however, the variance does not significantly change for the annular regime. Fig. 3.21.*b)* compares the active and passive amplitudinal components, in which the identity line represents equidistant or symmetric conditions between these components. The bubbly and bubbly to churn turbulent flows are characterized by their prominent active amplitudinal component, the churn turbulent flow falls closer to the identity line yet favors the active component, while the annular regime lies around

the identity line and is observed to have slightly more prominent passive components. Fig. 3.21.*c)* depicts the temporal portion of the active component and compares it to the void fraction. The clusters representing the different regimes show that the temporal distribution does not significantly change, except in the case of the bubbly flow regime which does show an overall increase in active phase duration. Overall, the regime progression shows a tendency to approach a symmetric temporal and amplitudinal distribution. Lastly, Fig. 3.21.*d)* compares the areas underneath the active phase and passive phase; the addition of these areas represents the average void fraction, therefore it quantifies which phase has the most significant contribution. As it would be expected, the active phase is consistently the primary void fraction source; nevertheless, the data for bubbly to churn turbulent regimes also shows that there is equitable contributions between the active and passive phases for this regime.

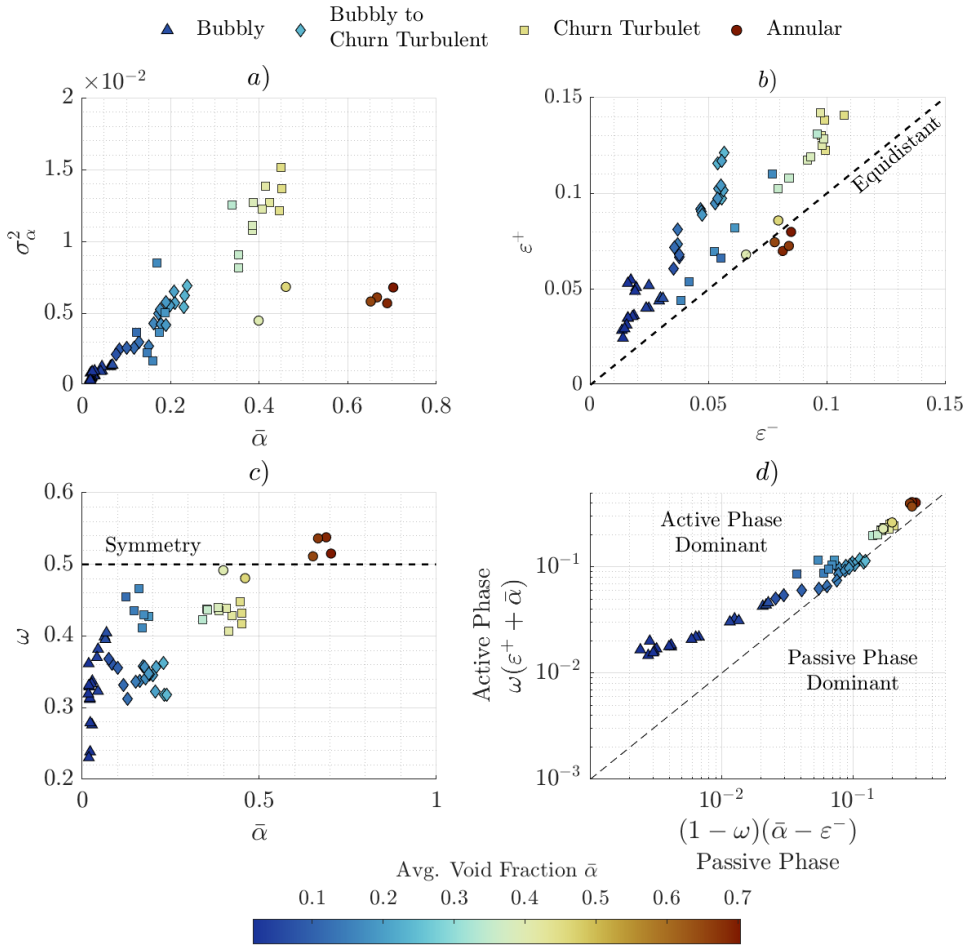

Fig. 3.21. Experimental signal characteristics and components derived from the temporal distribution model. *a)* variance vs average void fraction, *b)* active and passive amplitudinal displacements, *c)* temporal distribution vs average void fraction, and *d)* equivalent active vs passive void fraction areas.

The objective of this discussion is to add another layer of understanding to the phenomena being investigated. Generally, the standard deviation of the signal quantifies the spread of the data away from the mean and whose bounds are typically assumed to be symmetric. However, there are instances where these fall out of range and do not fully capture the characteristics of the signal. Here we introduce additional components which enhance in a simple manner the analysis of these complex signals.

3.6.6. Dynamic Bias Results

The relation between the dynamic bias and the centerline variance for the investigated flow regimes are shown in Fig. 3.22 for a $\lambda = 1$; the regimes are identified by individual markers and the color represents the average void fraction of the centerline signal. The dynamic bias strongly follows a linear scaling in relation to the signal's variance, the magnitude of all the signals analyzed remains below 1% for $\lambda = 1$; however, considering the turbulent churn regime and based on the scaling of the TOPFLOW paired with a ^{137}Cs isotopic-source can result in a void fraction error of ~1.3% and an x-ray source can result in a ~3.3% error.

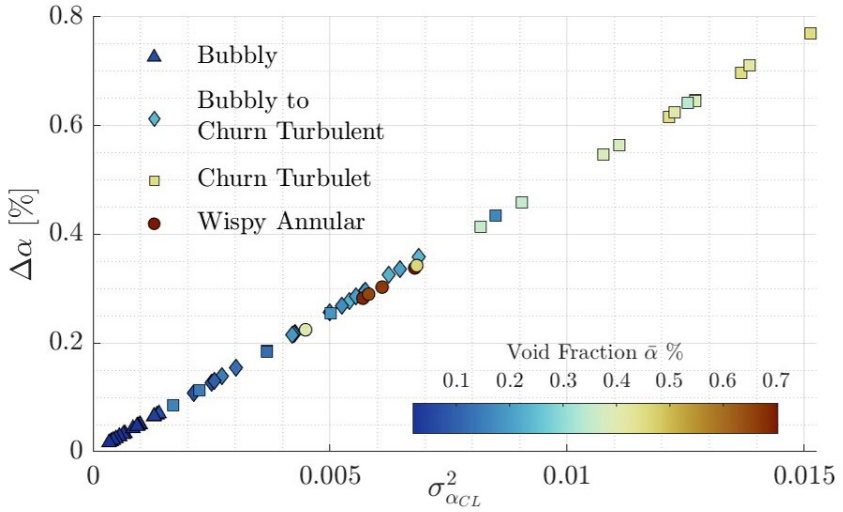

Fig. 3.22. Dynamic bias relation to the experimental signal variance for λ=1.

The analysis comparing the ideal dynamic bias to Harms's model and the proposed temporal distribution model are shown for each flow regime in Fig. 3.23; Harms's model is shown as the red scatter dots, while the proposed model is shown in the black scatter dots, these are plotted along with the bias identity line. The results show that both models lie near the identity line, the proposed model falls closer to the identity line, this is most noticeable in the bubbly to churn turbulent and churn turbulent regimes; this is further shown in zoomed plots of the bubbly regime shown in Fig. 3.23.*a*. Analogous to the analysis

performed in section 3.5.4 the RMSE was also estimated to compare the models prediction as a function of contrast attenuation factor λ for the studied flow regimes, the results are presented in Fig. 3.24. The RMSE grows exponentially with λ, nevertheless it is considerably small throughout the flow regimes analyzed. However, comparing Harms's model and the proposed model shows that the latter has higher accuracy given that its RMSE magnitude is consistently below Harms's model for all cases. the RMSE percentage decrease for the proposed model relative to Harm's for the range of λ improves by 50% to 58% for the bubbly regime, 40% to 59% for the bubbly to churn transitional regime, 36% to 56% for the churn regime, and 15% to 56% for the wispy annular. This affirms that approximating the temporal distribution of the flow improves the estimation of the dynamic bias.

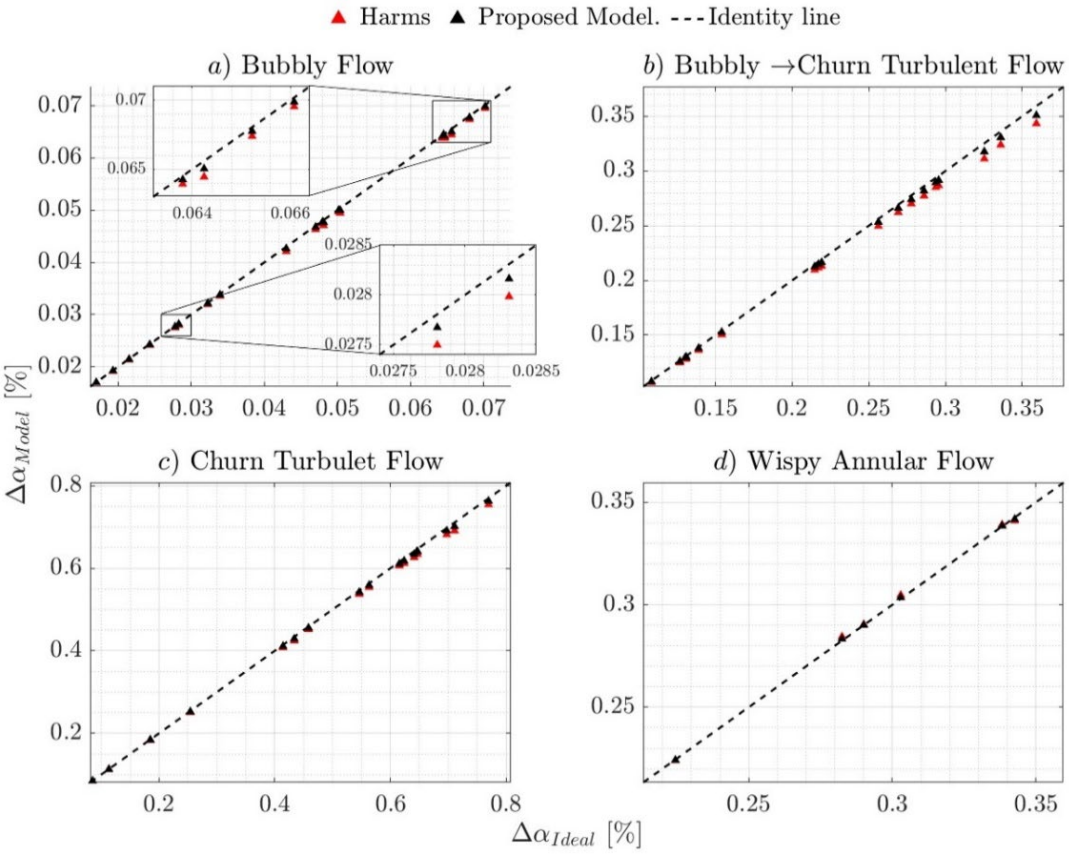

Fig. 3.23. One to one comparison between the ideal dynamic bias, Harms's model, and the proposed model for *a)* bubbly flow, *b)* bubbly to churn turbulent flow, *c)* churn turbulent flow, and *d)* annular flow.

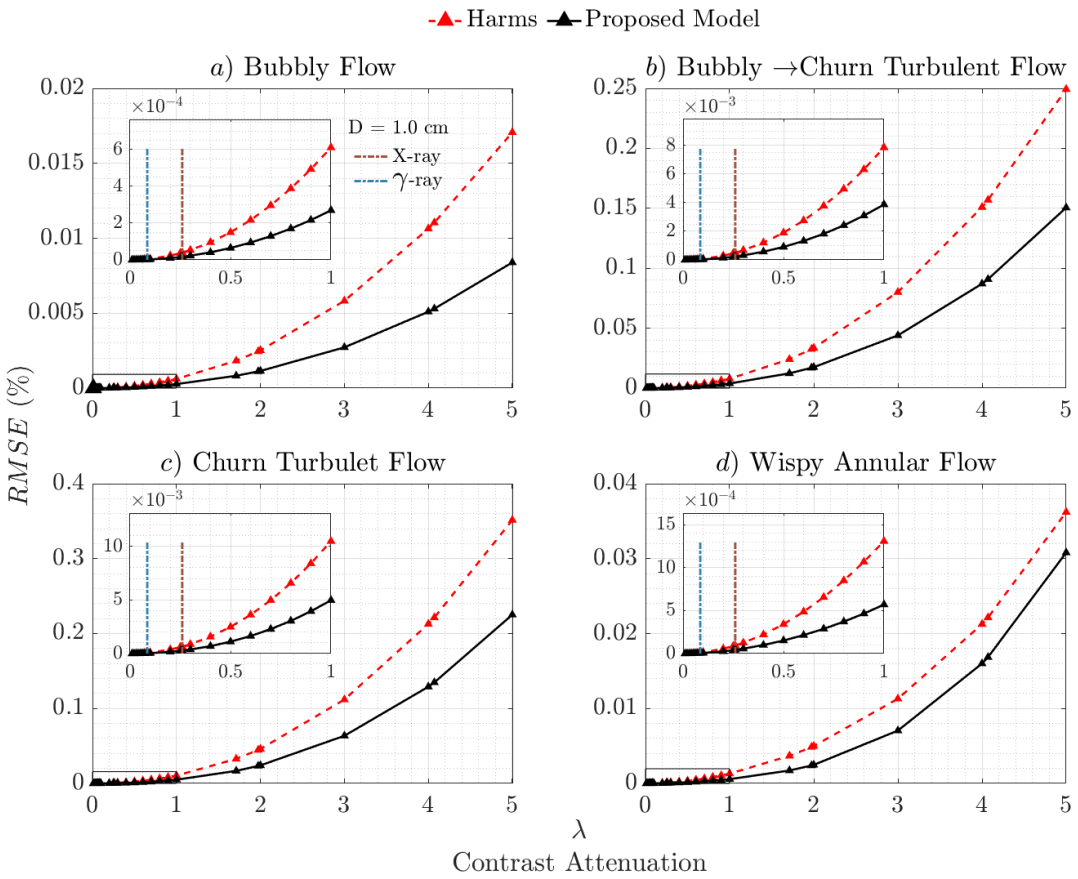

Fig. 3.24. RMSE estimation of Harms's model and proposed model for *a)* bubbly flow, *b)* bubbly to churn turbulent flow, *c)* churn turbulent flow, and *d)* annular flow.

3.7. Summary of Findings

The current chapter demonstrates that the dynamic bias in void-fraction measurements carried out using radiation transmission techniques is caused by an error build-up that occurs in the temporal integration of a time-varying exponential transmission function intrinsic to radiation detection measurements postprocessing. A new analytical expression was derived based on rectangular pulses. This new definition considers the effects that the temporal distribution ω, the amplitudinal distribution ξ, and the attenuation contrast factor λ have on the dynamic bias; the last parameter is determined by the radiation crossing length through the flow region, as well as the liquid and gas linear attenuation coefficient. The dynamic bias expression previously derived by Harms et al. [58] only focused on the amplitudinal component and assumed temporal symmetry, this expression is also encompassed in the new analytical definition. The rectangular pulse model serves as an exaggerated example due to its abrupt changes in signal value, however, it serves as the ideal function to characterize the behavior, evolution, and the outermost

limits of the dynamic bias. In addition, an expression for the critical temporal distribution which yields the largest dynamic bias was derived; this expression can be helpful in determining an experimental facility's susceptibility to the dynamic bias.

Next, numerical modeling following radiation transmission of simple void fraction signals was used to validate the methodology; the signals used include rectangular, sinusoidal, and triangular shaped pulses which were manipulated by modifying the duty cycle or full width half max such that it yields the predetermined average void fraction. The dynamic bias was then estimated from the simulated transmission signals, the detector integration window was varied in relation to the signal period. This showed that the dynamic bias builds up whenever the detector integration period is smaller than the phenomena period, and it reaches an asymptotic value when the detector period becomes significantly larger than the phenomena period. The build-up is shown to be reduced at fast sampling rates, given that under these conditions the flow appears to be stationary in respect to the measurement period. However, in radiation transmission measurements this is not always possible given that one must strike a balance between radiation counting statistics and temporal resolution. The asymptotic values of the dynamic bias obtained using 50% void fraction applied to the rectangular and sinusoidal signals matched to those reported by Andersson et al. [9] which validates the numerical modeling performed in this study. Additionally, the results obtained from the rectangular pulsed signals match the analytical results previously derived.

A method was developed to simplify arbitrary signals into an equivalent rectangular two-component model which preserves the average void fraction and the original signal's variance; the two-components refer to an active phase and a passive phase. The goal was to approximate the temporal distribution of the signal and from this, estimate the dynamic bias from the previously derived analytical expression. The dynamic bias prediction was compared for the three simplified signals between Harms's model and the proposed model. The results showed improvement in the dynamic bias prediction by the proposed model, which reinforces the importance of including the effects that the temporal distribution has on the dynamic bias.

In addition, experimental signals for bubbly, churn turbulent, and wispy annular flow regimes obtained from the TOPFLOW facility [112, 113] using WMS sensors were used as basis to simulate realistic radiation transmission measurements of said flow regimes, and the associated dynamic bias was analyzed. The dynamic bias was less than 1% at a contrast attenuation factor of $\lambda = 1$ for the experimental flow regimes analyzed; the churn turbulent flow regime had the largest bias due to its inherently larger signal fluctuation.

The values of TOPFLOW facility's contrast attenuation factor λ are 1.71 for a ^{137}Cs isotopic-source, and 4.07 for an x-ray source; this can result in a bias magnitude of ~1.3% for a ^{137}Cs and ~3.3% for an x-ray source. Harms's and the proposed models were used to predict the dynamic bias of the experimental signals; the results found both models to have adequate performance, with the proposed model consistently presenting more accurate results. The 90% bias buildup period for the bubbly regime ranged from 58 ms to 141 ms, for the bubbly to churn turbulent transition was 88 ms to 221 ms, for the churn turbulent regime it was 95 ms to 196 ms, and for the wispy annular regime it was 145 ms to 238 ms; the fast buildup occurs at short injection lengths where the flow has not fully developed, this error tends to buildup slower at further injection distances in which the flow has been fully developed. It is also worth noting that the fast-range buildup becomes slower as the flow conditions transition from bubbly to wispy annular. Although the dynamic bias was not significant for the experimental signals analyzed, it is recognized that transient plug flows with large variance can increase the influence of the dynamic bias.

CHAPTER IV

X-Ray Measurement Methods of Two-Phase Flow in Cylindrical Geometry

Nomenclature

Roman Variables

C	Constant or detector centerline
D_L	Left edge on detector plane
D_R	Right edge on detector plane
d	Distance
E	Energy
e_z	Unit-vector component in z
I	Source intensity/activity
L	Crossing length
M	Mass
r	Radial variable
T	Temperature
t	Temporal axis
V	Volume
v	Velocity
w	Weighted value
$\boldsymbol{x}$	Spatial location
z	Vertical axis

Greek Variables

α	Void fraction
β	Sum of weights
Γ	Thermal correction factor
δ	Material thickness
ε	Coefficient of thermal expansion
μ	linear attenuation coefficient
μ/ρ	Mass attenuation coefficient
ρ	Density
σ_x^2	Variance of variable x
Φ	Vertical correction angle
ψ	Fan angle
Ω	Radial correction angle

Subscripts & Superscripts

2φ	Two-phase flow
φ	Single phase
Air	Air filled
BH	Beam-hardening
$bias$	Biased condition
d	Detector
$edge$	Cross sectional edge

$Flow$	Flow region
G	Gas
H_2O	Water
i	Pixel index
$ideal$	Ideal condition
in	Incoming trace
L	Liquid or left-side
LB	Lower bound
m	Material
max	Maximum
min	Minimum
o	Original location or calibration condition
out	Outgoing trace
p	pipe, test section
R	Right side
s	Source
sd	Source-detector
so	Source-object
T	Temperature
UB	Upper bound
z	Vertical indexing

4.1. Overview

The following research aims to provide the necessary instrumentation and analysis tools to bridge the existing gap in two-phase flow data pertaining to the regimes covering inverted annular film boiling (IAFB), inverted slug film boiling (ISFB), through dispersed flow film boiling (DFFB). The analysis of these regimes presents inherit difficulties due to the high-temperature and high-pressure conditions required to achieve them. Said conditions affect the efficacy and performance of conventional instrumentation given that these are typically intrusive in nature (i.e. WMS, and needle probes). The need for a high-resolution database of these regimes was postulated in section 1.4. The post-CHF heat transfer (PCHT) test facility, designed and built by Dr. Qingqing Liu [108], intends to simulate these unprecedented conditions to ultimately characterize and obtain useful correlation of the aforementioned flow regimes. In the present research high-speed x-ray radiography is deployed to perform non-intrusive measurements of the PCHT facility. The main goals of the present research is to assess the majority of identified challenges of x-ray measurements applied to these particular experimental conditions, to develop and validate void fraction analysis methods, and lastly to apply these methods to the high-speed x-ray radiography measurements.

4.2. Materials and Methods

4.2.1. PCHT Experimental Facility

The purpose of post-CHF Heat Transfer (PCHT) test facility is to curate a detailed database of the two-phase flow regimes ranging from the IAFB to DFFB for the improvement of hydrodynamic and heat transfer models deployed in best-estimate thermal-hydraulic system codes. Preliminary studies on the feasibility and application of x-ray measurements for the PCHT facility were demonstrated by Adams et al. [1]. The PCHT facility is depicted in Fig. 4.1 and the individual components of the flow loop are summarized in the following:

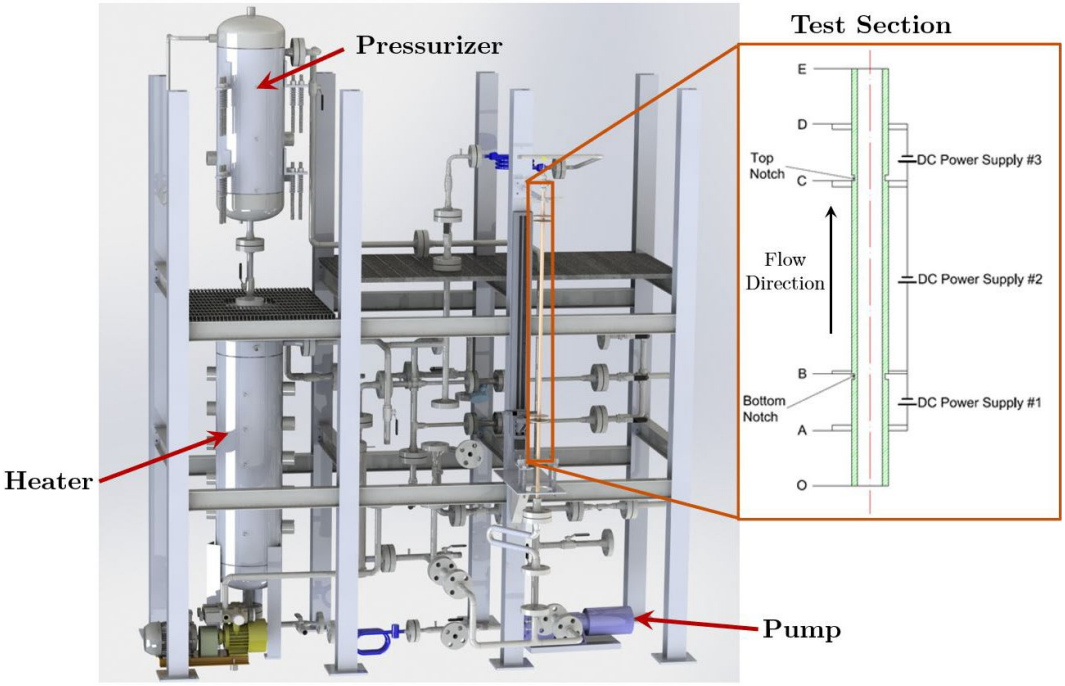

Fig. 4.1. PCHT experimental facility design by Liu et al. [108].

- **Reservoir/Heater** – this tank approximately holds 0.115 m^3 of storage capacity. It contains 10 heaters tasked with raising the bulk liquid temperature and degassing.
- **Pressurizer** - regulates the overall pressure of the flow loop and maintains the inlet working fluid in a liquid phase state.
- **Circulation Pump** – a centrifugal pump that directs the fluid towards the test-section.
- **Pre-Heater** – fine tunes the desired inlet temperature of the liquid prior to entering the test section.

- **Test Section** – this consists of a vertical 1.55 m long Incoloy-800H cylindrical tube with an inner diameter of 12.95 mm, a wall thickness of 3.05 mm, and is encased in silicon-based microporous insultation; the test section is subdivided into a bottom notch, a middle section, and a top notch. Three DC-power supplies are connected to the three sections, these apply a maximum current of 2.5 kA and a power of up to 34 kW to the heated section; this results in a controlled heat flux application into the test section. The flow direction is directed upward against the direction of gravity. Thermocouples have been welded to the outer surface of the test section to monitor the temperature.

- **Condenser** – this device is located at the outlet of the test section and is in charge of removing heat in order to condense the generated vapor into liquid such that it can be redirect it to the reservoir.

The presented descriptions summarize the primary components of PCHT facility, the test facility is explained in great detail in [109 - 111]. Nevertheless, as one can imagine, this is a fairly complex experiment with additional features and whose operational procedures are best elaborated by Liu [108].

4.2.2. High-Speed Radiography Imaging Setup

The PCHT contains a separate gantry frame system which mounts the high-speed x-ray imaging system. This gantry frame allows the imaging system to be displaced along the vertical direction of the test section. The radiation source is a standard medical x-ray tube with a tungsten anode depicted in Fig. 2.36, the equipment is rated up to 150 keV, and a max current of 500 mA. The detector imaging system consists of high-resolution CdTe detector panel with an effective detection area of 25.6 x 204.8 mm^2 and detector crystals with an active area of 100x100 μm^2. The source-detector distance, d_{sd}, was 1.230 m and the source-object distance d_{so} was 0.832 m, resulting in an estimated object magnification of about 1.48. The radiography imaging system geometry is represented in Fig. 2.18 with the exception of the rotational dependency. The present research will exploit the ray-tracing relations from Section 2.4 between rays and test section throughout the modeling and simulation process. The linear attenuation of the present materials in the test section is presented in Fig. 4.2 as well as a nominal 150 keV x-ray photon spectra filtered with a 0.5 mm Cu plate analogous to the x-ray source arrangement used throughout the measurements. The simulated x-ray spectrums in the present work were generated with the SpekCalc [145, 146] software.

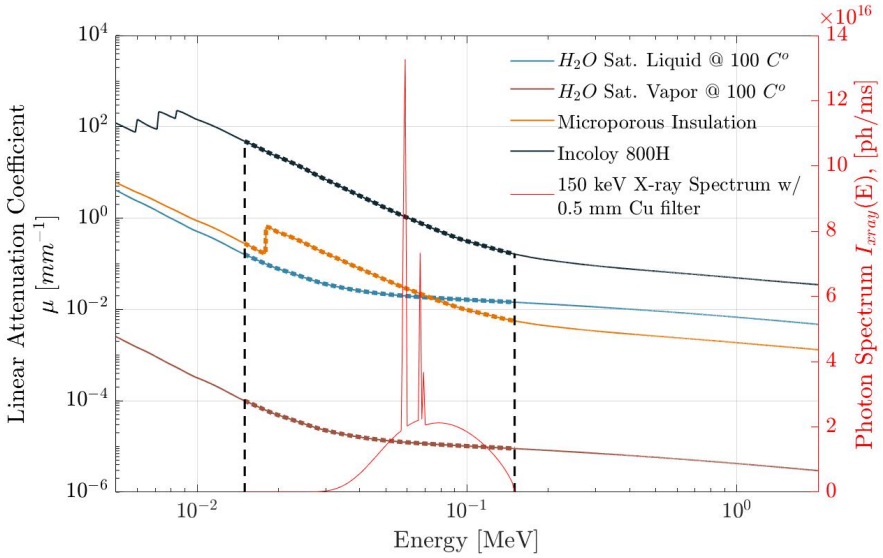

Fig. 4.2. Linear attenuation coefficients of the materials present in the post-CHF experiment; superimposed is a 150 keV x-ray spectrum with a 0.5 mm Cu filter, generated from SpekCalc [145, 146].

4.3. Challenges of High-Temperature Conditions on X-ray measurements

Radiation transmission measurements of high temperature and pressure dependent experiments present several challenges due to the changes in material properties and geometry. The influence of these thermally dependent effects needs to be considered to obtain quantitatively meaningful results. This section will focus in characterizing the identified thermal effects present in the PCHT experimental facility.

4.3.1. Density Changes and Thermal Expansion

The incorporation of the thermal effects and how this affects radiation measurements is directly expressed in the temperature dependence of the material density. It is assumed that the mass attenuation coefficient property of a given material is only dependent on the radiation energy and independent on the temperature; Drotning [36] uses this assumption to derive analytical expressions for the density and the coefficient of thermal expansion temperature dependencies using radiation transmission methods. Separate studies performed by Rao et al. [152] and Narender et al. [128] implement these methods to analyze the properties of CaO, MgO, and various aluminum alloys. The linear attenuation coefficient then becomes a function of temperature and radiation energy, this can now be expressed as

$$\mu_m(T,E) = \left[\frac{\mu}{\rho}(E)\right]_m \rho_m(T) \qquad \text{Eq.(4-1)}$$

where μ/ρ is the mass attenuation, ρ is the density, E is the radiation energy, and m denotes the specific

material; these include the Incoloy-800H (test section), microporous insulator, liquid, and vapor. The density's temperature dependence of the test section can be estimated using the linear thermal expansion coefficient provided by the vendor with the following expression:

$$\rho_p(T) = \frac{M}{V(T)} \approx \frac{\rho_{p,o}}{1 + 3\,\varepsilon(T - T_o)}, \qquad \text{Eq.(4-2)}$$

the subscript p denotes the pipe test section, o denotes the original/calibration conditions, M is the test section mass, V is the volume, T is the temperature, and ε is the coefficient of thermal expansion of the test section which is depicted in Fig. 4.3.*a*. The density has an inverse relation with the temperature-dependent volume; when the test section is heated and the volume increases, the density effectively decreases as depicted in Fig. 4.3.*b*. Next, we must consider the change in radius of the pipe which can be described with the following relations

$$\frac{1}{r}\frac{\partial r}{\partial T} = \varepsilon(T), \qquad \text{Eq.(4-3)}$$

$$r(T) = r_o e^{\int_{T_o}^{T} \varepsilon(\tau)\, d\tau}, \qquad \text{Eq.(4-4)}$$

in the case in which the thermal expansion is significantly small allows us to approximate it as

$$r(T) \approx r_o(1 + \varepsilon(T - T_o)). \qquad \text{Eq.(4-5)}$$

This relation can be used to estimate the increase in magnitude of the outer and inner radius, as well as the resulting pipe thickness depicted in Fig. 4.3.*c*. The change in geometry alters the source-object-detector relations, the radiation-traces sample a faintly-magnified version of the original pipe and perceive new conditions; this is translated to the increase in radius which affects the traversing chord length, the linear attenuation, and changes the trace's intersections with the cylindrical geometries. The resulting increase in radiation intensity due to these compound effects is shown in Fig. 4.3.*d* which highlights the percent increase as a function of operational temperature in comparison to ambient-calibration conditions; this only considers the increase due to the test section's density and increase in radius. As a small aside, while performing measurements of the PCHT experiment, spatial shifts of test section were encountered which further increase the difficulty of the analysis, these shifts were attributed to the thermal expansion of the materials supporting the test section.

Similarly, we must now consider the temperature effects of the liquid and gas phases following the density changes embedded in Eq.(4-1). The thermodynamic properties of H_2O have been widely rigorously researched and are tabulated in steam tables published by Wagner and Kretzschmar [189]; the pressure, volume, and temperature (P-V-T) relations for H_2O can be obtained from the steam tables. These relations

can be best understood by the P-V-T diagram in Fig. 4.4 for a substance that expands upon freezing such as water, this depicts the phase properties and phase-transitions for a given set of conditions; for now, only saturation conditions will be of interest. This highlights the complex conditions that need to be considered for high-temperature experiments. The present research uses the XSteam Matlab functions developed by Holmgren [68] in order to estimate the liquid and vapor densities for input temperature and pressure to simulate the plausible operational conditions of the post-CHF facility.

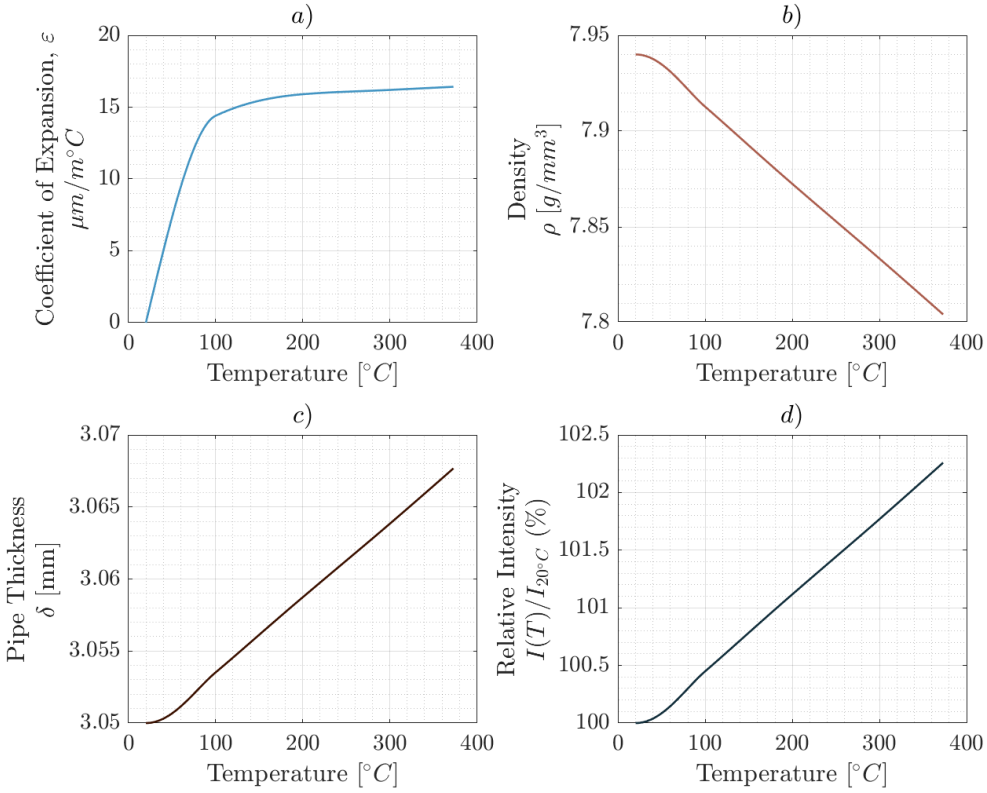

Fig. 4.3. Post-CHF Incoloy-800H test section temperature dependencies; *a)* Coefficient of thermal expansion, *b)* pipe density, *c)* pipe thickness, *d)* relative intensity considering changes in pipe and coolant density and chord length.

The centerline intensity recorded by the simulated detector is estimated using Eq.(2-65) which expressly uses the energy dependent source-flux, and the energy dependency of the linear attenuation coefficient thus considering the beam hardening effect that the photon spectrum undergoes; this effect is discussed in the next section. The simulated relative-intensity along the centerline of the test section is shown in Fig. 4.5 as a function of temperature; this considers the change in thermal expansion of the pipe and the change in density of the working fluids and pipe, this is then normalized by the intensity corresponding to 20°C liquid given that this is the highest attenuation arrangement, the relative-intensity is depicted for a ^{137}Cs source, and a 150 kV x-ray tube. The x-ray results show that the intensity captured whenever there is gas is

approximately 25% higher in comparison to the liquid at low temperatures. However, the difference in intensity between the two phases becomes narrower as it approaches the substance critical point with increase in temperature. This means that at high temperatures it becomes increasingly difficult to discern between the liquid and gas phases. Similarly, there is about 12% contrast for the gamma-ray photons, with an analogous narrowing of the contrast range between the liquid and gas as a function of temperature. It is important to clarify that this does not mean that the x-ray intensity is higher than the gamma-ray intensity, instead it means that there is higher attenuation contrast between the liquid and gas phases whenever x-rays are deployed due to propensity of high absorption at low photon energies. Additionally, the relative intensities of the liquid and the gas evolution with the temperature have similar shapes to the T-V (temperature- specific volume) relations for saturated H_2O, a direct result from the density dependency expressed in Eq.(4-1).

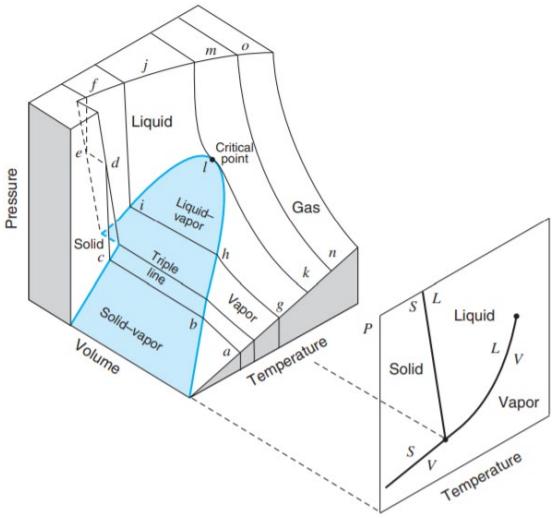

Fig. 4.4. P-V-T surface diagram of substance that expands on freezing, Borgnakke and Sonntag [21].

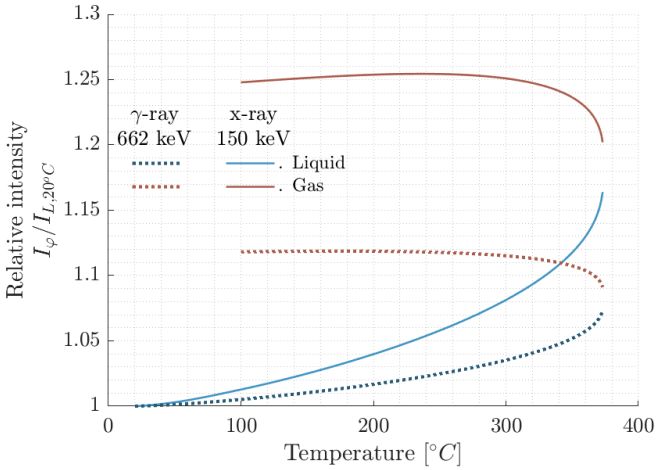

Fig. 4.5. Relative intensity in comparison to liquid at 20°C; 662 keV gamma-rays and 150 kV x-ray spectrum photons.

4.3.2. Beam Hardening

The beam hardening effect pertains to the energy dependent attenuation and how this affects the radiation spectrum in a non-linear manner by changing the photon distribution and its associated energies. As the ensemble of photons crosses a given material, the spectrum morphs as the low energy photons are preferentially absorbed due to their high interaction probability. This can be numerically evaluated by estimating the energy dependent attenuation corresponding to a given material; Fig. 4.6 is an example of an unfiltered spectrum, and the spectrum's beam hardening deformation caused by the liquid material as

well as the pipe material separately. The example serves to show how the photons that get through the pipe material are in the high-energy range of the spectrum.

The beam hardening process results in a deviation from the ideal void fraction estimation. To estimate the errors from this effect, we modify the two-phase flow radiation transmission expression in Eq.(3-1) for a detector panel to incorporate temperature and energy dependencies for a representative ideal void fraction

$$I_{2\varphi,BH}(\boldsymbol{x_d},\alpha,T)=\int_0^\infty C(\boldsymbol{x_s},E)\; e^{-[L_{Flow}[(1-\alpha)\;\mu_L(E,T)+\;\alpha\;\mu_G(E,T)]\;+\;\sum_i \mu_i(E,T)\delta_i]}\;dE. \qquad \text{Eq.(4-6)}$$

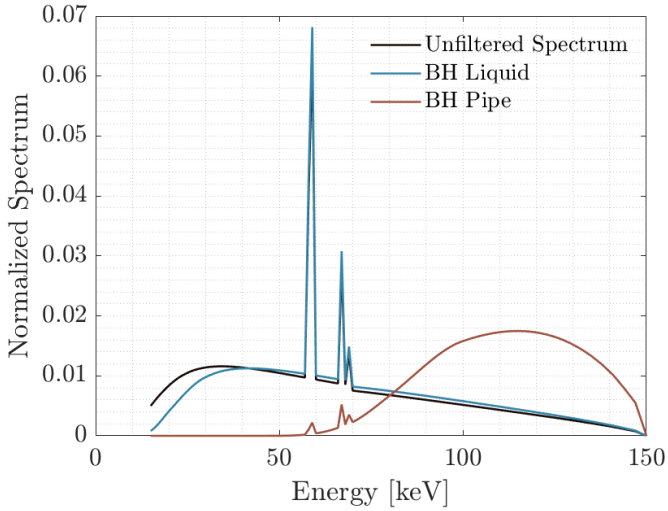

Fig. 4.6. Example of the beam hardening (BH) effect of an x-ray spectrum; depicted is the original unfiltered spectrum, the BH from the liquid only, and the BH with the pipe only.

Here, L_{Flow} are the crossing lengths of the radiation traces through the inner diameter described with equation Eq.(2-64), the function $C(\boldsymbol{x_s},E)$ represents the various non-attenuation related factors such as source spectrum, detector efficiency, and solid angle. Similarly, the all-liquid and all-gas transmissions are

$$I_{L,BH}(\boldsymbol{x_d},T)=\int_0^\infty C(\boldsymbol{x_s},E)\; e^{-[L_{Flow}\;\mu_L(E,T)\;+\;\sum_i \mu_i(E,T)\delta_i]}\;dE, \qquad \text{Eq.(4-7)}$$

$$I_{G,BH}(\boldsymbol{x_d},T)=\int_0^\infty C(\boldsymbol{x_s},E)\; e^{-[L_{Flow}\;\mu_G(E,T)\;+\;\sum_i \mu_i(E,T)\delta_i]}\;dE. \qquad \text{Eq.(4-8)}$$

We shall drop the $(\boldsymbol{x_d},T)$ dependences implying that these are embedded in the respective measurements. The temperature and beam hardened biased void fraction is then estimated as

$$\alpha_{BH}\;=\;\ln\left(\frac{I_{2\varphi,BH}}{I_{L,BH}}\right)\Big/\ln\left(\frac{I_{G,BH}}{I_{L,BH}}\right), \qquad \text{Eq.(4-9)}$$

and the absolute error induced by the beam hardening process is defined as

$$\Delta\alpha_{BH} = \alpha_{ideal} - \alpha_{BH}. \qquad \text{Eq.(4-10)}$$

In the present study, the PCHT facility was modeled at 100°C under saturation conditions for liquid and vapor H_2O, radiation transmission of the experimental facility and imaging system was then simulated for a void fraction range of $\alpha \in [0,1]$ with $d\alpha = 0.01$. The results of the absolute error are depicted in Fig. 4.7.*a*) at the center of the detector panel and *b)* along the radial axis of the detector. The results show that under these conditions the beam hardening of the x-ray spectrum produces a deviation as high as 0.01% in void fraction. The beam hardening errors are reduced along the radial axis due to the decrease in radiation trace lengths through the flow region.

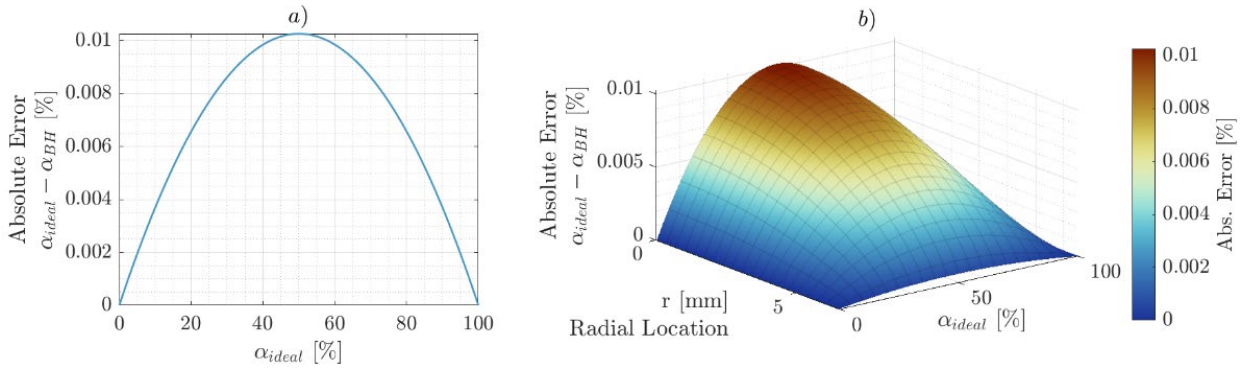

Fig. 4.7. Absolute error due to beam hardening at *a)* at center of the detector panel, and *b)* with radial location of the flow region.

The effects from beam hardening are unavoidable as they are embedded in the physics of the transport process, particularly for polychromatic x-ray systems; the simulations performed in this chapter will naturally consider these effects in all its models. In the case of the post-CHF facility, the test section serves as a hardening filter that reduces the spread of photon energies due to its relatively high attenuating properties; a result that is directly observed by the hardened spectrum depicted in Fig. 4.6. This results in a considerably low deviation from the ideal void fraction caused by beam hardening. These effects would become more prevalent in systems composed of low attenuation housing such as plastic-based piping. Nevertheless, the presence of high attenuation materials present drawbacks due to the decrease of available photons used for imaging. Operational adjustments of the imaging setup can be implemented to counteract some of these issues, these include using high amperage, low frequency frame rates, and long exposures. This aims to increase the number of recorded events and obtain statistically meaningful results along with the decrease of radiation noise. However, low frame rates suffer from parasitic spatial blurring due to the long integration time and spatial movement of the two-phase flow. A compromise must be struck between the temporal resolution and the radiation statistics given that they are dependent one on the other.

4.3.3. Calibration Mismatch

The most challenging aspect of high-temperature measurements results from the disparity in conditions between the experiment and the calibration measurements. Typically, calibration measurements are performed at ambient conditions given that it is difficult to sustain a stable arrangement of an all-liquid and all-gas system at high-temperatures; the latter can result in material failure due to thermal stresses and improper cooling. In addition, it is difficult to assure that no droplets exist in an all-steam system. Here, we investigate the deviation in the void fraction estimation that results from using uncorrected calibration measurements; this will be referred to as the temperature bias. To characterize this error, we will describe the biased void fraction as

$$\alpha_{T,bias} = \ln\left(\frac{I_{2\varphi}(\alpha_{ideal},T)}{I_{L,20℃}}\right)\Big/\ln\left(\frac{I_{Air,20℃}}{I_{L,20℃}}\right), \qquad \text{Eq.(4-11)}$$

where $I_{L,20℃}$ is the liquid calibration at room temperature, $I_{Air,20℃}$ is the gas calibration with air at room temperature, $I_{2\varphi}$ is the simulated two-phase flow measurement which is dependent on temperature T and the ideal input void fraction α_{ideal}, lastly the subscript $T,bias$ denotes the output bias void fraction of our system. As a reminder, the recorded intensities I integrate the energy dependencies, thus considering the x-ray spectrum beam hardening and thermal expansion effects from the present materials. The deviation of the output void fraction in comparison to the ideal void fraction is

$$\Delta\alpha = \alpha_{T,bias} - \alpha_{ideal}. \qquad \text{Eq.(4-12)}$$

The results of the biased void fraction and the associated deviation from the ideal are presented in Fig. 4.8.*a* and Fig. 4.8.*b* respectively; ideally, the system should map 1:1 the output void fraction to the ideal void fraction. The biased void fraction presents a linear relation to the ideal void fraction, as would be expected. However, this output void fraction is altered following the temperature dependent trend depicted in Fig. 4.5. The void fraction deviation depicts the progressive degradation from the ideal. At 100°C the output void fraction presents a deviation of about 2% for the all-liquid, and 6% deviation for the all-gas prediction. It becomes evident from the present analysis that thermal corrections are required to map the calibration measurements onto the experimental conditions; although this error was analyzed along the centerline, this needs to be considered at an individual detector element basis.

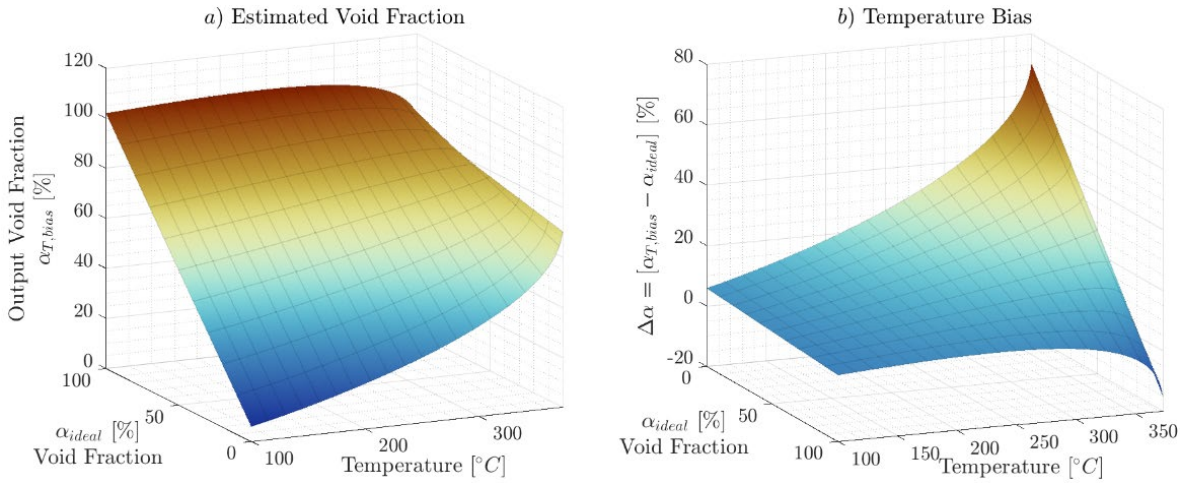

Fig. 4.8. Void fraction prediction from calibration measurements performed at room temperature in comparison to experimental conditions along the test-section centerline; *a)* predicted void fraction, *b)* deviation from the ideal void fraction.

4.3.4. Vibration

The vibration of the test section was the last identified challenge observed during the experimental operation of the facility which could not be solved prior to the publication of the present document. This vibration is associated with the production of vapor in addition to the transport of two-phase flow. The expected effect from the present vibration is a faint spatial blurring of the test section. The PCHT facility is currently being modified to remove the displacement caused by the thermal expansion and hopefully dampen the associated vibration.

4.4. Correction Methods

Understanding the challenges of performing radiation measurements of high-temperature experiments can help us formulate methods that account for the identified issues. This section will discuss the geometric and thermal corrections that were applied to the x-ray measurements of the PCHT facility. Naturally, these corrections are performed in the post processing step and need to be assessed at a case-by-case basis for each measurement.

4.4.1. Geometric Corrections

As briefly mentioned in the previous section, a spatial movement of the test-section was registered while performing high-temperature measurements; this movement manifested in the form of vertical rotation due to sum of torques, as well as radial shift. A geometric correction strategy was formulated to be realign the

temperature-based measurements with the calibration measurements; this can be summarizing in two applied transformations as depicted in Fig. 4.9, the first is the vertical rotation which transforms the coordinates from a tilted system with respect to the physical vertical normal. This vertical rotation transformation is described as

$$\begin{bmatrix} \hat{x}_d \\ \hat{y}_d \\ \hat{z}_d \end{bmatrix} = \begin{bmatrix} 0 & 0 & 0 \\ 0 & \cos\Phi & -\sin\Phi \\ 0 & \sin\Phi & \cos\Phi \end{bmatrix} \begin{bmatrix} x_d \\ y_d \\ z_d \end{bmatrix}. \qquad \text{Eq.(4-13)}$$

The presented definitions prescribe z along the vertical direction and y along the radial direction, this is implemented to remain consistent with the Cartesian coordinates of the imaging system depicted in Fig. 2.18. The angle Φ can be measured along the edge of the pipe by solving the arctan from the vertical and horizontal displacement of the pixels along this edge; in this research we can take advantage of the fact that the cylindrical geometry provides a clear boundary thus allowing us to exploit this feature. Otherwise, it would be important to derive these relation from stationary contrast features with known distances that can help determine the required vertical rotation in an empirical manner.

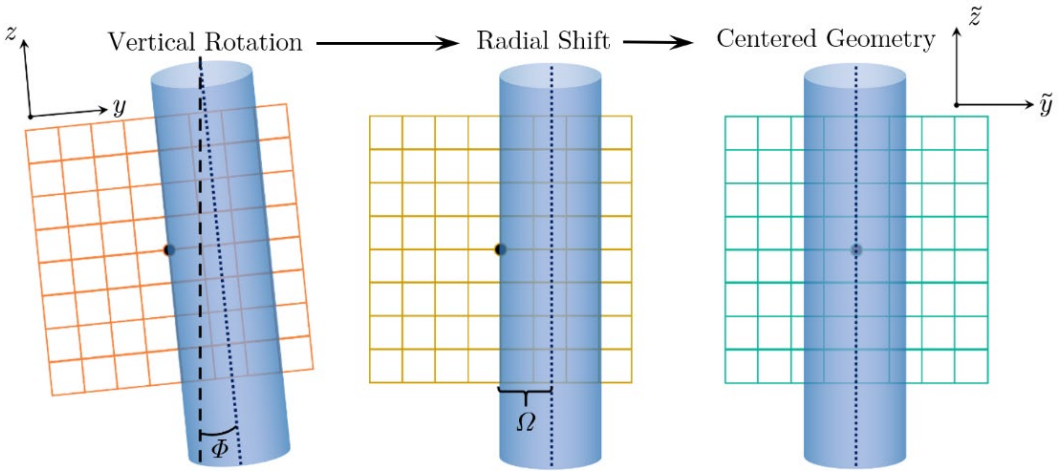

Fig. 4.9. Series of transformations applied to center the geometry.

The second transformation corresponds to a radial shift that must be applied to align the center of the geometry with the center of the detector field or image. In this case the cylinder is shifted out of sight from the detector centerline. Here, it is assumed that one of the detector traces traverses along the center of the cylindrical geometry. Based on this, we need to formulate the coordinates of a virtual detector that remains perpendicular to the trace that traverses along the center of the geometry as depicted in Fig. 4.10. Once again, we take advantage of the edges of the cylindrical geometry to derive an expression of the required radial shift. From the depiction of Fig. 4.10, the fan angles in respect to the centerline C_L of the detector in comparison to the left and right pixel-edges corresponding to the cylinder can be defined as

$$\psi_L = \tan^{-1}\left(\frac{C_L - D_L}{d_{sd}}\right) \quad \text{Eq.(4-14)}$$

$$\psi_R = \tan^{-1}\left(\frac{D_R - C_L}{d_{sd}}\right) \quad \text{Eq.(4-15)}$$

where D_L and D_R are the respective left and right edge locations on the detector plane. The total angle coverage of the cylindrical object can be approximated as

$$\psi \;=\; \psi_L + \psi_R. \quad \text{Eq.(4-16)}$$

By applying some shift Ω such that the centerline aligns with the center of the geometry, we equate

$$\frac{\psi}{2} = \psi_L + \psi_R \;-\; \Omega, \quad \text{Eq.(4-17)}$$

and then solve for the required shift yields

$$\Omega = \frac{\psi_R - \psi_L}{2}. \quad \text{Eq.(4-18)}$$

The radial-shift transformation is then applied to define the new detector $\tilde{\boldsymbol{x}}_{\boldsymbol{d}}$ as

$$\begin{bmatrix} \tilde{x}_d \\ \tilde{y}_d \\ \tilde{z}_d \end{bmatrix} = \begin{bmatrix} \cos\Omega & -(1+\varepsilon)\sin\Omega & 0 \\ (1+\varepsilon)\sin\Omega & \cos\Omega & 0 \\ 0 & 0 & 0 \end{bmatrix} \begin{bmatrix} \hat{x}_d \\ \hat{y}_d \\ \hat{z}_d \end{bmatrix} \quad \text{Eq.(4-19)}$$

where $(1+\varepsilon)$ denotes the thermal expansion factor; if the expansion in the high-temperature measurements is significant in comparison to the detector resolution such that this can be captured in the measurements, then the detector's radial direction needs to be magnified by the same factor to have an equivalent size with the calibration. Alternatively, the calibration measurements can be modified by shrinking the radial sampling direction of the detector by factor of $(1+\varepsilon)$. What is of importance is that the geometries become equivalent in length scales to have a 1:1 comparison between the calibration and the measurement. It is worth pointing out that Eq.(4-18) corresponds to a fan angle of an off-centered object which is not necessarily the same as the coverage of the same object when it is centered, mainly due to the change in perspective and the object magnification. To overcome such inconvenience, the radial-shift can be performed iteratively on a sample frame, realizing that with each sequential iteration, the object will shift closer to the detector center until the required shifting angle is zero; it is important to continuously add the applied shifts to keep track of the total to shift angle Ω to be applied for a set of captured frames. The strategy of the applied transformations is to formulate a detector coordinate system that aligns and centers the geometry; therefore, the data needs to be resampled from the original coordinate system to the newly derived system $\tilde{\boldsymbol{x}}_{\boldsymbol{d}}$; this will be the coordinate system we will be using to compare our measurements throughout this section.

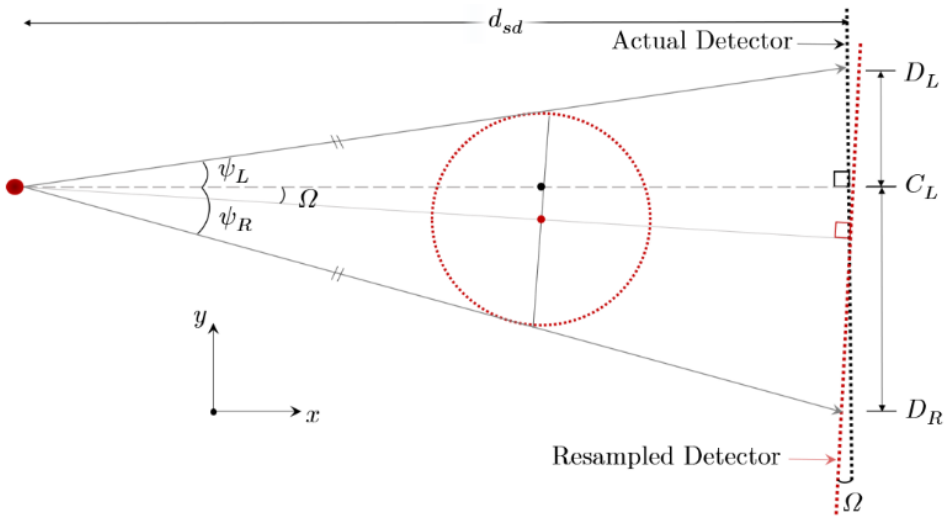

Fig. 4.10. Radial misalignment relations.

To validate the method, a proof of concept was carried out by modeling imaging system and the PCHT facility with induced rotation, shift, and expansion. The ray tracing methods discussed in section 2.4 were used to generate a synthetic radiograph of the facility as shown in Fig. 4.11. The prescribed geometric corrections were then applied to align the coordinate system and resample the radiograph.

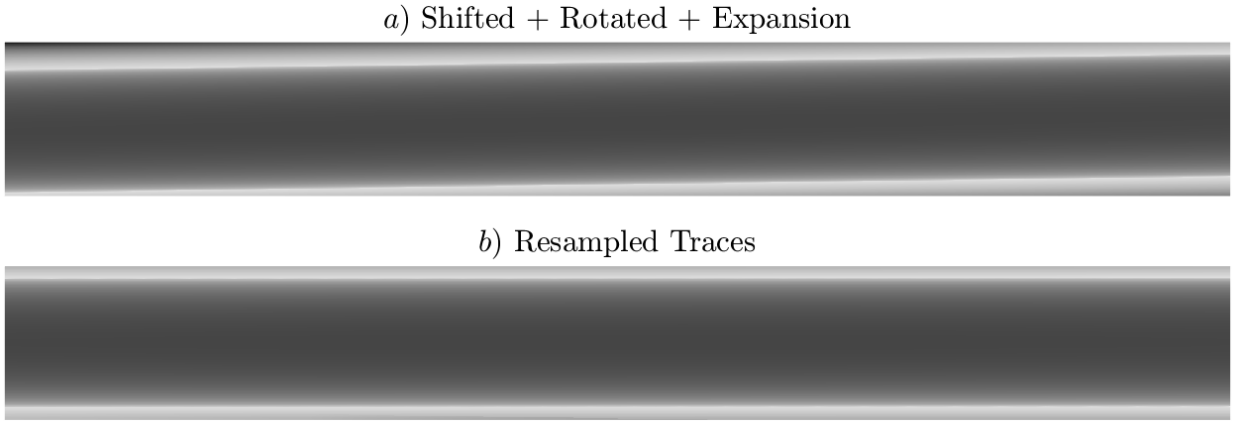

Fig. 4.11. Proof of concept of geometric correction methods. Synthetic radiograph of the modeled PCHT facility with *a)* induced spatial shifts and thermal expansion, *b)* resampled data to realign coordinate system.

4.4.2. Thermal Corrections

As has been previously demonstrated in Section 4.3.3, the mismatch conditions at which calibration measurements are performed in comparison to the experimental conditions leads to a growth of errors in the void fraction estimation; these consider thermal expansion, density changes, and the embedded x-ray beam hardening. Ideally, the needed corrections would be assessed in an experimental manner, however, it

is difficult to achieve the ideal conditions, particularly at significantly high temperatures. For the time being, we will rely on direct numerical estimations of the thermal scaling that needs to be applied at a pixel basis to map the calibration measurements onto the experimental conditions. This method was developed realizing that reducing the scaling factor to a single coefficient value would not fully solve the problem due to the attenuation variation captured throughout the detector panel, some traces perceive higher attenuation as they cross more cumulative lengths than others, particularly towards the vertical ends of the detector. Therefore, a direct numerical simulation is carried out to model the thermal effects at a given set of experimental conditions, and this is compared to the model obtained under the calibration conditions. In order to provide a realistic and thorough analysis, the spatial shifts need to be applied to the simulated models based on the preliminary experimental analysis, the required geometric correction are then used to operate on the equivalent models and the thermal correction for the all-liquid and all-gas systems can be obtained. The corresponding gas and liquid correction factors can then be described as

$$\begin{matrix}\text{Gas Correction} \\ Air\ 20℃\ \rightarrow H_2O\ 100℃\end{matrix}\ ;\quad \Gamma_G(\tilde{\boldsymbol{x}}_{\boldsymbol{d}}) = \ I^{G,H_2O}_{100℃}\ /\ I^{Air}_{20℃} \qquad \text{Eq.(4-20)}$$

$$\begin{matrix}\text{Liquid Correction} \\ H_2O\ 20℃\ \rightarrow H_2O\ 100℃\end{matrix}\ ;\quad \Gamma_L(\tilde{\boldsymbol{x}}_{\boldsymbol{d}}) = \ I^{L,H_2O}_{100℃}\ /\ I^{L,H_2O}_{20℃} \qquad \text{Eq.(4-21)}$$

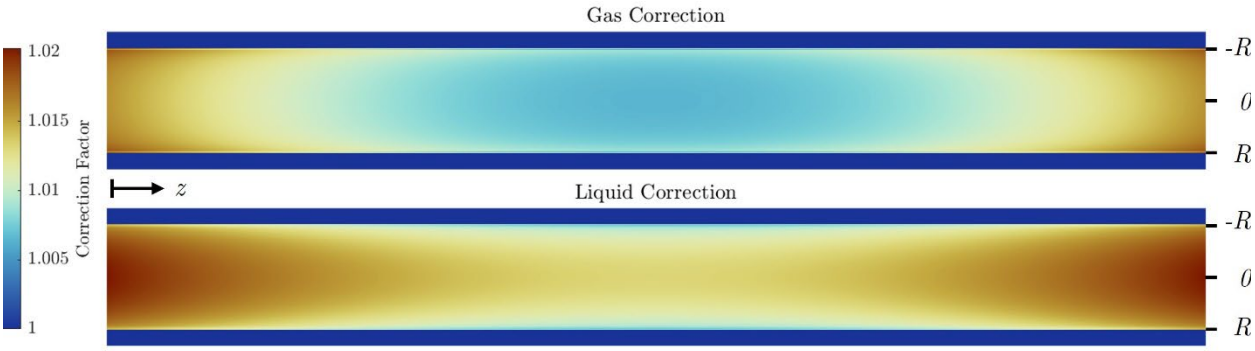

Fig. 4.12. Pixel-wise thermal correction maps for air 20°C to vapor at 100°C, and liquid water from 20°C to 100°C.

where the subscripts G and L denote the gas and liquid phases respectively. These expressions describe the ratio of the simulated radiation intensities registered at the given set of conditions, along with the transformed detector coordinates. This example denotes the correction needed for the cases that maps the calibration from 20°C to the saturation conditions of H_2O at 100°C, which will be most commonly used for the performed measurements; however, this can be performed to any needed set of conditions. An example of the post-CHF thermal correction factors of the gas and liquid conditions described by the expressions above is depicted in Fig. 4.12. The gas thermal corrections are low near middle of the pixels along the

central plane of the test section and increase in magnitude towards the vertical edges of the detector. The liquid thermal corrections are higher overall in comparison, and are as high as 2% near the vertical edges of the detector. It can be expected that the thermal corrections will become more significant with increased temperatures. To complete the discussion, the estimated void fraction now has to consider these thermal corrections, this is modified as follows:

$$\alpha(\tilde{\boldsymbol{x}}_{\boldsymbol{d}}) = \ln\left(\frac{I_{2\varphi}}{\Gamma_L\ I_{L,20℃}}\right) \Big/ \ln\left(\frac{\Gamma_G\ I_{Air,20℃}}{\Gamma_L\ I_{L,20℃}}\right), \qquad \text{Eq.(4-22)}$$

where the registered intensities are the experimental measurements with the calibrations scaled by their respective thermal correction factors.

4.5. Void Fraction Determination Methods

The present section details the additional methods developed and benchmarked for the analysis of the void fraction. Here, it is assumed that the data has been post-processed such that the radiographs have been properly scaled on to the experimental conditions and the void fraction is estimated from these using Eq.(4-22). Although the spatial locations were defined with the test section aligned and centered coordinate system $\tilde{\boldsymbol{x}}_{\boldsymbol{d}}$, now that the spatial traits of the test section are matched throughout the calibration and the measurement, the void fraction will be expressed in terms of detector pixels indexed with the script i

$$\alpha_{i,t} = \ln\left(\frac{I_{2\varphi,i,t}}{\Gamma_{L,i}\ I_{L,i}}\right) \Big/ \ln\left(\frac{\Gamma_{G,i}\ I_{G,i}}{\Gamma_{L,i}\ I_{L,i}}\right). \qquad \text{Eq.(4-23)}$$

This expression simplifies the notation of Eq.(4-22), for convenience, we drop the subscripts that denoted the conditions at which each corresponding measurement was performed. Nevertheless, we will keep the scaling factors present and will be treated as constants. In addition, the subscript t is added to denote the temporal dependency of subsequent frames under experimental conditions.

4.5.1. Axial Modeling and Validation

The methods developed aim to estimate the void fraction along the axial direction of the test section by reducing its dependencies from a 2D field to a representative cross-sectional average value. To accomplish this, we will exploit the relations derived in Section 2.4.1.3 of radiation-trace's intersections with cylinders to discretize the flow region of the post-CHF into cylinders of finite thickness Δz. In essence, the discretized slices of the cylindrical volume are independent regions of interest in which we will estimate the void fraction

from the measured radiographs. Let us first define the axial pixel locations from the detector plane to the object planes as

$$\begin{aligned} z_o &= \frac{\tilde{z}_d}{Mag}, \\ &= \left(\frac{d_{so}}{d_{sd}}\right) \tilde{z}_d, \end{aligned} \qquad \text{Eq.(4-24)}$$

where Mag is the imaging system magnification. The axial planes corresponding to the end caps of the cylindrical region must be defined within the vertical field of view of the detector; these edging planes can be described as

$$z_{edges} \;=\; \{z_{o,min},\; z_{o,min} + \Delta z, \ldots, z_{o,max} - \Delta z \;, z_{o,max}\}, \qquad \text{Eq.(4-25)}$$

and the associated cross-section is located at the center of the slice cylindrical volume between adjacent edge planes, z_{edges}; these are offset by $\Delta z/2$

$$z \;=\; \left\{z_{o,min} + \frac{\Delta z}{2}, \ldots, z_{o,max} - \frac{\Delta z}{2}\right\}. \qquad \text{Eq.(4-26)}$$

The strategy is to calculate the corresponding pixel-trace crossing path lengths through the sliced cylindrical volumes; we will denote these path lengths as $L_{i,z}$, correspondent to pixel i and crossing the cylindrical volume at axial height z. The weight of each path length is estimated in relation to the total sum of path lengths the cross the finite cylinder,

$$w_{i,z} = \frac{L_{i,z}}{\sum_i L_{i,z}}. \qquad \text{Eq.(4-27)}$$

The total sum of path lengths crossing through the finite volume is defined as

$$\beta_z = \sum_i w_{i,z}\,; \qquad w_{i,z} \in \mathbb{R}, \qquad \text{Eq.(4-28)}$$

in which we specify the need for the value of the pixel i to be real, otherwise this is considered a dead-pixel and needs to be neglected; ideally the value of $\beta_z = 1$ if the detector does not have any dead pixels. The cross-section average void fraction is then estimated as

$$\overline{\alpha}(z,t) = \frac{1}{\beta_z} \sum_i w_{i,z}\; \alpha_{i,t}\,; \quad w_i, \alpha_{i,t} \in \mathbb{R} \qquad \text{Eq.(4-29)}$$

where $\alpha_{i,t}$ is the pixel-wise radiograph measured with the detector panel where the subscript t denotes the temporal dependency from measuring subsequent frames; this space vs. time dependency yields a topology map of the evolution of the void fraction which will be relevant in the measurement analysis section.

The formulated method was benchmarked by generating randomized cases of synthetic two-phase flow conditions which include bubbly flow and inverted film boiling. These synthetic cases do not fully capture

the physical principles that dictate the behavior of these phenomena; however, they serve us as idealized samples validate the presented method. For the simulated cases, the cross-sectional slices had a thickness of $\Delta z = 0.5$mm and are centered at the defined planes spanning $z \in [-73.75, \ldots, 73.75]$. The first simulated case was bubbly flow, in which spheres representing bubbles with a corresponding vapor attenuation were placed in the flow region; the idealized void fraction of the bubbly flow from the simulated radiograph is shown in Fig. 4.13.*a)* and the estimated cross-section average void fraction is illustrated in Fig. 4.13.*b)*. The cross-sectional average estimation overlaps with the ideal void fraction; the discrepancies occur whenever there are abrupt changes such as valleys from adjacent or overlapping bubbles in which the average cannot resolve that spatial level of detail.

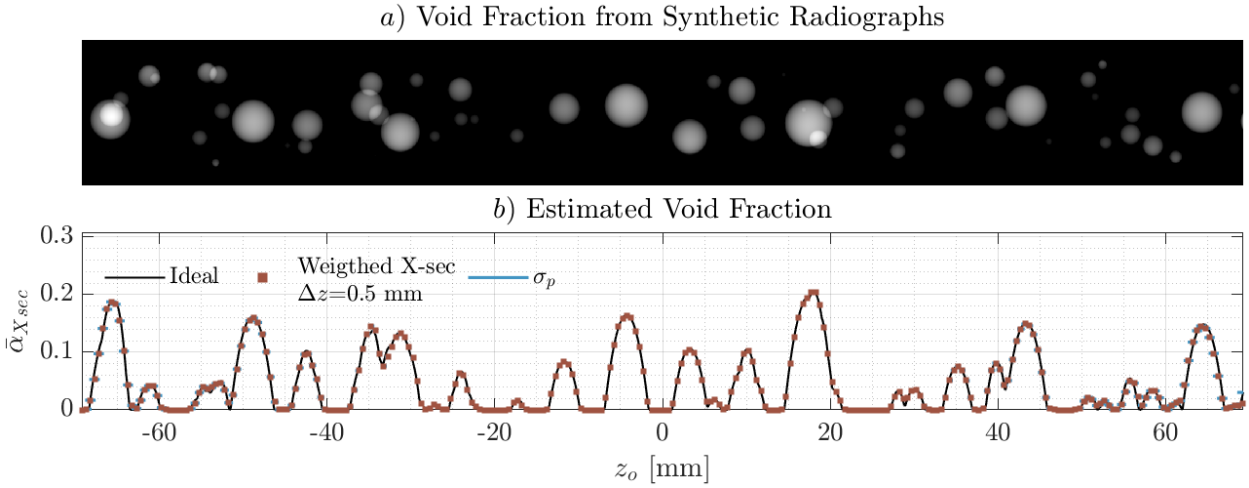

Fig. 4.13. Bubbly flow simulation; *a)* void fraction from radiographs, and *b)* void fraction comparison between the ideal and proposed cross-section average method.

The second simulated case represented film boiling conditions, this was done by imposing a gradual transition from zero void fraction onto a film boiling layer with an overall increase throughout the remaining axial length; surface waves were superimposed to give it the turbulent texture. The simulated results are depicted in Fig. 4.14, the cross-section average matches the ideal behavior, the ideal void fraction is a smooth function which yields a proper prediction from the proposed method. The spatial uncertainties associated to the developed method are also incorporated in Fig. 4.13.*b)* and Fig. 4.14.*b)*, these increase with axial distance away from the center of the detector; although they are difficult to depict in the figures. The axial radiation uncertainties will be assessed next.

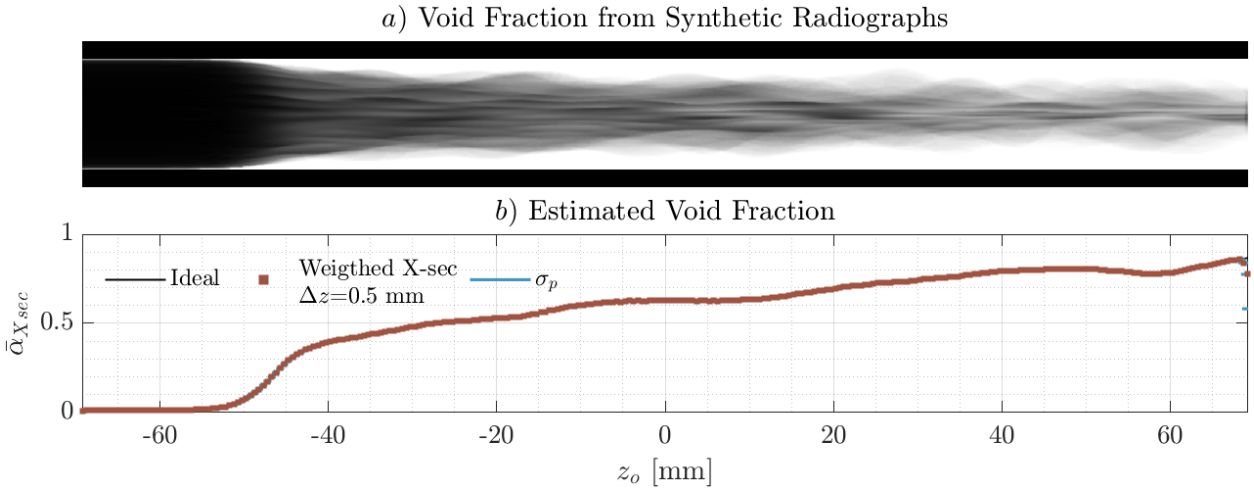

Fig. 4.14. Film boiling simulation; *a)* void fraction from radiographs, and *b)* void fraction comparison between the ideal and proposed cross-section average method.

Lastly, the estimation of the axial velocity can be derived from the axial position vs. time map collected from consecutive frames; this requires the differentiation of the cross-section average void fraction $\bar{\alpha}(z,t)$ in respect to the axial location z, and time t. The partial derivative in respect to time can be expressed using the chain rule as

$$\frac{\partial\,\overline{\alpha}}{\partial t} = \frac{\partial\,\overline{\alpha}}{\partial z}\,\frac{\partial z}{\partial t}\,, \qquad \text{Eq.(4-30)}$$

in which the last term is the definition of the velocity. By rearranging the expression above, we can then solve for the axial velocity as

$$\frac{\partial z}{\partial t} = \overline{v}(z,t) = \frac{\partial\,\overline{\alpha}}{\partial t}\Big/\frac{\partial\,\overline{\alpha}}{\partial z}. \qquad \text{Eq.(4-31)}$$

It is worth clarifying to the reader that this is an indication of the cross section average of the interphase velocity that is only applicable to features that present a strong void fraction gradient; for example, gas-liquid interfaces such as Taylor bubble caps and tails become ideal features to describe the velocity of these moving interfaces. On the contrary, large sections of homogenous void fraction such as the body of a Taylor bubbles do not yield instantaneous velocity value with this method.

4.5.2. Axial and Radiation Error Propagation

The spatial errors associated with the proposed cross section average method are derived in this section. Here, we consider the ray-traces entering and exiting axial locations from the flow region; this is an important distinction given that the ray traces can intercept several cross-sectional volumes along its path. Therefore, we consider the axial spread of the trace through the flow region. The geometric relations between

the source, detector, and cylindrical object which in this case is the flow region, have been extensively described in Section 2.4; these include the unit vectors associated with the ray traces as well as the distance traveled to intersect the cylinder. Now, we define the vertical height at which the traces intercept the cylinder using the z-component from the parametrized ray-trace described in Eq.(2-50),

$$z_{in} = z_s + d_{in}\, e_z, \qquad \text{Eq.(4-32)}$$

$$z_{out} = z_s + d_{out}\, e_z. \qquad \text{Eq.(4-33)}$$

As a friendly reminder to the reader, z_s is the source axial location, d_{in} and d_{out} are the distance traveled from the source to the flow region, and e_z is the z-component of the trace's unit vector. Although not explicitly denoted in Eq.(4-32) and Eq.(4-33), the unit vector and the traveling distances are functions of the source and detector locations; these dependencies are formulated in Section 2.4. Next, the error propagation formula is applied to the trace's incoming intercepting locations in terms of source and detector locations and their related uncertainties,

$$\begin{aligned}\sigma^2_{z_{in}} = \sigma^2_{x_s}\left(\frac{\partial z_{in}}{\partial x_s}\right)^2 + \sigma^2_{x_d}\left(\frac{\partial z_{in}}{\partial x_d}\right)^2 + \sigma^2_{y_s}\left(\frac{\partial z_{in}}{\partial y_s}\right)^2 + \\ \sigma^2_{y_d}\left(\frac{\partial z_{in}}{\partial y_d}\right)^2 + \sigma^2_{z_s}\left(\frac{\partial z_{in}}{\partial z_s}\right)^2 + \sigma^2_{z_d}\left(\frac{\partial z_{in}}{\partial z_d}\right)^2.\end{aligned} \qquad \text{Eq.(4-34)}$$

Similarly, the process is repeated for the outgoing intercepting locations,

$$\begin{aligned}\sigma^2_{z_{out}} = \sigma^2_{x_s}\left(\frac{\partial z_{out}}{\partial x_s}\right)^2 + \sigma^2_{x_d}\left(\frac{\partial z_{out}}{\partial x_d}\right)^2 + \sigma^2_{y_s}\left(\frac{\partial z_{out}}{\partial y_s}\right)^2 + \\ \sigma^2_{y_d}\left(\frac{\partial z_{out}}{\partial y_d}\right)^2 + \sigma^2_{z_s}\left(\frac{\partial z_{out}}{\partial z_s}\right)^2 + \sigma^2_{z_d}\left(\frac{\partial z_{out}}{\partial z_d}\right)^2.\end{aligned} \qquad \text{Eq.(4-35)}$$

The partial derivative expressions for z_{in} and z_{out} in terms of the source and detector spatial components are fully derived in Appendix C. The axial errors of the cross-section average are separated into an upper and lower bound; the lower bound corresponds to the entrance into the flow region, this will be closer to the source, and the upper bound corresponds to the exits of the flow region which are further from the source. The variance for the upper and lower bounds in the plane can be as a combination of independent measurements with unequal errors as described by Knoll [94], this is estimated using the weighted traces from Eq.(4-27) and variances described by Eq.(4-34) and Eq.(4-35); the lower and upper bound cross-section variances are respectively estimated as

$$\sigma^2_{z,LB} = \frac{1}{{\beta_z}^2} \sum_i {w_{i,z}}^2 \; {\sigma^2_z}_{in_i}, \qquad \text{Eq.(4-36)}$$

$$\sigma^2_{z,UB} = \frac{1}{{\beta_z}^2} \sum_i {w_{i,z}}^2 \; {\sigma^2_z}_{out_i}. \qquad \text{Eq.(4-37)}$$

Although these spatial uncertainty is plotted in Fig. 4.13 and Fig. 4.14, the results yield low values for cross-sections with thickness of $\Delta z = 0.5$mm; admittedly, the outcome of these is highly dependent on the geometrical setup. Additionally, these errors increase towards the vertical extremities of the detector as the traces become more probable of crossing multiple sections.

The second type of error associated to the void fraction is related to the radiation noise; the error propagation formula is applied to the pixel-wise void fraction expression in Eq.(4-23) for a single frame in the following manner,

$$\sigma^2_{\alpha,i} = \sigma^2_{I_{L,i}} \left(\frac{\partial \alpha_i}{\partial I_{L,i}}\right)^2 + \; \sigma^2_{I_{G,i}} \left(\frac{\partial \alpha_i}{\partial I_{G,i}}\right)^2 + \; \sigma^2_{I_{2\varphi,i}} \left(\frac{\partial \alpha_i}{\partial I_{2\varphi,i}}\right)^2. \qquad \text{Eq.(4-38)}$$

The void fraction's partial derivatives are

$$\frac{\partial \alpha_i}{\partial I_{L,i}} = \frac{1}{I_{L,i}} \left(\frac{\ln\left(\dfrac{I_{2\varphi,i}}{\Gamma_{L,i} I_{L,i}}\right)}{\ln\left(\dfrac{\Gamma_{G,i}\; I_{G,i}}{\Gamma_{L,i}\; I_{L,i}}\right)^2} - \; \frac{1}{\ln\left(\dfrac{\Gamma_{G,i}\; I_{G,i}}{\Gamma_{L,i}\; I_{L,i}}\right)} \right), \qquad \text{Eq.(4-39)}$$

$$\frac{\partial \alpha_i}{\partial I_{G,i}} = \frac{\ln\left(\dfrac{I_{2\varphi,i}}{\Gamma_{L,i}\; I_{L,i}}\right)}{I_{G,i}\; \ln\left(\dfrac{\Gamma_{G,i}\; I_{G,i}}{\Gamma_{L,i}\; I_{L,i}}\right)^2}, \qquad \text{Eq.(4-40)}$$

$$\frac{\partial \alpha_i}{\partial I_{2\varphi,i}} = \frac{1}{I_{2\varphi,i}\; \ln\left(\dfrac{\Gamma_{G,i}\; I_{G,i}}{\Gamma_{L,i}\; I_{L,i}}\right)}. \qquad \text{Eq.(4-41)}$$

The first and second term in Eq.(4-38) can be considered negligible in the case where sufficiently long or repeated measurements of the calibration are performed, thus reducing the uncertainties $\sigma^2_{I_{L,i}}$ and $\sigma^2_{I_{G,i}}$. The void fraction uncertainty is then reduced to

$$\sigma^2_{\alpha_i} = \; \sigma^2_{I_{2\varphi,i}} \left[\frac{1}{I_{2\varphi,i}} \ln\left(\frac{\Gamma_{G,i}\; I_{G,i}}{\Gamma_{L,i}\; I_{L,i}}\right)^{-1} \right]^2. \qquad \text{Eq.(4-42)}$$

Here, $\sigma^2_{I_{2\varphi_i}}$ would be required to be empirically measured through consecutive frames for a stationary object. However, if we consider the Poisson statistical behavior of radiation, it is then assumed that the count variance is equivalent to the measured counts, $\sigma^2_{I_{2\varphi,i}} = I_{2\varphi,i}$ for a given frame, which further allows us to simplify the associated variance and approximate it as

$$\sigma^2_{\alpha_{i,t}} \approx \frac{1}{I_{2\varphi,i}\left[\ln\left(\frac{\Gamma_{G,i}\ I_{G,i}}{\Gamma_{L,i}\ I_{L,i}}\right)\right]^2}. \qquad \text{Eq.(4-43)}$$

The resulting expression adds the temporal dependency of the experiment measurement frames which was previously omitted to analyze a single frame. It is also worth noting that in the case in which thermal corrections are not required and the calibration measurements match the experimental conditions, the thermal correction factors would be equivalent to one, slightly simplifying Eq.(4-43) to its ideal form. Now the analysis is expanded to the reduction of a cross-section averaged void fraction. Similar to what had been previously implemented for the geometric uncertainty of a weighted mean, the radiation-based void fraction variance is estimated as

$$\sigma^2_{\alpha_{z,t}} = \frac{1}{{\beta_z}^2}\sum_i {w_{i,z}}^2\ \sigma^2_{\alpha_{i,t}}. \qquad \text{Eq.(4-44)}$$

The error bar associated with cross-section average void fraction can be approximated considering a 99% confidence interval,

$$\Delta\alpha_{z,t} = 2.576\ \sigma_{\alpha_{z,t}}. \qquad \text{Eq.(4-45)}$$

An example of the proposed cross-section averaging method and the associated errors applied to a frame from the measurement Section 4.6.3 is depicted in Fig. 4.15. Here, we highlight the void fraction error bars formulated by Eq.(4-45), the spatial errors are small resembling those shown in Fig. 4.13 and Fig. 4.14. The cross-section average example features a Taylor bubble transiting from left to right, in which the tail has a sharp slope while the nose is slightly more gradual. Additionally, churning bubbles follow in the wake of the Taylor bubble.

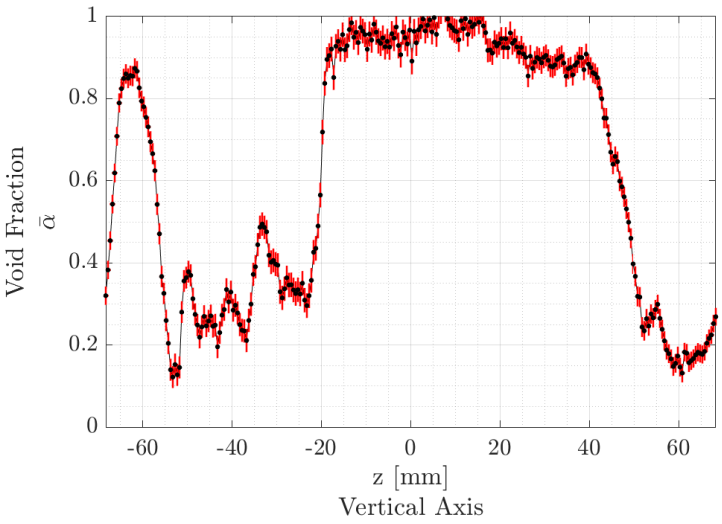

Fig. 4.15. Example of the cross-section averaging method and associated errors applied to a single measurement frame.

4.6. Pool Boiling Experimental Measurement Analysis

The conversation will now shift to the experimental measurements and implementation of the developed methods for high-speed and high-spatial resolution x-ray radiography measurements performed of the post-CHF facility. Preliminary measurements were performed under pool boiling conditions in which there was an absence of forced liquid circulation, resulting in a buoyancy driven vapor flow inside the test section. For the presented measurements in the incoming sections were performed under the same experimental conditions: the test-section pressure was sustained at 17 psi, the outer wall temperature was 100°C, and the heat flux was estimated to be 11kW/m^2. The x-ray was operated at 150 kV, the current was 200 mA, and the detector frame rate was 200 Hz. The test-section and imaging system parameters are described bellow. The flow regimes observed during the measurements were bubbly flow, nucleate boiling, nucleate boiling to slug-churn, and slug-churn; these will be discussed next in the respective order.

Experimental Conditions

- Subcooled Boiling 100°C
- No flow
- 820 mm source-object distance
- 410 mm object-detector distance
- 11 kW/m^2 heat flux
- 200 fps (frames per second)
- 800 ms radiation exposure time

Regimes Observed

- Bubbly Flow
- Nucleate Boiling to Churn
- Nucleate Boiling to Slug Churn
- Slug Churn

4.6.1. Bubbly Flow

The first and simplest regime analyzed is the bubbly flow regime. The void fraction obtained from the radiograph measurement is depicted in Fig. 4.16; the result shows three distinct bubbles traveling vertically, and a fourth bubble appears from the bottom at the end of the measurement time. The bubbles were observed to oscillate along the horizontal axis of the detector. However, due to the single imaging system constraint, it cannot be discerned whether the bubble is oscillating sinusoidally along the plane or helically traveling through the pipe; to obtain this type of data would require a stereographic imaging arrangement as proposed by Heindel et al. [60]. The cross-section average void fraction was estimated using the proposed

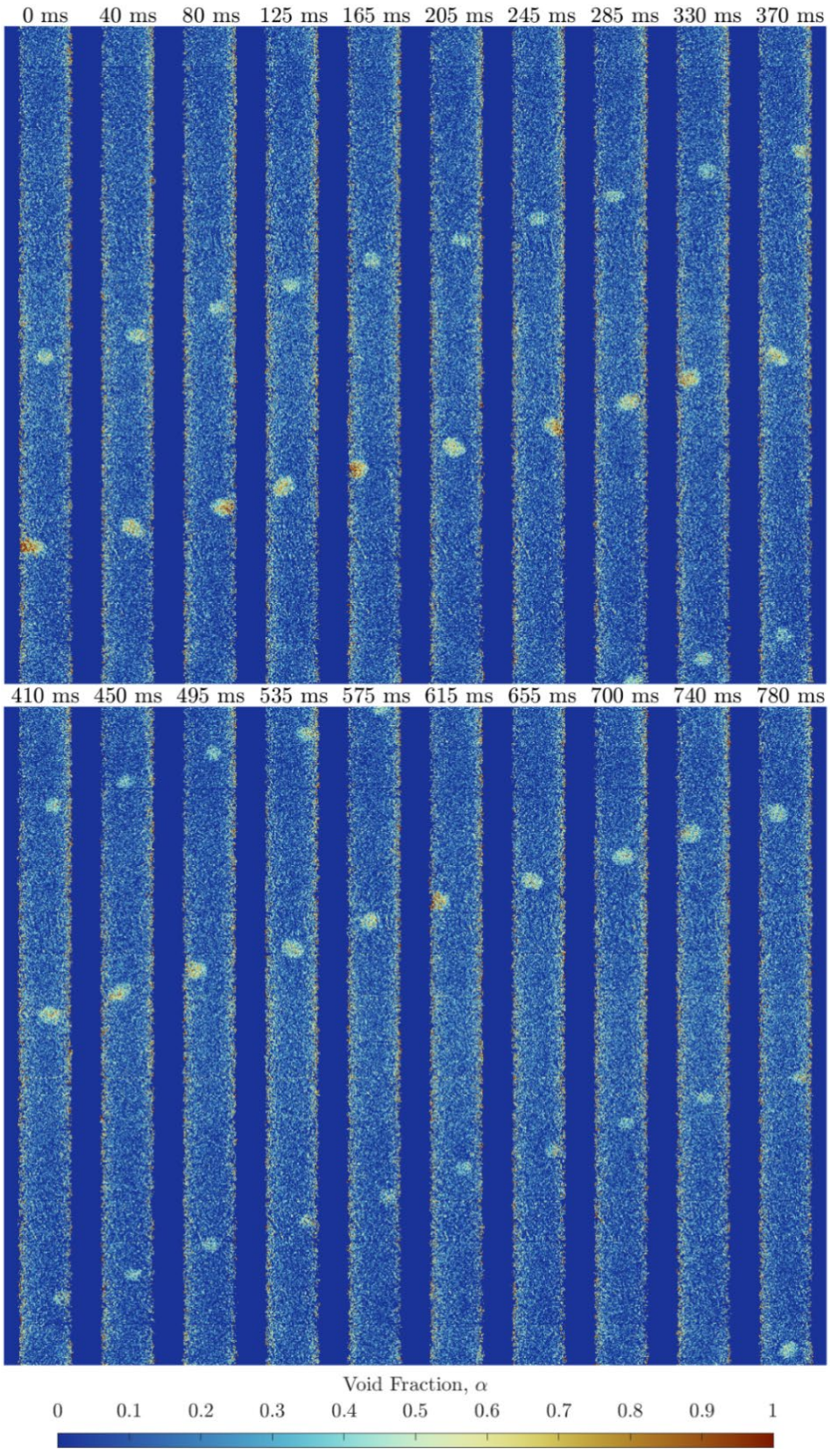

Fig. 4.16. Bubbly flow; spatial void fraction inside test section obtained from measured radiographs.

method described in Eq.(4-29) and depicted in Fig. 4.17 as a function of axial location vs time. The space vs. time map presents a patch behavior along the horizontal time-axis that is caused by the detector tiles which varies in intensity across these adjacent tiled regions. The results show the axial position of the bubbles throughout the measurement and quantify the equivalent void fraction of these. The axial paths present small fluctuations which represent a speeding up and slowing down of the bubbles; this simple case presents the perfect conditions to estimate the axial velocity using the derived relations from Eq.(4-30) and Eq.(4-31). The results of the velocity estimation are depicted in Fig. 4.18. as well as the resulting partial derivatives of the cross-section average void fraction. The estimated velocity map is noisy, however, it shows a consistent trend following the bubble paths in whose velocity value is about 0.1 m/s. It is worth noting that the partial derivative map with respect to the axial location in Fig. 4.18.*a)* is degraded due to the pixel level calibration and measurement mismatch from the aforementioned tiled regions. A more rigorous estimation can be performed by averaging the instantaneous velocity along the bubble paths; the result of these are shown in Fig. 4.19 for the three separate bubbles. Alternatively, the velocity can be estimated by tracking the peak of the bubbles. Lastly, this can also be estimated from the slope of the paths on the axial location vs. time diagram. The results of these three methods is tabulated in Table 4.1. The results from the three methods show close agreement, in particular between the simple slope calculation and the peak tracking, however, the cross-section average velocity is slightly underestimated in value.

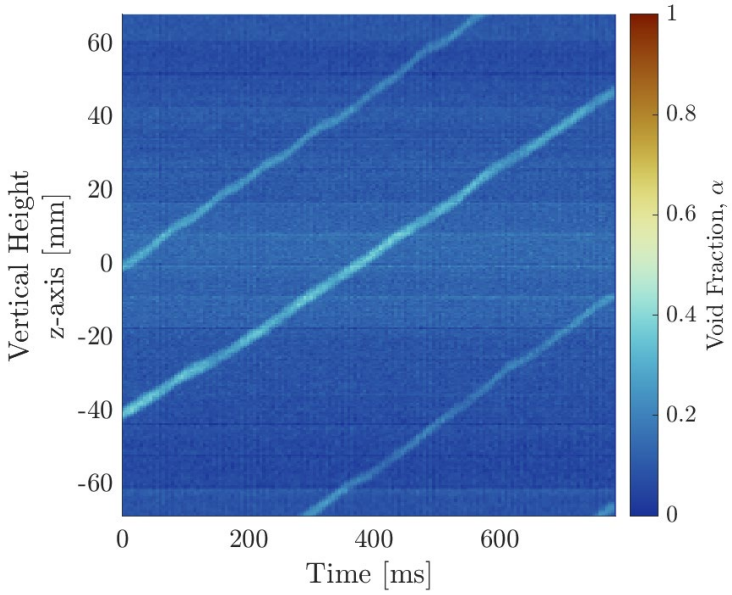

Fig. 4.17. Bubbly flow void fraction map as a function of axial location vs. time.

Table 4.1. Bubble velocity estimation from different methods

Method	Velocity Bubble #1 [m/s]	Velocity Bubble #2 [m/s]	Velocity Bubble #3 [m/s]
Slope	0.121	0.112	0.123
Peak Tracking	0.120	0.113	0.124
Velocity Map	0.107	0.112	0.111

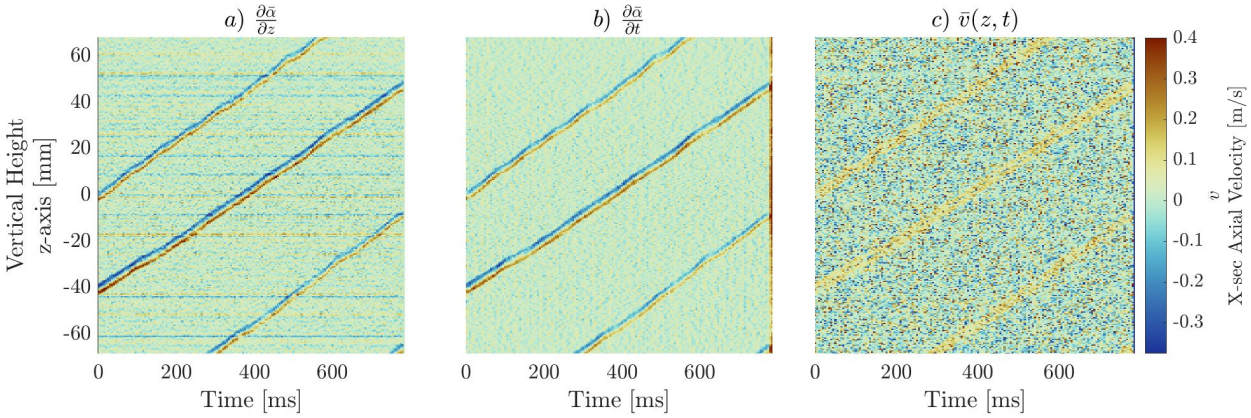

Fig. 4.18. Bubbly flow; *a)* partial derivative with space, *b)* partial derivative with time, and *c)* instantaneous velocity map.

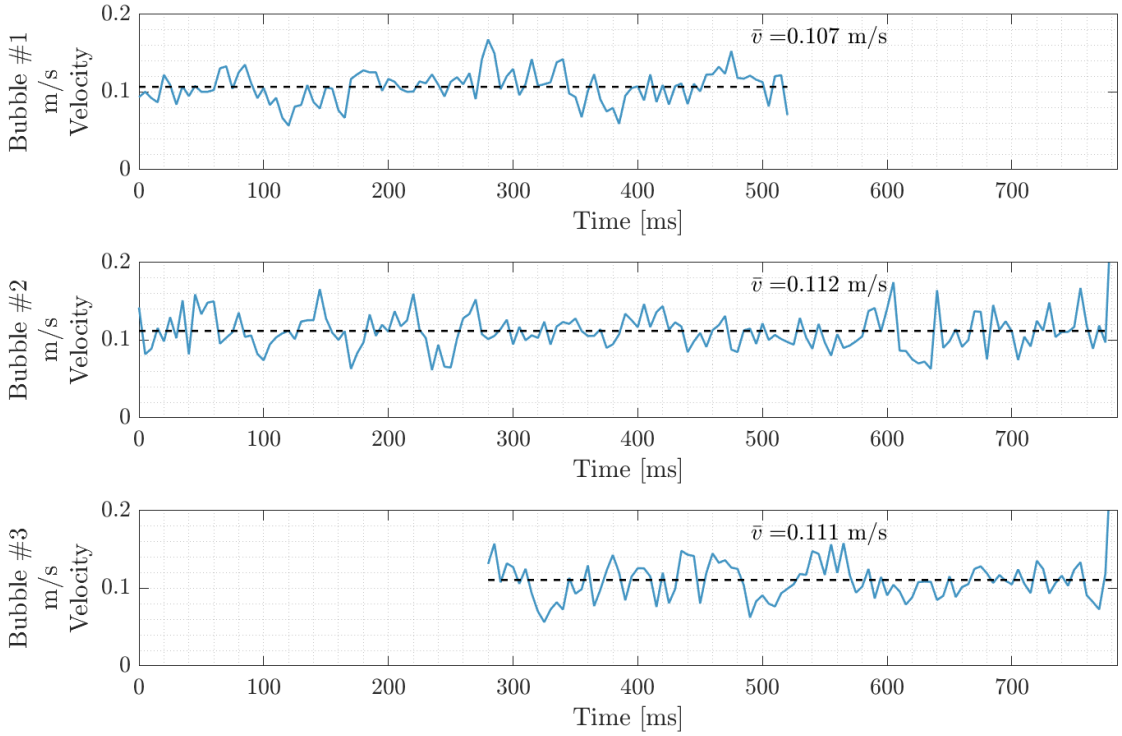

Fig. 4.19. Bubble velocity estimation from axial location vs. time map.

4.6.2. Nucleate Boiling to Churn Flow

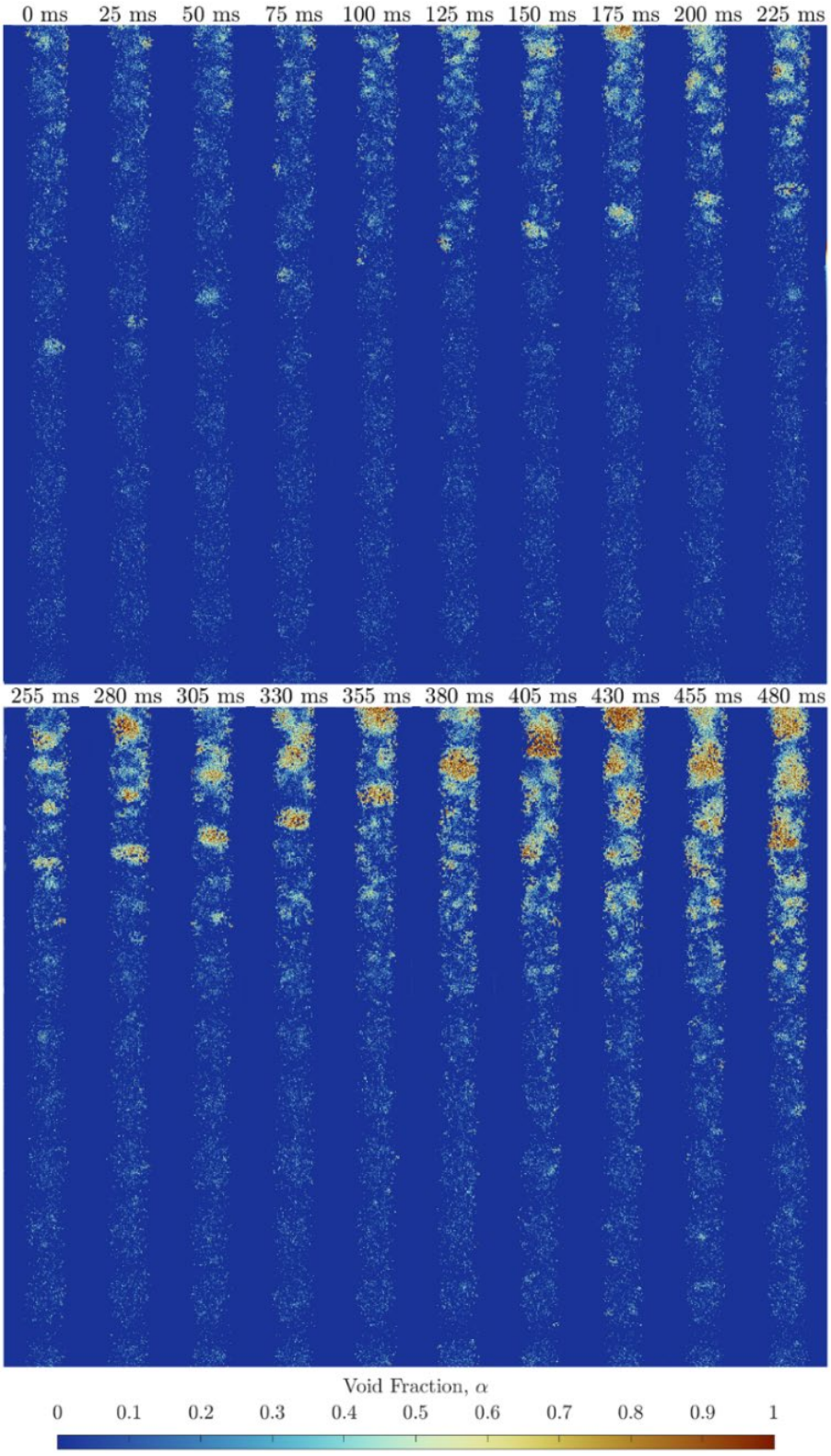

Fig. 4.20. Nucleate boiling to churn flow; spatial void fraction inside test section obtained from measured radiographs.

Nucleate boiling and initial stages of churn flow were captured throughout the x-ray radiography measurements; the corresponding void fraction frames obtained from the radiographs are depicted in Fig. 4.20. Nucleate boiling is initially observed near the top of the measured section, and the boiling front begins to propagate downward. As the production of bubbles increase, these begin to coalesce into large churning bubbles. An additional feature observed in this measurement is the trajectory of a significantly large bubble initially located near the middle of the field of view, as the bubble approaches the established nucleate boiling section from bellow, it begins to coalesce resulting in an increase in size and shaping into the initial stages of a Taylor bubble.

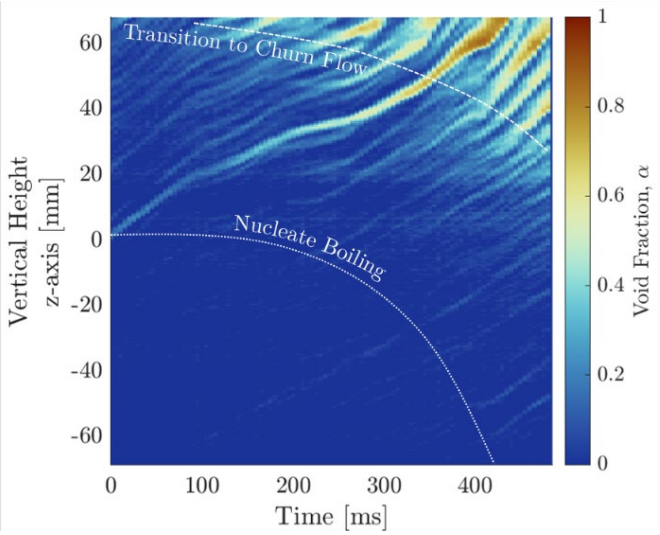

Fig. 4.21. Nucleate boiling to churn flow void fraction map as a function of axial location vs. time.

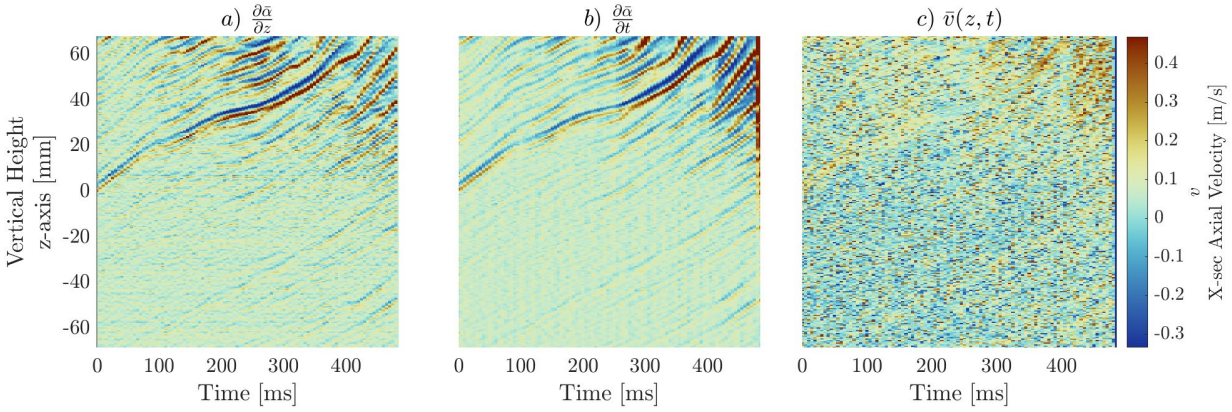

Fig. 4.22. Nucleate boiling to churn flow; *a)* partial derivative with space, *b)* partial derivative with time, and *c)* instantaneous velocity map.

Now we shift our focus onto the axial location vs. time map depicted in Fig. 4.21; the nucleate boiling phenomena is represented as low void fraction streaks nominally occurring above the labeled boundary, these begin to transition to the churn regime as said streaks widen and their corresponding void fraction increases. Similar to the previous analysis, the estimated velocity map is shown in Fig. 4.22, as well as the associated void fraction gradients. The velocity map is grainy in texture, nevertheless, clear trends can be

observed. This includes the relatively low velocity of about 0.1 m/s for the nucleate boiling regions, as the flow transitions to the churn regime, the bubble velocity increases to about 0.4 m/s. The spatial gradient map shows a patch behavior propagating along the horizontal time-axis that is product of the geometric corrections which result in a slight shift of the detector readout tiles, this is more prominent in Fig. 4.25.*a* in the next section.

4.6.3. Nucleate Boiling to Slug-Churn Flow

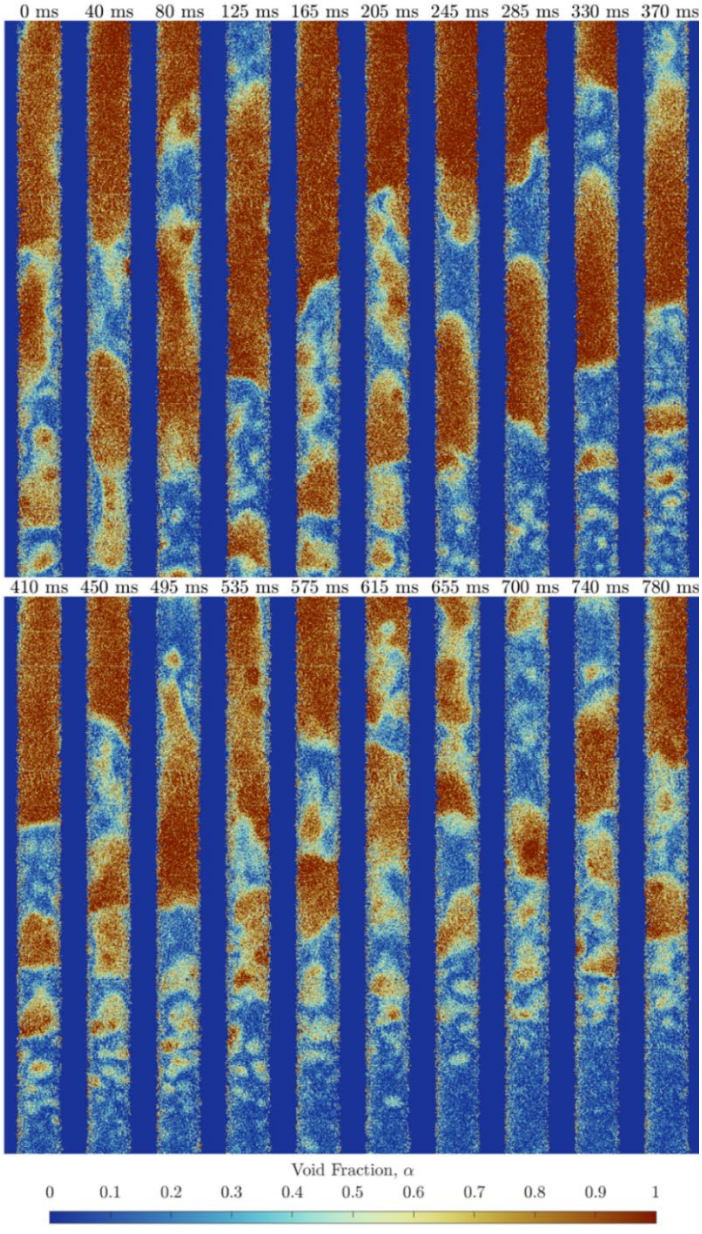

Fig. 4.23. Slug-churn flow and nucleate boiling; spatial void fraction inside test section obtained from measured radiographs.

The next flow regimes that was observed is the development of slug-churn flow with some instance of nucleate boiling as well; the corresponding void fraction frames obtained from the radiographs are depicted in Fig. 4.23. This measurement is perplexing due to the number of interactions that are observed. At first hand, one notices the elongated Taylor bubbles traveling upward immediately followed by sections of correspondent to churning flows; although, this is difficult to discern from the presented frames, it is a consistent observation throughout the measurement. Throughout these churn flow sections, bubbles of irregular shapes coalesce, beginning to transform into a Taylor bubble, these momentarily accelerate in the wake of other bubbles; this eventually allows the upstream Taylor bubble to the meet the tail of the Taylor bubble downstream. As these merge, a downward displacement of vapor occurs which results in a swirl effect. Lastly, once the observed Taylor bubbles move past the field of view, the nucleate boiling section begins to advance upward; this transition is recorded towards the end of the measured frames.

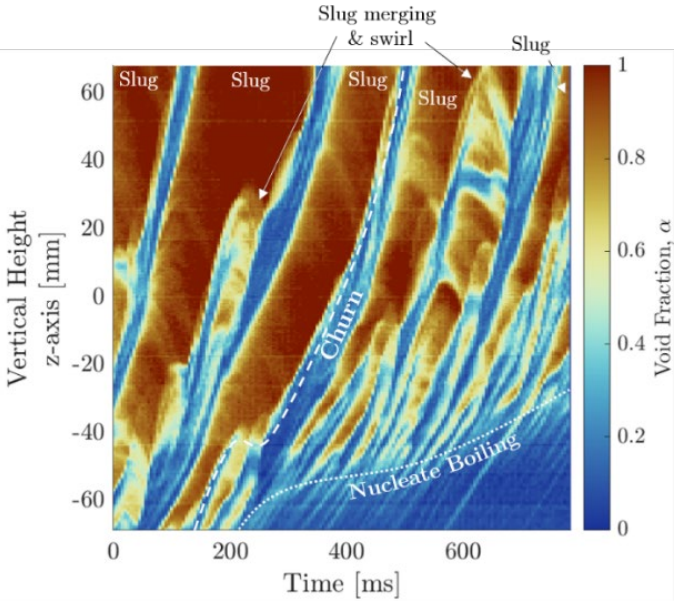

Fig. 4.24. Slug-churn flow and nucleate boiling void fraction map as a function of axial location vs. time.

The mentioned effects can also be observed in the void fraction map as a function of axial location vs. time, depicted in Fig. 4.24. Here, the Taylor bubbles are represented by the wide diagonal traversing features containing near unity void fraction. The merging of these is depicted wherever there is a large void fraction feature joining onto adjacent feature, namely other Taylor bubbles or churning bubbles; these junctions typically have a downward parabolic characteristic on the map. The churn flow is consistently represented by the scattered diagonal branches of growing void fraction, these widen as bubble coalition occurs and adjacent branches begin to merge, eventually transforming to Taylor bubbles. The nucleate boiling is then observed to emerge from the bottom with thin diagonal-like streaks resembling the features depicted in Fig. 4.21 from the previous section. The velocity map shown in Fig. 4.25.*c)* highlights the velocity at the Taylor bubble interfaces represented by strong void fraction gradients; these include the nose and tail of the Taylor bubbles. On the other hand, the body of the Taylor bubbles do not contain velocity values due to the

nearly-homogenous void fraction of these sections. The Taylor bubble's nose shows high velocity features, the tail typically travels at slower speed as these continue to grow and other bubbles merge onto this end. The velocity map also reinforces the downward displacement of gas whenever two Taylor bubbles merge, which results in negative velocity features. The churn region is characterized by the speeding up and slow down due to the chaotic interactions occurring. However, nucleate boiling and the early stages of the churn regime demonstrate comparatively slow but consistent transitions in the velocity map.

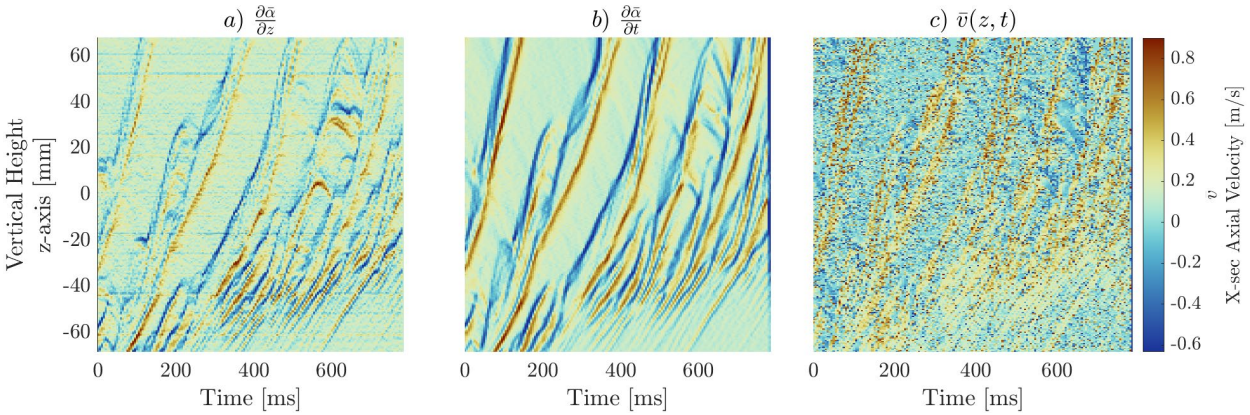

Fig. 4.25. Slug-churn flow and nucleate boiling; *a)* partial derivative with space, *b)* partial derivative with time, and *c)* instantaneous velocity map.

4.6.4. Slug-Churn Flow

The last performed measurement is characterized by the slug-churn regime as depicted by the radiography-based results shown in Fig. 4.26. In comparison to the previous measurement, the present Taylor bubbles are significantly larger, and the nucleate boiling front is not present. The observed effects follow those analyzed in the previous section in which the traversing Taylor bubbles are followed by a churn section in their wake. Montoya et al. [124] points out some of these hydrodynamic interactions that occur in the churn-turbulent regime, and suitably describes it as "large spiraling, transient, vortex-like structures which move throughout the system" (Montoya, 2016). The radiograph results capture the swirl-like motion most prominently at the head of the Taylor bubbles and the irregular-shaped medium-sized bubbles; this effect is distinctively observed at the bottom or the measured section from the frames at 125-370 seconds in which the churning structure swirls and merges to the overhead bubble. Although it is hard to discern from the images, liquid from above moves downward as the structure ascends. An adjacent effect is also observed in elongated churn and Taylor bubble structures in which there is a similar ripple-like displacement of liquid.

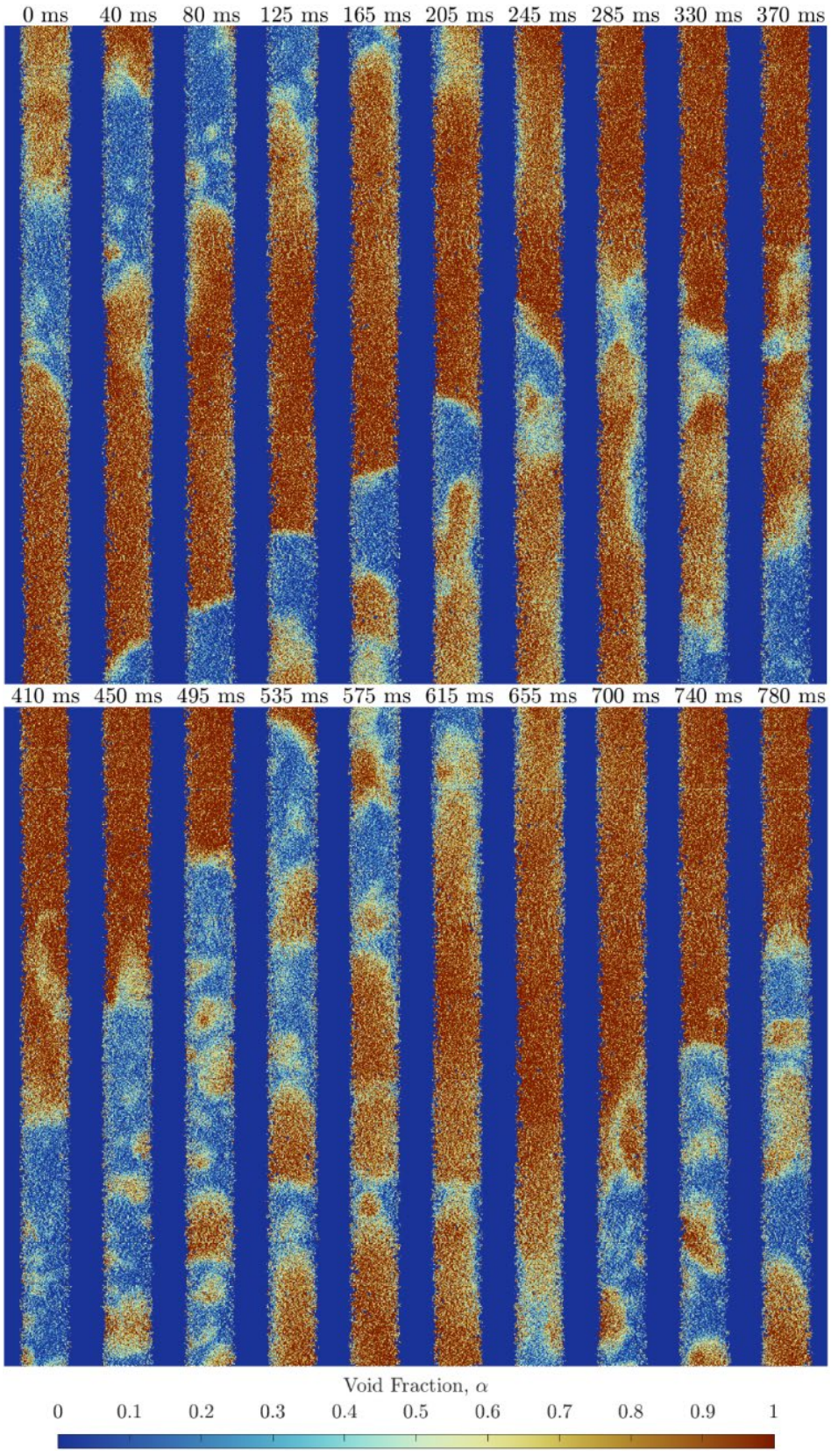

Fig. 4.26. Slug-churn flow; spatial void fraction inside test section obtained from measured radiographs.

The cross-section average void fraction is presented in Fig. 4.27; here, the Taylor bubbles are represented by the wide diagonal traversing features containing near unity void fraction. The merging of these is depicted wherever there is a large void fraction feature joining onto an adjacent feature, namely other Taylor bubbles or churning bubbles; these junctions typically have a downward parabolic characteristic on the map, in which the Taylor bubble from below penetrates onto the tail boundary of those above, the gas from the bubble below rushes to the one above, this draws more liquid to the cross section followed by a churning-swirl. The churn flow is consistently represented by the diagonal branches of growing void fraction which widen as bubble coalition occurs and merge onto adjacent features, eventually transforming to Taylor bubbles. Emphasis is placed on the descending flow and gas propagation in the form of light-shade streaks slanted downward that occur in the high-void fraction (Taylor bubble) and churn structures. The estimated velocity map is depicted in Fig. 4.28; presents some grainy-noise behavior, however, it captures the velocity trends of the void fraction and liquid interfaces. Some of these include the head and tails of the Taylor bubbles as well as the churning bubbles which travel at velocities ranging from 0.4 m/s to 0.8 m/s. Negative velocities are observed whenever there is a ripple traveling on the surface of the elongated bubble, and also whenever upstream and downstream bubbles merge thus generating a swirl.

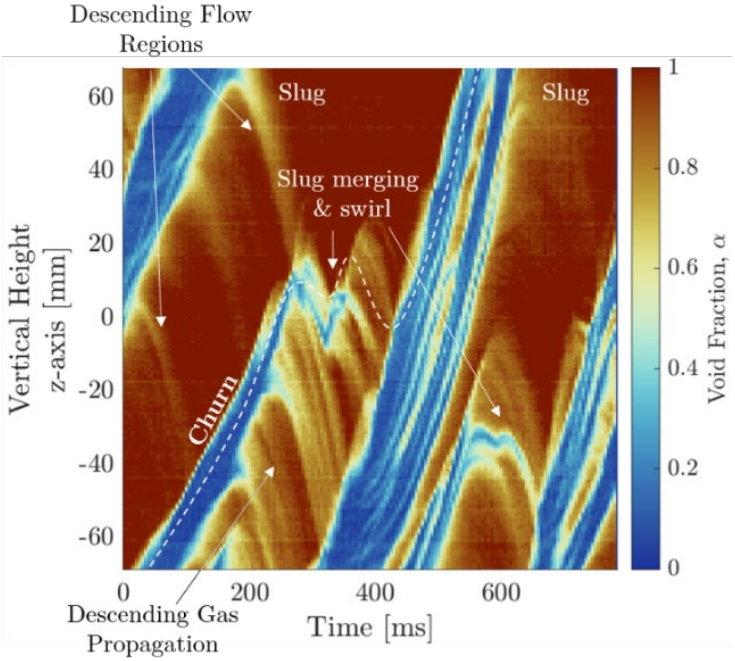

Fig. 4.27. Slug-churn flow void fraction map as a function of axial location vs. time.

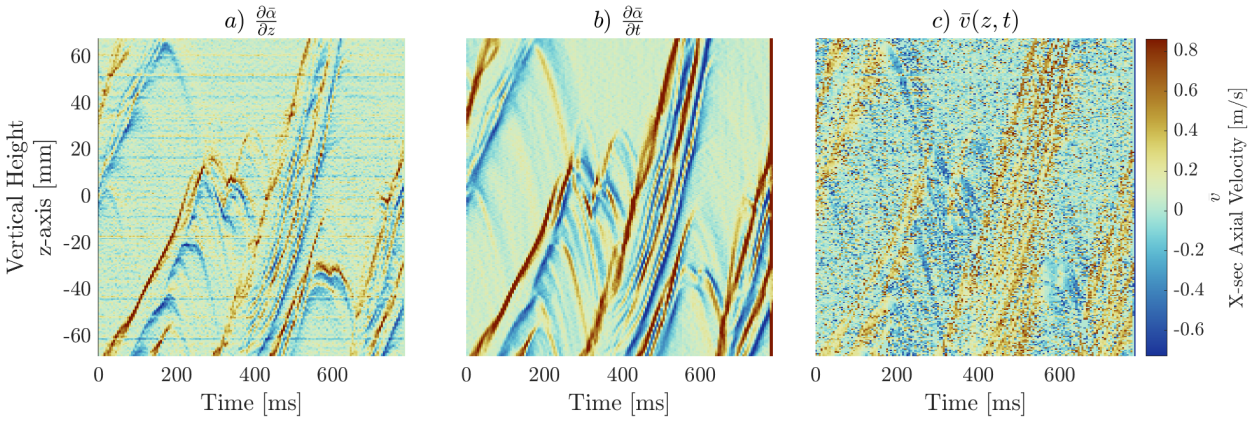

Fig. 4.28. Slug-churn flow; *a)* partial derivative with space, *b)* partial derivative with time, and *c)* instantaneous velocity map.

4.7. Summary of Findings

In the present work we identify the challenges of performing x-ray measurements of high-temperature and high-pressure experimental setups, these include the following: x-ray spectrum beam hardening, material density changes, calibration mismatch, test section thermal expansion, spatial shift and rotation of the test section, and vibration. The PCHT facility characterized by its cylindrical geometry was modeled using ray-tracing methods to simulate the radiation transport from the x-ray source, through the test section and onto the detector panel. The simulations were used to assess the effects of the identified challenges on the void fraction individually, fully considering material properties, physical processes, and energy-dependent attenuation; the only issue that was not analyzed was the effects caused by the test section vibration. The assessment from the separate effects can be summarized with the following:

- **Beam Hardening** – this considers the change of the x-ray spectrum in which there is a preferential absorption of the low energy range photons as the ensemble traverses through the present materials. This results in a deviation from the ideal void fraction due to the non-linearity mapping that occurs from the energy dependent attenuation. The absolute error in the void fraction was at most 0.01% which can be considered negligible. This arises from the high attenuation pipe material acting as a low-energy photon filter.
- **Density Changes** – the high-temperature operation of the experiment produces density changes of the present materials. The thermal expansion experienced by the test section decreases the density, this results in an increase in radiation intensity dependent on temperature. Similarly, the liquid and vapor density changes are dependent on operational pressure and temperature of the

facility. The liquid density decreases with increase in temperature, which yields an increase of the measured intensity. On the contrary, gas increases in density, which yields a decrease in measured radiation intensity. The relative contrast between the liquid and vapor phases decreases with increase in temperature; this is due to the reduced difference in density between the phases. The radiation relative contrast between the liquid and gas phases follows the shape of the liquid and vapor saturation curves from the T-V (temperature-volume) relations for saturation conditions of the working fluid.

- **Calibration Mismatch** – the calibration of the test section is performed at room temperature; the gas calibration is performed with air at atmospheric conditions; this is done because it is difficult to achieve a stable steam arrangement for calibration. The difference between the calibration and the operational conditions lead to the deviation of the estimated void fraction in comparison to the ideal; this deviation is aggravated with the increase in temperature. Subsequently, thermal correction maps were developed for the liquid and gas calibrations such that these are scaled accordingly to the experiment's conditions.
- **Shift & Rotation** – during the two-phase flow measurements, the test section was observed to shift and tilt in respect to its original location; these geometric allocations were respectively described by a radial shift and an axial rotation. A geometric correction method was developed, this was then tested by simulating cases which induce these types of movements and applying the correction strategy to align the modeled test section. Lastly, the correction strategies were applied to the measurements.

The void fraction analysis was supplemented by a cross-section average estimation derived from the ray-tracing methods used to describe the geometric relations of the experimental setup. The proposed method was benchmarked by modeling idealized bubbly and film-boiling cases, the estimation derived from the method presented close agreement with the ideal axial void fraction for both cases. Sequential temporal measurements allow us to build a cross-section average void fraction vs. time flow-topology map which depicts the evolution of the flow. The cross-section average velocity is then derived using the spatial and temporal partial derivatives of the void fraction.

Pool boiling measurements of the PCHT facility were performed under no flow conditions deploying the high-speed x-ray radiography imaging system; the post-processing was carried out applying the

geometric and thermal correction methods previously mentioned. The observed regimes throughout the measurement include bubbly flow, nucleate boiling, and slug-churn flow; in addition, instances of the transitions between these flow regimes were captured throughout the measurements. The cross-section average void fraction vs time yields a topographic-like map that serves to analyze the regimes observed throughout the measurements. The distinct features present in these topographic maps are used to describe associated phenomena occurring in these flow regimes. For example, a bubble is characterized as diagonal line of finite thickness, this represents the vertical displacement as a function of time. In the case of nucleate boiling, the bubbles represented as linear objects contain undulations, the finite width broadens as bubbles coalesce and more steam is generated. The churn regime transitions from these recognizable finite-width streaks to broader structures that have an overall positive displacement, but which can exhibit downward-slanted features represent descending liquid; said downward displacement of gas can be caused either by a propagating liquid wave observed as a surface undulation on the body of the bubble (whenever these are sufficiently long), by the vortex behavior of the churning bubbles, or by the swirl generated whenever two large bubbles merge. Lastly, when sufficient gas is accumulated by the churning structures, Taylor bubbles begin to form, these occupy the entire cross section and are followed by churning flow in their wake. The Taylor bubbles are represented as long sections of near unity void fraction, in which the head and tail of the bubble define the propagation boundaries of the void fraction. The velocity topographic-maps are derived by differentiation the void fraction map in the axial and temporal directions. Although the result of the velocity maps appear noisy, distinct features can be discerned which further help to quantify the velocity of the void fraction boundaries.

CHAPTER V

Tomographic Imaging of Void Fraction Inside an Adiabatic Rod Bundle Geometry.

Nomenclature

Roman Variables

A	Area
D	Diameter
d	Distance
Eo	Eotvos number
GP	Gauge pressure
G	Injection group
g	Gravity
h	Height
I	Radiation counts/ intensity/ activity
j	Superficial phase velocity
Lo	Capillary or Laplace length
M	Mass, or measurement
$\dot{m}$	Mass flow rate
N	Recorded counts
N_μ	Viscous Number
P	Pressure
p	Pitch or projection
p_w	Wetted perimeter
p_θ	Sinogram
r	Radial variable
T	Temperature
t	time
V	Volume

Greek Variables

α	Void fraction
γ	Gamma-ray yield
η	Absorption efficiency
θ	Angle
μ	linear attenuation coefficient or viscosity
ρ	Density
σ	Surface tension or Standard deviation
σ_x^2	Variance of variable x

Subscripts & Superscripts

ρ	Density
2φ	Two-phase flow
φ	Single phase
Air	Air filled
atm	Atmospheric conditions
b	Bubble
CT	Imaging system location
det	Detector
$dist$	Distorted bubble
DP	Differential pressure
Exp	Experiment
G *or* g	Gas
h	Hydraulic
i	Indexing variable
$ideal$	Ideal condition
in	Incoming trace
k	Indexing variable
L	Liquid or left-side
P	Pressure
p	Pitch
nps	Number of photons
sat	Saturation condition
sc	Subchannel
sd	Source-detector
$Sensors$	Sensor location
spg	Sparger
sph	Spherical bubble
$Steam$	Vapor
Top	Top of the bundle

5.1. Overview

Reactor fuel assemblies are composed of arrays of individual rods which house the nuclear fuel pellets. These structures are at the core of the nuclear reactors and are in charge of bridging the atomic scale at which fission reactions deposit energy within the nuclear fuel, and the macroscale at which the cladding-surface transfers the produced energy in the form of heat onto the coolant. The coolant serves the purpose of regulating the reactor temperature by removing said heat; typical coolants are water in the case of Light Water Reactors (LWRs), liquid sodium (^{23}Na) or molten Lead-Bismuth for Liquid Metal Fast Breeder Reactors (LMFBR), helium or carbon dioxide in the case of Gas Cooled Reactors, and various other salts for up-and-coming reactor designs. Nevertheless, in the present research the primary working fluid will use water, representative of LWR systems. In the previous chapter it was demonstrated how the liquid coolant changes to the vapor phase under saturation conditions when the heat is delivered at increased rates in the form of heat-flux (power per unit area). Reactor assembly studies with emphasis in flow dynamics and heat transfer phenomena are a focal research topic with ramifying impact regarding reactor design, operation, and safety.

The behavior of single-phase and two-phase flows is heavily dictated by the properties of the fluids and geometric arrangement of the flow section, these include: density, viscosity, surface tension, phase velocity, test section orientation, housing dimensions, material roughness with added complexities in the case of rod bundles which must consider lattice formation, rod diameter, and spacer grid. Factoring in all these effects result in a unique set of conditions that describe the turbulence and multi-phase interaction mechanisms in the system, therefore the outcome from every arrangement becomes unique. Nevertheless, our job as scientists is to identify common traits in these complex systems that can be characterized to help us develop the needed closure models or empirical relations to best improve reactor designs; the foundation of these relations is typically built using dimensionless numbers which describe qualities of the flow by comparing the balance between different forces such as inertial, buoyancy, viscous, and surface tension forces. The objective of the present research is to develop and apply novel radiation-based imaging methods to study two-phase flow rod bundle applications representative of LWR systems. To accomplish set objective, the Michigan Adiabatic Rod Bundle Experimental (MARBLE) facility has been designed and constructed in conjunction with the HRGTS scanner previously presented in Section 2.3.1. The present research is executed under the NRC project titled *Post-CHF Heat Transfer Instrumentation and Experimentation* which aims to establish a curated experimental database for the development and improvement of models implemented in the best-estimate system code TRACE and in subchannel codes such as COBRA-TF. This chapter will first review past-research and proceed to detail the scaling considerations, facility design and construction, CT simulations of the imaging system and the facility, lastly it will introduce the first set of measurements intended as a proof of principle. A rigorous experimental campaign will follow after the present research, building on the knowledge laid herein.

5.2. Michigan Adiabatic Rod Bundle Experiment (MARBLE)

This section will first focus on explaining the scaling considerations for the experimental facility in relation to LWR systems. It will then proceed to explain in extensive detail the design and construction of the MARBLE facility. Lastly, a shakedown test performed with the MARBLE facility is discussed in order to acquaint the reader with the data acquisition instrumentation, and the methods deployed to estimate parameters of interest.

5.2.1. Scaling from Vapor-Water to Air-Water Mixtures

The MARBLE facility is designed to simulate conditions inside LWRs, including BWR and PWR assemblies. BWR systems working principle is to boil water and generate steam, and thus it naturally operates in a two-phase flow arrangement. PWR systems on the other hand operate ideally in single phase, however it is important to understand the two-phase flow conditions that may occur in these reactors which occur under accident conditions. The design and operational parameters of typical LWR systems are tabulated in Table 5.1; the reactor geometry, pressure temperature, mass flow-rate parameters were obtained from Masterson [117], and Todreas and Kazimi [180], the liquid and vapor phase parameters were estimated with the RefProp [105] library based on the operational saturation conditions of the reactor. The MARBLE facility will be formally introduced in the next section; however, the design information of the facility has been included in Table 5.1 to compare side by side with LWR systems. From Table 5.1, it becomes clear that these reactors operate under harsh conditions which are otherwise hard to achieve in a laboratory setting not to mention the increasing budget costs. For this reason, experimental facilities resembling reactor systems tend to use adiabatic air-water mixture as their working fluids, a trait that will be applied in the present work. The scaling of the system was based on the dimensionless Eötvös (Eo) number

$$Eo = \frac{g(\rho_L - \rho_G)D_b^2}{\sigma} = \left(\frac{D_b}{Lo}\right)^2, \qquad \text{Eq.(5-1)}$$

which describes the ratio between the gravitational/buoyancy and surface-tension forces; the Eo number takes in the length scale of the bubble diameter as scale reference. This also leads us to introduce the capillary length Lo (or Laplace length)

$$Lo = \sqrt{\frac{\sigma}{g(\rho_L - \rho_G)}}, \qquad \text{Eq.(5-2)}$$

which further emphasizes the ratio between the aforementioned forces and has a direct relation to the Eo number. Ishii and Zuber [75] expressed the maximum spherical bubble size in a system as

$$D_{sph} = 4\sqrt{2}\ L_o\ N_\mu^{1/3}, \qquad \text{Eq.(5-3)}$$

In which N_μ is the viscosity number of the system

$$N_\mu = \frac{\mu_L}{\sqrt{\sigma \rho_L Lo}}. \qquad \text{Eq.(5-4)}$$

Similarly, they expressed the maximum distorted bubble diameter as

$$D_{dist} = 4\ Lo. \qquad \text{Eq.(5-5)}$$

The transverse migration of bubbles traveling in the shearing field of a fluid is determined by the diameter of the bubble and how the lift force is exerted on the bubble. As Tomiyama et al. [181] showed, the lift coefficient is positive for small bubble diameters in which the viscosity is relevant, and the coefficient becomes negative with increase in bubble diameter for which the surface tension and buoyancy become prevalent. The results from Tomiyama's experiment showed an outward migration of small bubbles away from the source of shear in the fluid towards the stationary wall; this simulated the shearing gradient that is formed from the bulk movement of the fluid. On the contrary, large bubbles migrate and conglomerate towards the bulk of the fluid. With this in mind, there exists a critical bubble diameter which occurs when the lift coefficient is equal to zero, which causes the bubble to continue its path in a rectilinear manner. Tomiyama formed a model for the lift coefficient stemming on a modified *Eo* number which considers the bubble's horizontal diameter; as bubbles increase in size, these deform towards an oblate shape with a larger horizontal diameter. The scaling of the MARBLE experiment was based on the scalability of the bubble dynamics in LWR at the operational saturation conditions, this requires attaining the same *Eo* for LWR systems and the experimental facility

$$Eo_{LWR} = Eo_{Exp}, \qquad \text{Eq.(5-6.}a\text{)}$$

and can be explicitly expressed as

$$D^2_{b,LWR}\left[\frac{g(\rho_L-\rho_G)}{\sigma}\right]^{Steam/Water}_{(P,T)_{sat}} = D^2_{b,Exp}\left[\frac{g(\rho_L-\rho_G)}{\sigma}\right]^{Air/Water}_{atm}; \qquad \text{Eq.(5-6.}b\text{)}$$

here, the bubble size is ungrouped from the parameters that describe the qualities of the gas-liquid mixture, the superscript of these denotes the mixture while the subscript denotes the pressure-temperature conditions. The expression in Eq.(5-6.b) can be transformed as ratios between the critical bubble diameter and the corresponding capillary length for the given systems

$$\left[\frac{D^2_{b,LWR}}{Lo^2_{LWR}}\right]^{Steam/Water}_{(P,T)_{sat}} = \left[\frac{D^2_{b,Exp}}{Lo^2_{Exp}}\right]^{Air/Water}_{atm}. \qquad \text{Eq.(5-6.c)}$$

The scaling factor R_{Lo} can then be defined as the ratio of critical bubble diameters, or alternatively capillary length scales,

$$R_{Lo} = \frac{D_b^{Exp}}{D_b^{LWR}} = \frac{Lo_{Exp}}{Lo_{LWR}}. \qquad \text{Eq.(5-7)}$$

From the current relation, it becomes evident that the scaling factor is dependent on the two-phase mixture properties described within the capillary lengths. These relations allow us to compare the required

scaling to appropriately replicate bubble dynamic phenomena from LWR systems to experimental conditions performed with air-water mixtures at standard atmospheric conditions. The ideal scaling factor in the case of a BWR assembly is 1.717, and in the case of a PWR assembly is 2.766. Based on the obtained scaling factors, parameters such as the rod diameter, pitch and hydraulic diameter need to be adjusted; the scaled parameters are tabulated in Table 5.2.

Table 5.1. Design and operational parameters of typical LWR systems. Information obtained from Todreas & Kazimi [180], as well as Masterson [117].

Parameter	Units	BWR	PWR	MARBLE
Outer Rod Diameter, D	[mm]	12.27	9.5	15.875
Pitch, p	[mm]	16.2	12.6	20.08
Subchannel Hydraulic Diameter, $D_{sc,h}$	[mm]	14.96	11.78	16.46
Subchannel Flow Area	[mm^2]	144.2	87.88	205.27
Assembly Rod Arrangement	-	8 x 8	17 x 17	8x8
Sat./Op. Pressure, P	[MPa]	7.14	15.5	0.1013
Sat./Op. Temperature, T	[^{o}C]	287.13	344.8	23
Sat. Liquid Density, ρ_L	[kg/m^3]	737.31	594.34	997.5
Sat. Vapor Density, ρ_G	[kg/m^3]	37.32	101.93	1.19
Surface Tension, σ	[N/m]	0.0173	0.0047	0.0723
Liquid Viscosity, μ_L	[Pa $\cdot$ s]	9.08E-5	6.82E-5	9.32E-4
Coolant Mass Flow Rate per Assembly, $\dot{m}_L$	[kg/s]	15.5	90	10
Eotvos number, Eo	$\frac{g(\rho_L-\rho_G)D_b^2}{\sigma}$, $\sim$	60.52	118.	36.62
Capillary Length Scale, Lo	$\sqrt{\frac{\sigma}{g(\rho_L-\rho_G)}}$, [mm]	1.59	0.98	2.7

The MARBLE facility is designed as an 8x8 rod assembly arrangement, the rod diameter is $D = 15.875$ mm based on commercially available cylinders (5/8" in diameter) with a rod thickness of 0.6 mm, a lattice pitch of $p = 21.08$ mm, and the corresponding subchannel hydraulic diameter is $D_{h,sc}$= 16.46 mm; the rod

bundle extends at a height of 3.8 m and has an estimated flow area of 15771.7 mm^2. The schematic of the MARBLE facility is depicted in Fig. 5.2, and Fig. 5.3, the facility will be discussed in the next section. Getting back on track, it is important to note that the hydraulic diameter is a representative length for non-circular hydraulic systems, the general expression for the hydraulic diameter is

$$D_h = \frac{4\ A_{fl}}{p_w}, \qquad \text{Eq.(5-8)}$$

In which A_{fl} is the flow area and p_w is the wet perimeter. In the case of a subchannel assembly, the hydraulic diameter can be described as

$$D_{h,sc} = \frac{4p^2 - \pi D^2}{\pi D} \qquad \text{Eq.(5-9)}$$

In which P is the rod pitch and D is the rod diameter. The actual scaling ratio for the various geometric parameters between the LWR system and the experimental facility can be respectively described for the subchannel hydraulic diameter, rod diameter, and assembly pitch:

$$R_{D_h} = \frac{D_{h,sc}^{Exp}}{D_{h,sc}^{LWR}}, \quad R_D = \frac{D^{Exp}}{D^{LWR}}, \quad R_p = \frac{D_p^{Exp}}{D_p^{LWR}}; \qquad \text{Eq.(5-10)}$$

We can define the geometric similarity between the nuclear reactor systems and the designed experiment using the ideal scaling expressed in Eq.(5-7) and the actual scaling in Eq.(5-10), these can be expressed as

$$R_{Geom,D_h} = \frac{R_{D_h}}{R_{Lo}}, \quad R_{Geom,D} = \frac{R_D}{R_{Lo}}, \quad R_{Geom,p} = \frac{R_p}{R_{Lo}}. \qquad \text{Eq.(5-11)}$$

Table 5.2. Scaled geometry from vapor-liquid mixtures at saturated conditions in LWR systems to air-water mixtures at atmospheric conditions.

Parameter	Ideal / BWR	Ideal / PWR
R_{Lo}	1.717	2.766
D [mm]	21.00	16.26
p [mm]	27.73	34.85
D_h [mm]	25.61	32.58

In this case we define the geometric similarity in terms of the ratio between hydraulic diameters. However, the geometric similarity for a given feature of the rod bundles such as rod diameters and assembly pitch requires the estimation of the ratio of said feature and the normalization of the estimated scaling factor R_{Lo}. The expressed relations can be used to determine the similarities between the experimental facility in comparison to the BWR and PWR system. The ideal scaling ratio $R_{Lo}(T,P)_{sat}$ shown in Fig. 5.1 is depicted

as a function of saturation pressure and temperature for LWR systems in reference to air-water mixture at atmospheric conditions; here, R_{Lo} is the ideal scaling ratio, and R_{Dh} is the comparison of hydraulic diameters. The circular markers map the scaling relative to BWR systems, and the triangular markers map the in relation to the PWR systems. The parameter ratios and the geometric similarities between the MARBLE facility in relation to BWR and PWR systems are tabulated in Table 5.3. The geometric similarities for the BWR system range from 64~75%, and in the case of the PWR system these range from 50~60%. The presented analysis focus on one flow aspect present in reactor assemblies, however it is important to consider other relevant conditions such as flow regimes, coolant flow, and friction factors.

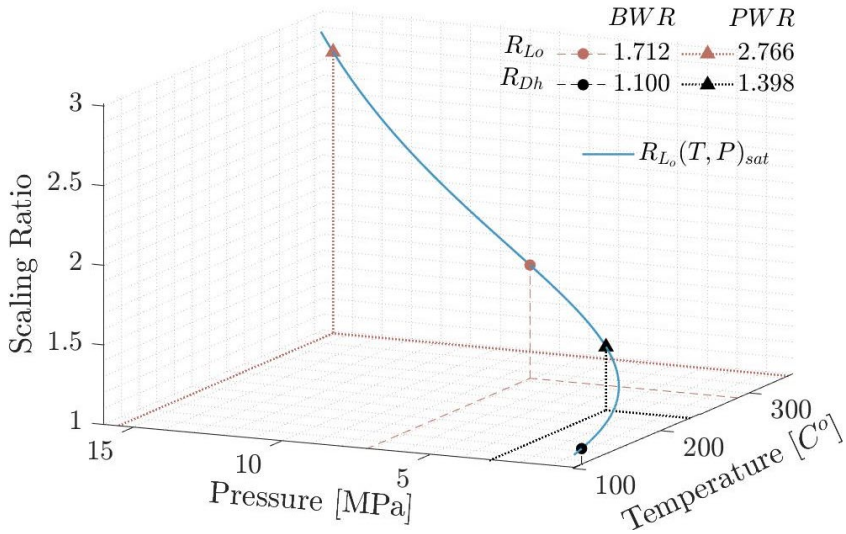

Fig. 5.1. Air-water mixture system scaling in relation to saturated conditions in vapor-water as a function of temperature and pressure. Mapping of ideal and actual scaling ratios.

Table 5.3. Geometric similarities between the MARBLE facility and LWR systems

	Parameter	MARBLE / BWR	MARBLE / PWR
Parameter Ratio	R_{Dh}	1.100	1.398
	R_D	1.294	1.671
	R_p	1.240	1.594
Geometric Similarity	$R_{Geom,Dh}$	0.643	0.505
	$R_{Geom,D}$	0.756	0.604
	$R_{Geom,p}$	0.724	0.576

5.2.2. Bundle Design & Construction

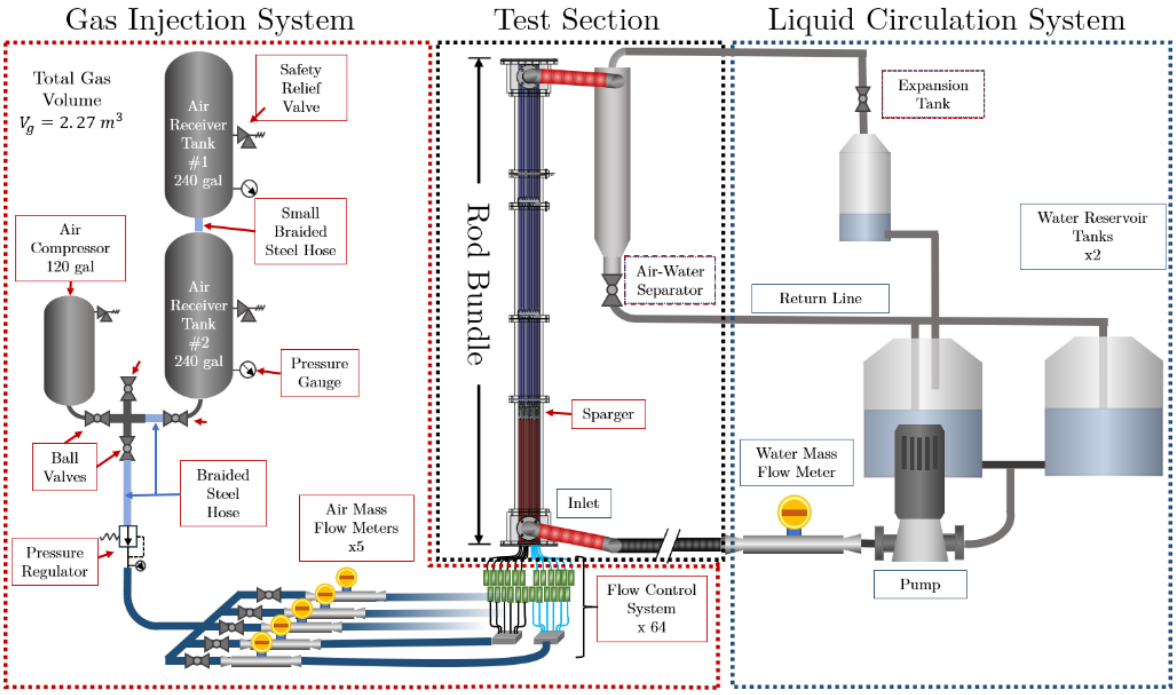

Fig. 5.2. MARBLE facility schematic; gas-circulation system, test section, and liquid circulation system.

The MARBLE facility has been fully assembled at the present time; the facility consists of three main systems: the gas injection system, the liquid circulation system, and the test section where the prior two consolidate. Fig. 5.2 serves as a schematic detailing the hydraulic aspects of the MARBLE facility. Although the geometric aspect had been previously mentioned in the previous section, it is worth reminding the reader that the MARBLE facility is an 8 x 8 rod assembly, with a rod diameter of $D = 15.875$ mm, a rod thickness of 0.6 mm, a lattice pitch of $p = 21.08$ mm. The design objective of the facility was to pair the rod bundle with a computed tomography (CT) scanning device to obtain detailed distributions of the void-fraction inside a bundle geometry for different combinations of liquid and gas superficial velocities, and investigate the effect of grid spacers and mixing vanes. The HRGTS presented in section 2.3.1 was built in house for this purpose, the design of the supporting structures surrounding the rod bundle took into consideration the dimensions and requirements of the HRGTS. This required the design of two separate structural gantry systems that allow independent mobility of the rod-bundle as well as the HRGTS scanner; this design would maximize the vertical coverage that the CT system could image, the design of the structural support system is depicted in Fig. 5.3. Additionally, the rod bundle houses two spacer grids placed at corresponding heights of 1.7 m and 2.6 m away from the bottom of the bundle in order to study the effects that mixing vanes

have on two-phase mixtures and gas migration. The spacer grid dimensions, and separation distance was chosen based on the scaling factor corresponding to the PWR systems presented in Table 5.3. Computational fluid dynamic (CFD) simulations of the inlet of the rod bundle were carried out in order to converge into a design that would allow the flow to best develop prior to the gas injection. The results from this showed that adding a compartmentalized redistribution blade would serve to straighten the flow. It is important to note that although the CFD simulations were performed, these were used as a support design tool and not as a primary focus of investigation. The assembled and functional facility is depicted in Fig. 5.4. The following subsections will describe the different systems, subsystems and components that comprise the MARBLE facility.

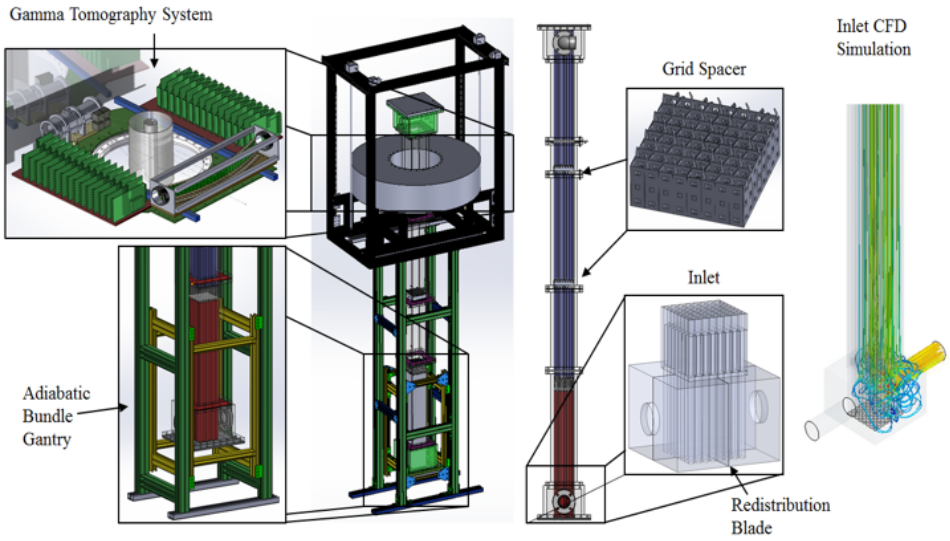

Fig. 5.3. MARBLE facility design: housing design, framing support, gantry systems, tomography system, spacer grids, and CFD simulation of rod bundle inlet.

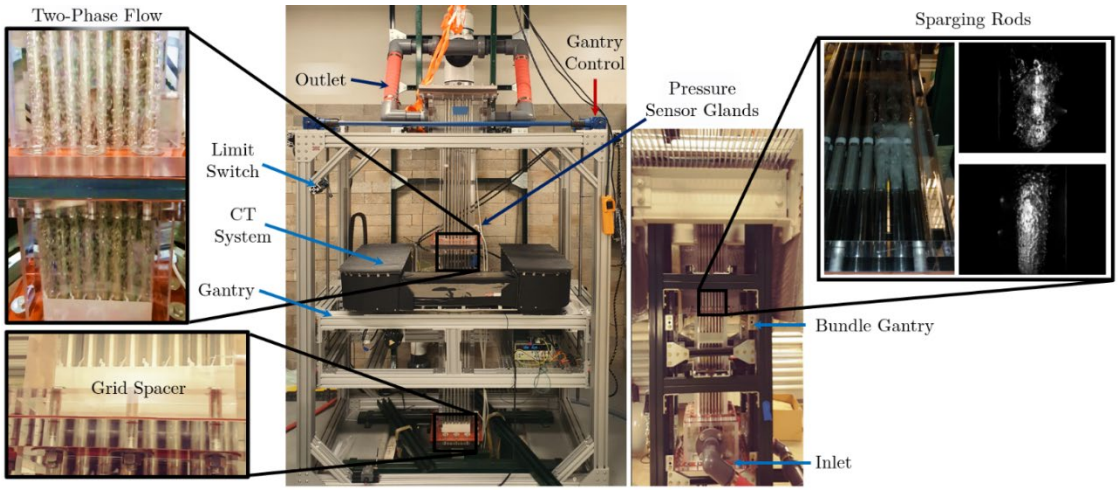

Fig. 5.4. Assembled MARBLE facility; example of two-phase flow, spacer grid, and sparging rods.

5.2.2.1. Gantry Systems

The rod bundle is supported by a 1-5/8" double channel unistrut frame which is fixed to the opening between the main floor and the basement floor; the frame is shown in Fig. 5.5. The test section is mounted on an inner gantry frame as depicted in Fig. 5.5, this allows the test section to move vertically for approximately 122 cm (48 inches), such that tomographic measurements can be performed at about 30.5 cm downstream from the sparger injection.

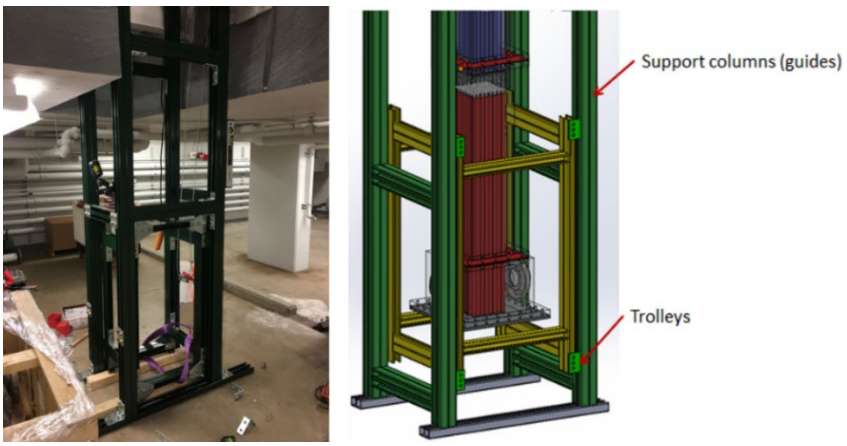

Fig. 5.5. Movable support gantry assembled (left) and design (right).

The HRGTS is mounted on a secondary gantry system in charge of displacing the CT scanner along the vertical direction. This gantry system consists of two separate aluminum frames. The first is the outer support frame highlighted in blue in Fig. 5.6.*a)*, the second is the CT platform highlighted in red; the later houses the rotary stage which mounts the HRGTS and is suspended on two screw jacks that pass through their corresponding acme nut. The platform is guided by four rail block systems, one on each corner of the frame, which are attached to the outer frame, these components are shown in greater detail in Fig. 5.7. The displacement of the platform is enacted by the gantry actuator mounted on top of the outer frame as shown in Fig. 5.6.*a-b)*. This system is comprised of two gear boxes connected via shafts to the two screw-jacks operated in "tension mode", the synchronized gearbox-screw-jack system is driven by a servomotor; the gantry actuator component arrangement is best depicted in greater detail in Fig. 5.6.*b)*. The gantry actuator system allows an axial displacement of 120 cm. The screw-jacks gear ratio is 1/20 and the ACME screw pitch is 4mm, allowing the system to move ~200mm/min, assuming a motor speed of 1000rpm. The finalized actuator gantry system is best depicted in Fig. 5.8. Lastly, the CT rotary stage is controlled by a DMM servomotor with three integrated limit switches highlighted in Fig. 5.9; the first limit switch is in charge of the rotary movement to constrain the system to a rotational range of 360°, the other two are a top and

bottom limit switch used to prevent the platform from over traveling past the designated limits. The system is fully disengaged whenever a limit switch is enacted.

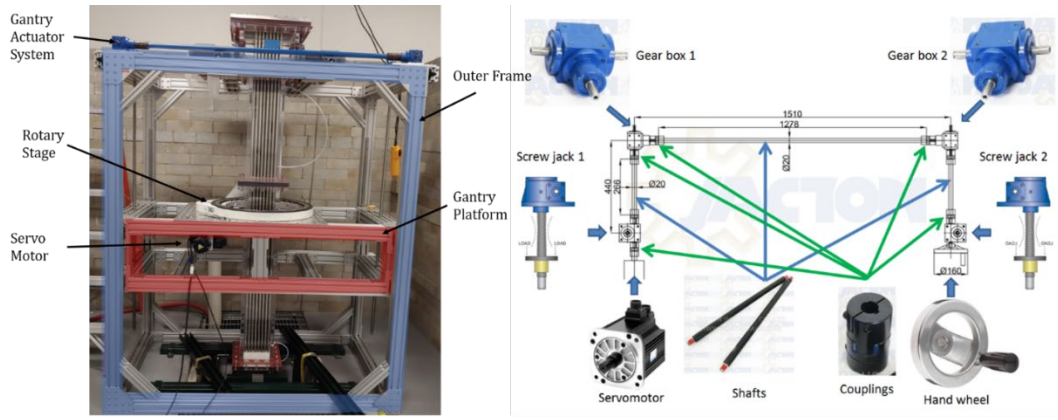

a) *b)*

Fig. 5.6. Gantry system layout: *a)* outer support frame is highlight in blue, gantry platform highlighted in red, the gantry actuator system is placed on-top of the outer frame and its layout is shown in panel *b)*.

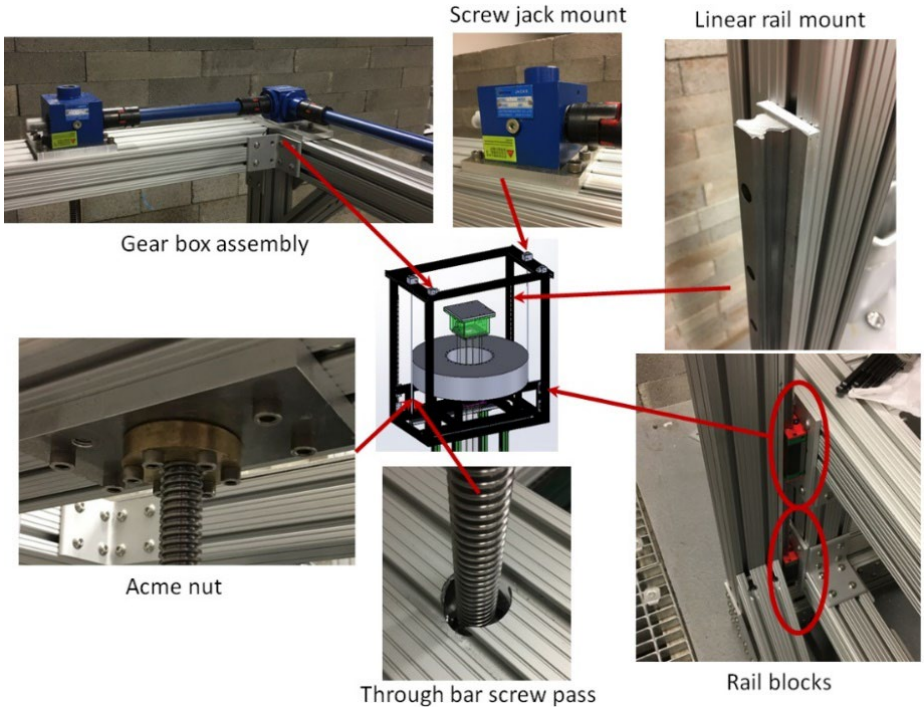

Fig. 5.7. Gantry system components relative to the gantry frame.

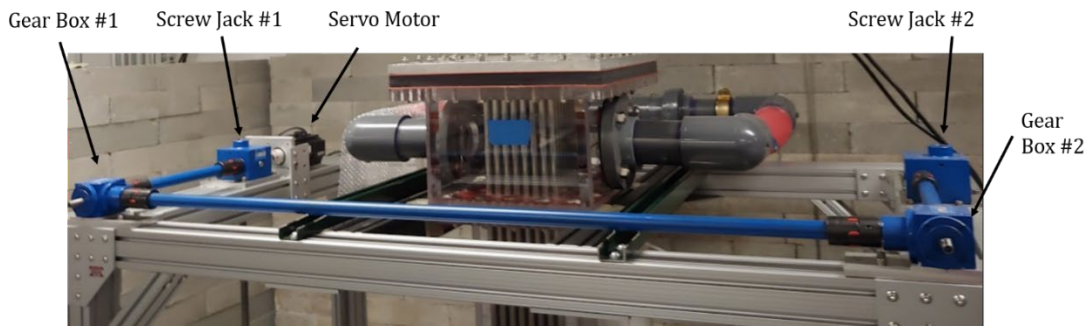

Fig. 5.8. Integrated gantry actuator system to the Adiabatic Bundle Experiment.

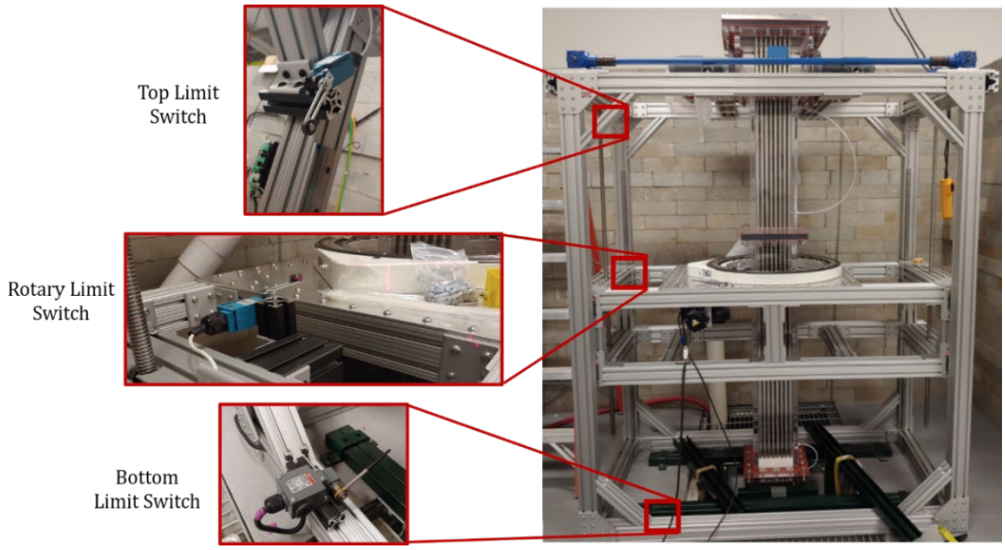

Fig. 5.9. Locations of the limit switches installed in the adiabatic bundle experiment.

5.2.2.2. Bundle Housing

The rod bundle housing consist of seven acrylic vertical duct sections as shown in Fig. 5.10; the acrylic housing has an inner area of 168.64×168.64 mm^2, an available flow area of 15771.7 mm^2, and spanning for a height of 3.8 m; the height of each section is detailed in Table 5.4. Custom made gaskets are placed between adjacent acrylic sections to seal the gaps. The sectional design provides easy access to install spargers, spacer grids, and the wire-mesh sensor. The axial distance between spacer grids was also scaled to 89.15mm based on the stipulated experiment scaling factor; details of the spacer grid are elaborated in Section 5.2.2.6. The wire mesh sensor (WMS) has not been installed but will be located between sections 5-6 with a PVC buffer used to space the adjacent acrylic sections; the WMS design is documented in Section 5.2.2.6.2. The rod bundle lid consists of a PVC buffer that acts as a top spacer grid and a 1.9 cm thick aluminum plate used to seal the upper region of the test section. The total height of the test section is approximately 3.88 m, this requires ample vertical clearance to construct and mount the test section. The

lab space assigned for the experimental facility at EMCFL allows access from the main floor to the basement space through floor apertures; therefore, the test section spans through two floors.

The inlet section (Sec.1) contains a flow stabilizing blade; several possible designs for the inlet flow distribution box were evaluated using CFD in order to determine the axial location of the air spargers and avoid air injection in a region where the flow is not yet fully developed; an example of the CFD simulation is depicted on the right of Fig. 5.3. Based on the results from the CFD simulations, it was decided to introduce the flow-stabilizing blade at the inlet in order to aid development of the flow at the site of the sparger gas injection. The manufactured flow stabilizing blade is shown in Fig. 5.11, as well as its assembly inside the inlet acrylic section. Detailed information of the sparging systems can be found in Section 5.2.2.4.2. The construction of the MARBLE facility is depicted in Fig. 5.12 which shows the insertion of rods and acrylic housing. Connector inserts were manufactured to connect rods, this can be used as a modular approach as well to simulate part length rods.

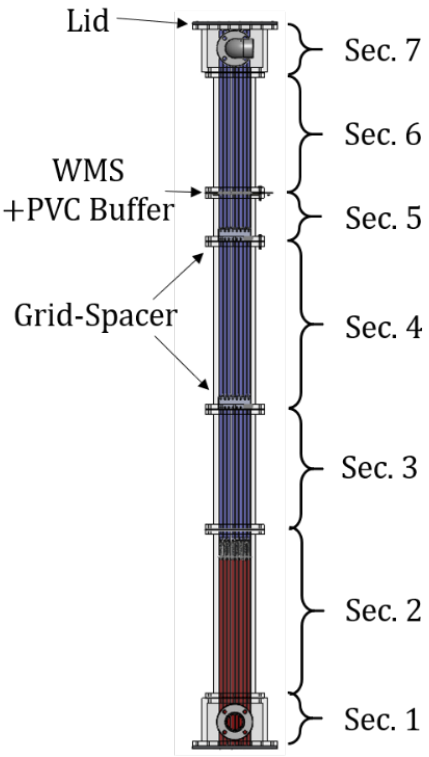

Fig. 5.10. Acrylic housing sections.

Table 5.4. Acrylic section heights

Section	Length [mm]
Sec. 1	249.2
Sec. 2	899
Sec. 3	635
Sec. 4	899
Sec. 5	254
PVC & 2x Gaskets	27.84
WMS +Gasket	3.42
Sec. 6	635
Sec. 7	249.2
PVC Lid	28.24
Total	3880.0

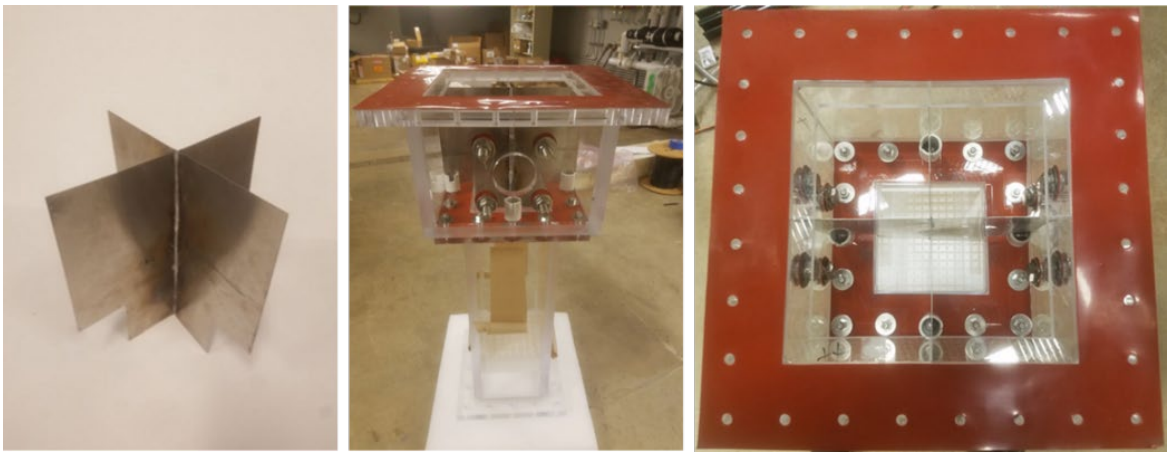

Fig. 5.11. Flow stabilizing blade (left), placement of the stabilizing blade inside inlet section (middle and right).

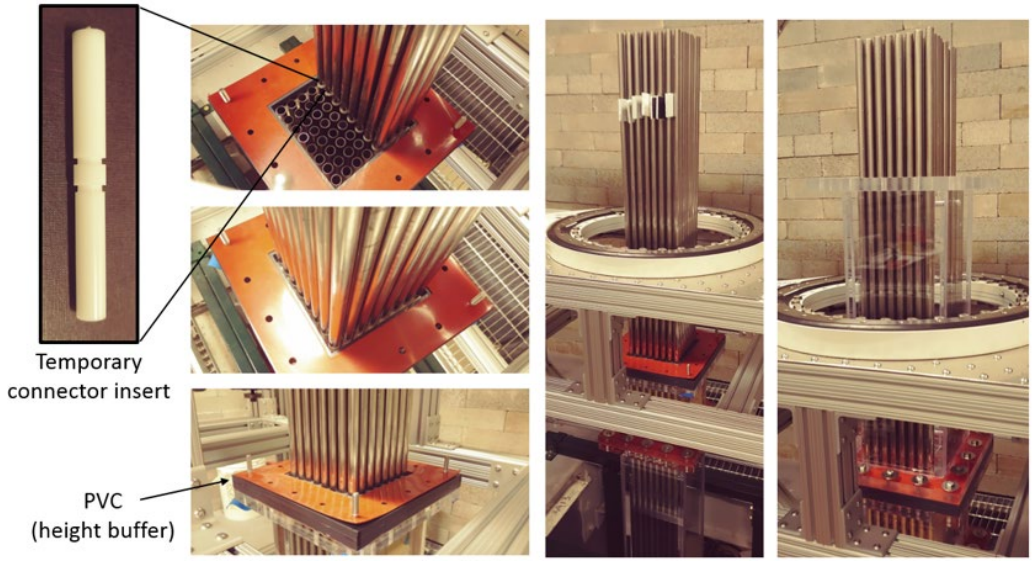

Fig. 5.12. Assembling of rod bundle, housing, PVC buffer, and connector inserts.

5.2.2.3. Liquid Circulation System

The liquid circulation system consists of two large water supply tanks connected to the main circulation pump. A recirculation line is placed around the pump and attached to this is the main drain line. the bulk of the fluid is directed from the pump through a coriolis mass-flow meter and is directed towards the experiment through an elephant trunk hose, this is then split into two flexible arms that attach into the inlet acrylic housing of the test section; the inlet of the test section is shown in Fig. 5.15. The water supply tanks are equipped with a bypass sand filtering system which activates periodically to clean and recirculate water inside the tanks during inactive periods. The schematic of the liquid circulation system is presented

in Fig. 5.13 and the assembled system is shown is Fig. 5.14; the latter figure shows the pump's VFD (variable frequency drive) and breaker system (on the top right).

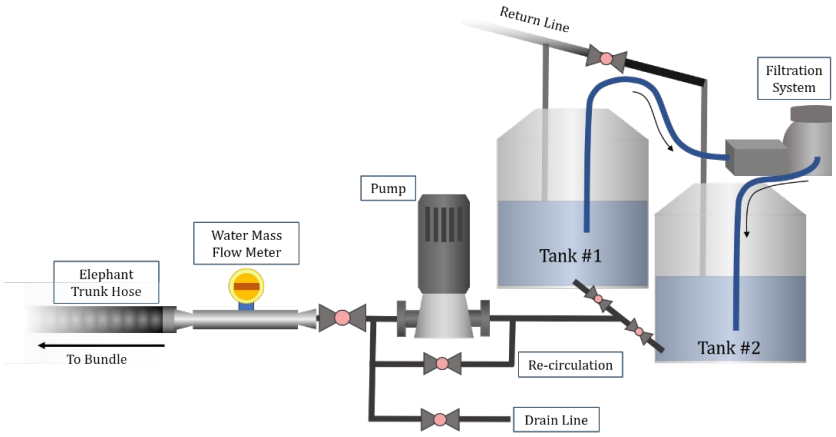

Fig. 5.13. Schematic of liquid circulation system.

Fig. 5.14. Assembled liquid circulation system.

Fig. 5.15. Elephant trunk hose split into two arms connected to the test section inlet.

5.2.2.4. Gas Injection System

The gas injection system is composed of several stages which consistently split and reduce the flow from a large-compressed air reservoir and onto the 64 individually controlled channel injections. This section documents the various working subsystems that comprise the gas injection system.

5.2.2.4.1. Gas Reservoir and Compression

The gas reservoir consists of two 240-gallon tanks connected in series to a 120-gallon air compressor tank. The total available gas reservoir volume is 2.27 m^3 and is charged with compressed air at 1034.2 kPa (150 Psi); this provides sufficient gas to operate the experiment in steady state mode. Each receiver tank is equipped with a 1379 kPa (200 Psi) safety relief valve, a pressure gauge, and a liquid drain valve placed on the bottom; these are represented in the diagram shown in Fig. 5.16 with the exception of the drain valves. The assembled system is shown in Fig. 5.17. The receiver tanks are connected onto the air-compressor system with a 60" steel braided hose which docks onto a 4-way cross; this serves as a flow diverter between the air compressor, the receiver tanks, main line and an alternative line. Each of the pneumatic lines that are connected to the cross are equipped with ball valves to enable/disable the flow through the specific paths. The ball valves are enumerated in Fig. 5.16 and the assembled system is shown in Fig. 5.17 and Fig. 5.18; the valve denoted as #1 isolates the receiver tanks, the valve denoted as #2 isolates the air compressor, the valve denoted as #3 isolates the main line directed towards the adiabatic bundle experiment, and the valve denoted as #4 was placed as an alternative line in case additional equipment needs to be connected. The tank reservoir is in a filling state when the ball valves #3 and #4 are closed, this allows the compressed air to fill all the tanks. During experimental operation, valve #3 is opened to allow flow towards the experimental facility. A pressure regulator is placed upstream from the gas-reservoir system in order to step down the pressure and stabilize the air directed towards the individual injection lines. This pressure regulator is placed immediately prior to the manifold which splits the main line into five smaller lines and is shown in Fig. 5.19 in the next section.

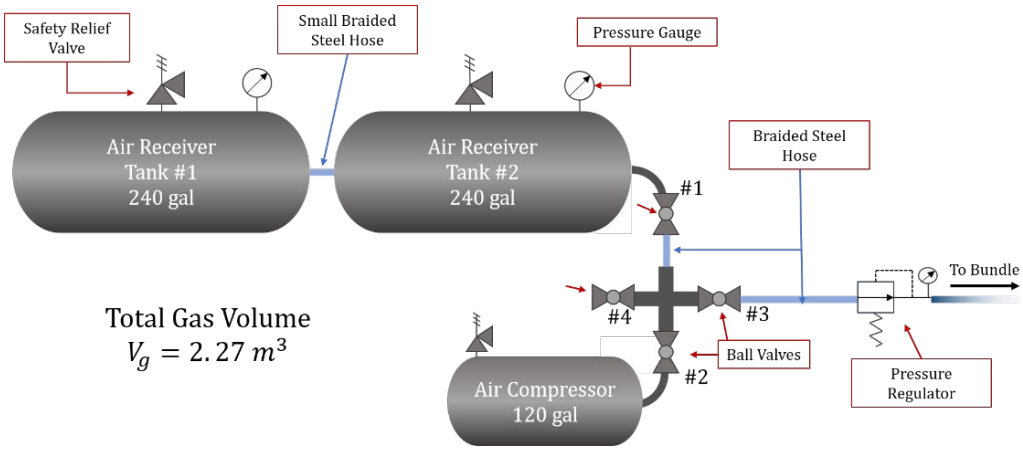

Fig. 5.16. Air reservoir and compressor system schematic.

Fig. 5.17. Assembled receiver tanks.

Fig. 5.18. Pneumatic cross intersection from air compressor to remainder of the system.

5.2.2.4.2. Gas Injection System

The gas coming from the reservoir system needs to be consistently split through several stages. The next step is splitting the flow into five separate lines, these represent partitioned groups assigned to the 8x8 arrangement (further explained in Fig. 5.24). Each line is equipped with a ball valve, filter, and a mass flow

meter. The manifold system is equipped with an absolute pressure transducer attached to the end of the manifold in order to monitor the incoming gas pressure. The assembled system is shown in Fig. 5.20.

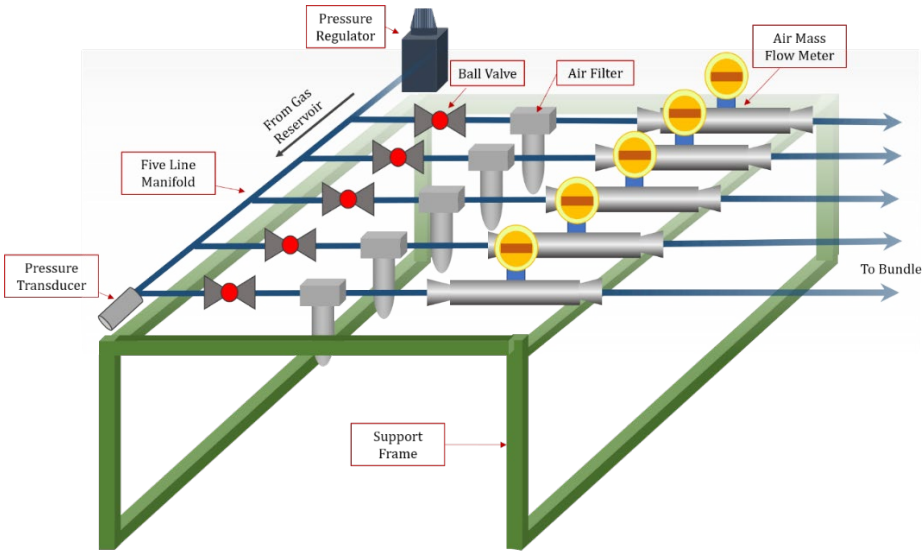

Fig. 5.19. Schematic of main line split into five lines, each line equipped with ball valve, air filter and mass flow meter.

The flow coming from the individual gas lines is further split by five groups of manifolds which finally reduces into the 64 individual gas lines that feed into the adiabatic bundle. The manifold system's inlet is a Barb adapter connected to a PVC coupling, and a two-way splitter. The flow is then directed to two manifold blocks which contain compression fittings and push-in elbows. The manifold blocks are also equipped with k-type thermocouple to acquire temperature data for each injection group. The manifold systems are arranged to direct four groups of 12 lines, and one group of 16 lines, 64 lines in total. The manifold system schematic is shown in Fig. 5.21 and an example of the assembled manifold system is presented in Fig. 5.22.

Fig. 5.20. Pressure regulator connected to the manifold system where the flow is split into five gas lines.

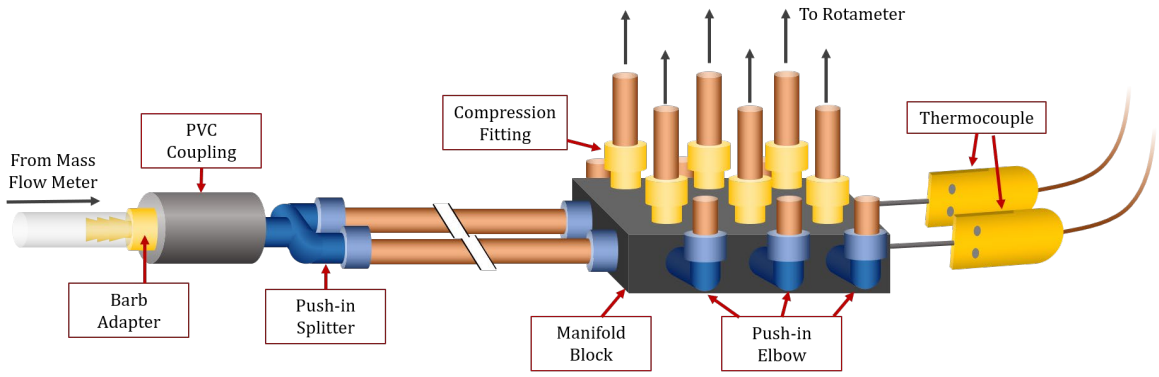

Fig. 5.21. Schematic of manifold system used to split the flow into individual channels.

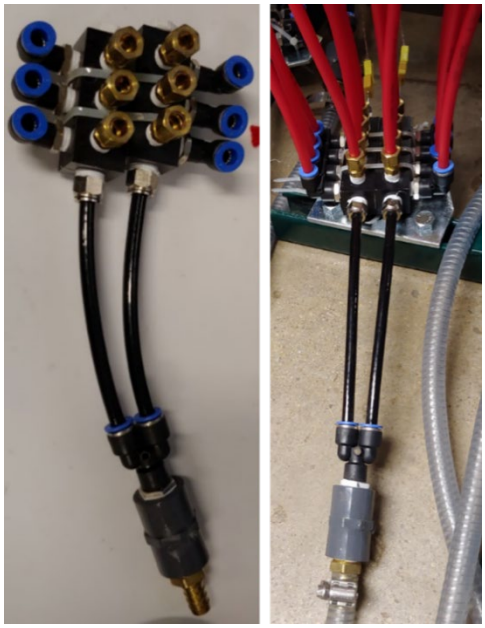

Fig. 5.22. Example of assembled manifold system.

The gas injection system incorporates individual gas flow-control rotameters for each corresponding channel of the MARBLE facility. In order to accommodate the 64 rotameters near the inlet of the spargers, mounting metal strips were designed to be placed on the experiment's gantry support frame; these are mounted in two sets of rows with a pitch of 6.35 cm (2.5 inches) between adjacent rotameters, placed along the three sides of the gantry frame closest to the main gas lines. A check-valve is connected upstream from the rotameter to prevent water backflow from the test section and into the air injection system. The schematic for the individual rotameter flow-control element is depicted on the right of Fig. 5.23. The fully assembled flow control system is presented in Fig. 5.24. The rotameter injection systems are color-coded to identify the five separate groups correspondent to the manifold systems; the group assignments are shown in the central diagram of Fig. 5.24 and denoted as G for each color-coded group. The individual channels

are identified with T representing top rotameters and B representing bottom rotameters. The manifold system that accommodates four groups of 12 channels is represented by groups G_1 through G_4, the central group denoted as G_5 accommodates 16 channels.

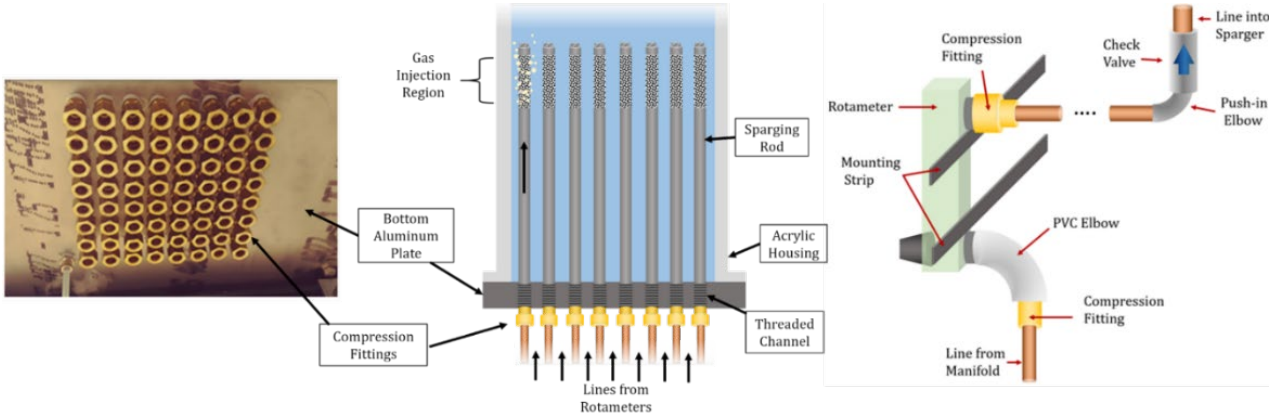

Fig. 5.23. Individual rotameter schematic (right), sparging rod injection (middle), and bottom plate compression fittings (left).

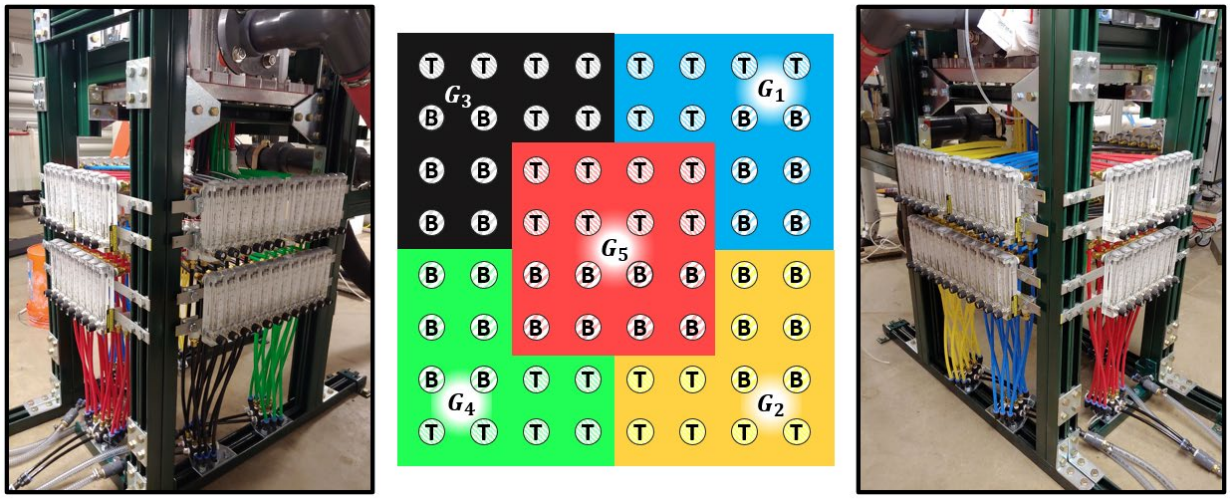

Fig. 5.24. Mounted gas injection system (left and right), connection layout with color coded groups (center), T denotes top connections and B denotes bottom connections.

The final stage of the gas injection system are the individual sparging rods of 1.125 m in length with an active gas injection length of 84 mm composed of a mesh porosity of 100 μm; the sparging rod outer diameter is 15.875 mm thus matching the rod element diameter which are mounted above the spargers. The bottom plate of the experiment was drilled and tapped such that the sparging rods could be screwed in place, brass compression fittings are placed underneath the plate shown on the left of Fig. 5.23; the schematic of the final injection stage is best visualized on the center panel of Fig. 5.23. Plastic insert adapters are attached to the top of the sparging rod to connect these to the remainder length of the assembly rods above. An example of the sparging rods gas injection is shown Fig. 5.25.

Fig. 5.25. Examples of sparging rod air injection.

5.2.2.4.3. Gas Removal

The vertical return line that connects to the outlet of the rod-bundle has been designed to incorporate an air separation section. The design consists in raising the flexible outlet arms of the experiment, which assists with further mixture separation due to the air buoyancy. The large separation volume drives the bulk buoyancy-separation of the air-water mixture as the air stratifies in this section. This volume increases the pipe diameter from 10.16 cm (4 inches) to 20.32 cm (8 inches) which effectively increases the cross-sectional area by a factor of four resulting in a decrease in velocity in this section that further enables the air-water separation. A butterfly valve is placed at the bottom of the separation volume, thus regulating the flow, and allowing the volume to be partially or fully filled with water. The top of the expansion volume is connected to an air exhaust-line that is directed across the upper yellow support frame (on the lab ceiling) and discharges to an auxiliary tank. A ball valve is placed prior to the tank in order to control the flow and regulate the pressure build-up in the system. The auxiliary tank in reality serves as an expansion tank to which air can be released, and also captures any liquid that makes it through the air separation line. Liquid from the expansion tank is drained from the first floor to the basement reservoir tanks by means of gravity. A support frame is built between the floor and the upper frame to reinforce the large separation volume; this frame holds the large piping with clamps distributed along the vertical height of the return line to minimize vibration. The designed return-line/mixture-separation system is depicted in Fig. 5.26; the design does not depict the butterfly valve placed at the bottom of the separation volume. The assembled system

is shown in Fig. 5.27 which aims to highlight the size of the individual components of the gas removal system, and its relative size in comparison to the rod bundle.

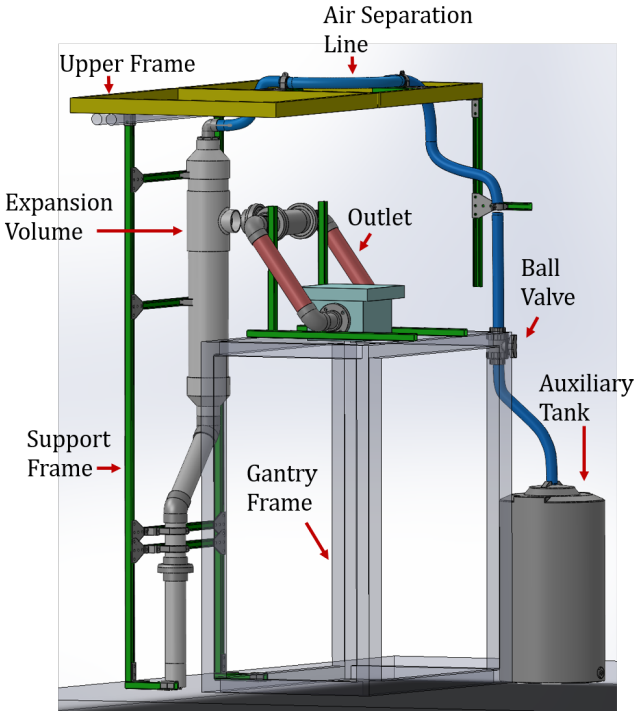

Fig. 5.26. Designed air-water separation system.

a) *b)* *c)*

Fig. 5.27. Assembled return line: *a)* installed butterfly valve, *b)* top-view of the expansion volume, and *c)* degassing line, ball valve with expansion tank.

5.2.2.5. Monitoring Sensors

Several sensors have been installed throughout the facility to monitor the conditions of the working fluids. These include the aforementioned gauge pressure sensor installed after the pressure regulator on the main gas supply line, as well as after the circulation pump. Thermocouples were also placed inside the

manifold systems to monitor the temperature of the gas prior to sparger injection. The MARBLE facility is equipped with two gauge pressure (GP) transducers installed near the outlet and at the sparger level of the bundle, these are denoted with the subscript Top and Spg respectively in Fig. 5.28; an additional thermocouple (TC) is installed next to sparger gauge pressure transduce in order to monitor the temperature and determine the boundary conditions next to the gas injection region. Additionally, six differential pressure sensors are installed on the same side of the rectangular rod-bundle housing, to monitor the pressure drops throughout the different sections, these are denoted as $\Delta P_{\#}$ in Fig. 5.28. The differential pressure sensors are connected in series such that adjacent sensors share a common port, therefore the high-pressure of one corresponds to the low-pressure of the next; the high pressure is directed downward towards the sparger, and the low pressure is directed upward towards the top of the bundle. The corresponding monitoring heights as well as the corresponding static head pressure ($\rho_L g h$) are also depicted in Fig. 5.28; here ρ_L is the liquid density assumed to be 998 kg/m3, g is gravity, and h is the relative height between two points. Kamei et al. [81] implemented an arrangement in which the differential pressure sensors were installed on all four sides of the experiment's housing and covered the same axial distance, the pressure drop results did not show any significant difference based on location. This provides reassurance that the pressure can be treated as a function of axial location and that local effects are minimal in comparison, thus justifying a single connection per axial location in the case of the MARBLE facility.

The implementation of pressure drop sensors is extensively used throughout the rod bundle experiments, as is illustrated in Table 1.3. Matsui [118] previously aimed to describe the flow regimes based on differential pressure fluctuations, nevertheless this is a hard task given that only one aspect of the flow is being considered, particularly for complex geometries such as reactor assemblies. Since, pressure drop measurements have been complimented with gamma-densitometry methods in order to improve the description of the two-phase flow as detailed by Vassallo et al. [186]. Although the purpose in the present description is to characterize the performance of the differential pressure sensors, useful guidance was found from the mentioned literary sources. Here we perform simple proof of concept to validate the results obtained from the differential pressure sensors. First, we define the pressure across the bundle using the gauge pressure as

$$\Delta P_{GP} = GP_{spg} - GP_{Top}. \qquad \text{Eq.(5-12)}$$

Next, we must define the differential pressure for an individual sensor; based on the way the connections

are established in Fig. 5.28, this requires the addition of the static liquid head pressure corresponding to the ports that the differential sensor monitors as

$$\Delta P_{Sensor} = P_A - P_B + \rho_L g h_{AB}, \qquad \text{Eq.(5-13)}$$

where A and B are the vertically high and low ports correspondingly. This is an intuitive procedure demonstrated by Vassallo et al. [186]. Now by rearranging the above expression we obtain

$$\Delta P_{Sensor} + \rho_L g h_{AB} = P_A - P_B. \qquad \text{Eq.(5-14)}$$

Therefore, it is observed that the difference in pressure between the high and low port results in the addition of the equivalent liquid head to the differential pressure sensor reading. Now we can define the total pressure drop across the bundle using the sum of the differential pressure sensor readings as well as the corresponding static head pressures,

$$\Delta P_{DP} = \sum\nolimits_i \Delta P_{Sensor,i} + \rho_L g h_i, \qquad \text{Eq.(5-15)}$$

where the subscript i denotes the corresponding bundle sections between measuring ports, the subscript DP denotes the total pressure drop estimation obtained from the differential pressure sensors.

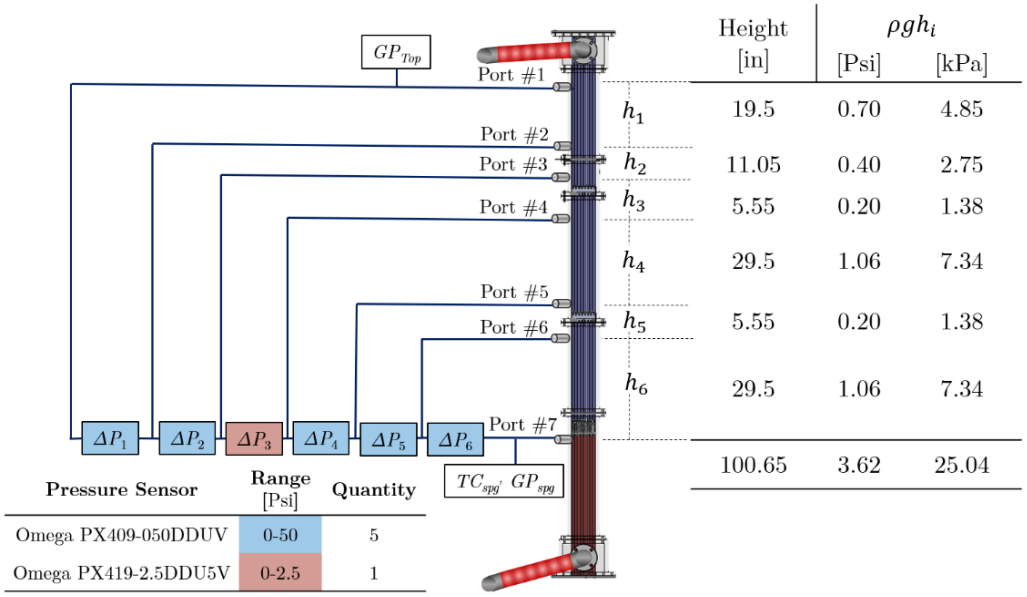

	Height [in]	$\rho g h_i$ [Psi]	$\rho g h_i$ [kPa]	
h_1	19.5	0.70	4.85	
h_2	11.05	0.40	2.75	
h_3	5.55	0.20	1.38	
h_4	29.5	1.06	7.34	
h_5	5.55	0.20	1.38	
h_6	29.5	1.06	7.34	
	100.65	3.62	25.04	Total

Pressure Sensor	Range [Psi]	Quantity
Omega PX409-050DDUV	0-50	5
Omega PX419-2.5DDU5V	0-2.5	1

Fig. 5.28. Pressure transducer arrangement.

5.2.2.6. Future Upgrades

This section briefly touches on additional instrumentation that was manufactured for the MARBLE facility but that was not implemented during the scope of the present research. These are planned upgrades that will be incorporated in the future.

5.2.2.6.1. Spacer Grid

The spacer grids used in the MARBLE facility were also scaled following the postulated scaling factor, which is adapted to the design pitch and rod diameter of the assembly design. The current spacer grids deployed in the MARBLE facility were manufactured using 3D printing methods as shown in Fig. 5.29. These pieces are characterized by their thin wall thickness and protruding mixing vanes; however, the mixing vanes are subject to breakage due to the brittleness of the printed plastic material as was experienced during flow tests.

The spacer grid was redesigned to be manufactured from stainless steel plates; this consists of eight custom designed plate pieces separated into two categories, outer and inner. The outer plates' mixing vanes and support springs point inward and have female mating slots to lock with the inner plate; all four pieces have different symmetry therefore are unique in their manufacturing. The inner plates are designed for the longitudinal (row) and latitudinal (column) directions, with mating slots placed on the top or bottom depending on the direction of the part. The spacer grid assembly requires a higher quantity of the inner plates given that they repeat every other row/column. Fig. 5.30 shows the designed individual plates on top and the assembled spacer grid on the bottom. The plates were manufactured in 24 gauge (0.025"), 304-stainless steel. The metal forming of the springs and mixing vanes, as well as the welding process were performed in house; an example of an assembled spacer grid is depicted in Fig. 5.31.

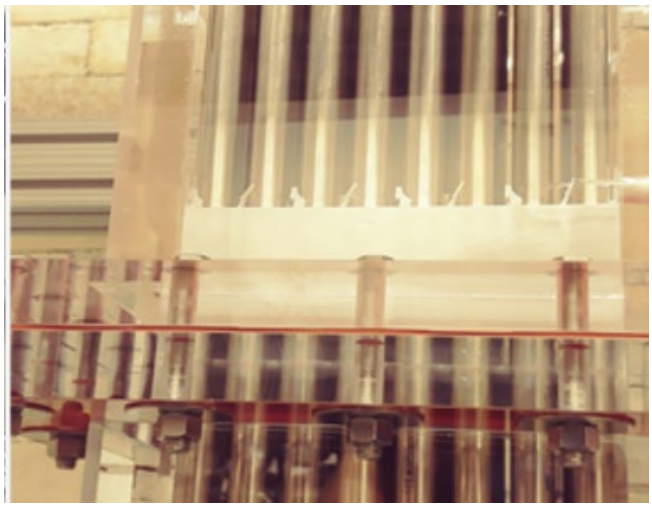

Fig. 5.29. Example of 3D-printed spacer grid.

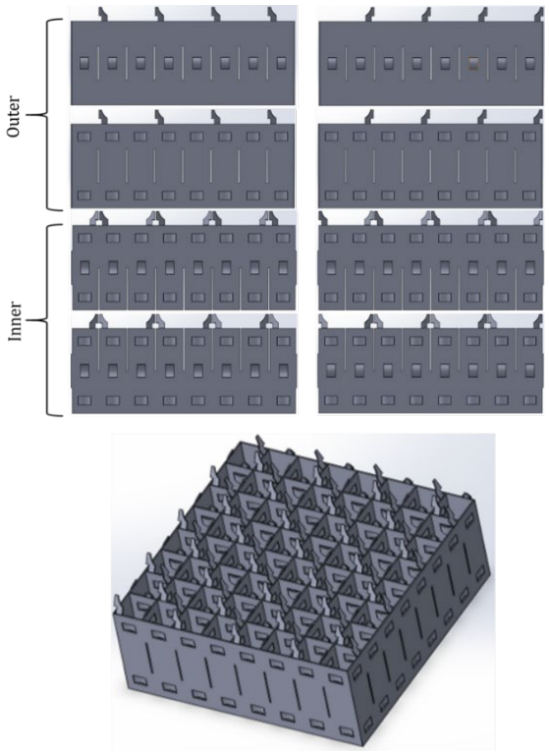

Fig. 5.30. Design of eight separate spacer grid plates (top), assembled spacer grid (bottom).

Fig. 5.31. Metal formed spacer grid.

5.2.2.6.2. Wire Mesh Sensor

The wire-mesh-sensor (WMS) board was custom designed to match the acrylic housing opening and through holes. The WMS consists of a 48x48 grid with an electrode spacing and spatial resolution of 3.5 mm. The signals are transmitted over three DB-25 connection sites, grouped into 16 wires per connection, the receiver connections are also split into three DB-25 connections, each in charge of 16 receptor wires. The WMS acquisition system will be located at a distance of about 21.8 cm above from the second spacer grid.

The incorporation of the WMS into the adiabatic facility requires the implementation of custom inserts which do not interfere with the WMS transmission wires, but which also connect the assembly rods. This includes separate designs for the top and bottom sections. The design of the inserts involves a 3x3 slot arrangement, each slot is 2.1 mm in diameter and has a depth of 15 mm. Fiber glass rods are cut and inserted into the slots to connect top and bottom inserts; the selected material is sufficiently sturdy to support the weight of the supported rods and is also non-conductive which ensures this does not affect the data acquisition process of the WMS. The fiberglass rods are narrow enough to pass through the WMS grid

shown in the zoomed in portion of Fig. 5.32. The schematic for the WMS and the inserts is shown in Fig. 5.33. The bottom rods were observed to protrude at different heights during the assembling process; therefore, the bottom inserts were designed with custom active heights denoted as H1 in Fig. 5.33 such that the inserts equalize the heights to the same plane. The design of the top inserts are standardized and have an active height of 10 mm. The bulk body of the insert is designed to match the inner diameter of the rod (within a tolerance of 0.005”), the body is then tapered to a smaller diameter to facilitate the insertion process. The assembly of designed inserts is shown in Fig. 5.34. The inserts were also manufactured using 3D printing methods.

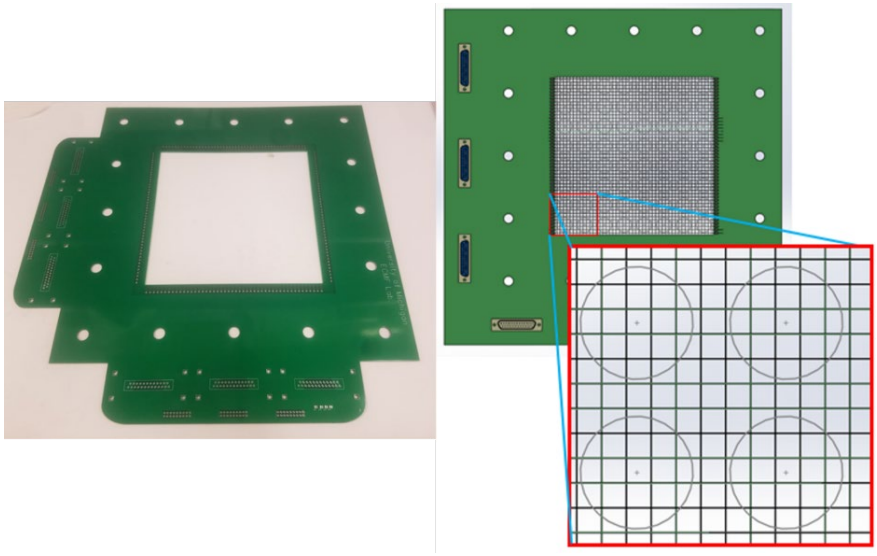

Fig. 5.32. Wire-mesh sensor design.

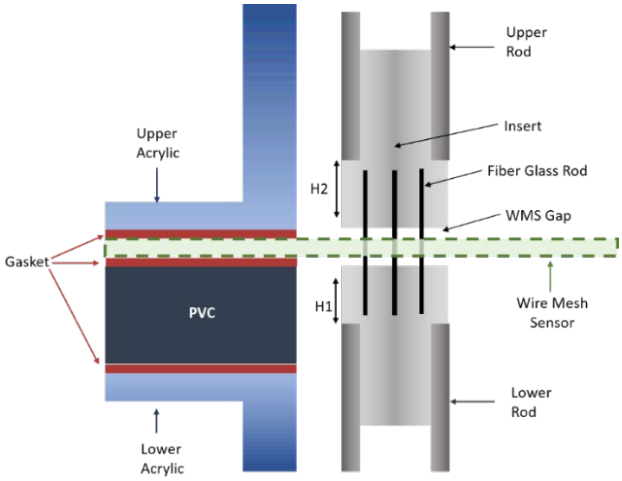

Fig. 5.33. Wire mesh sensor and rod insert schematic.

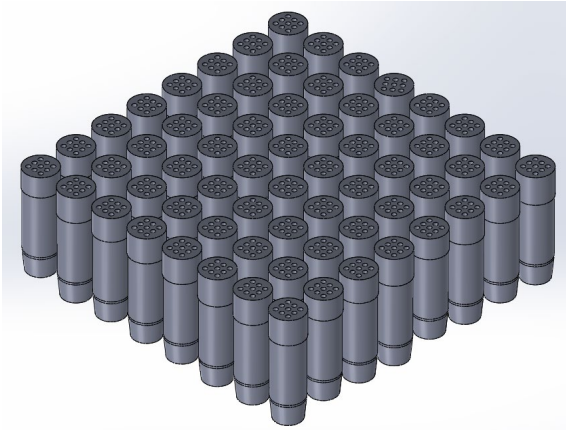

Fig. 5.34. Rod insert assembly design to be used in below WMS plane.

5.2.3. Determination of Superficial Velocities

The conversation will now shift and explain the applied methods used to determine the superficial gas velocity, which is an important parameter required to define the experimental boundary conditions and establish the flow regimes associated with the given flow geometry. To estimate this parameter, we must first determine the gas density as a function of the measured temperature T, and bundle pressure P; the latter needs to be converted to absolute pressure and can be considered for the various pressure locations measured throughout the bundle. In the present research we estimate the gas density using the RefProp [105] database for dry air. The variance of the estimated gas density is obtained by applying the error propagation formula as

$$\sigma_{\rho_g}^2 = \sigma_P^2 \left(\frac{\partial \rho_g}{\partial P}\right)^2 + \sigma_T^2 \left(\frac{\partial \rho_g}{\partial T}\right)^2. \qquad \text{Eq.(5-16)}$$

The superficial gas velocity can then be estimated from the gas mass-flow rate $\dot{m}_g$, the flow area A_{fl}, and the calculated gas density

$$j_g = \frac{\dot{m}_g}{A_{fl}\ \rho_g(P,T)}. \qquad \text{Eq.(5-17)}$$

The variance of the estimated superficial gas velocity is similarly derived using the error propagation formula:

$$\sigma_{j_g}^2 = \sigma_{\dot{m}_g}^2 \left(\frac{\partial j_g}{\partial \dot{m}_g}\right)^2 + \sigma_P^2 \left(\frac{\partial j_g}{\partial P}\right)^2 + \sigma_T^2 \left(\frac{\partial j_g}{\partial T}\right)^2. \qquad \text{Eq.(5-18)}$$

Lastly, the liquid superficial velocity is estimated using the same general relations as Eq.(5-17), and substituting the liquid mass flow rate and density,

$$j_L = \frac{\dot{m}_L}{A_{fl}\ \rho_L(P_{spg}, T_{spg})}. \qquad \text{Eq.(5-19)}$$

Similarly, the liquid density is also estimated as a function of the sparger gauge-pressure and temperature, this is done using the RefProp [105] database for water for the remainder of this research; here the liquid density is assumed to be constant throughout the bundle height due to water's incompressibility properties.

5.2.4. Shakedown Test

In the current section we present a two-phase flow shakedown test in order to demonstrate the operation of the MARBLE facility. The test was carried out by circulating water at around 10 kg/s, the gas reservoir tanks were charged to their maximum capacity of 1034.2 kPa (150 Psi), the pressure regulator was set to

482.6 kPa (70 Psi) and data was sampled at a rate of 500 ms. Prior to the release of the gas, a prolonged measurement of the all-liquid system is carried out for a period of about 10 minutes. The transient event was then initiated by opening the main gas line and injecting air into the bundle with all 64 rotameters fully open, this resulted in an initial rise in pressure throughout the bundle as depicted in Fig. 5.35.*a*; the sparger pressure rose to about 57.0 kPa (8.27 Psi), the top of the bundle rose to 37.0 kPa (5.37 Psi), and the circulation pump outlet pressure increased to 116.0 kPa (16.82) Psi. Subsequently, a decrease in pressure throughout the system is observed once the gas reservoir pressure drops below the 482.6 kPa threshold imposed by the pressure regulator. Eventually, the pressure becomes asymptotic as the system reaches equilibrium with the air compressor supply. At the end of the transient event, a prolonged measurement of the liquid is performed once again. The transient event is depicted throughout Fig. 5.35.*a*, which plots the gauge pressure for the top of the bundle, sparger, and pump. The total gas mass flow shown in Fig. 5.35.*b* is obtained as the sum of the 5 x Coriolis gas mass flow meters, the depicted trend follows the pressure curves depicted in Fig. 5.35.*a*. Similarly, the liquid mass flow is shown in Fig. 5.35.*c* which depicts a decrease in the liquid mass flow to about 9 kg/s in response to the increase in pressure experienced by the pump; this is followed by an exponential build up back to normal operation as the pressure in the system decreases.

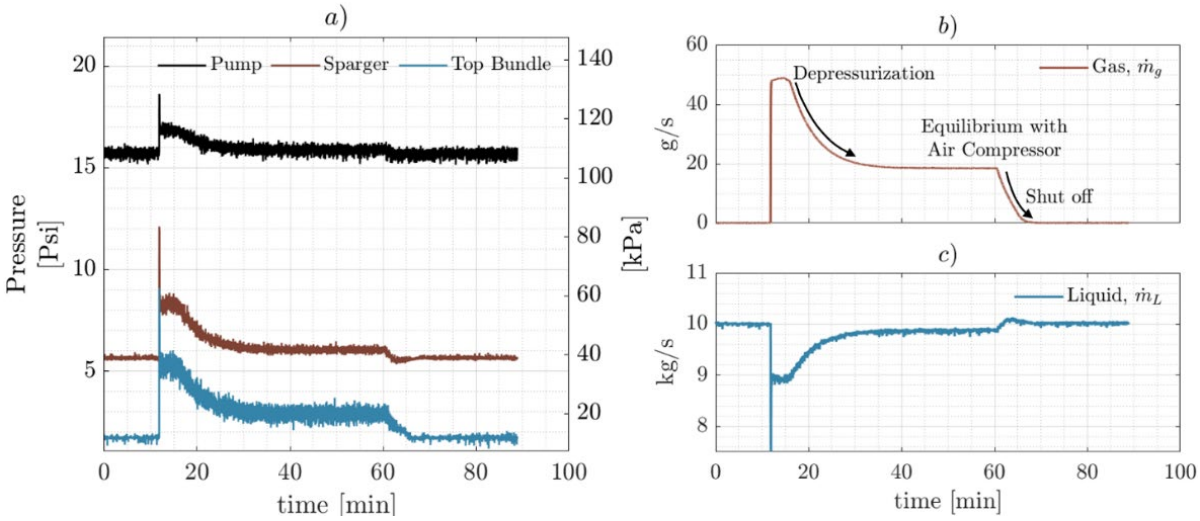

Fig. 5.35. Shake down test; *a)* gauge pressure of the pump, sparger, and top of the bundle; *b)* gas mass flow rate; *c)* liquid mass flow rate.

The sparger temperature presented in Fig. 5.36.*a)*, increased subtly by a little over 1 C°. This temperature is used as reference to estimate the gas density at the spargers and at the top of the bundle, as shown in Fig. 5.36.*b)*. The density trends follow the sparger's pressure curve depicted in Fig. 5.35.*a)* given that the density is directly proportional to the pressure, while the temperature does not significantly

increase. Additionally, the estimated density near the top of the bundle is lower than at the sparger. The estimated gas superficial velocity is shown in Fig. 5.36.*b)* for the sparger as well as the top of the bundle. The superficial gas velocity at the sparger level is about 1.6 m/s during the initial stage of the transient, afterwards, it settles to about 0.7 m/s as the system reaches equilibrium with the gas supply from the air compressor. The estimated superficial gas velocity at the top of the bundle is larger than at the injection. Following the inverse relation with the density from Eq.(5-17) results in an overall increase in superficial gas velocity at the top of the bundle. The liquid superficial velocity shown in Fig. 5.36.*c)* is a scaled representation of the liquid mass-flow rate depicted in Fig. 5.35.*c)*.

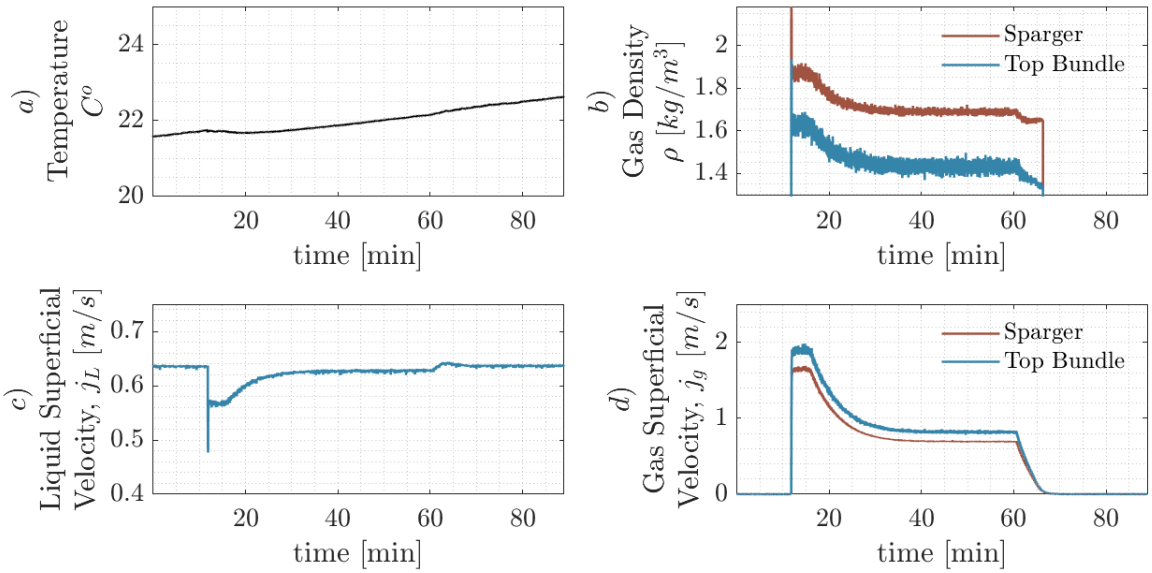

Fig. 5.36. *a)* Sparger temperature, *b)* estimated gas density at the sparger and at the top of the bundle, *c)* superficial liquid velocity, and *d)* estimated gas superficial velocity at the sparger and at the top of the bundle.

The bundle pressure drop for the two proposed methods described by expressions Eq.(5-12) and Eq.(5-15) are depicted in Fig. 5.37.*a)*; the methods namely being the estimation based on the gauge pressure (*GP*) sensors and from the differential pressure (*DP*) sensors. It is important to add that the curves represent moving average values (with a 5 sample window) of the pressure drop given that the data is noisy, which makes it difficult to depict of the trend, however this is only implemented for visual purposes. The pressure drop of the bundle is the highest during the all-liquid operation, however, during the two-phase transient, the pressure drop lowers. This effect is caused by the overall change in density that the bundle experiences due to the water-gas mixture. To be clear, the overall pressure of the system rises as observed in Fig. 5.35.*a)*, but the relative difference in pressure between the sparger level and the top of the bundle decreases

due to the effective density reduction in comparison to the all-liquid system. As the gas injection slowly terminates, the pressure drop returns to the all-liquid system value; the small deviation is suspected to arise from trapped gas in the pressure glands. The two methods show significantly good agreement and follow the same trend, thus reassuring that the post-processing application of the differential pressure sensors is being properly applied.

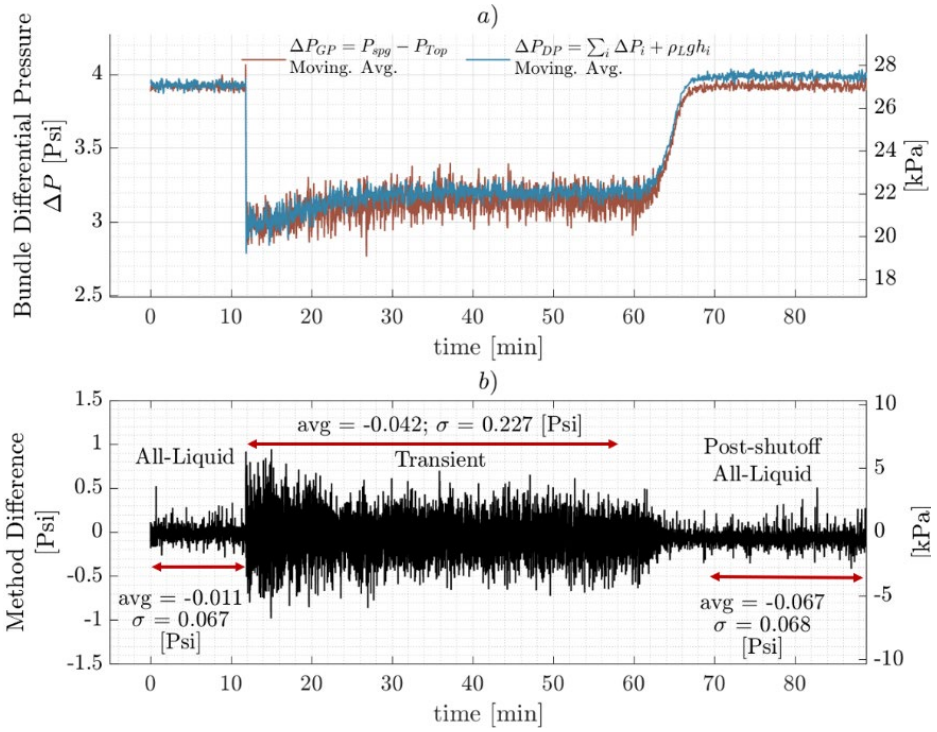

Fig. 5.37. ***a)*** **Pressure drop estimated from the gauge pressures, and from the differential pressure sensors.** ***b)*** **absolute difference between the two methods with average and standard deviation values shown prior, during and post transient.**

The relative difference between the two methods was estimated to quantify their agreement; this relative difference was defined as

$$\Delta P_{Methods} = \Delta P_{GP} \; - \; \Delta P_{DP}, \qquad \text{Eq.(5-20)}$$

and is plotted in Fig. 5.37.*b)*, highlighting the values for the average difference and standard deviation of the corresponding all-liquid and transient sections. The relative difference results quantify an average deviation of about 0.46 kPa (0.067 Psi) at most between the two methods. The standard deviation is about 0.47 kPa (0.068 Psi) for the all-liquid system; however, this grows to about 1.57 kPa (0.227 Psi) during the two-phase flow transient. These results show proper agreement between the pressure sensor instrumentation, with the standard deviation increasing whenever a two-phase system is present, nevertheless, this is to be

expected given the chaotic nature of these conditions. More importantly, the pressure drop validation between the gauge pressures and the differential sensors assures us that the pressure can be approximated for an arbitrary height throughout the bundle, specifically to estimate the resulting superficial gas velocity at the CT measurement plane.

5.3. Modeling of MARBLE and HRGTS

The current section discusses the modeling process of the MARBLE facility in order to perform CT reconstruction simulations based on the HRGTS detector design. These simulations are used to fine tune the reconstruction parameters and gain insight into the performance of the HRGTS as an advanced measurement tool deployed for two-phase flow applications.

5.3.1. Modeling of MARBLE

Simulations of the MARBLE facility were conducted in order to estimate the imaging performance of the HRGTS; previously the imaging resolution of the system was determined to be between 0.71 – 1.0 mm shown in Section 2.3.1.2 and demonstrated by Adams et al. [2]. The forward projection of the MARBLE facility and the HRGTS were modeled using the ray-tracing methods discussed in Section 2.4 and by estimating the mass attenuation of the present materials applying Eq.(2-12); the detector system was simulated as individual detector-element volume objects in order to increase the fidelity of the imaging process by inducing the spatial blurring from these. This section will focus on determining the ideal reconstruction parameters including pixel size and sinogram filter. To achieve this, a parametric study of the effects of the pixel size and the applied sinogram filter is conducted using the noiseless sinogram. The parametrized pixel sizes were assigned as divisible values of the rod-pitch/subchannel (21.08 mm) and span divisible values between 10 to 250, corresponding to pixel resolutions of 2.108 mm/pix to 0.0843 mm/pix. The filters of interest include the following: Ram-Lak, Shepp-Logan, Cosine, Hamming and Hann. The idealized attenuation map is rendered for the imposed pixel size based on the geometric layout of the test section, the linear attenuation coefficient is assigned to the individual object-regions such as acrylic housing, stainless steel rods, and flow area. The reconstruction is then obtained by performing filter back projection (FBP) based on the imposed pixel size and applied filter. Examples of the ideal attenuation map and the reconstructed objects are shown in Fig. 5.38 for the all-liquid and for the all-gas bundle system.

The pixel-wise RMSE is estimated to assess the agreement between the idealized attenuation map μ,

and the noiseless reconstruction $\hat{\mu}$; this can be described as follows:

$$RMSE = \sqrt{\frac{1}{K}\sum_{k}^{K}(\mu_k - \hat{\mu}_k)^2}, \qquad \text{Eq.(5-21)}$$

where k denoted the pixel-wise operation, and the error is averaged over the pixel population K. The evaluation of the RMSE for case of the Ram-Lak filter is depicted in Fig. 5.39 where the all-liquid and all-gas systems are compared; the scatter dots represent the imposed pixel sizes, and the continuous curves depict moving averages using a 5 sample window. The moving average curve initially decrease to a valley as the pixel size is reduced from its initial coarse value, this the increases once it becomes increasingly fine; in the latter. The results show that there is a region of pixel sizes in which the reconstruction and ideal map have the highest agreement where the RMSE is minimized; this region spans roughly between pixel sizes of 0.6 to 1.2 mm in length; this range coincides with the determined resolution range of the CT system. Lastly, the results also show that the all-liquid system has a lower associated error than the all-gas system for pixel values within and greater than those established for the optimal region.

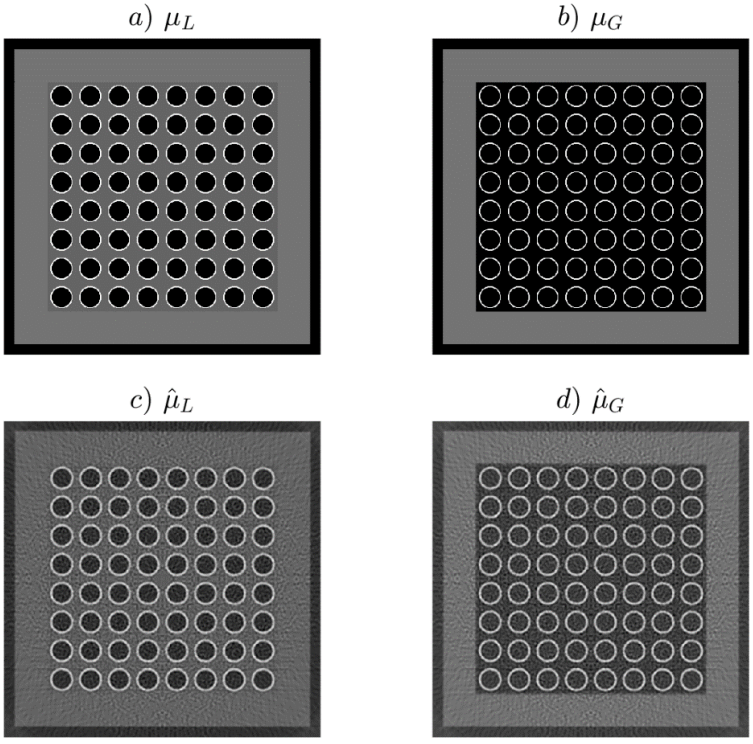

Fig. 5.38. Ideal attenuation maps of the MARBLE facility for *a)* all-liquid system, and *b)* all-gas system. Ram-Lak filter used for the FBP reconstruction for the corresponding *c)* all-liquid system, and *d)* all-gas system

The process was repeated for the remainder of the filters, the moving average results are compared in Fig. 5.40. The performance of the filters becomes distinctive in the minimized region, the Ram-Lak filter

yielded the lowest associated error while the Hann filter yielded the largest associated error. The effects of the filter converge to similar values when the pixel size was further reduced bellow optimal region. However, the results show a proper agreement between the imaging resolution of the system and the range of pixel sizes that result in an optimal quantitative agreement. For the remainder of the research, a pixel size of 0.68 mm will be used; this results in an equivalent subchannel width of 31 pixels per subchannel.

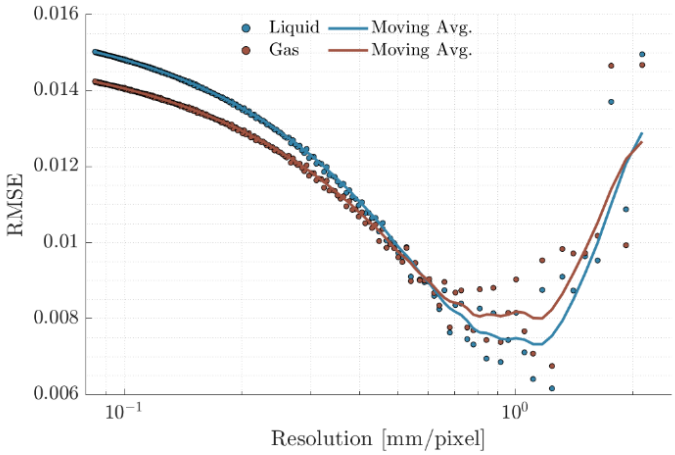

Fig. 5.39. Parametric study between the pixel size and RMSE using the Ram-Lak filter for the all-liquid and all-gas systems.

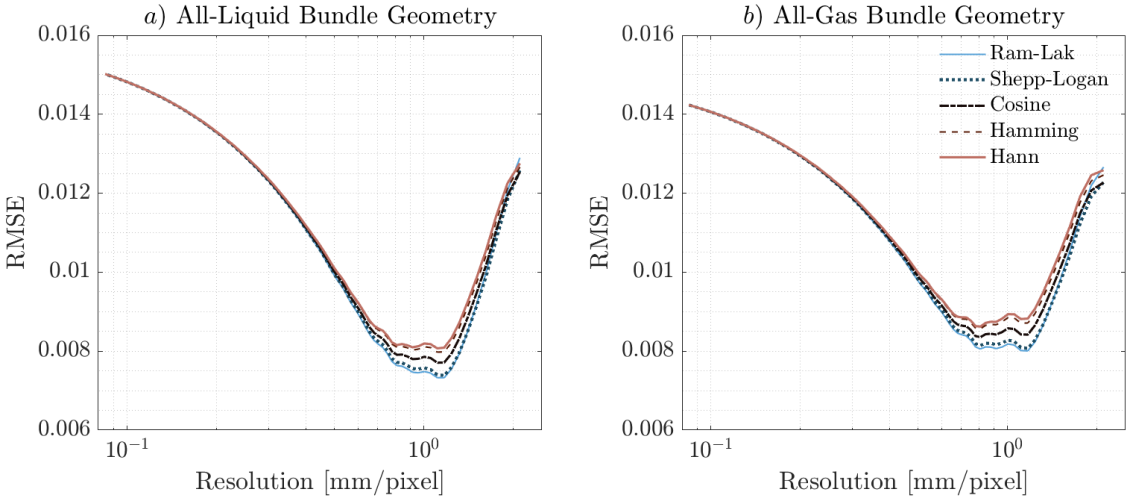

Fig. 5.40. Moving-average results of the parametric study between the pixel size and RMSE for various filters; *a)* all-liquid system and *b)* all-gas system.

5.3.2. Determination of the Void Fraction

The discussion is now shifted to the estimation of the void fraction in two-phase flows deploying CT imaging methods; this topic can be revisited in Section 2.2.3 in which CT reconstruction is explained. To estimate the void fraction, we first need to perform calibration measurements of the system under all-liquid conditions which will be denoted as $\hat{\mu}_L$, and under all-gas conditions denoted as $\hat{\mu}_G$ as shown in Fig. 5.38;

the latter is typically measured when the test section is dry and at atmospheric conditions. The calibration measurements can be performed with long exposure times in order to improve the statistical certainty in the reconstruction process.

The two-phase flow measurements are performed next, the post processing of these requires a mindful approach due to the dynamic nature of the two-phase conditions. Typically, repeated short exposure measurements are performed at every angular location in order to best capture the dynamic behavior of the flow. Intuition would first tell us to take the average of the measured radiation counts, however this incorporates a small deviation from the true average behavior, formally known as the dynamic bias; a topic covered in section 3.3. In order to minimize said bias, we modify the definition provided by Hampel et al. [54] to proper average the radiation transmission for a dynamic systems; this is adapted for the sinogram as follows:

$$p_{\theta,2\varphi}(r) = -\frac{1}{K}\sum_{k=1}^{K}\left[\ \ln\left(\frac{I_{k,2\varphi}(r,\theta)}{I_o}\right)\ \right], \qquad \text{Eq.(5-22)}$$

where k indexes the measurements performed for detector r at angle θ, and K is the total number of measurement iterations; here, j can be considered the temporal sifting variable. It is important to highlight that the averaging procedure is performed outside the logarithmic operation, which requires the individual measurements to be normalized by the *flat field* followed by the logarithmic conversion. The reader should note that the applied *flat field* intensity needs to be scaled appropriately to the exposure time of the two-phase measurements, and also considering the change in activity when measurements are performed temporally far apart in which the source may have experienced a significant change in activity. This special treatment allows us to properly build the sinogram for the two-phase flow cases, or for any dynamic system. The sinogram is then passed through the FBP procedure to reconstruct the two-phase map $\hat{\mu}_{2\varphi}$. The spatial void fraction is then estimated as

$$\hat{\alpha} = \frac{\hat{\mu}_L \ - \ \hat{\mu}_{2\varphi}}{\hat{\mu}_L \ - \ \hat{\mu}_G}. \qquad \text{Eq.(5-23)}$$

The void fraction defined above is obtained by performing reconstruction differentiation between the all-liquid and two-phase normalized by the calibration difference.

5.3.1. Radiation Noise Analysis

Next, radiation noise is incorporated to assess the imaging performance of the HRGTS and the capability to quantitatively estimate the void fraction for various radiation intensities. Following the ray-tracing modeling process performed in the previous section, the cases for the all-gas (empty) and all-liquid system (full) are used as calibration while the two-phase case imposes the void fraction distribution of interest. For the present study, the void fraction distribution was ranged homogeneously throughout the designated rod-centered subchannel regions (64 regions total), the void fraction was varied from 1.5% to 96% absolute void-fraction, with increments of 1.5%. This arrangement was chosen due to its easy implementation in the simulation; however, it would be expected that a channel-centered subchannel arrangement would yield similar results. Fig. 5.41 depicts the all-liquid, all-gas, and two-phase reconstructions, as well as the differential images and the ideal void-fraction from the noise-free reconstructions. It is important to note that during the image differentiation between attenuation maps, the metal rods are eliminated due to their similar reconstructed-attenuation values. This allows the flow region of interest to be isolated and considered in the void fraction calculation; this is visually observed in throughout the differential images and spatial void fraction depictions in Fig. 5.41.

The simulations were carried out for a range of flat filed radiation intensities corresponding to the number of photons arriving at each detector; the nps flat field is described as follows:

$$I_{nps} = \frac{I_{source}\ \gamma\ \eta\ A_{det}\ t}{4\ \pi\ d_{sd}^2\ p} \qquad \text{Eq.(5-24)}$$

where I_{source} is the source activity (in Becquerels), γ is the gamma-ray yield of the source, η is the detector efficiency at the given gamma-ray energy, A_{det} is the detector-element area which is 12 mm^2 for the HRGTS detectors, t/p is the measurement time per projection, $4\ \pi\ d_{sd}^2$ is the geometric source-detector factor accounting for solid angle. The measured intensity varies from measurement to measurement primarily according to the source activity, and exposure time per projection; the efficiency and geometric variables remain constant. The nps values of [500, 1000, 5000, 10000, 50000] were used for the simulations. In the case of the HRGTS, the radioactive source is a nominally 15 Ci ^{192}Ir source which decays relatively quickly with a 74.2-day half-life. This range of nps values therefore may be considered to represent the decay of the source or various exposure times per projection at a given activity.

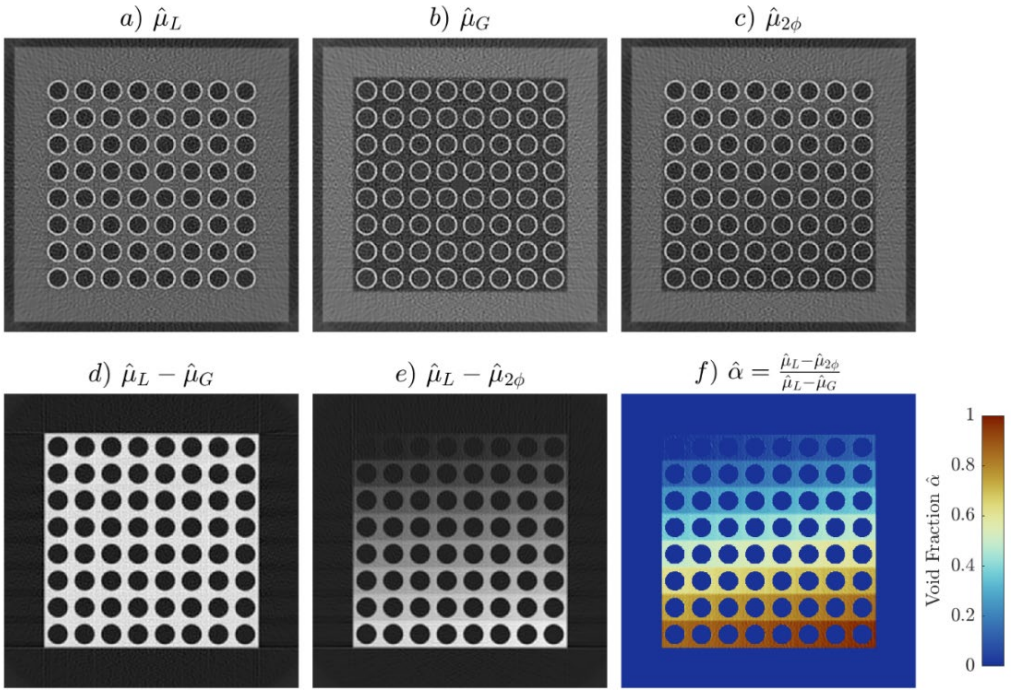

Fig. 5.41. Noiseless reconstructions for simulated *a)* all-liquid , *b)* all-gas, and *c)* two-phase cases. Differential maps for *d)* liquid – gas, *e)* liquid – two-phase, and *f)* spatial void fraction.

The forward projections correspond to the ideal (noise-free) sinogram for the three cases. Then, according to the different nps values, Poisson-noise is added to each projection in which the mean corresponds to the ideal-recorded counts at the detector. The variance of the Poisson distribution is equivalent to the mean of the distribution; therefore, the standard deviation of the recorded counts is $\sigma_{det} = \sqrt{I_{det}}$. The addition of random Poisson-noise incorporates the inherently stochastic process of radioactive decay; this procedure was done only for the two-phase case, which would need to be repeated for different flow conditions and bundle height desired. The calibration measurements need to be executed only once, therefore a prolonged measurement can be performed such that the statistical noise becomes negligible. The number of sampled projections was maintained at 1080 to approximate the expected rate of data acquisition during continuous rotation. FBP was then implemented to obtain the reconstruction for each noisy case. The procedure was applied to 100 different repetitions for each nps case. The results from each of the 100 samples were then spatially averaged in order to obtain the mean void fraction at a subchannel basis. Fig. 5.42.*a)* depicts the estimated average void fraction over the nps-repetitions and its relation to the expected void fraction. The predicted void fraction from the generated noise cases follows the identity line for all cases; the zoom in window in Fig. 5.42.*a)* shows that the higher nps cases fall closer to the identity line,

nevertheless, there is proper agreement for the applied cases. This procedure serves as a fundamental check of the simulation and its prediction capabilities. The difference between the predicted void fraction and the ideal void fraction is shown in Fig. 5.42.*b)*; here, the lower nps tends to underestimate the void fraction by as low as 1.5%. However, the difference shows that there is a structural bias of ± 0.5% for the large nps cases that is perhaps related to the resolution limitations combined with spatial averaging methods.

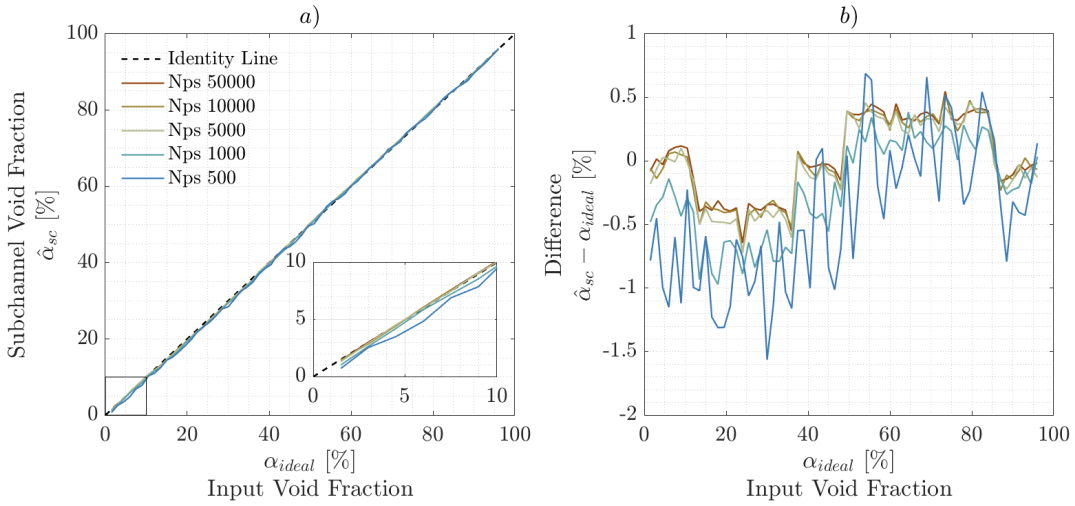

Fig. 5.42. ***a)*** **Ideal vs simulated void fraction for various nps values.** ***b)*** **Absolute error in measured void fraction as a function of the void fraction, averaged over 100 repetitions of the simulation.**

The subchannel void-fraction standard deviation was calculated over the sets of noisy subchannel cases for each nps value used; this is estimated as

$$\sigma_{\alpha_{sc}} = \sqrt{\frac{1}{K}\sum_{k}^{K}(\alpha_{sc,k} - \bar{\alpha}_{sc})^2}. \qquad \text{Eq.(5-25)}$$

The standard deviation results depicted in Fig. 5.43.*a* show that low radiation count measurements have large variation in their void-fraction estimation, while large radiation counts result in a reduce this variation; in the case of 500 nps the standard deviation is larger than 1%, and for the case of 50000 nps the standard deviation is reduced to about 0.25%. The relative standard deviation (RSD) was

$$\textit{Relative Std} \;=\; 100 \times \frac{\sigma_{\alpha_{sc}}}{\bar{\alpha}_{sc}}, \qquad \text{Eq.(5-26)}$$

the results are shown in Fig. 5.43.*b*; this value is used to estimate the magnitude of the standard deviation relative to the average value. The results show that the RSD decreases with $1/\bar{\alpha}_{sc}$, but more importantly, it serves to highlight the how low radiation fluxes as is the case for the 500 nps, result in higher RSD, and how this is reduced with increase in radiation counts.

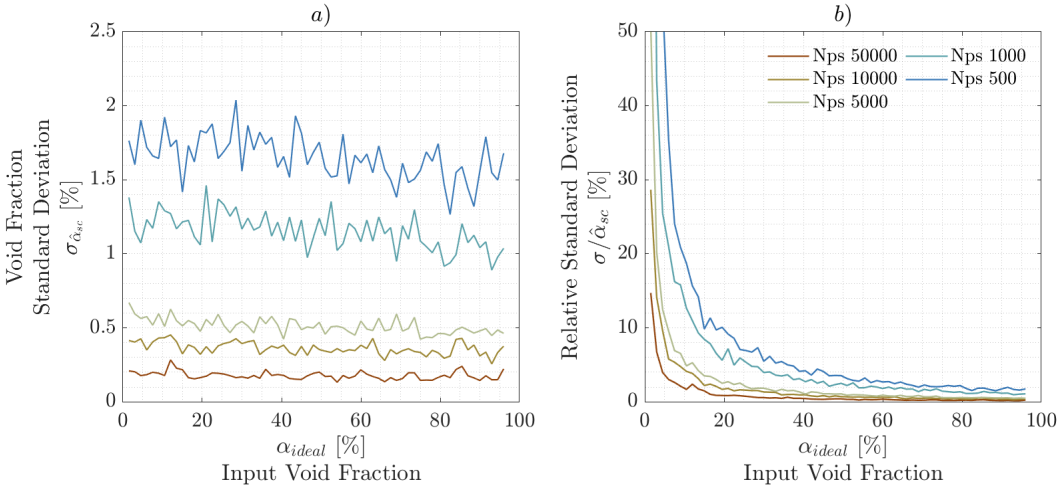

Fig. 5.43. ***a)*** **Standard deviation of the subchannel void fraction, and** ***b)*** **the relative standard deviation for the various nps cases.**

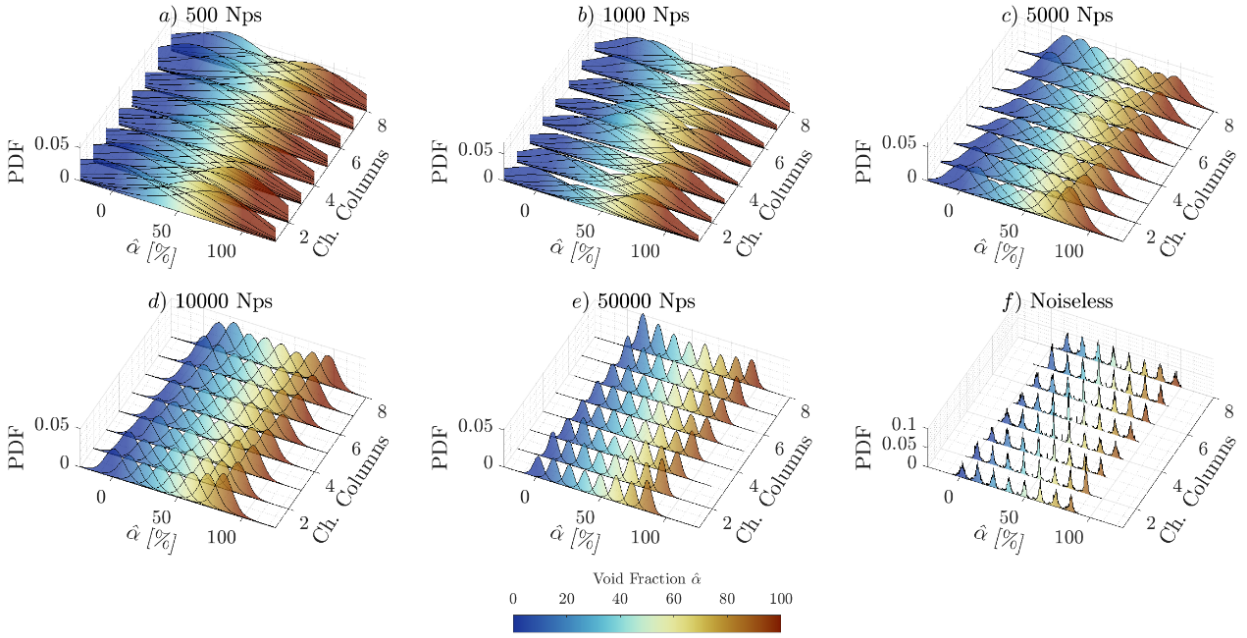

Fig. 5.44. Subchannel regions pixel-wise void fraction distribution for different noise incorporated flat field counts (nps); ***a)*** **500,** ***b)*** **1000,** ***c)*** **5000,** ***d)*** **10000,** ***e)*** **50000, and** ***f)*** **noiseless/ideal reconstruction.**

The void-fraction distribution of pixels for individual subchannel regions with variation of noise induced counts are shown in Fig. 5.44; the regions are arranged in bundle-columns following the ideal void fraction distribution from Fig. 5.41.*f)*. The distributions serve to show the spread of the estimated pixel values for the various regions. This further exemplifies the effects of low radiation counts on the estimation of the void fraction with improved radiation counts. Although difficult to visualize, the distributions are broad at

low radiation counts, with values that that deviate significantly from the nominal 0% and 100% void fraction range. As the radiation counts are increased, the spreads contract and it becomes clear that the distributions have gaussian qualities. It is important to clarify that the average value for each subchannel region follows the corresponding ideally-imposed void fraction, however the spatial pixel-wise population has a large variation throughout the reconstruction process. The spread of the distributions remains consistent throughout the subchannels for each nps case, meaning that it is highly influenced by the radiation flux and weakly affected by the subchannel void fraction. The distributions for the ideal-noiseless case shown in Fig. 5.44.*f)* are narrow, however, these represents the limitation of the FBP reconstruction with the modeled imaging system. Similarly, the pixel distribution can be visualized for the flow-region, to represent the cumulative behavior of the two-phase flow. In the case of low radiation counts, the distribution presents a gaussian behavior that spreads broadly past the 0% and 100% range. This then begins to shape into a continuous uniform distribution with increase in radiation counts; this is particularly observed in the case of 50000 radiation flat field as well as the ideal noiseless reconstruction.

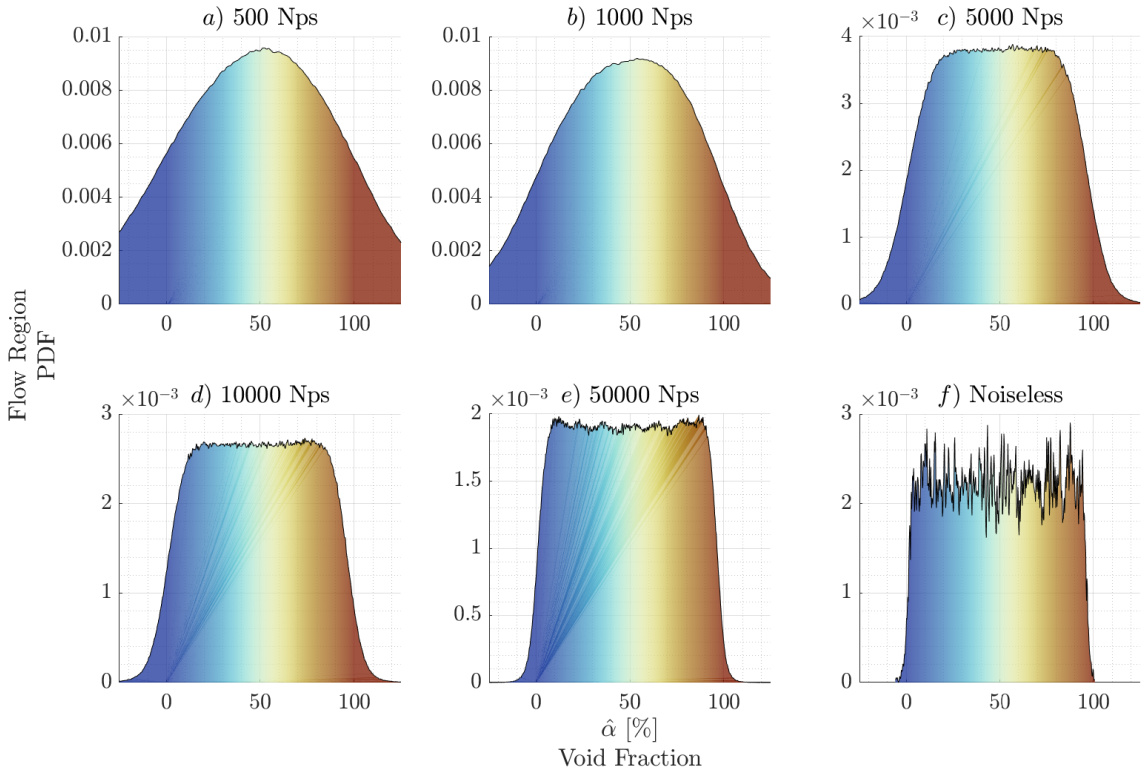

Fig. 5.45. Flow region pixel-wise void fraction distribution for various flat field noise induced counts; *a)* 500, *b)* 1000, *c)* 5000, *d)* 10000, *e)* 50000, and *f)* noiseless/ideal reconstruction.

5.4. CT Measurements and Results

The deployment of the HRGTS as an advanced two-phase flow measurement instrument is discussed in this section. First, measurements of two small scale prototype mock-bundles are performed to compare the estimated void fraction from the ideal case. Afterwards, measurements of the MARBLE facility are discussed for two separate gas injection configurations at similar boundary conditions.

5.4.1. Prototype Testing

In order to test experimentally the accuracy of void fraction measurements, a 4x4 bundle mockup was manufactured and imaged using the HRGTS. The mockup consisted of two 3D printed holders, one which holds the 4x4 array of stainless-steel tubes (the same used in the adiabatic bundle facility), and the other which holds the plastic cylinders inserted above the subchannel used to model various configurations of gas/liquid distributions (the plastic has similar attenuation coefficient as water). Fig. 5.46 shows the small-scale bundle mockup. Three different cases were arranged and measured, the empty case had the plastic inserts removed, the full case had all inserts of the same diameter, 11.1 mm, these being the largest available that could fit in the subchannel. The varied case was performed using three "full" subchannels, five "varied" sized inserts with diameters of [9.6, 8.0, 6.4, 4.8, 3.3] mm and one empty subchannel. Tomographic data was collected for 360^{o} projections with incremental steps of 1^{o}, one second measurement per projection, using a collimator and a 4 mm lead filter, with an estimated source activity of 2.4 Ci on the date that the measurement was performed. The source-object distance was 34 cm. The reconstructed tomograms are presented in Fig. 5.47 for the calibrations, varied void fraction, and the differential images along with the subchannel arrangement. The void fraction was calculated as an average over the subchannels, the results are shown in Fig. 5.48. The results show very good agreement between the expected subchannel-averaged void fraction (based on insert diameter) and the measured void fraction from the tomographic reconstructions. An absolute error of 1-2% was observed across the measured void fractions.

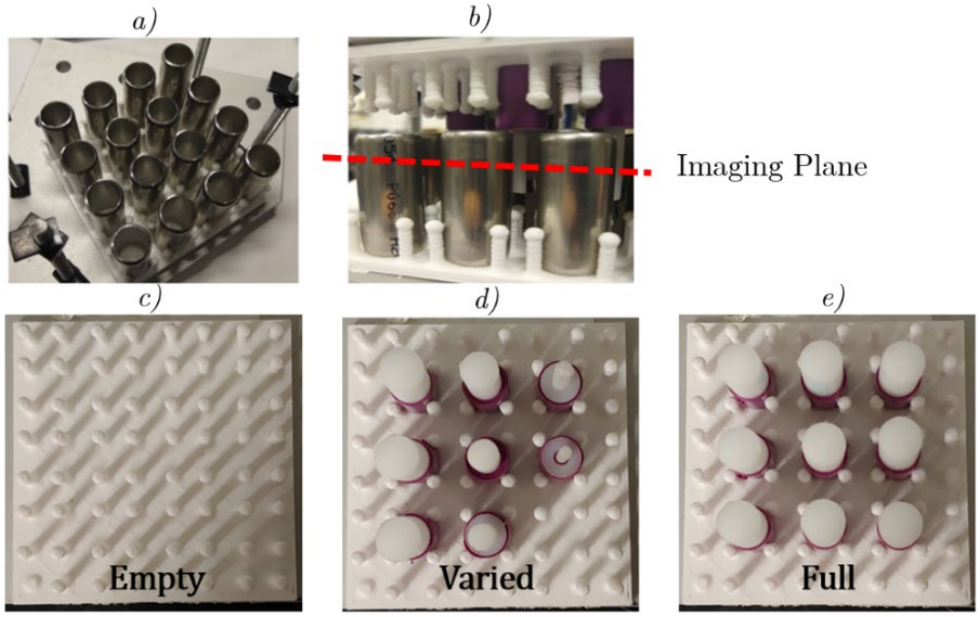

Fig. 5.46. ***a)*** **Array of 4x4 stainless steel rods,** ***b)*** **mock bundle and insert arrangement,** ***c)*** **empty arrangement,** ***d)*** **varied void fraction inserts, and** ***e)*** **full insert arrangement.**

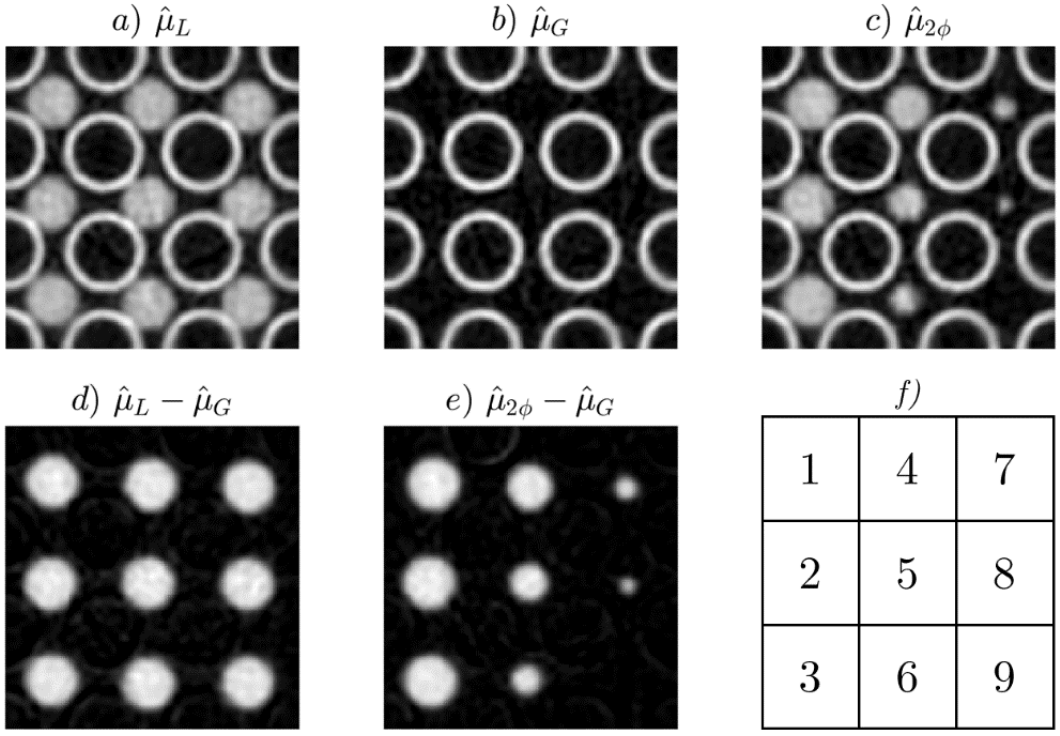

Fig. 5.47. Stainless steel mock bundle tomographic reconstruction; a) full, b) empty, ***c)*** **two-phase d) full - empty, e) two-phase - empty, and** ***f)*** **subchannel arrangement.**

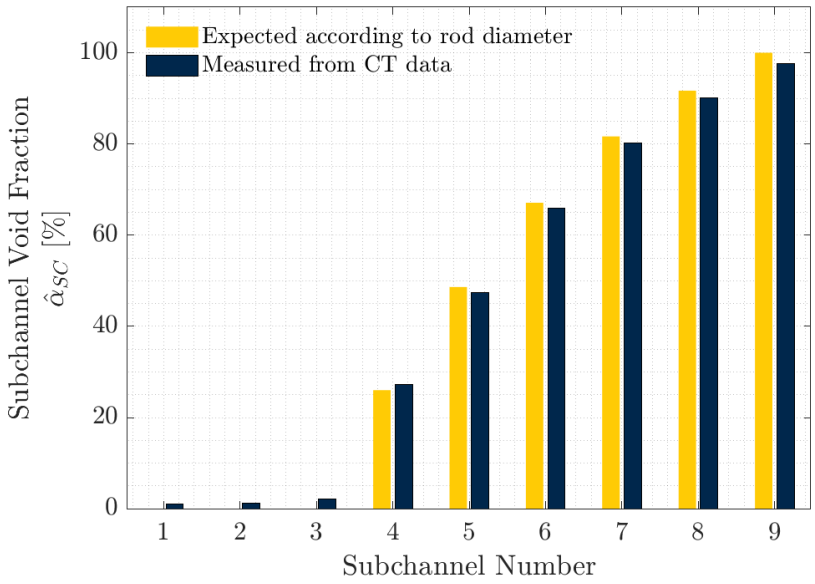

Fig. 5.48. Void fraction results of stainless-steel bundle mockup.

A second test was performed in which the 4x4 stainless steel tubes were replaced with a 4x4 array of Incoloy tubes with an outer diameter of 9.6 mm and a thickness of 1.1 mm, while holding the same assembly pitch. The same varied diameter inserts were used as in the previous case. The Incoloy bundle mockup is shown in Fig. 5.49 alongside the test inserts. The tomographic reconstructions and the associated differential images are shown in Fig. 5.50. The void fraction results are shown in Fig. 5.51.

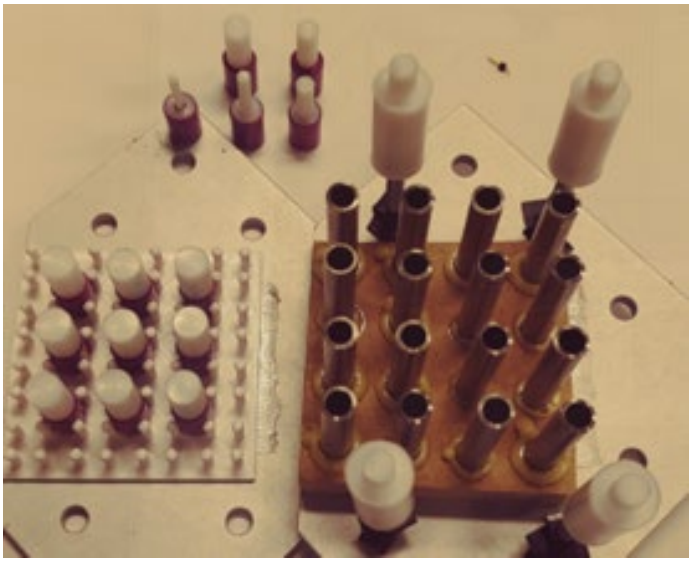

Fig. 5.49. Incoloy 4 x 4 array mockup.

Similar to the adiabatic bundle mockup test, the void fraction results show very good agreement between the expected and the measured sub-channel void fraction, with an absolute error up to about 1-

2%. This shows that the added attenuation from the thicker walled pins did not have any significant effect on the void fraction accuracy. These results strongly support the overall accuracy and validity of the HRGTS for measuring subchannel void fraction for thermal-hydraulic systems.

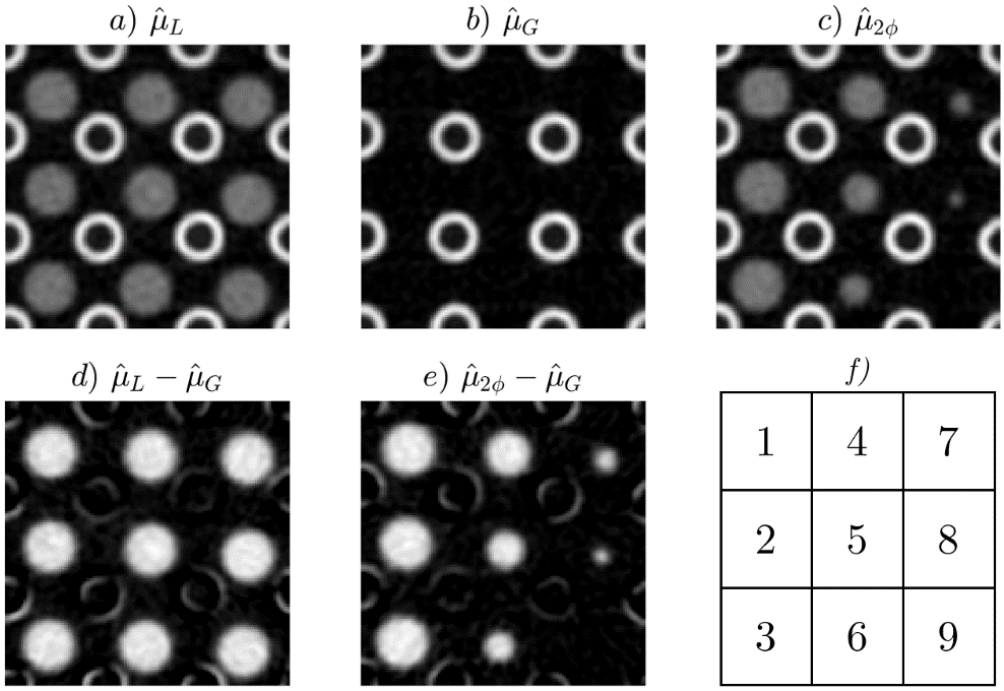

Fig. 5.50. Incoloy array mockup tomographic reconstruction; a) full, b) empty, *c)* two-phase d) full - empty, e) two-phase - empty, and *f)* subchannel arrangement.

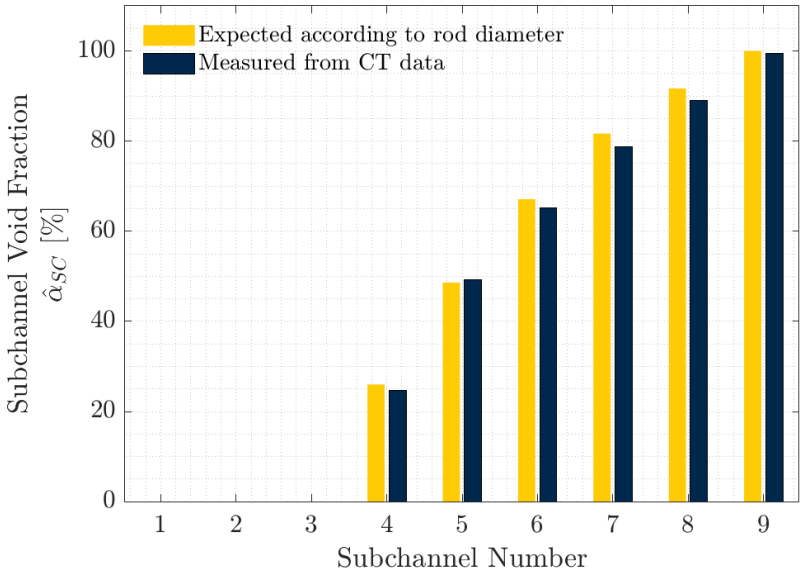

Fig. 5.51. Void fraction results of Incoloy adiabatic bundle mockup.

5.4.2. Experimental Results

In this section we introduce the first tomographic measurements of the MARBLE facility performed with the HRGTS, the experimental conditions are presented in Table 5.5,. The flat field was measured prior to mounting the HRGTS onto the gantry system; a 4 mm lead plate was placed in front of the source (for all measurements) in order to reduce the radiation flux and avoid detector pileup, a short exposure time of 50 ms was imposed to avoid detector counting saturation, this included 12000 measurement iterations for a total exposure time of 10 minutes; to give perspective the counts recorded per flat field iteration over the 50 ms was on the order of 8300 counts. The flat field is then scaled appropriately according to the exposure time of the measurement of interest. The CT measurements were performed at the height of Port #3 in Fig. 5.28, with a distance of 1.0 cm away from the top of the spacer grid. All the measurements were performed over a range of 360° with incremental steps of 1°. The total exposure time of the calibration measurements were 135 minutes, and for the two-phase flow cases it was 45 minutes per measurement; the calibration measurements which include the all-liquid and all-gas system as well as the differential image are depicted in Fig. 5.52. The most attenuating case, when the system is full, presented a low count rate on the order of 550 counts over 150 ms. The reconstructed calibration images show that some of the rods inside the bundle were filled up with water during operation, a detail best visualized by the enumerated, black-colored locations in the differential image. The corresponding calibration sinograms are presented in Fig. 5.53, these show the expected projection attenuation range of the MARBLE facility.

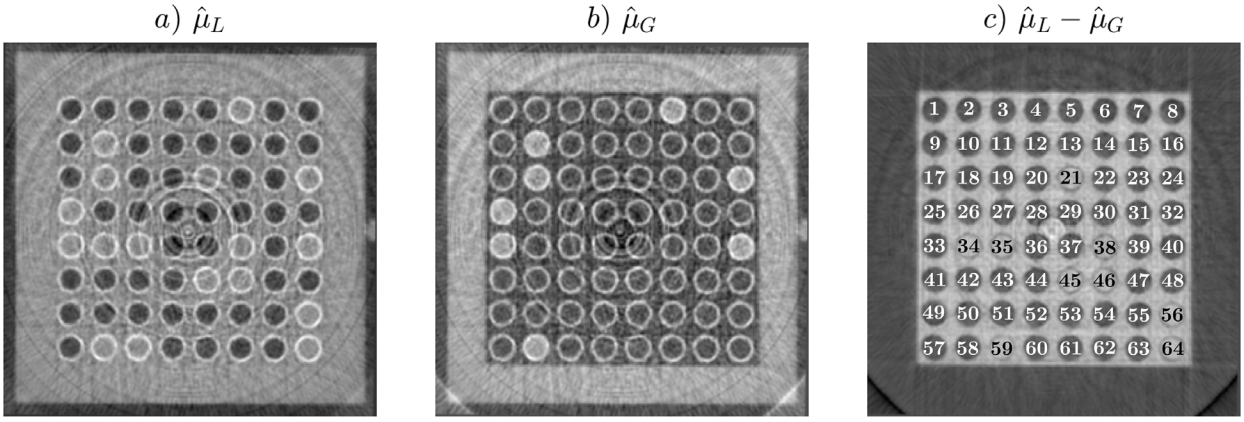

Fig. 5.52. Example of the calibration CT measurements of the MARBLE facility: a) all-liquid calibration, b) all-gas calibration, c) full vs gas differential image with enumerated rod locations.

The two-phase flow measurements presented in this section consist of two types of gas-injection configurations. The first is a uniform distribution injection in which all 64 sparging-rods were open. The

second type of injection arrangement used the 4-central rods in the bundle. The experimental matrix involved respective measurements for targeted gas superficial velocities at the sparger level of $j_{g,spg}$ = [0.5, 0.25, 0.05, 0.025] m/s for both injection configurations with a total of eight measurements; the cases were carried out from high to low superficial velocity conditions for both arrangements. The selection for these two types of injection configurations serves to highlight the CT systems capability of capturing different spatial distributions while imposing similar initial gas-injection conditions.

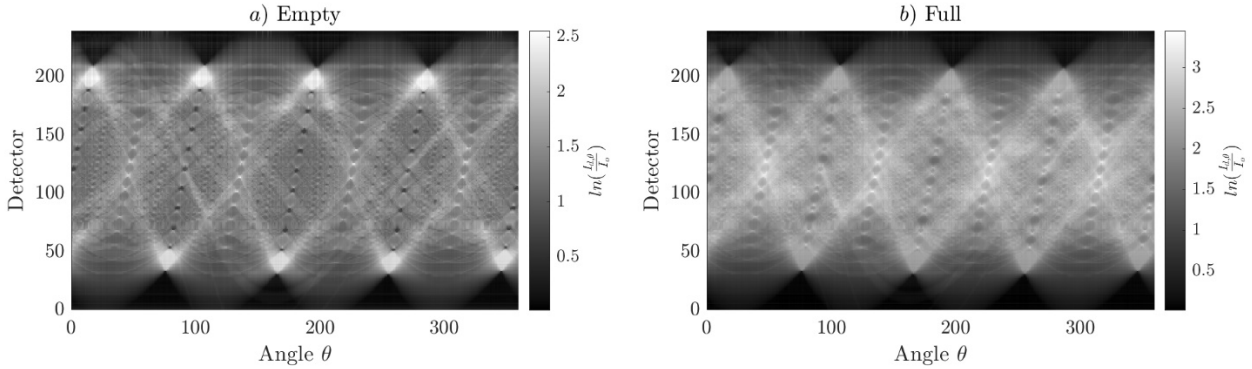

Fig. 5.53. Sinogram from calibration measurements for the system *a*) empty, and for the system *b*) full.

Table 5.5. Gamma-source and detector parameters

Measurement	Focal Spot [mm]	Source Activity [Ci]	Exposure per iteration [ms]	Number of iterations per degree	Number of Angular projections	Total Exposure Time [min]
Flat Field	1.5	10.2	50	12000	1	10
All-Liquid	1.5	9.8	150	150	360	135
All-Gas	1.5	9.3	150	150	360	135
Two-Phase	1.5	9.9	150	50	360	45

5.4.2.1. Uniform Injection Configuration

The uniform injection configuration was achieved by designating the gas mass-flow throughout the injection groups (shown in the center panel of Fig. 5.24) with percent distribution of 18.75% for groups G_1 through G_4, and 25.0% for G_5; this percent distribution is selected due to the higher number of spargers, 16 total, associated with group G_5 in comparison to G_1 through G_4 which contain 12 spargers each. The

experimental parameters are tabulated in Table 5.6, the estimated void fraction results obtained with CT methods are shown in Fig. 5.54 and the pixel-wise distributions for the corresponding measurements are shown in Fig. 5.55; these are arranged from highest to lowest gas superficial velocity and labeled as M-1 through M-4. A mask was applied to remove the rod regions and isolate the flow region. The superficial gas velocities at the CT imaging plane result in slightly higher values than the initial value at the sparger, this is due to the effective density decrease and expansion of the gas as it travels vertically throughout the rod bundle height. The void fraction distribution inside the bundle shows a visible progressive increase corresponding from low to high superficial gas velocities. In the case of M-1, two regions of relatively high void fraction are depicted towards the bottom-left and top-right regions of the bundle; these two features appear to be rotationally symmetric about the center of the bundle. The M-2 case shows a more homogeneous gas distribution with some low void fraction features in that occur in the middle of the subchannel regions due to effects from the mixing vanes. The cases of M-3 and M-4 are characterized by low void fraction content; these appear to have high void-fraction content around some of the rods, however this is a reconstruction artifact that occurs because the rods were filling with water during the measurements, which affected the nearby reconstruction region. at low gas injection conditions, it became increasingly difficult to ensure that all the sparging rods injected gas into the system with some rods experiencing more resistance than others, nevertheless, the flow for the individual groups was fixed.

The void fraction distribution inside the bundle presented in Fig. 5.55 depict a visible shift in the distribution in relation to the superficial gas velocities. The cross-section average void fraction is estimated as the average pixel-wise value over the flow region (ignoring rod regions). Similarly, the standard deviation is estimated over the pixel-wise population and best represents the spread of the pixel-wise distribution. The average void fraction follows the high to low trend imposed by the superficial gas velocity, however the standard deviation is significantly high, which indicates a large spatial variation throughout the pixel values. The standard deviation is as high as 19.62% for the M-1 measurement, the distribution narrows with decrease in void fraction and superficial gas velocity, with a standard deviation of 12.81% for the M-4 measurement.

Next and most importantly, the subchannel average void fraction was estimated by isolating and collapsing these local regions following the procedures reported by Adams et al [3] and Diaz et al. [33]; the results are presented in Fig. 5.56. In the case of the M-1 measurement (largest superficial velocity), the gas agglomeration towards diagonally opposite corners becomes more prominent and easier to visualize; at this

moment it is hard to explain the source of these spatial modes, nevertheless it remains an interesting feature of this measurement. The largest average void fraction for these regions is about 48~51%. The M-2 case has a reduced void fraction and contains a precursor pattern to the aforementioned spatial modes. For the M-3 and M-4 cases, the void fraction is reduced considerably.

Table 5.6. Experimental parameters for the uniform gas injection arrangement.

Parameter	**M-1**	**M-2**	**M-3**	**M-4**
$\dot{m}_L \pm \sigma_L$ [kg/s]	10.212 ± 0.02	10.245 ± 0.024	10.284 ± 0.018	10.275 ± 0.017
$j_L \pm \sigma_{j_L}$ [m/s]	0.649 ± 0.001	0.651 ± 0.001	0.654 ± 0.001	0.654 ± 0.001
$\dot{m}_g \pm \sigma_{\dot{m}_g}$ [g/s]	12.56 ± 0.124	6.512 ± 0.089	1.27 ± 0.019	0.576 ± 0.015
$T_{spg} \pm \sigma_{T_{spg}}$ [°C]	23.792 ± 0.065	24.387 ± 0.128	24.9 ± 0.061	25.492 ± 0.054
Parameters at the Sparger Injection (*spg*)				
$P_{spg} \pm \sigma_{P_{spg}}$ [kPa]	40.236 ± 0.648	38.528 ± 0.46	38.71 ± 0.314	39.05 ± 0.242
$\rho_{g,spg} \pm \sigma_{g,spg}$ [kg/m^3]	1.661 ± 0.008	1.638 ± 0.005	1.637 ± 0.004	1.638 ± 0.003
$j_{g,spg} \pm \sigma_{j_{g,spg}}$ [m/s]	0.479 ± 0.005	0.252 ± 0.004	0.049 ± 0.001	0.022 ± 0.001
Parameters at the CT Imaging Plane				
$P_{CT} \pm \sigma_{P_{CT}}$ [kPa]	24.053 ± 0.539	21.544 ± 0.320	20.018 ± 0.188	20.125 ± 0.179
$\rho_{g,CT} \pm \sigma_{g,CT}$ [kg/m^3]	1.471 ± 0.006	1.439 ± 0.004	1.418 ± 0.002	1.417 ± 0.002
$j_{g,CT} \pm \sigma_{j_{g,CT}}$ [m/s]	0.541 ± 0.006	0.287 ± 0.004	0.057 ± 0.001	0.026 ± 0.001
$\overline{\alpha} \pm \sigma_\alpha$ [%]	38.34 ± 19.62	29.99 ± 19.26	8.83 ± 15.85	4.53 ± 12.81

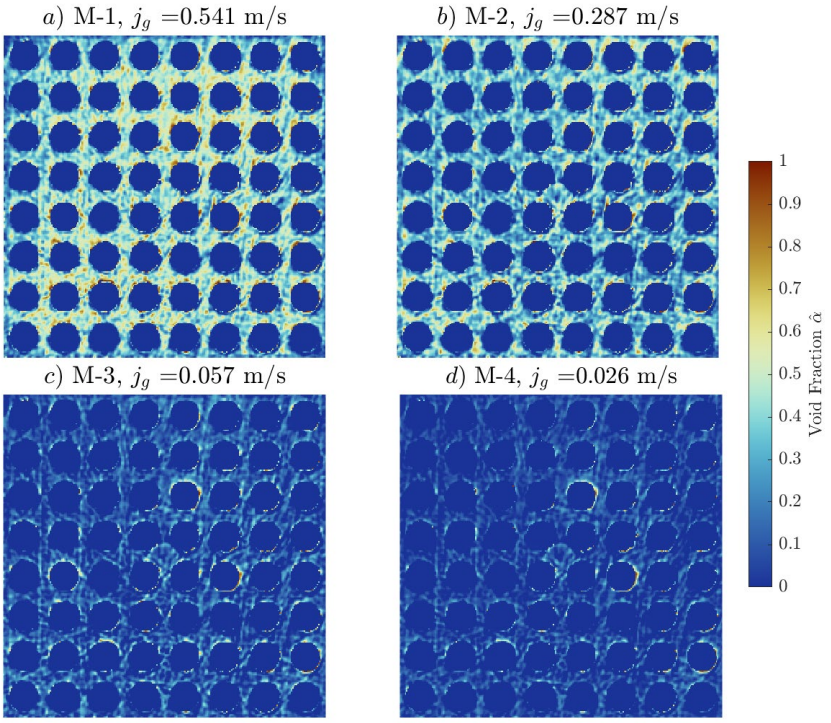

Fig. 5.54. Uniform gas injection with superficial velocities estimated at the CT scanning measurement plane. Spatial void fractions: *a)* j_g =0.541 m/s, *b)* j_g =0.287 m/s, *c)* j_g =0.057 m/s, *d)* j_g =0.026 m/s.

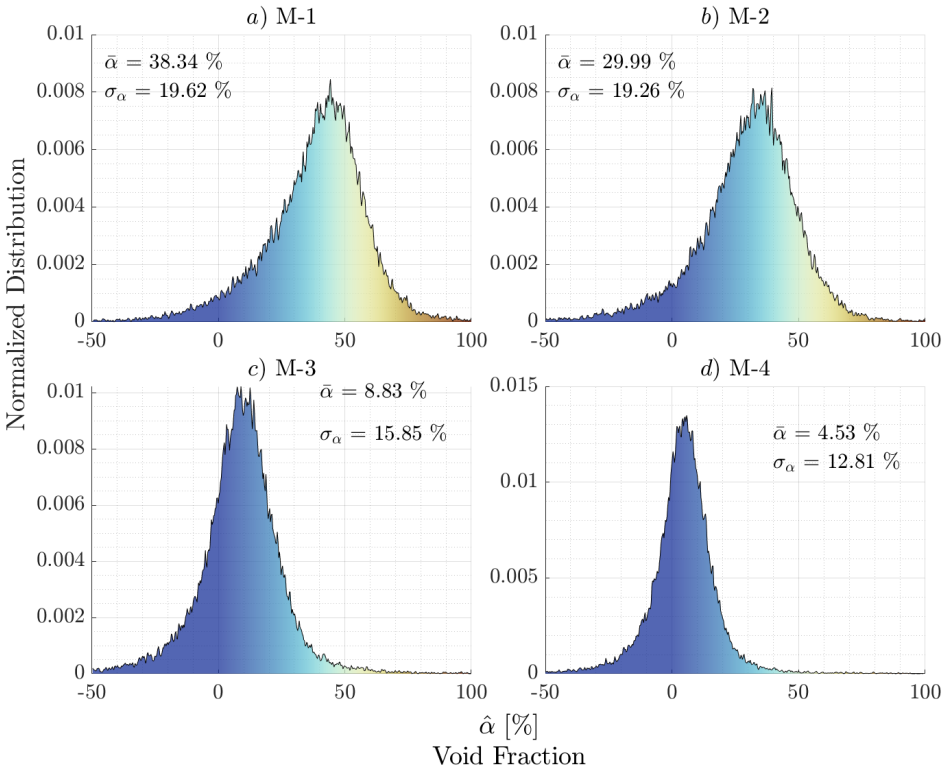

Fig. 5.55. Corresponding pixel-wise void fraction distributions for uniform injection configuration: *a)* M-1, *b)* M-2, *c)* M-3, *d)* M-4.

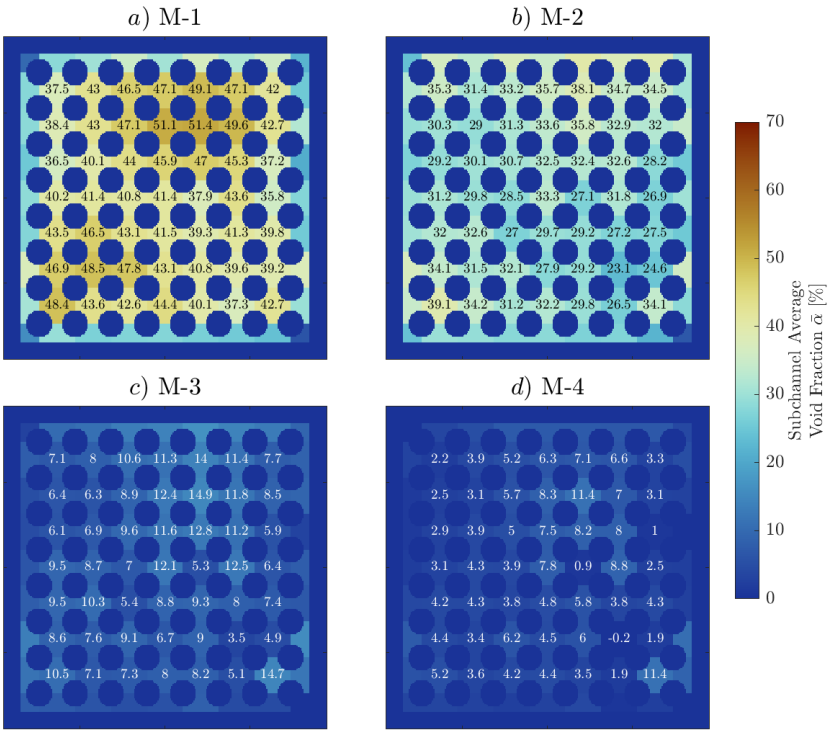

Fig. 5.56. Subchannel average void fraction estimation for uniform injection configuration.

5.4.2.2. Central Rods Injection

The second arrangement in which the central four rods injected air into the bundle was achieved by directing the mass flow rate through the central group G_5 (shown in the center panel of Fig. 5.24). The superficial gas velocity at the sparger was analogous to the previous case with slight differences due to the difficulty of achieving the exact same conditions; the experimental parameters for the present set of measurements are tabulated in Table 5.7. The spatial void fraction results are depicted in Fig. 5.57 as well as their corresponding distributions in Fig. 5.58. Similar to the previous section, a mask is applied to remove the rods and emphasize the flow region. The results for the present arrangement depict the evolution of the void fraction throughout the center region of the bundle with increased gas superficial velocity j_g. For low j_g conditions, the gas remains localized towards the core of the assembly. As j_g increases, the gas cross-migrates outward towards the outer boundaries of the assembly, with the highest gas concentration remaining at the center of the geometry. In the cases of M-5 and M-6, the gas reaches the boundary interface with the acrylic housing. The cross-section average void fraction and the associated standard deviation are better quantified by the corresponding distributions; for this arrangement the distributions are asymmetric, containing a more prominent skewness. It is worth pointing out that for the M-5 case, the distribution becomes platykurtic in which the shape distorts towards the larger range of void fraction values; this is

analogous to the simulation case which depicts a nearly uniform distribution shown in Fig. 5.45. The average void fraction in this case is consistently lower than those from the uniform configuration. However, the standard deviation remains high for this arrangement as well which quantifies the large void fraction variation.

Similar to the analysis from the previous section, the subchannel average void fraction is depicted in Fig. 5.59. For the present configuration, the void fraction is primarily concentrated towards the core of the assembly. The M-5 measurement shows a maximum subchannel void fraction of 61.3%. It is worth noting that the peak void fraction for this configuration is about 10% larger than for the uniform case. The void fraction has a radial symmetry around the central (peak) subchannel, this feature remains consistent for the remainder of the cases with correspondingly decreasing void fraction values.

Table 5.7. Experimental parameters for the four central rods gas-injection arrangement.

Parameter	**M-5**	**M-6**	**M-7**	**M-8**
$\dot{m}_L \pm \sigma_L$ [kg/s]	10.084 ± 0.022	10.201 ± 0.021	10.276 ± 0.017	10.278 ± 0.016
$j_L \pm \sigma_{j_L}$ [m/s]	0.641 ± 0.001	0.649 ± 0.001	0.654 ± 0.001	0.654 ± 0.001
$\dot{m}_g \pm \sigma_{\dot{m}_g}$ [g/s]	12.872 ± 0.202	6.357 ± 0.086	1.293 ± 0.016	0.610 ± 0.008
$T_{spg} \pm \sigma_{T_{spg}}$ [°C]	25.826 ± 0.023	26.167 ± 0.033	26.534 ± 0.023	26.938 ± 0.03
Parameters at the Sparger Injection (*spg*)				
$P_{spg} \pm \sigma_{P_{spg}}$ [kPa]	42.558 ± 1.841	40.523 ± 1.264	39.021 ± 0.5	39.049 ± 0.382
$\rho_{g,spg} \pm \sigma_{g,spg}$ [kg/m^3]	1.677 ± 0.021	1.651 ± 0.015	1.632 ± 0.006	1.630 ± 0.004
$j_{g,spg} \pm \sigma_{j_{g,spg}}$ [m/s]	0.487 ± 0.010	0.244 ± 0.004	0.050 ± 0.001	0.024 ± 0.001
Parameters at the CT Imaging Plane				
$P_{CT} \pm \sigma_{P_{CT}}$ [kPa]	24.635 ± 1.807	22.155 ± 1.083	20.164 ± 0.322	20.098 ± 0.267
$\rho_{g,CT} \pm \sigma_{g,CT}$ [kg/m^3]	1.468 ± 0.021	1.437 ± 0.013	1.412 ± 0.004	1.410 ± 0.003
$j_{g,CT} \pm \sigma_{j_{g,CT}}$ [m/s]	0.551 ± 0.012	0.280 ± 0.004	0.058 ± 0.001	0.027 ± 0.001
$\overline{\alpha} \pm \sigma_\alpha$ [%]	31.99 ± 20.45	20.65 ± 17.84	6.65 ± 14.45	3.65 ± 13.08

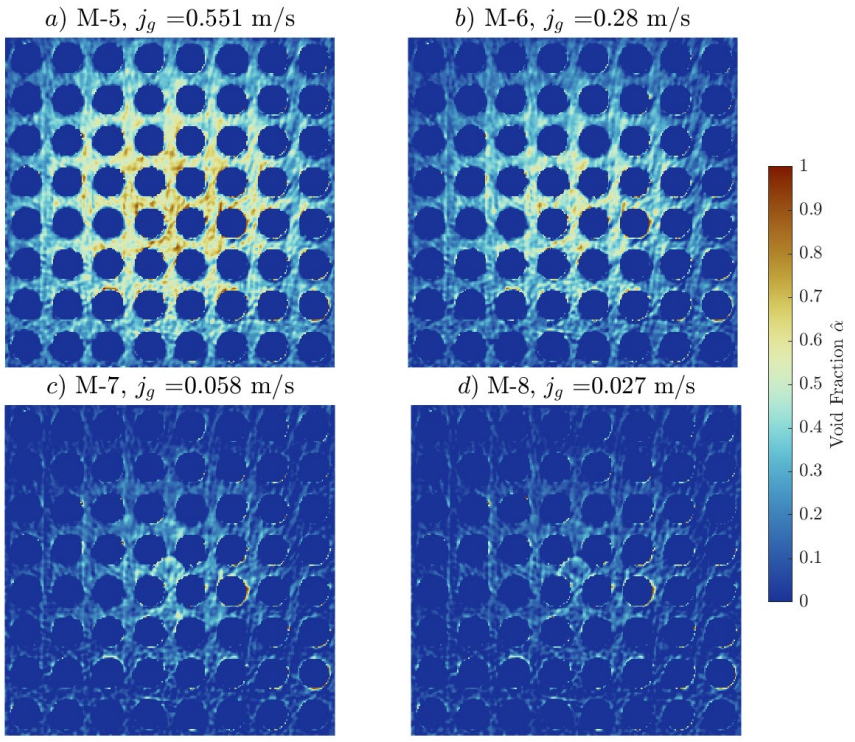

Fig. 5.57. Four central rods gas-injection with superficial velocities estimated at the CT scanning measurement plane. Spatial void fractions: *a)* j_g =0.551 m/s , *b)* j_g =0.280 m/s, *c)* j_g =0.058 m/s, *d)* j_g =0.027 m/s.

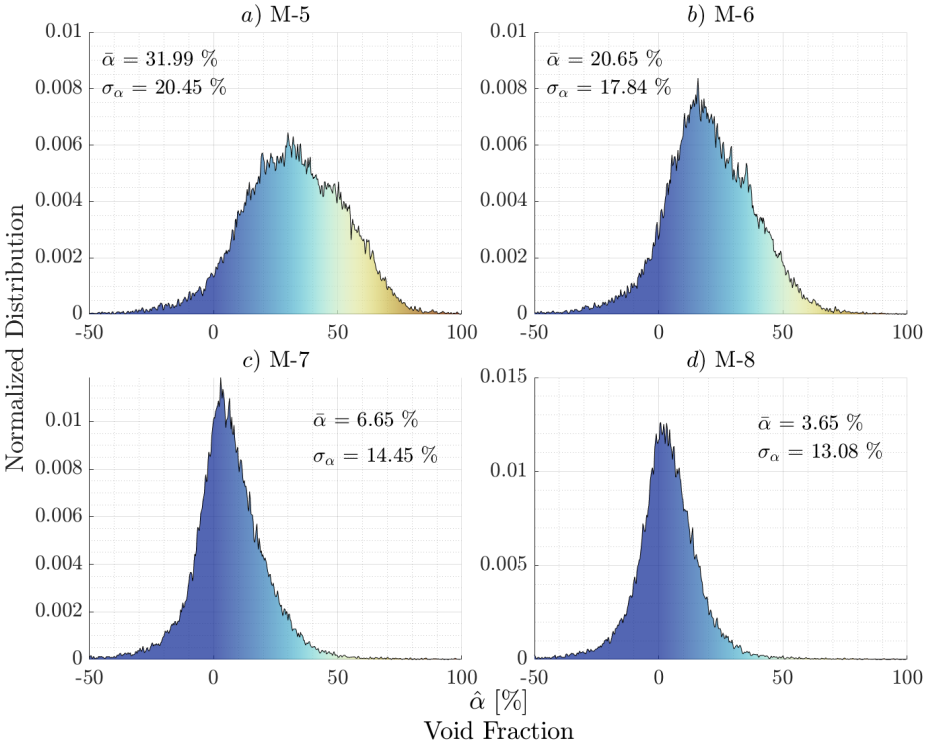

Fig. 5.58. Corresponding pixel-wise void fraction distributions for central four rods injection: *a)* M-5, *b)* M-6, *c)* M-7, *d)* M-8.

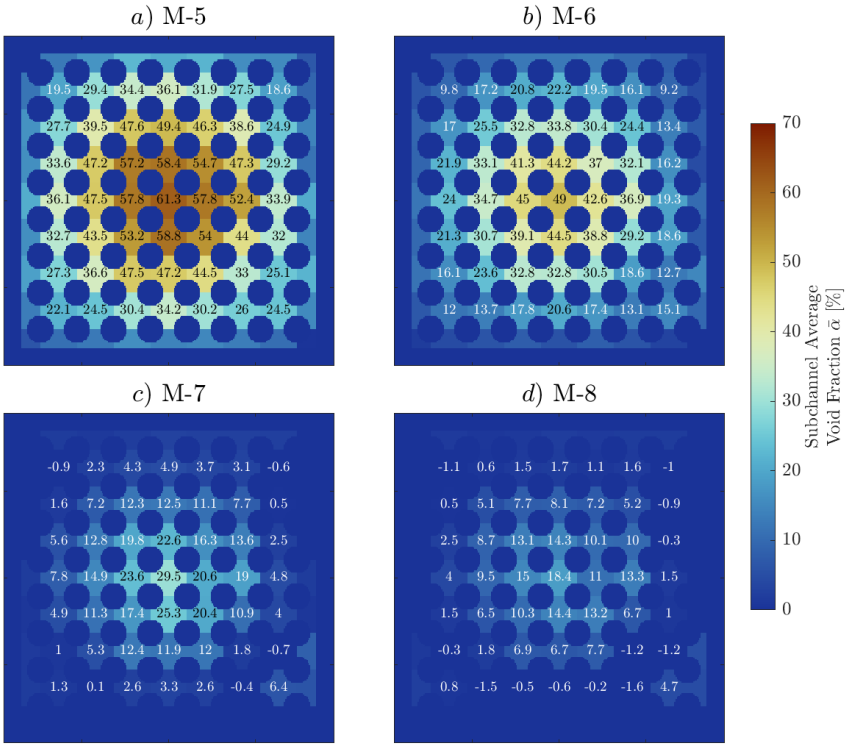

Fig. 5.59. Subchannel average void fraction estimation for central-four rod injection configuration.

5.4.2.3. Configuration Comparison

The location of the measurements for an 8x8 rod bundle two-phase flow regime map are depicted in Fig. 5.60.*a*. the present analysis references the proposed map by Liu et al. [107] based on the data originally obtained by Paranajpe et al. [138 - 140], however, there are geometric differences from the reference rod bundle arrangement and the MARBLE facility; the reference lattice pitch is 16.7 mm, and the rod diameter is 12.7 mm, resulting in a difference in scaling factor of about 1.25 (in which the MARBLE facility is larger). For the time being, this will serve as a guide for the measurement flow regimes while data from the MARBLE facility is collected. Based on the flow regime locations, both configurations lie within the bubbly to cap bubbly regions, in respective low to high superficial gas velocity arrangement. Both configurations are characterized by similar superficial liquid velocity, nevertheless, in the zoomed panel in Fig. 5.60.*b* it is observed that the liquid superficial velocity slightly decreases with increase in superficial gas velocity, this is caused by the overall increase in pressure in the system which slightly affects the circulation pump. The uniform configuration has a larger superficial liquid velocity for high gas superficial velocities in comparison to the central-four rod injection. The flow region average void fraction is plotted against the superficial gas

velocity in Fig. 5.60.*c*. The results show that the uniform configuration has a consistently larger average void fraction, however, they both follow an increasing trend in relation to the escalation in superficial gas velocity.

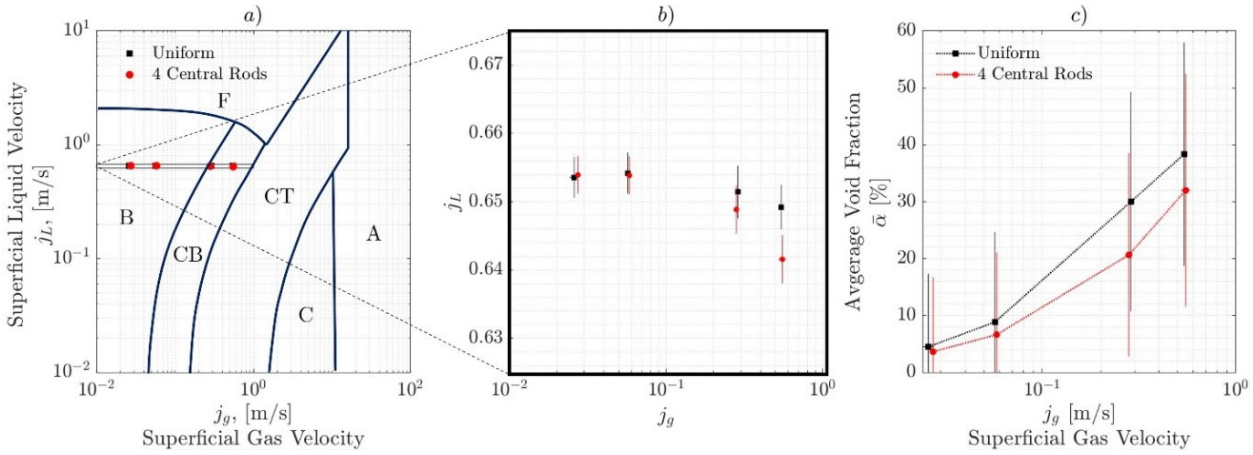

Fig. 5.60. ***a)*** **Flow regime map for vertical 8 x 8 rod bundle with air-water proposed by Liu et al. [107] from data obtained by Paranajpe et al. [138 - 140]. Bubbly (B), Finely dispersed bubbly (F), Capp Bubbly (CB), Cap Turbulent (CT), Churn (C), Annular (A).** ***b)*** **zoomed in region for the presented measurements.** ***c)*** **average void fraction relation to the superficial gas velocity.**

5.5. Summary of Findings

The MARBLE facility has been assembled at the ECMF lab at the University of Michigan. The facility has been specifically designed to measure high-resolution void-fraction distributions in a bundle geometry, for the validation of CFD and subchannel codes. The facility consists of an 8x8 rod bundle assembly characterized by a lattice pitch of 21.08 mm, rod diameter of 15.875 mm and a rod thickness of 0.6 mm. The gas injection is accomplished by 64 individual sparging rods located at the bottom of the assembly; this arrangement permits the air flow control for individual sparging channels in the assembly. The air is supplied from a large air reservoir composed of two 240-gallon tanks and a 120-gallon air compressor; the reservoir is nominally charged to 150 Psi. The gas supply pressure is stepped down by a pressure regulator, afterwards the flow is divided into five supply groups, these are then further divided by manifolds that supply individual sparging rods. The facility's operation is demonstrated by presenting a transient shakedown test which serves to highlight the bundle monitoring sensors, as well as explain how the experimental parameters are determined. The primary focus of the test is emphasized on the pressure sensors installed throughout the height of the facility, these are used to determine the air density and gas superficial

velocity.

The High-Resolution Gamma-Tomography System (HRGTS) detailed in section 2.3.1, is purposed with performing computed tomography measurements of the void fraction distribution inside the MARBLE facility. Simulations of the MARBLE facility paired with the HRGTS are carried out to assess the imaging capabilities of the CT scanner. The optimal pixel reconstruction size was determined by performing a parametric study in which the pixel size is progressively gradually decreased, and the resulting reconstruction is compared with the ideal model by estimating the RMSE; the pixel size was maintained as a divisible value of the rod-bundle subchannel size. The process was carried out for the various applied filters in the FBP process including the following: Ram-Lak, Shepp-Logan, Cosine, Hamming and Hann. The results for the tested filters depict a pixel-size range of 0.6 to 1.2 mm/pixel in which the RMSE is minimized. It was determined that a pixel size of 0.68 mm/pixel (31 pixels/subchannel) and the Ram-Lak filter are the appropriate settings in the reconstruction process. Next, the accuracy of the reconstructed void fraction obtained from the imaging reconstruction simulations was determined by varying the local subchannel void fraction from 1.5% to 96% across the 64 channels, with increments of 1.5%. Additionally, radiation noise was incorporated at various intensity levels to simulate low to high radiation fluxes representative of the decrease in activity or adjustment to the measured exposure time per projection; the investigated flat-field radiation intensities were [500, 1000, 5000, 10000, 50000] counts per projection, the noise incorporation procedure was carried out for 100 cases per simulated radiation intensity. The obtained results show that at low radiation counts the measured void-fraction presents larger fluctuations from the ideally imposed void-fraction, increase in counts dampens these fluctuations and approaches the idealized behavior. The standard deviation of the subchannel void fraction showed a decrement with respect to the increase radiation intensity. The pixel-wise void-fraction distribution for the subchannel regions was also investigated throughout the imposed radiation intensities as well as the noiseless case. The noiseless or idealized case revealed the fact that the estimated void-fraction will yield a narrow gaussian distribution for induvial regions, which highlights the reconstruction limitation of the CT system. The noise-based results showed that the pixel-distribution for individual regions had a broad gaussian distribution for low radiation counts. The increase in radiation counts progressively narrowed the Gaussian-bell distribution and approached the idealized (noiseless) pixel-wise distribution for the largest applied radiation counts.

The first set of CT void-fraction measurements of the MARBLE facility were carried for two different gas injection configurations. The first arrangement consists of a uniform gas injection in which all 64 rods

supply gas into the test section. For the second arrangement, the four central rods of the bundle are utilized to inject air into the system. The targeted injection gas superficial velocities at the sparger level were j_g = [0.5, 0.25, 0.05, 0.025] m/s for both cases. The CT measurements capture the spatial distribution of the void fraction throughout the measurements and the progression from high to low void fraction associated with the imposed gas superficial velocities. The presented CT measurements represent a successful demonstration of the promising deployment of the HRGTS as a non-intrusive tool for void fraction measurements. Future research will focus on performing a detailed experimental matrix of two-phase flow conditions inside the MARBLE facility to create a high-spatial resolution database for bundle geometries.

CHAPTER VI

Tomographic Imaging of Fuel Relocation Inside Sodium Fast Reactor Test Assemblies During Severe Accidents

6.1. Motivation

Deployment of Gen-IV reactors require a rigorous process involving R&D, testing, and licensing to make sure the reactor design meets the safety requirements under all Design Basis Accident (DBA) scenarios. It is also important to assess severe accident conditions that might ultimately result in fuel failure, cladding breach, and relocation of fuel inside the reactor vessel. A large part of the current knowledge of severe accident phenomena is based on Light Water Reactors (LWR) systems as detailed by Jacquemain et al. [78]. Hofmann [67] reports a thorough summary of the physical and chemical processes occurring during accident conditions for LWRs and identifies different operational temperature regimes driven by the heat-up rates leading to localized fuel rod and core damage, extended core damage, and total core destruction. The progression of fuel relocation is a complex multi-physics coupled process which presents various prognostication challenges; in these, the reactor changes its geometric arrangement thus altering both neutronic feedback and coolant flow area, hotter regions of the assembly become increasingly blocked by relocating material hampering the heat removal by the coolant, the coupled effects ultimately create a local positive feedback in which the heat-up rate escalates causing further cladding and fuel to melt.

The Sodium-cooled Fast Reactor (SFR) design established its inherent safety features through its passive heat removal demonstrated by the EBR-II experiment [144]. Research on DBAs and severe accident scenarios was carried out throughout the seventies and eighties. A wide range of phenomena were investigated including loss of flow and localized sodium boiling [42, 53, 86, 79], blockage and fuel dispersal modeling [38, 92, 190], fuel element failure [93], and molten fuel coolant interactions (FCI) [28, 79, 115,

172]. Since, computational capabilities have improved significantly, these are able to assess blockage accidents [48], fuel relocation and severe accidents [178, 195]. Nevertheless, experimental data remains a priority to further understand these complex processes and benchmark the multi-physics models implemented in computational codes; however, recreating the experimental conditions typical of fuel during severe accidents is challenging. Significant research on FCI has been focused on several aspects including simulated molten-jet interactions with coolant [98], fragmentation of molten metals in sodium pool [129], and metallic fuel discharges in coolant channels [82, 61, 90]. Schleisiek et al. [162] conducted extensive experiments with pre-imposed blockages embedded in fuel assemblies for liquid-metal reactors (LMR) that were tested in the BR2 reactor. The blockages were composed of active fissile material and alternatively of inert material, these covered roughly 30% of the assembly cross section and were in the center region or the periphery of the assembly. The assemblies were subjected to transient events which briefly induced sodium boiling and dryout conditions, ultimately resulting in cladding and fuel melting. A range of results were observed in the post-irradiation examination including fuel degradation, fuel fragmentation, fuel swelling, liquefaction of the cladding while the fuel pallets remained intact, complete fuel and cladding melting leading to melt cavities. A major conclusion drawn from this study was the assembly's damage dependency to the fuel burnup; low burnup resulted in localized minor damage, increase in burnup augmented the damage escalation through cladding-fuel failure and melting events. Bachrata et al. [14] draws the accident phenomena similarities and differences between pressurized water reactors (PWR) and SFR systems, how these compare and mitigation strategies which could be implemented to prevent them.

Further work of the severe accident conditions that could potentially lead to advanced core disruption and cladding breach have been investigated by Kim et al. [90 - 89] at Argonne National Lab (ANL). Within the ANL SFR test program, fuel assemblies were tested in an experimental facility that recreates severe accident conditions for fuel typical of SFR designs. In the present section, selected test assemblies obtained from the Argonne's Metallic Uranium Safety Experiment (MUSE) facility, referred to as the Pin Bundle Metallic Fuel Relocation (PBR) assemblies, have been analyzed using advanced imaging techniques. X-ray and gamma-ray computed tomography (CT) measurements of the PBR assemblies have been performed using the Michigan High-Resolution Tomographic Imaging (CHROMA) facility by the Experimental and Computational Multiphase Flow Lab (ECMFL) at the University of Michigan. The advanced imaging techniques have been used to depict the complex fuel relocation structures formed under severe accident conditions and the axial flow blockage in the test sections of the assembly has been quantified.

Tomographic measurements of nuclear fuels (U, Pu) are difficult to perform given that these materials are characterized by their relatively high densities and high-Z, resulting in severe attenuation of photons interacting with the material. Successful CT measurements of LWR damaged test assemblies were performed by Blanc et al. [18] in which a linear electron accelerator with a maximum energy of 5.5 MeV generated x-ray photons used for imaging. Other studies of fast breeder reactor (FBR) assemblies were reported by Ishimi et al. [76, 77], in which 9 MeV x-ray photons were generated for imaging. Additional work reported early on by Sawicka et al. [160] used 50 Ci ^{60}Co and ^{192}Ir gamma-ray sources to perform CT measurements of fuel pellets and post-irradiation PWR assemblies. These examples give perspective of the photon energy and radiation flux required to image highly attenuating nuclear materials. Consideration of tomographic methods applied to reactor applications is a growing topic; the present study focuses in applying these methods to characterize fuel relocation structures in mock-up fuel assemblies of sodium-cooled reactors post severe accident conditions.

6.2. Materials and Methods

6.2.1. Pin Bundle Metallic Fuel Relocation Assemblies

The Pin Bundle Metallic Fuel Relocation (PBR) experiment tested at the Metallic Uranium Safety Experimental (MUSE) facility is explained in detail by Kim et al. [89]. The experiment was conducted by injecting molten depleted uranium into the sodium filled PBR assembly to investigate the relocation behavior of the metallic fuel in case of severe accidents in SFRs. The PBR assemblies were manufactured following the prototype generation-IV sodium cooled fast reactor (PGSFR) fuel assembly [104] design as shown in Fig. 6.1 (b). The test sample has a total height of 0.706 m, the design specifications consist of a 19-pin tight lattice arrangement, with a rod pitch of 8.436 mm, rod length of 0.475 m, cladding outer diameter of 7.4 mm, cladding thickness of 0.5 mm, and a wire wrap diameter of 0.889 mm; geometric properties of the PBR assembly are summarized in Table 6.1. The fuel material is pure depleted uranium metal blocks with a melting temperature of 1132 C^{o} [19]. The fuel cladding material is HT-9M steel with an approximate melting temperature of 1475 C^{o} [46], the cladding filling is composed of aluminum oxide. The top 57.15 mm section of the cladding was left empty to allow the flow of fuel inside. The molten uranium metal is dropped from graphite crucible to the diaphragm of the test section using a pneumatic cylinder. Once the diaphragm is broken, the molten fuel drops by means of gravity into the test section, this is denoted as the fuel path shown in Fig. 6.1 (a). Under the assumption that the uranium velocity is zero

when the diaphragm breach occurs results in an estimated molten fuel velocity of 1.58 m/s at the top of the upper plenum of the assembly. The experimental conditions for which the PBR assemblies were tested are as follows.

- In the PBR-1 experiment, 772.5 g of the uranium were heated to 1652 °C, and were introduced by dropping the molten fuel into the upper plenum of the assembly, allowing the material to sporadically disperse through the subchannel and inner cladding regions. Prior to the dropping of the molten fuel, the sodium temperature in the subchannel was 635 °C at thermocouple (TC) 3. When the cladding breach occurred due to the eutectic formation, the fuel dropped into the cladding was ejected into the sodium coolant channel. This was a condition for investigating the relocation behavior of the fuel in a state where the core disruption has progressed to some extent.
- In the PBR-2 experiment, 768.3 g of the uranium were heated to 1671 °C. The molten uranium was inserted in a controlled manner through a guide funnel composed of Alumina Silicate (Grade A Lava) which directed the molten material into seven central cladding pins. Prior to the injection of the molten fuel, the sodium temperature in the subchannel was 676 °C at TC 3. The molten uranium could only be ejected into the sodium channel via the eutectic formation. This allowed only horizontal ejection of uranium into the subchannel, which simulates the initial cladding rupture.

Table 6.1. PBR assembly specifications

Property	Units	Value
Rod Pitch	[mm]	8.436
Rod Length	[m]	0.475
Rod Outer Diameter	[mm]	7.4
Rod Thickness	[mm]	0.5
Wire Wrap Diameter	[mm]	0.889
Casing Hexagonal Minor Diameter	[mm]	38.86
Wet Perimeter	[mm]	629.39
Hydraulic Diameter	[mm]	3.04
Flow Area	[mm^2]	478.83
Total Sample Heights	[m]	0.706

The radiographs presented in Fig. 6.1 show the fuel relocation for the PBR assemblies, (left) PBR-1 core disruption, and (right) PBR-2 cladding breach. Highlighted in red are the three assembly sections measured using CT imaging. The first section is located between TC 8 and 9 of PBR-1, the second section is located between TC 2 and 3 of PBR-1, the third section is located between TC 6 and 7 of PBR-2.

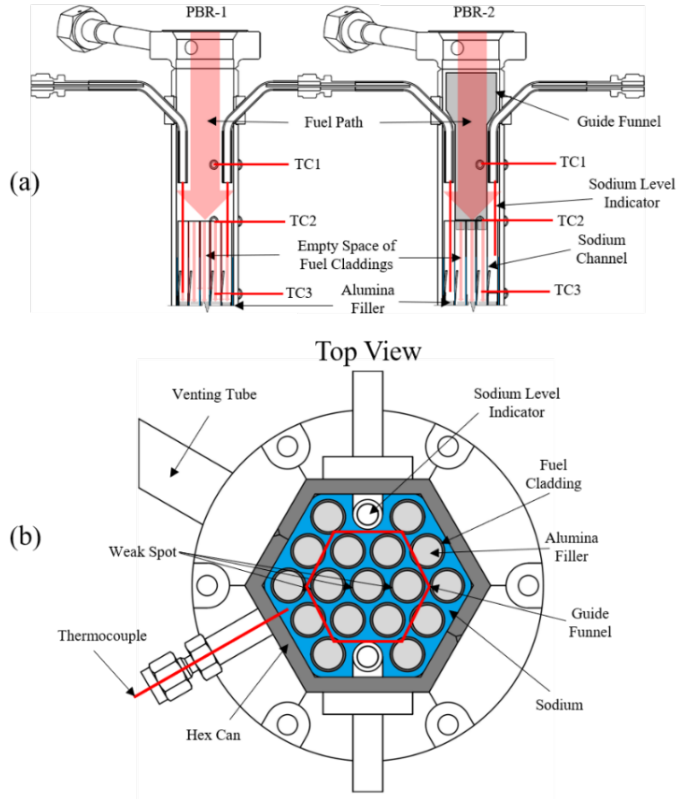

Fig. 6.1. (a) Cross section and (b) top view of PBR assemblies.

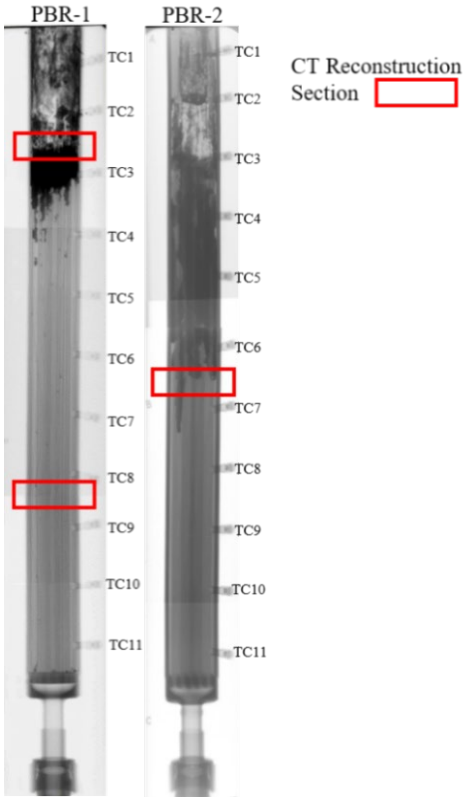

Fig. 6.2. Radiographic images of PBR-1 (left) and PBR-2 (right) test samples. Measurement performed at ANL.

6.2.2. Radiation Imaging Methods

The first set of measurements were conducted using the x-ray source, operated at a nominal voltage of 150 kV and a focal spot of 0.6 mm. The current was varied between 25 and 200 mA depending on the section being measured (sections with a larger Uranium content leads to higher photon attenuation and therefore require a higher photon flux, and therefore current, to be imaged). The exposure time was ranged between 1000 and 2000 ms per angular measurement. The reason for the variation of exposure time was due to the power imparted on the anode target of the x-ray tube, dictated by the voltage and current; this can rapidly heat the target resulting in a longer measurement dead time to allow cool down between

measurements. The CdTe detector presented in section 2.3.2 was operated at 100 fps; the fast frame rate prevents the detector from saturating during the detector integration time. The detector features an energy threshold which discriminates counting events below the set energy; The default detector energy threshold of 15 keV was used during the measurements performed for the PBR-1 TC 8-9, and PBR-2 TC 6-7 sections. The energy threshold was increased to 40 keV for the measurement of the PBR-1 TC 2-3 sections in which higher photon flux was used (due to the applied high current) and where higher energy photons would be the primary source for imaging in this highly attenuating section as seen in Fig. 6.2. The x-ray and detector operational parameters for the three measured sections are summarized in Table 6.2. Frames capturing the initial x-ray power-up were neglected, only full power frames were considered throughout the measurements.

Table 6.2. X-ray tube and detector operational parameters

Measurement Section	Voltage [kV]	Current [mA]	Exposure time per degree [ms]	Fps	Detector Threshold [keV]	Focal Spot [mm]
PBR-1 TC 2 & 3	150	200	1600	100	40	0.6
PBR-1 TC 8 & 9	150	50	2000	100	15	0.6
PBR-2 TC 6 & 7	150	25	1000	100	15	0.6

The measurements of the flat fields for each of the selected measurement areas were performed three times in order to reduce the flat field variance, as previously discussed. The measurement convergence was assessed from the flat field measurements by using a stationary 20 x 20 voxel window and calculating the cumulative average of the window count rate as a function of frames sampled, as shown in Fig. 6.3. Random permutations of the considered frames create statistical bands of the average count rate convergence under the assumption that the process is stochastic. The average count rate converges to 3188 counts per frame (exposure of 10 ms/frame) when utilizing the entire set of flat fields; however, the continuously sampled average count rate shows that the measurement is biased by the x-ray power variation as it follows specific path, meaning that it is not a random process. Discontinuities which represent the three different flat field measurements are also observed. The x-ray measurements were corrected by applying a power scaling factor determined from the flat field window across the independent measurements. Similarly, the cumulative standard deviation is calculated as a function of number of frames considered, which also shows the discontinuity from subsequent measurements. However, the standard deviation converges to about 4 counts/frame as is shown on the right of Fig. 6.3.

The second set of measurements were performed with the ^{192}Ir radioactive source. In this case, additional lead shielding was placed in front of the CdTe detector to protect the electronics, leaving an aperture for the effective detection area. The exposure time per degree was one minute, consequently longer in comparison to the x-ray measurements. Longer measurement times are required due to the detector's lower photon efficiency at the higher photon energies, shallow crystal depth for interaction, and lower photon emission of the gamma source in comparison to the x-ray source. The detector was operated at 10 frames per second with the default 15keV energy threshold. Table 6.3 summarizes the detector operational parameters, and radioactive source activity at the time the measurements were performed.

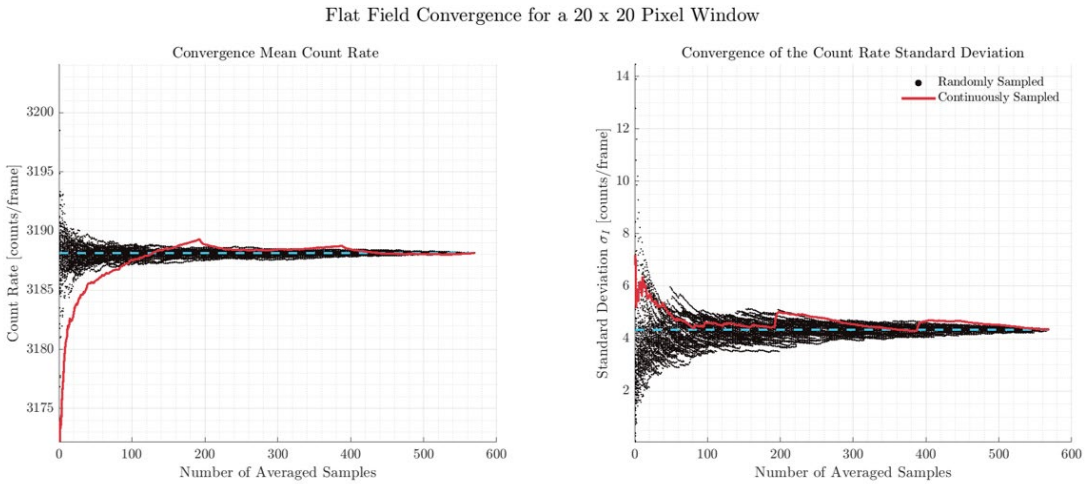

Fig. 6.3. X-ray convergence analysis of the cumulative average count rate (left) and cumulative standard deviation (right) as functions of number of considered frames.

The flat field average count rate convergence was also analyzed for the gamma-ray source measurements, and the results are presented in Fig. 6.4. The convergence analysis shows proper average count rate convergence, and the continuously sampled average count rate exhibits the stochastic nature of the radioactive decay process of the source. The converged count rate standard deviation is about 2.42% of the converged count rate.

Table 6.3. Gamma-ray measurement parameters

Measurement Section	Source Activity [Ci]	Exposure time per degree [ms]	fps	Detector Threshold	Focal Spot [mm]
PBR-1 TC 2 & 3	13.3	6000	10	15kV	1.5
PBR-1 TC 8 & 9	13.4	6000	10	15kV	1.5
PBR-2 TC 6 & 7	12.3	6000	10	15kV	1.5

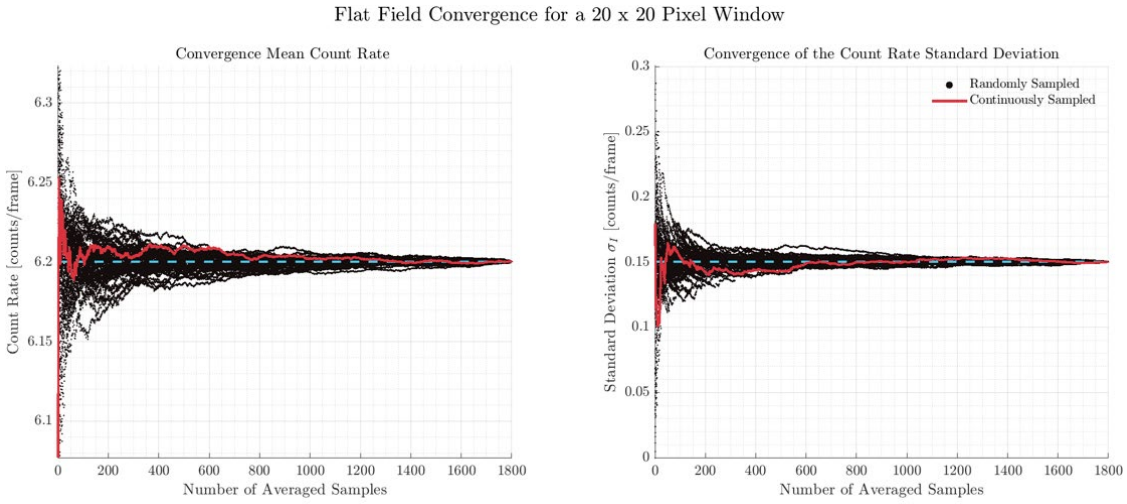

Fig. 6.4. Gamma-ray convergence analysis of the cumulative average count rate (left) and cumulative standard deviation (right) as functions of number of considered frames.

6.3. Results and discussion

6.3.1. X-ray Measurements

The focus of this discussion is the PBR tomographic measurements performed using x-rays. The first measured section was located between TC 8 and 9 of the PBR-1 assembly (see Fig. 6.2), as observed in the radiograph shown in panel (A) of Fig. 6.5; the section contains three small high-attenuating fragments. These fragments are presumed to have dislodged during the initial impact of the molten fuel being dropped onto the upper plenum of the assembly. The reconstructed tomogram of the test sample is shown in Fig. 6.6, the three fragments are shown in planes *a* through *c*, plane *d* shows an example of the assembly without any high-attenuation content present. The cross-sectional tomograms presented in panel (A) of Fig. 6.6 reference the radiograph planes displayed in panel (A) of Fig. 6.5. The tomogram shows that the assembly has not suffered structural damage and the three fragments are trapped between the assembly casing and the rods. The flow area voxels have slight contrast difference with the Alumina filling inside the rods. The assembly casing shows increased contrast towards the vertices, which is an effect deriving from the x-ray photon spectrum, where the beam is not as hardened at angles in which the vertices are at the edge of the field of view.

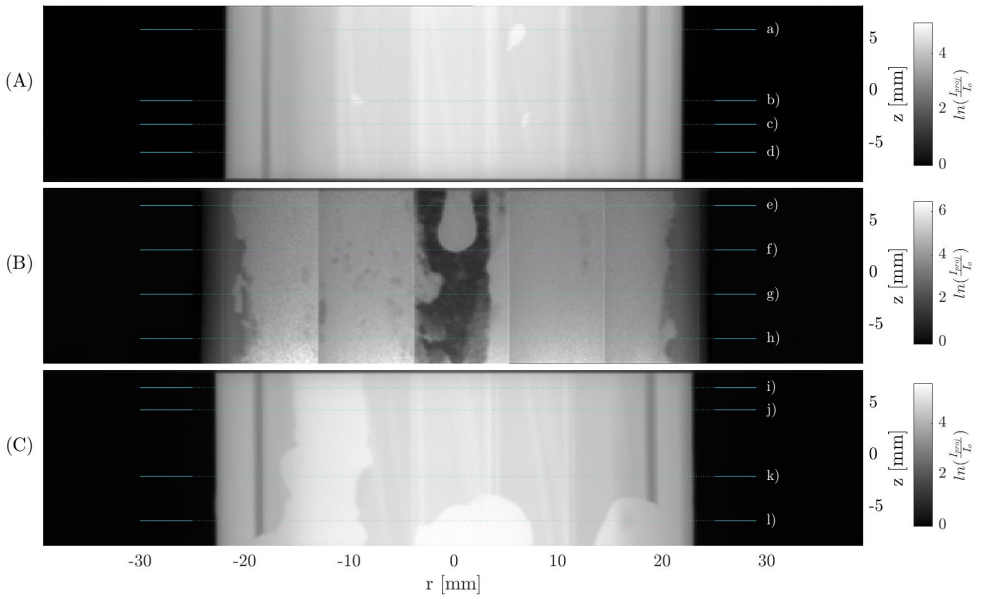

Fig. 6.5. X-ray radiograph example of the tomographic measurements. PBR-1 TC 8&9 shown in panel (A), TC 2&3 shown in panel (B), and PBR-2 TC 6&7 shown in panel (C).

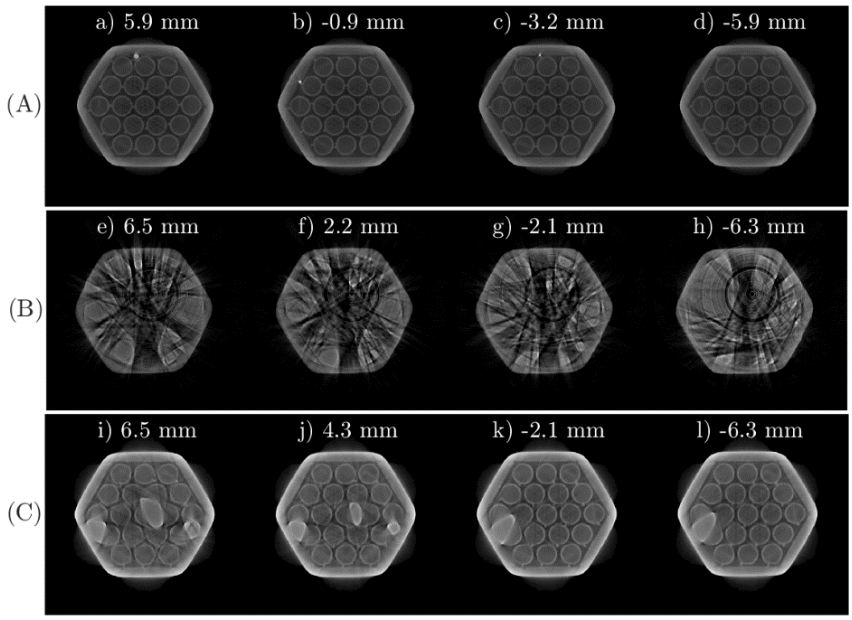

Fig. 6.6. X-ray tomogram of PBR-1 TC 8 & 9 shown in panel (A), TC 2&3 shown in panel (B), and PBR-2 TC 6&7 shown in panel (C).

The second section measured was between TC 2 and 3 of the PBR-1 assembly. This section contains large amounts of high-attenuation materials, as shown in the radiograph in panel (B) of Fig. 6.5. Additionally, the radiograph shows tiled behavior throughout the measurement; these are observed as shadows between detector panel regions, primarily due to the detector being held at a 40 keV energy threshold combined with a high photon flux. The tomogram shown in panel (B) of Fig. 6.6 presents high

photon starvation artifacts characterized as streaks, which are observed throughout the entirety of the reconstructed tomogram. The photons generated by the x-ray tube cannot penetrate through the material present in this section, rendering the reconstruction unresolved and challenging any quantitative analysis of this section.

The third measured section was performed between TC 6 and 7 of the PBR-2 assembly. This region contains three distinct structures, as shown in the radiograph shown in panel (C) of Fig. 6.5. The structures appear as flat silhouettes, once again hinting at photon starvation challenges in the measurement. The reconstructed tomograms in panel (C) of Fig. 6.6 map the spatial location of the structures, however it does not resolve the inner regions of these. They do not exhibit distinct features, their shapes are oblong because the dense material is optically thick throughout the angular range for which the measurements were performed, severely attenuating photons traversing these regions. Furthermore, the photon starvation streaks emanating from these structures degrade the reconstruction of objects in the vicinity due to the angular obstruction of these structures.

The tomogram local linear attenuation distribution of the three x-ray measurements are plotted in Fig. 6.7 following the procedures stated in Section 3.3. From the previous results, it was established that the PBR-1, TC 8 and 9 section contains the least amount of relocated fuel with only small dislodged fragments present; this is reflected in the shape of the distribution as it abruptly decreases approaching the 0.39 cm^{-1} linear attenuation. Low residuals follow beyond this reference value corresponding to the voxels from the three high-attenuating fragments. Several other features were identified, the tail before the abrupt decrease belongs to the test assembly casing in which the vertices have increased values; the cladding and aluminum oxide fillings have distinct associated peaks in the distribution. The flow area is the least attenuating medium which lies at the beginning of the distribution. This measurement serves as reference of the linear attenuation distribution of an unperturbed assembly. The linear attenuation distribution of the PBR-1, TC 2 and 3 section has a long high attenuation tail, however, it does not present any specific features. The distribution is smoothed following the trend of the previously described reference distribution. The PBR-2, TC 6 and 7 section linear attenuation distribution contains many similar features that were described in the reference distribution, such as the aluminum oxide and cladding peaks following a larger amount of higher-attenuation content past the 0.39 cm^{-1} reference.

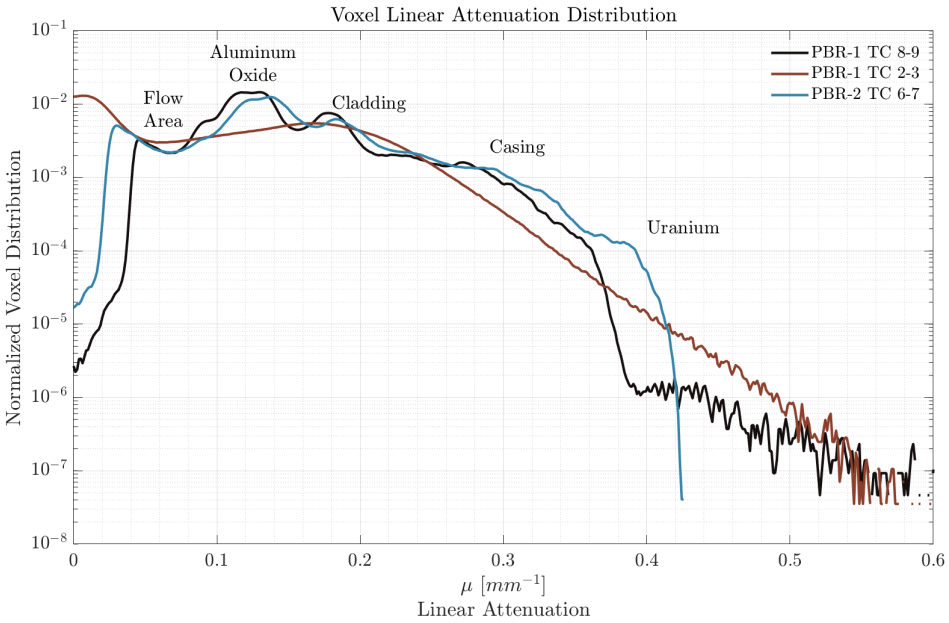

Fig. 6.7. Voxel linear attenuation distribution for the three sections measured using x-rays.

6.3.2. Gamma-ray Measurements

The measurements were repeated with the previously described ^{192}Ir gamma-ray source. The TC 8 and 9, PBR-1 gamma-ray radiograph shown in panel (A) of Fig. 6.8 is similar to the x-ray tomographic results presented in panel (A) of Fig. 6.5. The gamma-ray measurement shows higher contrast between the three fragments present and the surrounding assembly material. The fragment shown in plane *a* has a 1.7 mm diameter and its largest length is about 2.9 mm. The second fragment, displayed in plane *b* has a 0.7 mm diameter and its largest length is about 1.7 mm. The third fragment, displayed in plane *c* has a 0.5 mm diameter and in its largest length about 1.7 mm. plane *d* is a reference example of the unperturbed test assembly, it also defines the rod positions that will be used for further analysis. The reconstructed tomogram has improved contrast between the dense fragments, cladding, casing, rod filling, and flow area in comparison to the x-ray measurements of the same section. Attenuation distinction is particularly important between the rod fillings and the flow area regions to perform the flow blockage analysis discussed in the next section.

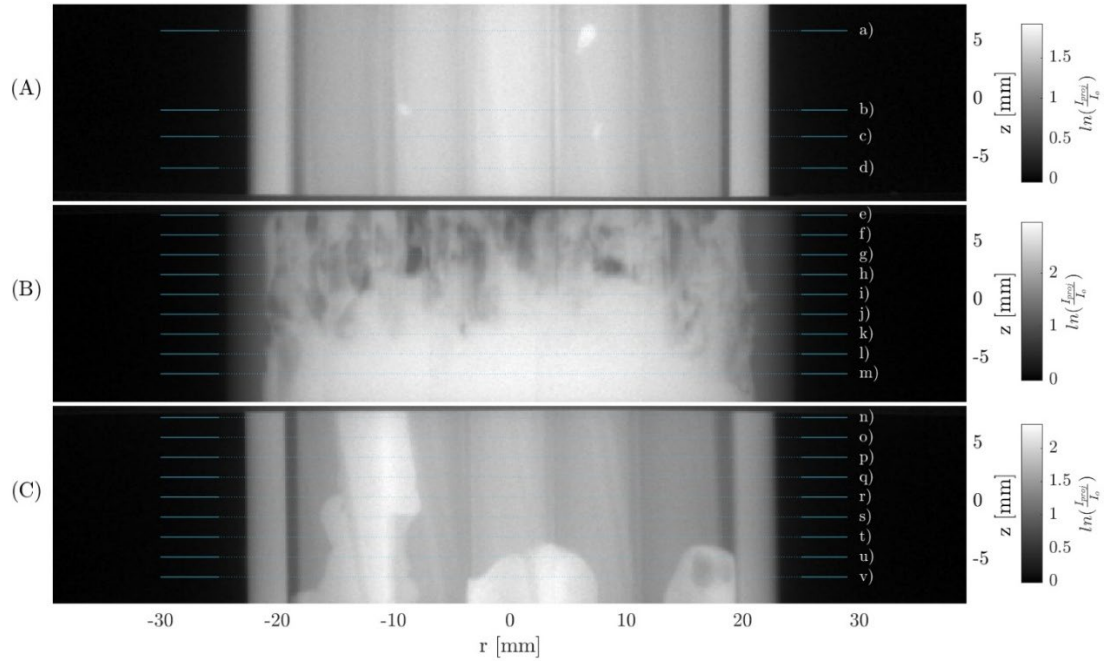

Fig. 6.8. Gamma-ray radiograph example of the tomographic measurements. PBR-1 TC 8&9 shown in panel (A), TC 2&3 shown in panel (B), and PBR-2 TC 6&7 shown in panel (C).

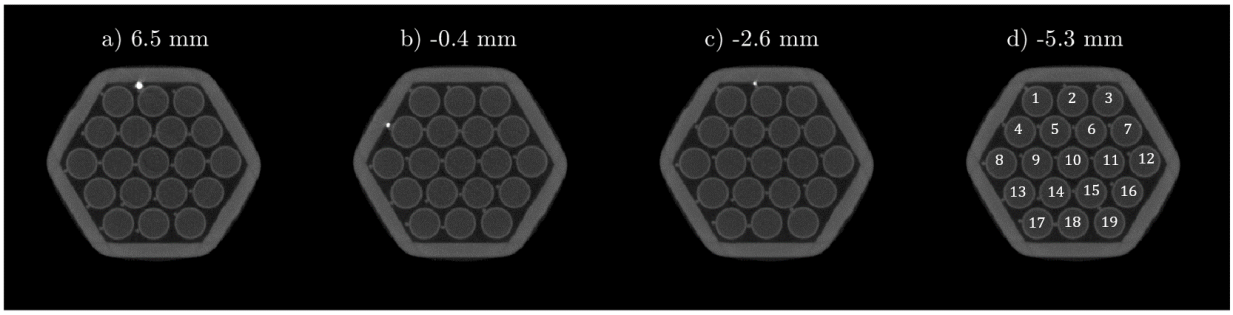

Fig. 6.9. Gamma-ray tomographic reconstruction of PBR-1, TC 8&9, planes reference Fig. 6.8 radiograph.

The second measurement with the gamma-ray setup was performed between TC 2 and 3 of the PBR-1 test sample. This region was determined to be optically thick for the x-ray photon energy discussed in the previous subsection. The gamma-ray radiograph presented in panel (B) of Fig. 6.8 shows higher photon penetration, particularly in the upper plenum of the section, while the medium and lower plenum remain impenetrable at the measured gamma-ray source activity and energy. The cross-sectional tomogram planes are displayed in Fig. 6.10, plane-a serves as a reference map of the additional XZ and YZ tomogram slices presented in Fig. 6.11 and Fig. 6.12 respectively; the subscripts of these slices reference the plane location in Fig. 6.10. The tomogram contains traces of photon starvation streaks wherever the relocated fuel is located, nevertheless, it is an improved result in comparison to x-ray measurement of the same region. The

results show the complete and partial disintegration of the assembly rods located in positions [2, 5, 6, 9, 10, 11, 14, 15, 18] (see Fig. 6.9 position reference) evident in planes *e*-*h* of Fig. 6.10. The relocated fuel adheres to the surviving cladding walls and permeates the subchannel regions; this is best shown in planes *e*-*g*. For example, the slices $\mathtt{yz}_{1-2}$ (subscripts denotes slices 1 through 2) in Fig. 6.12 depicts how the relocated fuel adheres to the casing, inner and outer rod walls located in position 1 and 3. Another example is the rod located in position 8 shown in plane *g*, which contains high-attenuation material filling the inner region of the rod, trapped during the spontaneous insertion of molten relocating material from above. The $\mathtt{xz}_{1-5}$ slices show attenuation gradient values of the material inside the rod which can be attributed to eutectic phases between the cladding and the relocated fuel reported by Kim et al. [90, 88]. The quality of the reconstructed tomogram degrades sharply past plane *h*. This is also observed in the lower plenum of the XZ and YZ slices, where the photon starvation hinders the lower portion of the tomogram and can no longer be resolved. The tomogram and radiograph hint that the section is increasingly plugged with relocated fuel below the measured region.

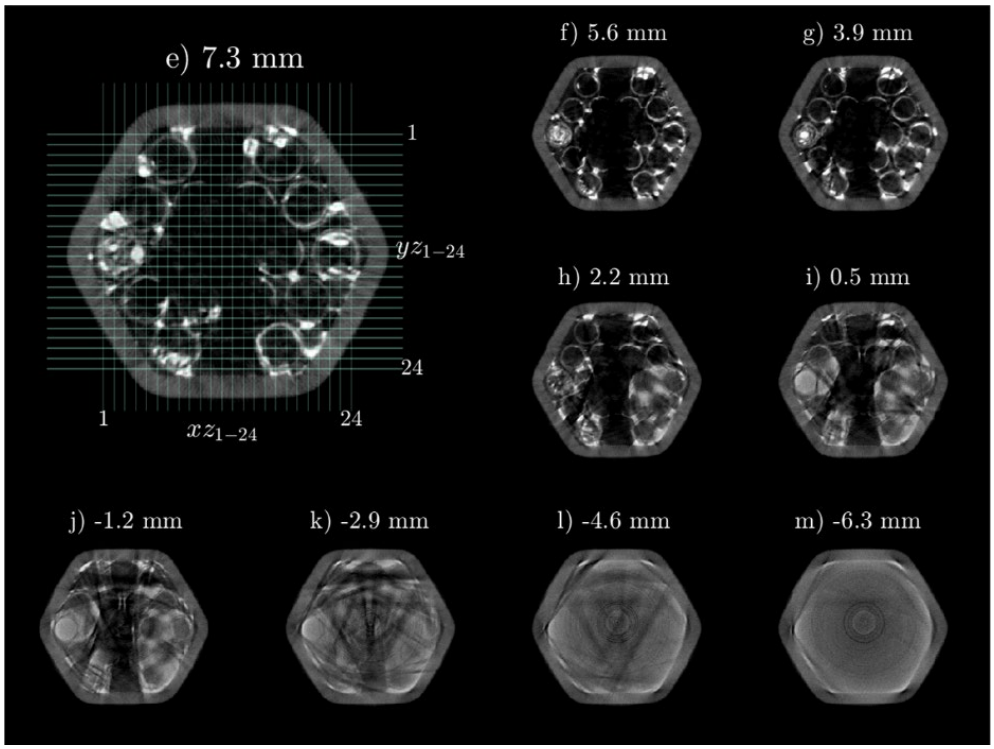

Fig. 6.10. Gamma-ray tomographic reconstruction of PBR-1, TC 2 & 3, planes reference radiograph in panel (B) of Figure 6.9.

Fig. 6.11. XZ slices of PBR-1, TC 2 & 3

Fig. 6.12. YZ slices of PBR-1, TC 2 & 3

The radiograph of the section between TC 6 and 7 of the PBR-2 test shown in panel (C) of Fig. 6.8 illustrates the same three columnar structures that were previously observed in the x-ray measurement; however, increased photon penetration is observed as more distinct features in the structures become visible. The tomogram cross sections are shown in Fig. 6.13, with plane n serving once again as the reference map of additional XZ and YZ slices presented in Fig. 6.15 and Fig. 6.16 respectively. The three distinct structures that were previously mapped in the x-ray results are spatially resolved in this measurement. It is important to recall that the fuel relocation of the PBR-2 test sample was completed by pouring the molten material into the rods, therefore fuel relocation into the subchannel as observed in the tomogram results of Fig. 6.13 is accomplished by breaching the cladding. The relocated fuel protrudes into the cladding at the material interface; however, structural integrity of the assembly is maintained in this region in comparison to the upper section of PBR-1. The planes o and p show the leading edge of the central and right structures. The central structure contains a small void of approximately 0.8 mm in diameter which is observed in slices $\mathtt{xz}_{14}$ and $\mathtt{yz}_{15}$ (potentially too small for the reader to see). Voids of this type, occurring inside the relocation fuel have been previously reported by Kim et al. [90, 88], most likely caused by sodium boiling. The structure on the right presents a large void which can be detailed in slices $\mathtt{xz}_{19-23}$ and $\mathtt{yz}_{16-21}$; this void has an irregular contour as observed in plane o, its height and diameter are approximately 3.28 mm and 3.47 mm respectively using view $\mathtt{yz}_{18}$ as a reference. The third structure on the left spans across the entire vertical field of view; the progression from planes n through v depicts how part of the relocating material diverts into the adjacent subchannel. Preliminary radiographs from Fig. 6.2 reveal that these columnar structures traveled through the subchannel due to gravity.

The tomogram voxel linear attenuation distributions were calculated for the three measurements performed with the gamma-ray setup; these are depicted in Fig. 6.14. The voxel distribution of the PBR-1 test sample between TC 8 and 9 shows distinct peaks representing the flow area, alumina filling, cladding and casing, the distribution sharply drops past the 0.09 $\mathtt{cm}^{-1}$ reference value, voxels above this value correspond to the three relocated fragments observed in this section. The distribution of the measurement performed between TC 2 and 3 of PBR-1 shows a smooth distribution with a peak located at the cladding and casing linear attenuation value. The distribution has a long tail representing a vast quantity of high attenuating material. The lower plenum corresponding to the unresolved region and values belonging to the eutectic formations which occur at the cladding and relocating material interface largely contribute to the tail of the distribution. The PBR-2 TC 6 and 7 test sample distribution exhibits the distinct peak features

pertaining to the assembly materials that were characteristic in the PBR-1, TC 8 and 9 assembly, with the addition of the fuel relocation peak located at 0.18 cm^{-1}. The distributions obtained from the gamma-ray measurements accentuate the sharper material contrast through the better-defined peaks and distinction with the relocated fuel.

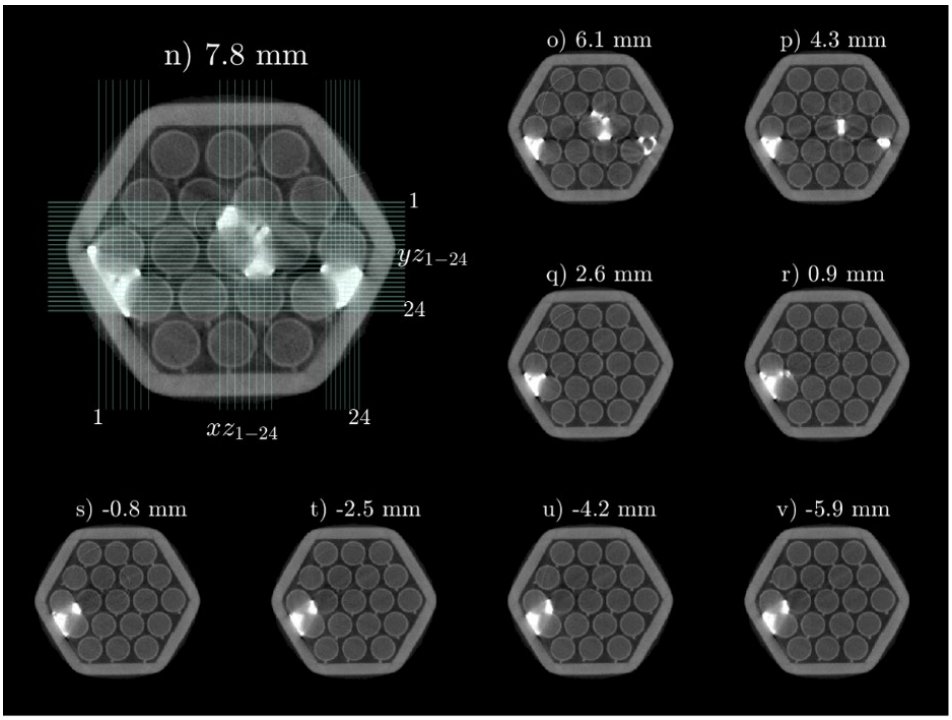

Fig. 6.13. Gamma-ray tomographic reconstruction of PBR-2, TC 6 & 7, planes reference radiograph in panel (C) of Figure 6.9.

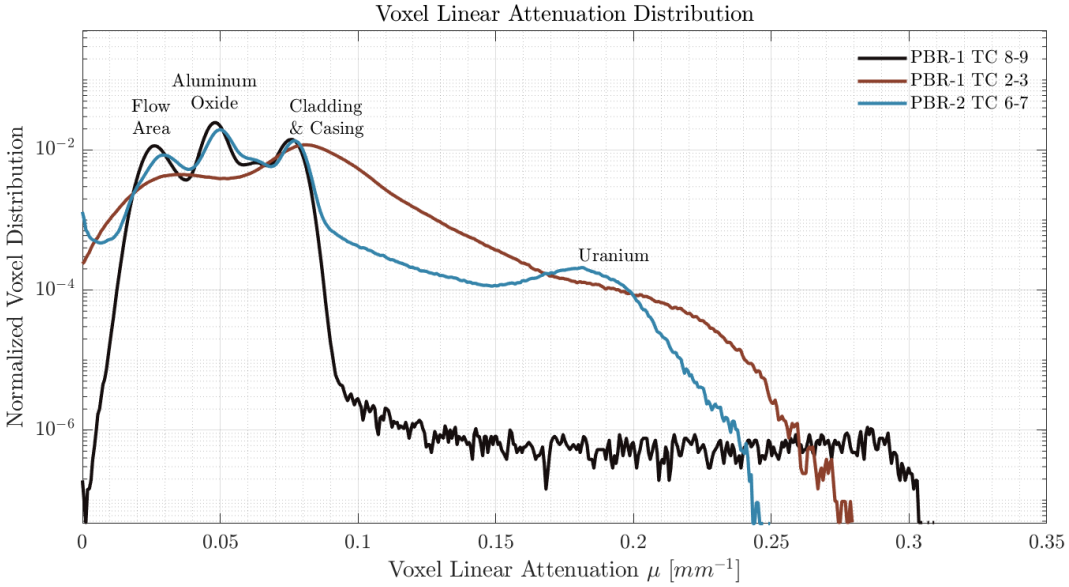

Fig. 6.14. Voxel linear attenuation distribution for the three sections measured using gamma-rays.

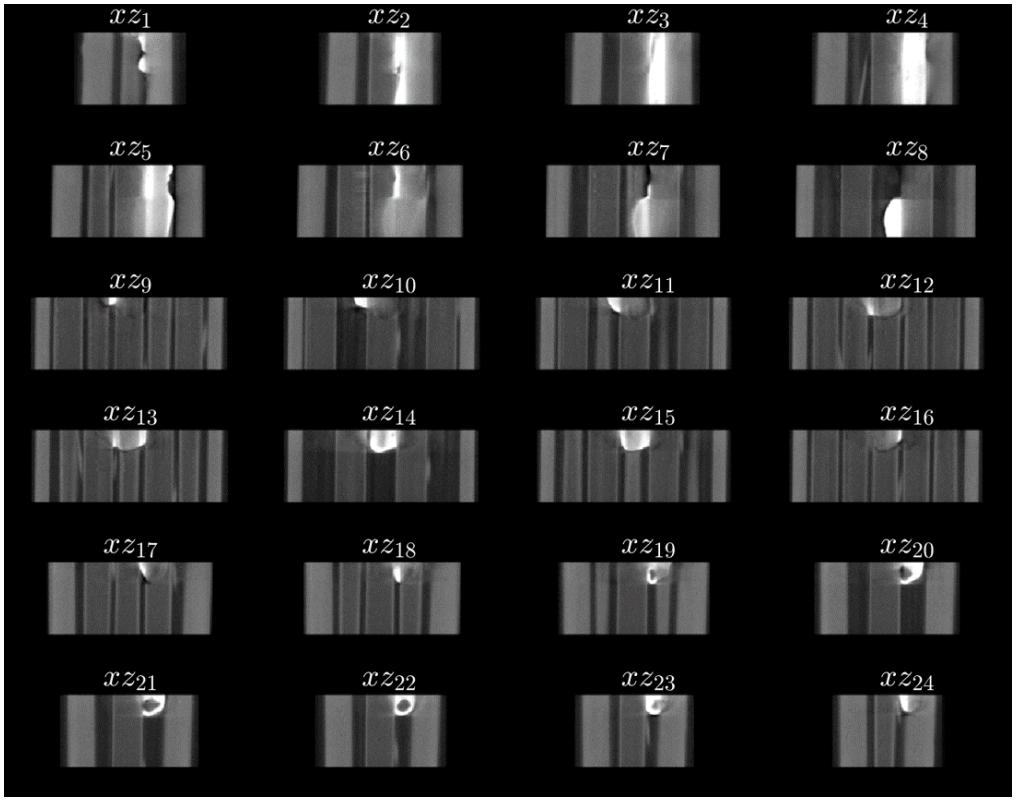

Fig. 6.15. XZ slices of PBR-2, TC 6 & 7.

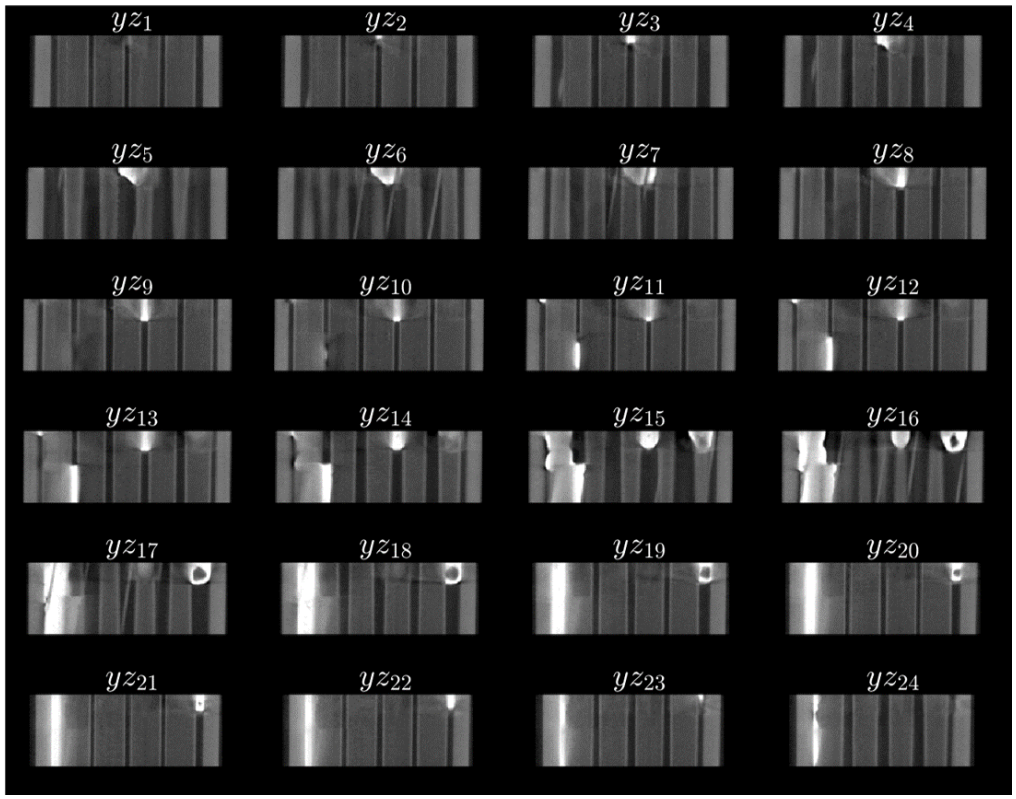

Fig. 6.16 YZ slices of PBR-2, TC 6 & 7.

6.3.3. Assembly Flow Blockage

The flow blockage was assessed using the unperturbed cross sections of the PBR-1, TC 8 and 9 measurements to build a mask and isolate the flow region. The mask does not cover the wire wrap given that this is a helical structure that rotates around the rod's outer diameter. Nevertheless, the wire wrap is accounted by thresholding the wire wrap and any residual cladding attenuation values. The ideal flow area based on the provided drawings of the test assembly is 478.83 mm^2 (found in Table 6.1), the mask estimated flow area is 463.45 mm^2, this is a 3.21% error which arises from manufacturing tolerances and wet perimeter voxels located at the boundary of the flow area and the material wall. The flow blockage was estimated using the methods described in section 3.3; the results are presented on the right of Fig. 6.17. The largest fragment in this region occupies approximately 0.62% of the flow area at most, followed by a 0.23% and 0.14% blockage from the remainder smaller fragments. The total molten fuel mass estimated in this section is 0.14 g of fuel material, representing 0.02% of the inserted mass. Additional 3D rendering of the tomogram presented Fig. 6.17 give perspective to the amount of relocation fuel (white isosurface) in comparison to the test assembly (teal isosurface).

The flow region for the PBR-1, TC 2 and 3 section had to be redefined, given that various rods had partially and completely disintegrated, the test section can then accommodate more coolant volume in this region; therefore, the flow area was redefined as the inner hexagonal cross section of the casing. Blockage material was also defined as attenuating objects above the flow channel reference attenuation, this being approximately 0.037 cm^{-1} corresponding to the right side of the flow area peak in Fig. 6.14. The appropriate mask was generated and applied to the PBR-1, TC 2 and 3 tomogram. The resulting flow blockage depicted on the right of Fig. 6.18 shows that in the upper plenum the blockage ranges from approximately 15% to 40%, with a large uncertainty of the present material in the region bellow; the blockage steadily increases when approaching the unresolved region. The molten fuel mass cannot be estimated in this section because of the molten mixture of fuel and rod material. The 3D rendering gives dimensionality to the fuel relocating structures, resulting in complex shapes, trapped in the subchannels, these are attached to the cladding and casing walls, particularly appreciated in the top view on the left.

The last flow blockage analysis was performed for the PBR-2, TC 6 and 7 section using the same mask that was developed for the PBR-1, TC 8 and 9 section. The upper plenum presents a blockage of approximately 16%, the blockage decreases to 5% past the leading edge of the two relocating slug structures, the results are shown on the right of Fig. 6.19. The total molten fuel mass estimated in this section is 10.7

g, representing 1.4% of the inserted mass. The 3D rendering details how the diverting branch from the left structure migrates onto the adjacent subchannel; this view also shows the large void present on the right most structure.

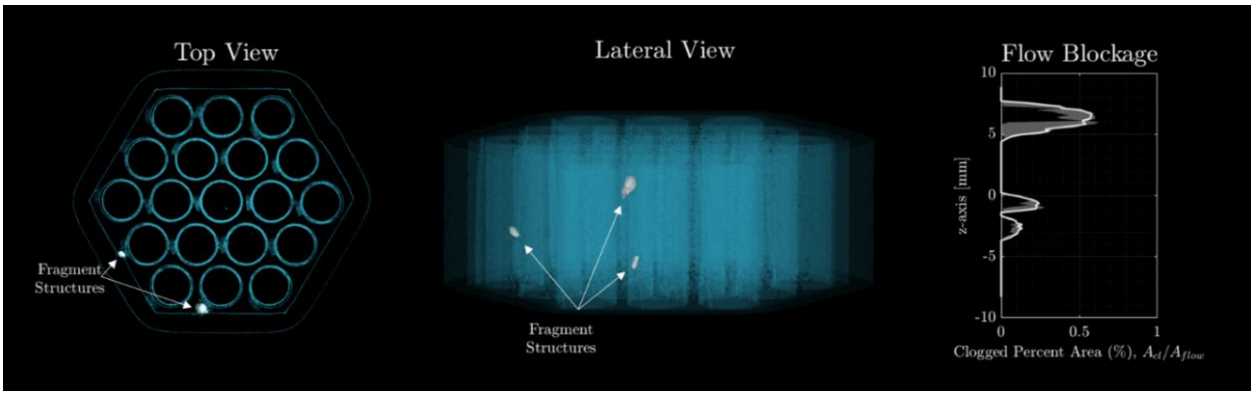

Fig. 6.17. PBR-1, TC 8 &9 rendering top view (left), lateral view (middle), and flow blockage results (right).

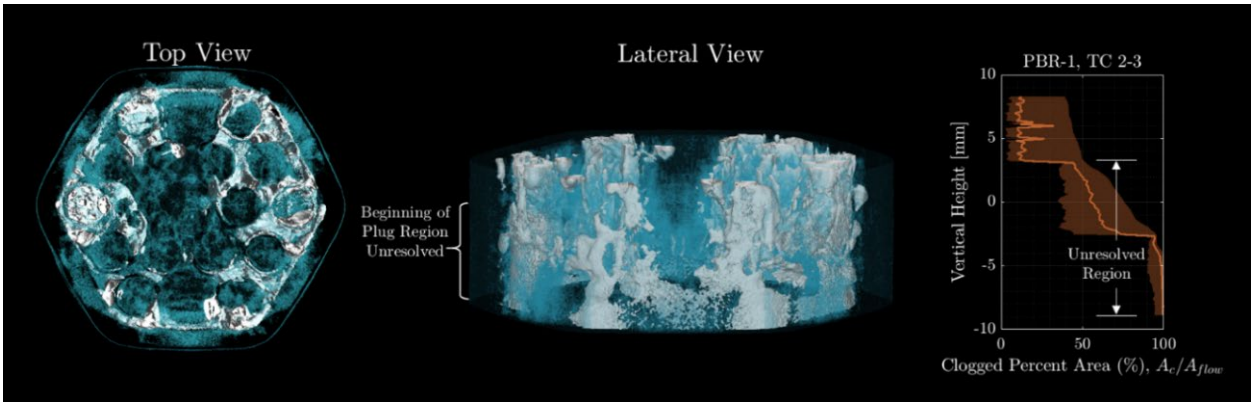

Fig. 6.18. PBR-1, TC 2 & 3 rendering top view (left), lateral view (middle), and flow blockage results (right).

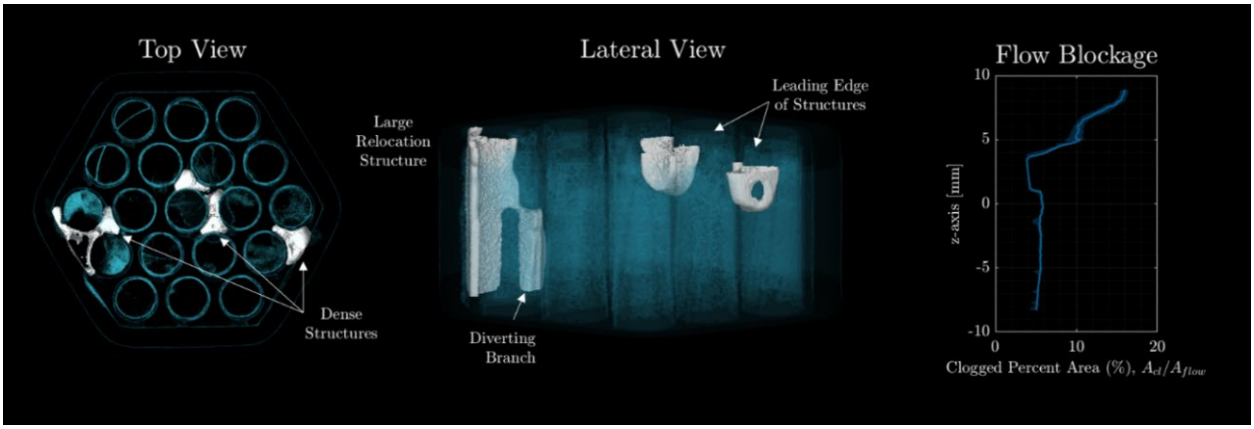

Fig. 6.19. PBR-2, TC 6 & 7 rendering top view (left), lateral view (middle), and flow blockage results (right).

6.4. Summary of Findings

Understanding of accident progression is an important consideration in the design and operation of nuclear reactors. The present study aimed to perform high spatial resolution CT measurements of two SFR assemblies which recreated the fuel relocation process during severe accident conditions, as further detailed in Kim et al. [88-90]. The first assembly analyzed in the present paper (PBR-1 test section) represented the state of an SFR fuel assembly after a severe accident scenario resulting in advanced core disruption. The second assembly (PBR-2 test section) recreated cladding breach conditions without extensive core disruption. Three sections of the test assemblies were measured, corresponding to a range from small, medium to large quantities of relocated fuel present in the field of view.

The first set of tomographic measurements were performed using x-rays as photon source. These measurements were able to resolve small fragments of relocated fuel; with increased quantities of relocated fuel, the spatial location of the structures could still be mapped, however, the inner regions of the relocated structures could not be resolved. The section with the largest amount of relocated fuel presented a significant amount of photon starvation artifacts, which hindered the x-ray imaging reconstruction. The second set of tomographic measurements were performed using a nominal 15Ci gamma-ray source. These measurements resulted in improved reconstructed tomograms on which the analysis of the flow blockage was based. The conclusions from the three measured sections are the following:

- The PBR-1, TC 8&9 section contains small dense fragments trapped between the wire-wrap, cladding wall, and assembly casing. These fragments were dislodged during the initial insertion of the molten uranium into the assembly. This section contained several planes free of dense material which were used as reference for the linear attenuation distribution of an unperturbed assembly, from which a mask was generated to isolate the available flow area. The flow blockage was assessed for values above the cladding and casing linear attenuation, isolating the relocated fuel. The flow blockage in this section was less than 1% due to the size of the fragments present.
- The PBR-1, TC 2&3 section exhibited the highest structural damage. The tomogram displayed the partial and complete disintegration of the central assembly rods. Vast quantities of molten material are located in the subchannels, these relocation structures adhere to the surviving cladding wall and assembly casing. Material trapped inside the inner rod exhibited gradient linear attenuation values hinting to eutectic phases formed between the relocating material and cladding. The quality

of the tomogram degrades towards the lower plenum of this section due to high photon starvation effects which hinder the reconstruction towards the bottom of the tomogram. The guidelines to determine the flow blockage for this section had to be redefined given that the available volume for flow increased in the upper plenum, therefore the flow area was then defined as the casings inner hexagonal wall. The blockage material was determined as linear attenuation values above those corresponding to the flow area. The blockage in the upper plenum ranged from 14 % to about 40%, it steadily increases in the medium plenum in the lower plenum, however this region was determined to be unresolved from the degradation of the tomogram quality. The quantity of attenuating material in the lower plenum of this section approaches the capabilities of the imaging system.

- The PBR-2, TC 6&7 section is characterized by three separate relocating structures which migrated through the subchannels, the leading edge of two of these structures were captured. The relocation fuel protrudes into the cladding that it encounters. Cross migration was observed as the material from the largest structure diverts into the neighboring subchannel. A small void embedded inside one of the dense structures was observed. Kim et al. [88-90] attributes these to possible sodium boiling inside the relocating material. The flow blockage in this section was estimated to be approximately 16% in the upper plenum; however, past the leading edge of two of the fuel relocation slug structures, the blockage decreases to approximately 5% for the middle and lower plenum based on the remaining relocated structure.

The gamma-tomography results provided detailed high-spatial resolution information of the relocated structures that the measurement campaing intended to measure. Despite promising initial results, its limitations were also acknowledged in sections with significantly large amounts of high-attenuating material which became highly optically thick for the gamma-ray photons to penetrate through. These sections require higher energy x-ray and gamma-ray photons to perform accurate imaging reconstruction. It is noteworthy to mention that depleted uranium, the material imaged in the present work, is used as a gamma-ray shielding agent in the industrial and medical field. The set of measurements presented in this work provide the first glance of tomographic methods used to characterize severe accident progression inside SFR assemblies.

CHAPTER VII

Conclusions And Remarks

The broad objective of the present research was to support the development of radiation imaging systems and analysis methods for nuclear reactor applications, with a special emphasis on the study of two-phase flow phenomena and a minor focus on the non-destructive assessment of accident conditions in fuel assemblies. The pillar behind the presented research lies upon the principles of radiation transmission and detection. The central theme of this research is the study of two-phase flow, in which we exploit the difference in density between gas and liquid to capture the effective change in intensity of the passing radiation; herby we can quantify the gas content in the system, which is also known as the void fraction, with high spatial resolution. This research explores the application of various radiation transmission imaging modalities throughout the presented work which include high-speed x-ray radiography, gamma-ray fan-beam CT, and cone beam CT. Adjacent to the experimental endeavors, much of the effort was also focused on modeling the various imaging systems, performing radiation noise analysis, and assessing the void fraction prediction accuracy and its potential limitations.

Radiation-based measurement techniques have been widely applied for two-phase flow studies, and technological advancements have improved the data acquisition rates, and spatial resolutions. These techniques present inherit advantages due to their non-intrusive nature and the capability to survey opaque and complex geometries. Previously, a phenomenon identified as the dynamic bias had been first described in 1971, with only a hand-full of studies embarking on the topic. This bias is an error build-up that occurs during the measurement time integration interval of an exponentially-fluctuating transmission function. After the logarithmic conversion of the measured signal, followed by the averaging procedure, the resulting average embeds a slight deviation from its ideal value. The root of this bias stems in the Shannon-Nyquist sampling theorem, in which fast sampling frequencies (relative to the two-phase signal) temporally resolve the signal and virtually minimize this error in the frame. On the other hand, prolonged exposure frames enable the build-up of this error as it reaches an asymptotic value. This investigation introduces a new analytical expression of the dynamic bias derived from the analysis of rectangular signals. The new

expression simplifies intricate signals into a representative rectangular-like signal composed of a passive phase and an active phase which preserves the average value and standard deviation of the original signal. In essence, the proposed model considers the peak-to-peak fluctuation and the temporal distribution of a signal; this latter was neglected in the previous model. The new model was tested using numerical methods with well-behaved signals and adapted experimental signals. The results showed a significant improvement in comparison to the previous model. Whilst this work considers the transmission along a single transmission element, future investigations should expand onto more intricate imaging modalities such as CT to evaluate the compound effects that the dynamic bias may have in the reconstruction process.

The advanced instrumentation developed in the present research was commissioned by the NRC to support the study of two-phase flows inside Light Water Reactors (LWR). To accomplish set objective, the High-Resolution Gamma-Tomography System (HRGTS) was designed and built in-house at the Experimental and Computational Multiphase Flow (ECMF) laboratory. This imaging system was developed by the post-doctoral researcher Dr. Robert Adams with contributions of the present author. The HRGTS imaging system is able to achieve a spatial resolution of less than 1.0 mm. In conjunction, the Michigan Adiabatic Rod Bundle Experiment (MARBLE) was designed and constructed at the ECMF lab under the same project scope. The facility consists of an 8 x 8 rod bundle geometry that is modeled and scaled based on the critical bubble diameter determined for LWR systems. The facility deploys individually controlled injections for all 64 channels, thus permitting custom gas-distribution injection arrangements into the flow channel which can simulate custom assembly power profiles. The facility contains spacer grids with mixing vanes which are installed at scaled distances based on PWR scaling factor. Preliminary CT measurements of the MARBLE facility were performed with the HRGTS for two different gas injection configurations: uniform and assembly-entered distributions. The tests were performed at the same axial location with a liquid superficial velocity of $j_L = 0.65$ m/s gas injection velocities $j_g = [0.5, 0.25, 0.05, s0.025]$ m/s for both injection configurations. The void fraction CT results show the spatial evolution and increased gas content as a function of superficial of gas-injection velocity. The spatial void fraction was then collapsed to subchannel average, a method developed with particular interest for the validation of subchannel analysis codes. The contributions of presented research focused on the development and validation of the HRGTS prior to its deployment for void fraction measurements of the MARBLE facility. Initial measurements are carried out to demonstrate the proof of concept and the data post-processing methods developed for this experiment. Future efforts will concentrate in performing an extensive experimental expedition to compile

a high-spatial resolution database of two-phase flow conditions inside rod-bundle geometries aimed to improve and validate computational models. This modular flexibility of the MARBLE facility paired with the HRGTS paves the way for wide assessment of void fraction conditions under various assembly power profile arrangements, for which a 3D high resolution imaging database can be established.

Parallel research efforts were conducted at the Post-CHF (PCHF) experimental facility within the same NRC project scope that aims to improve the models which describe regimes extending from inverted annular film boiling (IAFB), inverted slug film boiling (ISFB), through dispersed flow film boiling (DFFB); the experimental facility was designed and constructed by Dr. Qingqing Liu. The contributions of the presented research focused on the developing analysis tools and methods to quantify the void fraction using high-speed x-ray radiography methods. In this case the test section consists of a tubular Incoloy tube with an inner diameter of 12.95 mm, extending 1.55 in height, and heated by means of DC power with a maximum power of 34 kW. The radiation imaging system was comprised of a 150 kV medical x-ray tube and a 256 x 2048 pixel^2 CdTe detector panel; each detector pixel has an effective detection area of 0.1 x 0.1 mm^2. Throughout the initial measurements performed there were several difficulties identified of performing x-ray measurements of high-temperature and high-pressure conditions, these include: thermal expansion, change in density, position shift, and x-ray spectrum beam hardening. Modeling of the test section paired with the radiation imaging system were conducted with a custom ray-tracing tool to quantify the compound effects of high-temperature conditions. From the results, it was concluded that spatial and temperature-based scaling corrections need to be applied in order to properly map the calibration conditions to the experimental high-temperature conditions; these corrections consider the density and thermal expansion changes of the materials. The test section position shift was also addressed by recreating this effect in the simulation process, and a correction strategy was then established. Lastly, the modeling tool also served to formulate a ray-tracing based cross-sectional averaging procedure of the void fraction which was tested with randomly generated bubbly and film boiling two-phase flow. The averaged estimation was shown to be highly accurate in comparison to the ideally imposed void fraction. Once the most prominent issues were addressed, pool boiling measurements were performed and the developed methods were used to post-process the data. Various regimes were observed throughout the radiography images, these included: bubbly, nucleate boiling, churn flow, and slug flow. These features were also identified and discussed in terms of the axial cross-section average vs. time; these plots depict the void fraction migration along the axial direction as a function of time. The results show a promising path for the deployment of the high-speed radiography

system for future experimental measurements performed at the PCHF facility. Future research will involve measurements beyond post-CHF conditions, these will aid to improve models used in best-estimate codes.

The last task covered pertains to the non-destructive inspection and of test assemblies which replicate hypothetical accident conditions inside Sodium Fast Reactors (SFR). The Pin Bundle Metallic Fuel Relocation (PBR) assemblies utilize depleted uranium to simulate initial stages of cladding breach and fuel migration, as well as advanced stages of core disruption; these accident scenario tests were conducted by Dr. Taeil Kim at Argonne National Laboratory. To carry-out the non-destructive measurements of these PBR assemblies, we designed and constructed the Michigan High Resolution Tomographic Imaging (CHROMA) system at the ECMF lab. The CHROMA facility consists of a 1.0m in diameter rotary stage, capable of accommodating a medical x-ray tube or the 15Ci ^{192}Ir radioisotopic source, and mounts the previously mentioned 256 x 2048 pixel^2 CdTe detector panel; the system was shown to achieve a spatial resolution of 0.4 mm. The first set of Cone-beam CT measurements were performed with the x-ray source. The CT reconstructions resolve the assembly in high detail wherever molten material was not present. On the contrary, the sections in which the molten-fuel (highly attenuating material) were present resulted in photon-starvation streak-artifacts. The inner fuel regions could not be resolved due to these complications. The second set of measurements were performed with the ^{192}Ir radioisotope. The resulting reconstructions improved significantly, in particular the sections in which a moderate amount of fuel was present were resolved. However, sections in which large amounts of molten material were present developed streak-artifacts. The ^{192}Ir measurements were used to quantify the assembly flow blockage as a function of axial location; these used the empty sections unperturbed sections of the assembly as a reference. Overall, this study serves to highlight the advantages of deploying strong monoenergetic sources to image highly attenuating materials such as uranium.

APPENDICES

Appendix A. Triangular Signal

The triangular pulsed signal can be described using piece wise temporal functions. The definition of ω represents the full width half max (FWHM) of the gas phase which in this case is equivalent to half of the pulse duration. In the present work, two separate definitions are used to generate the temporal void fraction functions, the first is used when the desired average void fraction is lower than ½. Here, the gas is pulsed with a maximum peak-to-peak amplitude ξ for the range $0 < \omega \leq 1/2$. Therefore, the liquid phase can be described as the remaining passive phase whenever the pulse is over. The signal can be defined by the piecewise relations as

$$\alpha_G(w,\xi) = \begin{cases} \dfrac{\xi w}{\omega} & \text{for } \ 0 \leq w \leq \omega \\ \xi\left(2 - \dfrac{w}{\omega}\right) & \text{for } \omega \leq w \leq 2\omega \\ 0 & \text{otherwise} \end{cases} \qquad \text{Eq.(A. 1)}$$

The variable w is used to sift through the signal cycle and the subscript G denotes the gas pulse. The average of the signal is obtained from the piecewise sections and can be expressed as

$$\bar{\alpha}_G(\omega,\xi) = \int_0^{\omega} \frac{\xi w}{\omega}\ dw + \int_{\omega}^{2\omega} \xi\left(2 - \frac{w}{\omega}\right)\ dw, \qquad \text{Eq.(A. 2.}a\text{)}$$

$$\bar{\alpha}_G(\omega,\xi) = \ \xi\omega. \qquad \text{Eq.(A.2.}b\text{)}$$

The variance of the gas pulse can then be defined as

$$\sigma^2_{\alpha_G} = \int_0^{\omega} \left(\frac{\xi w}{\omega} - \bar{\alpha}_G\right)^2 dw + \int_{\omega}^{2\omega} \left(\xi\left[2 - \frac{w}{\omega}\right] - \bar{\alpha}_G\right)^2 dw, \qquad \text{Eq.(A.3.}a\text{)}$$

$$\sigma^2_{\alpha_G} = \frac{2\xi^2\omega}{3} - \xi^2\omega^2. \qquad \text{Eq.(A.3.}b\text{)}$$

The second definition of the triangular signal occurs in the case where the liquid phase is pulsed, and the gas phase is dominant. To remain congruent, the FWHM of the liquid pulse is defined as $(1-\omega)$, therefore the gas phase FWHM is defined $1/2 < \omega \leq 1$; the temporal void fraction in this case is defined as:

$$\alpha_L(w,\omega,\xi) = \begin{cases} 1-\dfrac{w\xi}{1-\omega} & \text{for } \ 0 \le w \le (1-\omega) \\ \xi\left(\dfrac{w}{1-\omega}-1\right) & \text{for } \ (1-\omega) \le w \le 2(1-\omega) \\ \xi & \text{otherwise} \end{cases}, \qquad \text{Eq.(A.4)}$$

where the subscript L denotes liquid pulsed phase. The average void fraction is obtained following the process expressed in Eq.(A.2.a), this case simplifies to:

$$\bar{\alpha}_L(\omega,\xi) = \int_0^{(1-\omega)} 1-\frac{w\xi}{1-\omega}\ dw + \int_{(1-\omega)}^{2(1-\omega)} \xi\left[\frac{w}{1-\omega}-1\right] dw \ + \int_{2(1-\omega)}^{1} \xi\ dw, \qquad \text{Eq.(A.5.}a\text{)}$$

$$\bar{\alpha}_L(\omega,\xi) = \ 1-\omega-\xi+2\xi\omega. \qquad \text{Eq.(A.5.}b\text{)}$$

The associated variance of the liquid pulse is

$$\begin{aligned} \sigma^2_{\alpha_G}(\omega,\xi) = &\int_0^{(1-\omega)} \left(1-\frac{w\xi}{1-\omega}-\bar{\alpha}_G\right)^2 dw \\ &+ \int_{(1-\omega)}^{2(1-\omega)} \left(\xi\left[\frac{w}{1-\omega}-1\right]-\bar{\alpha}_G\right)^2 dw \ + \int_{2(1-\omega)}^{1} (\xi-\bar{\alpha}_G)^2 dw, \end{aligned} \qquad \text{Eq.(A.6.}a\text{)}$$

$$\sigma^2_{\alpha_G}(\omega,\xi) = \xi-\frac{4}{3}\xi^2+\omega-5\xi\omega+\frac{16}{3}\xi^2\omega-\omega^2+4\xi\omega^2-4\xi^2\omega^2. \qquad \text{Eq.(A.6.}b\text{)}$$

Putting it all together, the triangular pulse applied in this study is defined as

$$\alpha_{Tri}(w,\xi) = \begin{cases} \alpha_G(w,\omega,\xi) & \text{for} \quad 0<\omega\le\dfrac{1}{2} \\ \alpha_L(w,\omega,\xi) & \text{for} \quad \dfrac{1}{2}<\omega\le 1 \end{cases}. \qquad \text{Eq.(A.7)}$$

Appendix B. Sinusoidal Signal

The sinusoidal pulse or signal can also be described using piece wise temporal functions. Similarly, to the case shown in Appendix A, the gas is pulsed with a peak-to-peak amplitude ξ for a duration twice the FWHM. The signal can be described by the piecewise relations as

$$\alpha_G(w) = \begin{cases} \frac{\xi}{2}\left[\cos\left(\pi\left[\frac{w}{\omega}+1\right]\right)+1\right] & \text{for } 0 \le w \le 2\omega \\ 0 & \text{otherwise} \end{cases}. \qquad \text{Eq.(B.1)}$$

The average void fraction is

$$\bar{\alpha}_G(\omega,\xi) = \int_0^{2\omega} \frac{\xi}{2}\left[\cos\left(\pi\left[\frac{w}{\omega}+1\right]\right)+1\right] dw, \qquad \text{Eq.(B.2.}a\text{)}$$

$$\bar{\alpha}_G(\omega,\xi) = \omega\,\xi. \qquad \text{Eq.(B.2.}b\text{)}$$

The variance of this gas pulse is

$$\sigma^2_{\alpha_G}(\omega,\xi) = \int_0^{2\omega}\left(\frac{\xi}{2}\left[\cos\left(\pi\left[\frac{w}{\omega}+1\right]\right)+1\right]-\bar{\alpha}_G\right)^2 dw + \int_{2\omega}^{1}\bar{\alpha}_G{}^2\, dw, \qquad \text{Eq.(B.3.}a\text{)}$$

$$\sigma^2_{\alpha_G}(\omega,\xi) = \frac{3\xi^2\omega}{4} - \xi^2\omega^2. \qquad \text{Eq.(B.3.}b\text{)}$$

Similarly as before, the liquid pulse is described based on the FWHM duration of the gas phase, this being $(1-\omega)$ throughout the range of $1/2 < \omega < 1$; the piecewise function is then

$$\alpha_L(w) = \begin{cases} \frac{\xi}{2}\left[\cos\left(\frac{\pi w}{1-\omega}\right)+1\right] & \text{for } 0 \le w \le 2(1-\omega) \\ \xi & \text{otherwise} \end{cases}. \qquad \text{Eq.(B.4)}$$

The average void fraction is

$$\bar{\alpha}_L(\omega,\xi) = \int_0^{2(1-\omega)} \frac{\xi}{2}\left[\cos\left(\frac{\pi w}{1-\omega,}\right)+1\right] dw + \int_{2(1-\omega)}^{1} \xi\, dw, \qquad \text{Eq.(B.5.}a\text{)}$$

$$\bar{\alpha}_L(\omega,\xi) = \omega\,\xi, \qquad \text{Eq.(B.5.}b\text{)}$$

and the variance is defined as

$$\sigma^2_{\alpha_L}(\omega,\xi) = \int_0^{2(1-\omega)}\left(\frac{\xi}{2}\left[\cos\left(\frac{\pi w}{1-\omega,}\right)+1\right]-\bar{\alpha}_L\right)^2 dw + \int_{2(1-\omega)}^{1}(\xi-\bar{\alpha}_L)^2\, dw, \qquad \text{Eq.(B.6.}a\text{)}$$

$$\sigma^2_{\alpha_L}(\omega,\xi) = \xi^2 \left[\frac{5\,\omega - 1}{4} - \omega^2 \right]. \qquad \text{Eq.(B.6.}b\text{)}$$

The piecewise sinusoidal function implemented in this study is

$$\alpha_{Sine}(w,\xi) = \begin{cases} \alpha_G(w,\omega,\xi) & \text{for} \quad 0 < \omega \leq \dfrac{1}{2} \\ \alpha_L(w,\omega,\xi) & \text{for} \quad \dfrac{1}{2} < \omega \leq 1 \end{cases}. \qquad \text{Eq.(B.7)}$$

Appendix C. Cylindrical Error Propagation Terms

The partial derivative terms of the axial locations where the ray-traces intersect a cylindrical geometry are expressed in this section. The expressions were obtained using Wolfram Mathematica Software. The nearside incoming z-location intersection terms are listed as follows:

$$\frac{\partial z_{in}}{\partial x_d} = \frac{d_{in}\ e_x\ e_z}{M}\left(\ \frac{2(a-1)}{a} - 1\right) + \frac{e_z}{2\ a\ M}\ \left[{e_x}^2 x_s + e_x\ e_y\ y_s - x_s + \frac{4c\ e_x}{\sqrt{b^2-4ac}}(1-a) - \ \frac{b}{\sqrt{b^2-4ac}}(x_s - {e_x}^2 x_s - e_x e_y y_s)\right] \quad \text{Eq.(C.1)}$$

$$\frac{\partial z_{in}}{\partial x_s} = \frac{d_{in}\ e_x\ e_z}{M}\ \left(1 - \frac{2(a-1)}{a}\right) + \ \frac{e_z}{2\ a\ M}\left[e_x\ e_y\ y_s - \ M\ e_x + x_s - {e_x}^2\ x_s + \frac{b}{\sqrt{b^2-4ac}}\ (M\ e_x - x_s + {e_x}^2\ x_s + e_x\ e_y\ y_s) + \frac{4\ M\ a\ x_s}{\sqrt{b^2-4ac}} + \ \frac{4c\ e_x}{\sqrt{b^2-4ac}}(a-1)\right] \quad \text{Eq.(C.2)}$$

$$\frac{\partial z_{in}}{\partial y_d} = \frac{d_{in}\ e_y\ e_z}{M}\left(\frac{2(a-1)}{a} - 1\right) + \frac{e_z}{2aM}\left[e_x\ e_y\ x_s - y_s + {e_y}^2 y_s + \frac{4c\ e_y}{\sqrt{b^2-4ac}}(1-a) - \frac{b\ (y_s - e_x\ e_y\ x_s - {e_y}^2\ y_s)}{\sqrt{b^2-4ac}}\right] \quad \text{Eq.(C.3)}$$

$$\frac{\partial z_{in}}{\partial y_s} = \frac{d_{in}\ e_z\ e_y}{M}\left(1 - \frac{2(a-1)}{a}\right) + \frac{e_z}{2aM}\left[e_x\ e_y\ x_s - M\ e_y + y_s - {e_y}^2 y_s + \ \frac{4c\ e_y}{\sqrt{b^2-4ac}}(a\ -1) + \frac{4a\ y_s\ M}{\sqrt{b^2-4ac}} - \frac{b}{\sqrt{b^2-4ac}}(Me_y + e_x\ e_y\ x_s - y_s + {e_y}^2\ y_s)\right] \quad \text{Eq.(C.4)}$$

$$\frac{\partial z_{in}}{\partial z_d} = \frac{d_{in}}{M} + \frac{d_{in}\ {e_z}^2}{M} + \frac{{e_z}^2}{a\ M}\left(\frac{b}{2} - \frac{2\ a\ c}{\sqrt{b^2-4ac}}\right) \quad \text{Eq.(C.5)}$$

$$\frac{\partial z_{in}}{\partial z_s} = 1 - \frac{d_{in}}{M} - \frac{d_{in}\ ez^2}{M} + \frac{ez^2}{aM}\left(\frac{2\ c\ a}{\sqrt{b^2-4ac}} + \frac{e_y\ y_s - \ e_x\ x_s}{2}\right) \quad \text{Eq.(C.6)}$$

The backside outgoing z-location intersection terms are listed as follows:

$$\begin{aligned}\frac{\partial z_{out}}{\partial x_d} = \frac{e_x e_z d_{out}}{M}\left(\frac{a-1}{a^2} - 1\right) \ + \ \frac{e_z}{2aM}({e_x}^2 x_s + e_x\ e_y\ y_s - x_s) \\ + \frac{e_z}{2aM\sqrt{b^2-4ac}}[b(x_s - {e_x}^2 x_s - e_x\ e_y\ y_s) + 4ce_x({e_x}^2 + {e_y}^2 - 1)]\end{aligned} \quad \text{Eq.(C.7)}$$

$$\begin{aligned}\frac{\partial z_{out}}{\partial x_s} = \ \frac{e_x e_z d_{out}}{M}\left(1 + \frac{1-a}{a^2}\right) + \\ \frac{e_z}{a\ M}\Bigg[x_s - Me_x - {e_x}^2 x_s + e_x e_y y_s \\ + \frac{4\ c\ e_x(1-{e_x}^2 - e_x {e_y}^2) - 4\ a\ x_s\ M + b\ (Me_x - xs + {e_x}^2 x_s + e_x e_y y_s)}{2\sqrt{b^2-4ac}}\Bigg]\end{aligned} \quad \text{Eq.(C.8)}$$

$$\begin{aligned}\frac{\partial z_{out}}{\partial y_d} = -\frac{e_z e_y d_{out}}{M}\left(1 + \frac{1-a}{a^2}\right) \ + \frac{e_z}{2\ M\ a}\Bigg(e_x e_y x_s - y_s + {e_y}^2 y_s \\ + \frac{b(y_s - e_x e_y x_s - {e_y}^2 y_s) - 4ce_y(1-a)}{\sqrt{b^2-4ac}}\Bigg)\end{aligned} \quad \text{Eq.(C.9)}$$

$$\begin{aligned}\frac{\partial z_{out}}{\partial y_s} = \ \frac{e_z e_y d_{out}}{M} - \frac{e_y d_{out}}{M\ a^2}({e_x}^3 + {e_y}^3 - e_y) \\ + \ \frac{e_z}{2Ma}\Bigg(y_s - Me_y - e_x e_y x_s - {e_y}^2 y_s \\ + \frac{b(Me_y + e_x e_y x_s - y_s + {e_y}^2 y_s) - 4c({e_x}^3 - e_y + {e_y}^3) - 4May_s}{\sqrt{b^2-4ac}}\Bigg)\end{aligned} \quad \text{Eq.(C.10)}$$

$$\frac{\partial z_{out}}{\partial z_d} = \ 1 - \frac{d_{out}}{M} + \frac{{e_z}^2 d_{out}}{M}\left(1 - \frac{1}{a}\right) + \ \frac{{e_z}^2}{2Ma}\left(-b + \frac{-4ca + b^2}{\sqrt{b^2-4ac}}\right) \quad \text{Eq.(C.11)}$$

$$\frac{\partial z_{out}}{\partial z_s} = \ \frac{d}{M} + \ \frac{{e_z}^2 d_{out}}{M}\left(\frac{1}{a} - 1\right) + \frac{{e_z}^2}{2Ma}\left(b + \frac{4ca - b^2}{\sqrt{b^2-4ac}}\right) \quad \text{Eq.(C.12)}$$

Appendix D. X-Ray Power Correction

Measurements performed with medical x-ray sources suffer from non-constant power exposure, an effect that was registered while using the CdTe detector panel deployed in the present research. This manifests as a progressive increase in measured radiation intensity as a function of time or frame. This can be evaluated by adding the intensities of a stationary region in the detector panel. An example of five independently concatenated measurements are depicted on the left side of Fig. D.1, these show the progressive increase of the registered intensity. This effect becomes a bias whenever a average value is being estimated over a measurement and hence a correction needs to be formulated; the convergence of a 20 x 20 pixel window is depicted in Fig. 6.3 as an example of the frames required to achieve a converged average. In order to account for the power inconsistency throughout the performed measurements, we devise a strategy to account for this undesired effect.

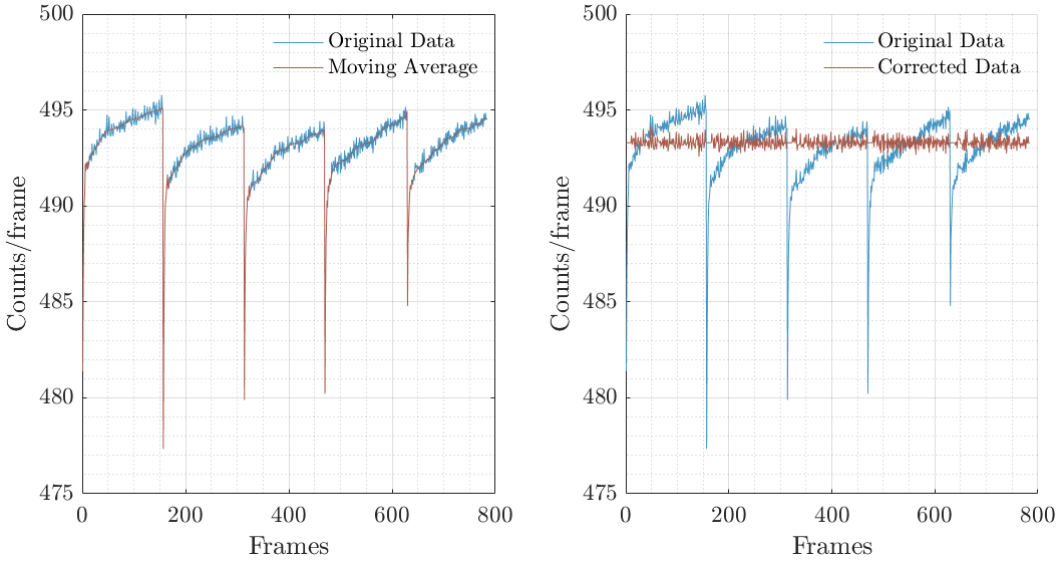

Fig. D.1. Power correction process: *a)* moving average of the original registered intensity, and *b)* corrected intensity as functions of frames.

The general idea is to perform a simple moving average (SMA) operation to generate a smooth function which follows the ramp-up trend of the power function $f(t)$. This is constrained to have the same values at the start and end of each individual measurement. The temporal power correction factor C is then estimated

as the original function's average $\bar{f}$ value normalized by the SMA function Γ as

$$C(t) = \frac{\bar{f}}{\Gamma(t)}. \qquad \text{Eq.(D.1)}$$

The power in the fame sequence is then transformed to a constant value by multiplying the measurements by the power correction factor. Here we formulate the corrected power series $\hat{f}$ as an example, the correction results are shown on the right side of Fig. D.1;

$$\hat{f}(t) = f(t)C(t). \qquad \text{Eq.(D.2)}$$

In practice, the correction factor is applied to each frame in order to counteract the ramping effect.

BIBLIOGRAPHY

1. Adams R., Petrov, V., Manera, A., "Advanced high-resolution radiation-based measurement techniques for detailed void-fraction measurements in fuel bundles and high-pressure test sections", Proc. of the 17th Int. Topical Mtg. on Nuclear Reactor Thermal Hydraulics (NURETH-17), Xi'an, China, Sep 3 – Sept 9 (2017).
2. Adams, R., Diaz, J., Petrov, V., & Manera, A. (2019). Development and testing of a high-resolution fan-beam gamma tomography system with a modular detector array. Nuclear Instruments and Methods in Physics Research Section A: Accelerators, Spectrometers, Detectors and Associated Equipment, 942, 162346.
3. Adams, R., Diaz, J., Petrov, V., & Manera, A. (2021). Simulation and experiments on the feasibility of using gamma tomography for void fraction measurements in nuclear fuel bundle mock-ups. Annals of Nuclear Energy, 154, 108073.
4. Adams, R., Zboray, R., & Prasser, H. M. (2016). A novel fast-neutron tomography system based on a plastic scintillator array and a compact D–D neutron generator. Applied Radiation and Isotopes, 107, 1-7.
5. Ahn, T., Hsun, P., Diaz, J., Manera, A., Petrov, V., "An Experimental Study on Startup Characteristics of Sodium-Filled Heat Pipe, Using In-House High-Resolution and High-Speed Radiation-Based Imaging System". Proc. of the 19th Int. Topical Mtg. on Nuclear Reactor Thermal Hydraulics (NURETH-19), Brussels, Belgium, March 6-11, 2022
6. Akio Tomiyama, Hidesada Tamai, Iztok Zun, and Shigeo Hosokawa. Transverse migration of single bubbles in simple shear flows. Chemical Engineering Science, 57 (11): 1849-1858, 2002.
7. Akiyama, Y., Hori, K., Miyazaki, K., Nishioka, H., & Sugiyama, S. (1995). Evaluation of in bundle void fraction measurement data of PWR fuel assembly.
8. Andersen, A. H., & Kak, A. C. (1984). Simultaneous algebraic reconstruction technique (SART): a superior implementation of the ART algorithm. Ultrasonic imaging, 6(1), 81-94.

9. Andersson, P., Sundén, E. A., Svärd, S. J., & Sjöstrand, H. (2012). Correction for dynamic bias error in transmission measurements of void fraction. Review of Scientific Instruments, 83(12), 125110.

10. Anklam, T. M., & Miller, R. F. (1983). Void fraction under high pressure, low flow conditions in rod bundle geometry. Nuclear Engineering and Design, 75(1), 99-108.

11. Arai, T., Furuya, M., & Shirakawa, K. (2021). Development of Subchannel Void Sensor for Wide Pressure and Temperature Ranges and Its Application to Boiling Flow Dynamics in a Heated Rod Bundle. Nuclear Technology, 1-19.

12. Arai, T., Furuya, M., Kanai, T., & Shirakawa, K. (2012). Development of a subchannel void sensor and two-phase flow measurement in 10× 10 rod bundle. International journal of multiphase flow, 47, 183-192

13. Arai, T., Furuya, M., Takiguchi, H., Nishi, Y., & Shirakawa, K. (2019). Void-fraction measurement with high spatial resolution in a 5× 5 rod bundle by linear-accelerator-driven X-ray computed tomography over a wide pressure range. Flow Measurement and Instrumentation, 69, 101614.

14. Bachrata, A., Bertrand, F., Marie, N., & Serre, F. (2020). A Comparative Study On Severe Accident Phenomena Related to Melt Progression in SFR and PWR. Journal of Nuclear Engineering and Radiation Science.

15. Barrett, J. F., & Keat, N. (2004). Artifacts in CT: recognition and avoidance. Radiographics, 24(6), 1679-1691.

16. Berge, L., Estre, N., Tisseur, D., Payan, E., Eck, D., Bouyer, V., ... & Pluyette, E. (2018). Fast high-energy X-ray imaging for Severe Accidents experiments on the future PLINIUS-2 platform. IEEE Transactions on Nuclear Science, 65(9), 2573-2581.

17. Bieberle, A., Hoppe, D., Schleicher, E., & Hampel, U. (2011). Void measurement using high-resolution gamma-ray computed tomography. Nuclear Engineering and Design, 241(6), 2086-2092.

18. Blanc, J. Y., Clement, B., & Hardt, P. (1996). Fuel bundle examination techniques for the Phebus fission product test (No. IAEA-TECDOC--921).

19. Bleise, A., Danesi, P. R., & Burkart, W. (2003). Properties, use and health effects of depleted uranium (DU): a general overview. Journal of environmental radioactivity, 64(2-3), 93-112.

20. Bonolis, L. (2004). Enrico Fermi's scientific work. In Enrico Fermi (pp. 314-393). Springer, Berlin,

Heidelberg.

21. Borgnakke, C., & Sonntag, R. E. (2020). Fundamentals of thermodynamics. John Wiley & Sons.

22. Breitenmoser, D., Manera, A., Prasser, H. M., & Petrov, V. (2019). High-resolution high-speed void fraction measurements in helical tubes using X-ray radiography. In 18th International Topical Meeting on Nuclear Reactor Thermal Hydraulics (NURETH-18) (pp. 3554-3567). American Nuclear Society.

23. Buss, S., & Buss, S. R. (2003). 3D computer graphics: a mathematical introduction with OpenGL. Cambridge University Press.

24. Carmignato, S., Dewulf, W., & Leach, R. (Eds.). (2018). Industrial X-ray computed tomography. Berlin: Springer International Publishing.

25. Chadwick, M. B., Herman, M., Obložinský, P., Dunn, M. E., Danon, Y., Kahler, A. C., ... & Young, P. G. (2011). ENDF/B-VII. 1 nuclear data for science and technology: cross sections, covariances, fission product yields and decay data. Nuclear data sheets, 112(12), 2887-2996.

26. Chen, S. W., Liu, Y., Hibiki, T., Ishii, M., Yoshida, Y., Kinoshita, I., ... & Mishima, K. (2012). Experimental study of air–water two-phase flow in an 8× 8 rod bundle under pool condition for one-dimensional drift-flux analysis. International Journal of Heat and Fluid Flow, 33(1), 168-181.

27. Chen, S. W., Ruan, P. S., Lin, M. S., Yu, Y. C., Lee, J. D., Yang, J. H., ... & Pei, B. S. (2020). Experimental investigation on local/global void distribution of air-water two-phase flow in a 3× 3 rod bundle channel under low-flow conditions. International Journal of Heat and Fluid Flow, 85, 108623.

28. Cheng, S., Matsuba, K. I., Isozaki, M., Kamiyama, K., Suzuki, T., & Tobita, Y. (2015). SIMMER-III analyses of local fuel-coolant interactions in a simulated molten fuel pool: effect of coolant quantity. Science and Technology of Nuclear Installations, 2015.

29. Compton, A. H. (1923). A quantum theory of the scattering of X-rays by light elements. Physical review, 21(5), 483.

30. Damsohn, M., & Prasser, H. M. (2010). Experimental studies of the effect of functional spacers to annular flow in subchannels of a BWR fuel element. Nuclear Engineering and Design, 240(10), 3126-3144.

31. Delacroix, D., P. Guerre, J., Leblanc, P., & Hickman, C. (2002). Radionuclide and radiation

protection data handbook 2002. Radiation protection dosimetry, 98(1), 1-168.

32. Derbyshire, R. T., Hewitt, G. F., & Nicholls, B. (1964). X-radiography of two-phase gas-liquid flow (No. AERE-M-1321). United Kingdom Atomic Energy Authority. Research Group. Atomic Energy Research Establishment, Harwell, Berks, England.

33. Diaz, J., Adams, R., Petrov, V., Manera, A. High Resolution Gamma-Ray Tomography Imaging for Detailed Void Fraction Measurement in High-Pressure Flow Loops. Proc of ATH-18 Conference Orlando, FL, U.S, November 11-15, 2018.

34. Diaz, J., Adams, R., Petrov, V., Manera, A., Detailed Measurements of Void-Fraction Distribution in an Adiabatic Fuel Bundle Performed with High Resolution Gamma-Ray Tomography Imaging. Proc of NURETH-18 Conference, Portland, OR, U.S, August 18-23, 2019

35. Domínguez-Jiménez, D. Y., & Alva-Sánchez, H. (2021). Energy spectra due to the intrinsic radiation of LYSO/LSO scintillators for a wide range of crystal sizes. Medical Physics.

36. Drotning, W. D. (1979). Thermal expansion of solids at high temperatures by the gamma attenuation technique. Review of Scientific Instruments, 50(12), 1567-1570.

37. Duderstadt, J. J., & Hamilton, L. J. (1976). Nuclear Reactor Analysis, John Wiley & Sons. Inc., New York.

38. El-Genk, M., & Cronenberg, A. W. (1978). An assessment of fuel freezing and drainage phenomena in a reactor shield plug following a core disruptive accident. Nuclear Engineering and Design, 47(2), 195-225.

39. Emma, P., Akre, R., Arthur, J., Bionta, R., Bostedt, C., Bozek, J., ... & Galayda, J. (2010). First lasing and operation of an ångstrom-wavelength free-electron laser. nature photonics, 4(9), 641-647.

40. Energy, G. H. N. (2007). The ABWR Plant General Description.

41. Enomoto, S., Maeda, S., & Senoo, M. (1981). A simplified method for preparation of 137Cs pollucite γ-ray source. The International Journal of Applied Radiation and Isotopes, 32(8), 595-599.

42. Fauske, H. K., & Dwyer, O. E. (1973). Transient liquid-metal boiling and two-phase flow. Argonne National Lab., IL.

43. Feldkamp, L. A., Davis, L. C., & Kress, J. W. (1984). Practical cone-beam algorithm. Journal of the Optical Society of America a, 1(6), 612-619.

44. Fessler, J. A. (1996). Mean and variance of implicitly defined biased estimators (such as penalized maximum likelihood): Applications to tomography. IEEE Transactions on Image Processing, 5(3), 493-506.

45. Fessler, J. A. (2009). Analytical tomographic image reconstruction methods. Image Reconstruction: Algorithms and Analysis, 66, 67.

46. Foulds, J. R. (1986). Thermal history of HT-9 weldment heat-affected zones during welding. Journal of Nuclear Materials, 141, 434-438

47. Frisch, O. R. (1939). Physical evidence for the division of heavy nuclei under neutron bombardment. Nature, 143(3616), 276-276.

48. Fukano, Y. (2019). Development and validation of SAS4A code and its application to analyses on severe flow blockage accidents in a sodium-cooled fast reactor. Journal of Nuclear Engineering and Radiation Science, 5(1).

49. Funaki, M., Ando, Y., Jinnai, R., Tachibana, A., & Ohno, R. (2007). Development of CdTe detectors in Acrorad. In International Workshop on Semiconductor PET (pp. 1-8).

50. Gandini, A. (2004). From the Chicago Pile 1 to next-generation reactors. In Enrico Fermi (pp. 204-221). Springer, Berlin, Heidelberg.

51. Gehrke, R. J. (1973). The decay of 192Ir. Nuclear Physics A, 204(1), 26-32.

52. Gramuglia, F., Frasca, S., Ripiccini, E., Venialgo, E., Gâté, V., Kadiri, H., ... & Bruschini, C. (2021). Light Extraction Enhancement Techniques for Inorganic Scintillators. Crystals, 11(4), 362.

53. Haga, K. (1984). Loss-of-flow experiment in a 37-pin bundle LMFBR fuel assembly simulator. Nuclear engineering and design, 82(2-3), 305-318.

54. Hampel, U., & Wagner, M. (2011). A method for correct averaging in transmission radiometry. Measurement Science and Technology, 22(11), 115701.

55. Hampel, U., Bieberle, A., Hoppe, D., Kronenberg, J., Schleicher, E., Sühnel, T., ... & Zippe, C. (2007). High resolution gamma ray tomography scanner for flow measurement and non-destructive testing applications. Review of scientific instruments, 78(10), 103704.

56. Han, X., Shen, X., Yamamoto, T., Nakajima, K., Sun, H., & Hibiki, T. (2019). Experimental study on local interfacial parameters in upward air-water bubbly flow in a vertical 6× 6 rod bundle. International Journal of Heat and Mass Transfer, 144, 118696.

57. Harms, A. A., & Forrest, C. F. (1971). Dynamic effects in radiation diagnosis of fluctuating voids. Nuclear Science and Engineering, 46(3), 408-413.

58. Harms, A. A., & Laratta, F. A. R. (1973). The dynamic-bias in radiation interrogation of two-phase flow. International Journal of Heat and Mass Transfer, 16(7), 1459-1465.

59. Heath, R L. Gamma-ray spectrum catalogue: Ge(Li) and Si(Li) spectrometry. Third edition, volume 2. United States: N. p., 1974. Web.

60. Heindel, T. J., Gray, J. N., & Jensen, T. C. (2008). An X-ray system for visualizing fluid flows. Flow Measurement and Instrumentation, 19(2), 67-78.

61. Heo, H., Park, S. D., Jerng, D. W., & Bang, I. C. (2016). Visual study of ex-pin phenomena for SFR with metal fuel under initial phase of severe accidents by using simulants. Journal of nuclear science and technology, 53(9), 1409-1416.

62. Hewitt, G. F., & Roberts, D. N. (1969). Studies of two-phase flow patterns by simultaneous x-ray and flash photography (No. AERE-M-2159). Atomic Energy Research Establishment, Harwell, England (United Kingdom).

63. Hibiki, T., & Ishii, M. (2002). Distribution parameter and drift velocity of drift-flux model in bubbly flow. International Journal of Heat and Mass Transfer, 45(4), 707-721.

64. Hibiki, T., & Ishii, M. (2003). One-dimensional drift–flux model for two-phase flow in a large diameter pipe. International Journal of Heat and Mass Transfer, 46(10), 1773-1790.

65. Hibiki, T., Takamasa, T., & Ishii, M. (2004, January). One-dimensional drift-flux model and constitutive equations for relative motion between phases in various two-phase flow regimes at microgravity conditions. In International Conference on Nuclear Engineering (Vol. 4689, pp. 377-386).

66. Hilgers, K., Sudár, S., & Qaim, S. M. (2005). Experimental study and nuclear model calculations on the 192Os (p, n) 192Ir reaction: Comparison of reactor and cyclotron production of the therapeutic radionuclide 192Ir. Applied radiation and isotopes, 63(1), 93-98.

67. Hofmann, P. (1999). Current knowledge on core degradation phenomena, a review. Journal of nuclear materials, 270(1-2), 194-211.

68. Holmgren, M. (2006). X steam for Matlab. www. x-eng. com, accessed October, 21, 2006.

69. Hooker, H. H., & Popper, G. F. (1958). A gamma-ray attenuation method for void fraction

determinations in experimental boiling heat transfer test facilities (No. ANL-5766). Argonne National Lab., Lemont, Ill.

70. Hosokawa, S., Hayashi, K., & Tomiyama, A. (2014). Void distribution and bubble motion in bubbly flows in a 4× 4 rod bundle. Part I: Experiments. Journal of Nuclear Science and Technology, 51(2), 220-230.

71. Huesman, R. H. (1984). A new fast algorithm for the evaluation of regions of interest and statistical uncertainty in computed tomography. Physics in Medicine & Biology, 29(5), 543.

72. Identification of flow regimes in vertical gas-liquid two-phase flow using differential pressure fluctuations. *International Journal of Multiphase Flow*, 10(6), 711-719.

73. Iguchi, T. (1981). Void fraction in simulated PWR fuel bundle during reflood phase. Journal of Nuclear Science and Technology, 18(12), 957-968.

74. Inoue, A., Kurosu, T., Aoki, T., Yagi, M., Mitsutake, T., & Morooka, S. I. (1995). Void fraction distribution in BWR fuel assembly and evaluation of subchannel code. Journal of Nuclear science and Technology, 32(7), 629-640.

75. Ishii, M., & Zuber, N. (1979). Drag coefficient and relative velocity in bubbly, droplet or particulate flows. AIChE journal, 25(5), 843-855.

76. Ishimi, A., Katsuyama, K., & Furuya, H. (2019). Restructure behavior analysis in fast breeder reactor MOX fuel by X-ray CT. Journal of Nuclear Science and Technology, 56(11), 981-987.

77. Ishimi, A., Katsuyama, K., Maeda, K., Nagamine, T., Asaga, T., & Furuya, H. (2012). Upgrading of X-ray CT technology for analyses of irradiated FBR MOX fuel. Journal of nuclear science and technology, 49(12), 1144-1155.

78. Jacquemain, D., Cenerino, G., Corenwinder, F., Raimond, E. I., Bentaib, A., Bonneville, H., ... & Meignen, R. (2015). Nuclear power reactor core melt accidents. Current State of Knowledge.

79. Johnson, T. R., Baker Jr, L., & Pavlik, J. R. (1974). Large-scale molten fuel--sodium interaction experiments (No. CONF-740401--P2).

80. Julia, J. E., Hibiki, T., Ishii, M., Yun, B. J., & Park, G. C. (2009). Drift-flux model in a sub-channel of rod bundle geometry. International journal of heat and mass transfer, 52(13-14), 3032-3041.

81. Kamei, A., Hosokawa, S., Tomiyama, A., Kinoshita, I., & Murase, M. (2010). Void fraction in a

four by four rod bundle under a stagnant condition. Journal of Power and Energy Systems, 4(2), 315-326.

82. Kamiyama, K., Saito, M., Matsuba, K. I., Isozaki, M., Sato, I., Konishi, K., ... & Vassiliev, Y. S. (2013). Experimental study on fuel-discharge behavior through in-core coolant channels. Journal of nuclear science and technology, 50(6), 629-644.

83. Kataoka, I., Ishii, M., & Serizawa, A. (1984). Local formulation of interfacial area concentration and its measurements in two-phase flow (No. NUREG/CR--4029). Argonne National Lab.

84. Kataoka, I., Ishii, M., & Serizawa, A. (1994). Sensitivity analysis of bubble size and probe geometry on the measurements of interfacial area concentration in gas-liquid two-phase flow. Nuclear Engineering and Design, 146(1-3), 53-70.

85. Kemmer, J. (1984). Improvement of detector fabrication by the planar process. Nuclear Instruments and Methods in Physics Research Section A: Accelerators, Spectrometers, Detectors and Associated Equipment, 226(1), 89-93.

86. Kikuchi, Y., Daigo, Y., & Ohtsubo, A. (1977). Local sodium boiling behind local flow blockage in simulated LMFBR fuel subassembly. Journal of Nuclear Science and Technology, 14(11), 774-790.

87. Kim, S., Fu, X. Y., Wang, X., & Ishii, M. (2000). Development of the miniaturized four-sensor conductivity probe and the signal processing scheme. International journal of heat and mass transfer, 43(22), 4101-4118.

88. Kim, T., Fortner, J., Harbaruk, D., Gerardi, C., Farmer, M., & Chang, Y. I. (2018). Experimental studies on eutectic formation between metallic fuel and HT-9M cladding in a single-pin core structure of a sodium-cooled fast reactor. Journal of Nuclear Materials, 505, 105-118.

89. Kim, T., Harbaruk D., Lisowski , D., Bremer, N., Farmer, M., Grandy, C., & Chang, Y. I. (2020). Experimental Studies on Metallic Fuel Relocation in a Pin Bundle Core Structure of a Sodium-Cooled Fast Reactor. Nuclear Engineering and Design (under review).

90. Kim, T., Harbaruk, D., Gerardi, C., Farmer, M., & Chang, Y. I. (2017). Experimental studies on metallic fuel relocation in a single-pin core structure of a sodium-cooled fast reactor. Nuclear Engineering and Design, 322, 204-214.

91. Kinahan, P. E., Defrise, M., & Clackdoyle, R. (2004). Analytic image reconstruction methods. In Emission Tomography (pp. 421-442). Academic Press.

92. Kirsch, D. (1974). Investigations on the flow and temperature distribution downstream of local coolant blockages in rod bundle subassemblies. Nuclear Engineering and Design, 31(2), 266-279.

93. Klickman, A. E., Thompson, D. H., Ragland, W. A., Wright, A. E., Palm, R. G., & Page, R. J. (1982). Review of recent ANL safety experiments in SLSF and TREAT (No. CONF-820704--51). Argonne National Lab.

94. Knoll, G. F. (2010). Radiation detection and measurement. John Wiley & Sons.

95. Kok, H. V., & Van der Hagen, T. H. J. J. (1999). Design of a simulated void-reactivity feedback in a boiling water reactor loop. Nuclear technology, 128(1), 1-11.

96. Kok, H. V., Van der Hagen, T. H. J. J., & Mudde, R. F. (2001). Subchannel void-fraction measurements in a 6× 6 rod bundle using a simple gamma-transmission method. International journal of multiphase flow, 27(1), 147-170.

97. Kok, K. D. (Ed.). (2016). Nuclear engineering handbook. CRC Press.

98. Kondo, S., Konishi, K., Isozaki, M., Imahori, S., Furutani, A., & Brear, D. J. (1995). Experimental study on simulated molten jet-coolant interactions. Nuclear Engineering and Design, 155(1-2), 73-84.

99. Krane, K. S., & Halliday, D. (1988). Introductory nuclear physics (Vol. 465). New York: Wiley.

100. Kuchment, P. (2014). The Radon transform and medical imaging. Society for Industrial and Applied Mathematics.

101. Kui Zhang, Yuqiao Fan, Wenxi Tian, et al. Pressure drop characteristics of two-phase flow in a vertical rod bundle with support plates. Nuclear Engineering and Design, 300(15): 322-329, 2016.

102. Kumamaru, H., Kondo, M., Murata, H., & Kukita, Y. (1994). Void-fraction distribution under high-pressure boil-off conditions in rod bundle geometry. Nuclear Engineering and Design, 150(1), 95-105.

103. Larsen, E., Kiedrowsky, B., (2019). *Nuclear Reactor Theory II* [Lecture Noes]. Department of Nuclear Engineering and Radiological Sciences, University of Michigan.

104. Lee, C. B., Cheon, J. S., Kim, S. H., Park, J. Y., & Joo, H. K. (2016). Metal fuel development and verification for prototype generation IV sodium-cooled fast reactor. Nuclear Engineering and Technology, 48(5), 1096-1108.

105.Lemmon, E. W., Bell, I. H., Huber, M. L., & McLinden, M. O. (2018). NIST Standard Reference Database 23: Reference Fluid Thermodynamic and Transport Properties-REFPROP, Version 10.0, National Institute of Standards and Technology. Standard Reference Data Program, Gaithersburg.

106.Liang, M., Kang, K., Zhang, Z., & Lou, X. (2006). Low count bias in gamma ray thickness detection and its correction. Nuclear Instruments and Methods in Physics Research Section A: Accelerators, Spectrometers, Detectors and Associated Equipment, 568(2), 912-914.

107.Liu, H., & Hibiki, T. (2017). Flow regime transition criteria for upward two-phase flow in vertical rod bundles. International Journal of Heat and Mass Transfer, 108, 423-433.

108.Liu, Q. (2020). Post-CHF Heat Transfer Experiments and Modeling at Subcooled and Low-quality Conditions (Doctoral dissertation).

109.Liu, Q., Lv, Q., Shi, S., Sun, X., & Kelly, J. (2016). Design of post-CHF heat transfer experiments for high-pressure and high-flow conditions. In Proc. 2016 Int. Congress on Advances in Nuclear Power Plants (ICAPP 2016) (pp. 17-20). San Francisco, CA.

110.Liu, Q., Shi, S., Sun, X., & Kelly, J. (2018). Thermal hydraulic performance analysis of a post-CHF heat transfer test facility. Nuclear Engineering and Design, 339, 53-64.

111.Liu, Q., Shi, S., Wang, L., Sun, X., & Kelly, J. (2017). Thermal analysis of a test facility for post-CHF heat transfer experiments. In 2017 Japan-US Seminar on Two-Phase Flow Dynamics, Sapporo, Hokkaido, Japan, June 22-24.

112.Lucas, D., Beyer, M., Kussin, J., & Schütz, P. (2010). Benchmark database on the evolution of two-phase flows in a vertical pipe. Nuclear engineering and design, 240(9), 2338-2346.

113.Lucas, D., Beyer, M., Szalinski, L., & Schütz, P. (2010). A new database on the evolution of air–water flows along a large vertical pipe. *International Journal of Thermal Sciences*, 49(4), 664-674.

114.Ma, Z., Ye, T., Ren, Q., Pan, L., Bu, S., Zhang, L., & Sun, W. (2020). Friction and local pressure loss characteristics of a 5× 5 rod bundle with spacer grids. Annals of Nuclear Energy, 140, 107106.

115.Magallon, D., Hohmann, H., & Schins, H. (1992). Pouring of 100-kg-scale molten UO2 into sodium. Nuclear technology, 98(1), 79-90.

116.Manera, A. (2003). Experimental and analytical investigations on flashing-induced instabilities in natural circulation two-phase systems: Applications to the startup of boiling water reactors.

117.Masterson, R. E. (2019). Nuclear Reactor Thermal Hydraulics: An Introduction to Nuclear Heat

Transfer and Fluid Flow. CRC Press.

118.Matsui, G. (1984). Identification of flow regimes in vertical gas-liquid two-phase flow using differential pressure fluctuations. International journal of multiphase flow, 10(6), 711-719.

119.Meitner, L., & Frisch, O. R. (1939). Disintegration of uranium by neutrons: a new type of nuclear reaction. Nature, 143(3615), 239-240.

120.Mesina, G. L. (2016). A history of RELAP computer codes. Nuclear Science and Engineering, 182(1), v-ix.

121.Mitsutake, T., Morooka, S., Suzuki, K., Tsunoyama, S., & Yoshimura, K. (1990). Void fraction estimation within rod bundles based on three-fluid model and comparison with X-ray CT void data. Nuclear engineering and design, 120(2-3), 203-212.

122.Mizutani, Y., Tomiyama, A., Hosokawa, S., Sou, A., Kudo, Y., & Mishima, K. (2007). Two-phase flow patterns in a four by four rod bundle. Journal of Nuclear Science and Technology, 44(6), 894-901.

123.Mohanta, L. (2015). Theoretical and experimental study of inverted annular film boiling and regime transition during reflood transients.

124.Montoya, G., Lucas, D., Baglietto, E., & Liao, Y. (2016). A review on mechanisms and models for the churn-turbulent flow regime. Chemical Engineering Science, 141, 86-103.

125.Morooka, S., Ishizuka, T., Iizuka, M., & Yoshimura, K. (1989). Experimental study on void fraction in a simulated BWR fuel assembly (evaluation of cross-sectional averaged void fraction). Nuclear Engineering and Design, 114(1), 91-98.

126.Morooka, S., Ishizuka, T., Kagawa, T., & Yoshimura, K. (1988). Void fraction in simulated BWR fuel assembly, 1. Nippon Genshiryoku Gakkai-Shi, 30(10), 925-932.

127.Murao, Y., & Iguchi, T. (1982). Experimental modeling of core hydrodynamics during reflood phase of LOCA. Journal of Nuclear Science and Technology, 19(8), 613-627.

128.Narender, K., Rao, A. S. M., Rao, K. G. K., & Krishna, N. G. (2013). Temperature dependence of density and thermal expansion of wrought aluminum alloys 7041, 7075 and 7095 by gamma ray attenuation method.

129.Nishimura, S., Zhang, Z. G., Sugiyama, K. I., & Kinoshita, I. (2007). Transformation and fragmentation behavior of molten metal drop in sodium pool. Nuclear engineering and design,

237(23), 2201-2209.

130. Noll, Douglas. "Computed Tomography Notes, Part 1." BME/EECS 516 Medical Imaging Systems, 2004, https://web.eecs.umich.edu/~dnoll/BME516_04/ct1.pdf.

131. Nordgren, J., Bray, G., Cramm, S., Nyholm, R., Rubensson, J. E., & Wassdahl, N. (1989). Soft x-ray emission spectroscopy using monochromatized synchrotron radiation. Review of Scientific Instruments, 60(7), 1690-1696.

132. NRC, U. (2010). TRACE V5. 0 Theory Manual, field equations, solution methods, and physical models. United States Nuclear Regulatory Commission.

133. Nuclear Regulatory Commission. (2021, June 16). Power reactors | nrc.gov. Power Reactors. Retrieved October 27, 2021, from https://www.nrc.gov/reactors/power.html.

134. Nunez, D. (2020). High-Resolution Experiments of Momentum-and Buoyancy-Driven Flows for the Validation and Advancement of Computational Fluid Dynamics Codes (Doctoral dissertation).

135. October 2021 Monthly Energy Review U.S. - Energy Information Administration - EIA . U.S. Energy Information Administration (EIA). (2021, October). Retrieved October 28, 2021, from https://www.eia.gov/totalenergy/data/monthly/pdf/mer.pdf.

136. Osakabe, M., Koizumi, Y., & Tasaka, K. (1984). Interfacial drag coefficient of air-water mixture in rod bundle. Journal of Nuclear Science and Technology, 21(11), 882-884.

137. Ott, K. O., & Neuhold, R. J. (1985). Introductory nuclear reactor dynamics. American nuclear society.

138. Paranjape, S., Chen, S. W., Hibiki, T., & Ishii, M. (2011). Flow regime identification under adiabatic upward two-phase flow in a vertical rod bundle geometry. Journal of fluids engineering, 133(9).

139. Paranjape, S., Ishii, M., & Hibiki, T. (2010). Modeling and measurement of interfacial area concentration in two-phase flow. Nuclear engineering and design, 240(9), 2329-2337.

140. Paranjape, S., Stefanczyk, D., Liang, Y., Hibiki, T., & Ishii, M. (2008, January). Global flow regime identification in a rod bundle geometry. In International Conference on Nuclear Engineering (Vol. 48167, pp. 421-429).

141. Pepin, C. M., Bérard, P., Perrot, A. L., Pépin, C., Houde, D., Lecomte, R., ... & Dautet, H. (2004). Properties of LYSO and recent LSO scintillators for phoswich PET detectors. IEEE Transactions

on Nuclear Science, 51(3), 789-795.

142.Petrick, M., & Swanson, B. S. (1958). Radiation Attenuation Method of Measuring Density of a Two-Phase Fluid. Review of Scientific Instruments, 29(12), 1079-1085.

143.Pidol, L., Kahn-Harari, A., Viana, B., Virey, E., Ferrand, B., Dorenbos, P., ... & van Eijk, C. W. (2004). High efficiency of lutetium silicate scintillators, Ce-doped LPS, and LYSO crystals. IEEE Transactions on Nuclear Science, 51(3), 1084-1087.

144.Planchon, H. P., Singer, R. M., Mohr, D., Feldman, E. E., Chang, L. K., & Betten, P. R. (1986). The experimental breeder reactor II inherent shutdown and heat removal tests—results and analysis. Nuclear Engineering and Design, 91(3), 287-296.

145.Poludniowski, G. G. (2007). Calculation of x-ray spectra emerging from an x-ray tube. Part II. X-ray production and filtration in x-ray targets. Medical physics, 34(6Part1), 2175-2186.

146.Poludniowski, G. G., & Evans, P. M. (2007). Calculation of x-ray spectra emerging from an x-ray tube. Part I. Electron penetration characteristics in x-ray targets. Medical physics, 34(6Part1), 2164-2174.

147.Prasser, H. M., Baldauf, D., Fietz, J., Hampel, U., Hoppe, D., Zippe, C., ... & Will, G. (2003). Time resolving gamma-tomography for periodically changing gas fraction fields and its application to an axial pump. Flow Measurement and Instrumentation, 14(3), 119-125.

148.Prasser, H. M., Böttger, A., & Zschau, J. (1998). A new electrode-mesh tomograph for gas–liquid flows. Flow Measurement and Instrumentation, 9(2), 111-119.

149.Qazi, M. K., Guido-Lavalle, G., & Clausse, A. (1994). Void fraction along a vertical heated rod bundle under flow stagnation conditions. Nuclear engineering and design, 152(1-3), 225-230.

150.Qin, S., Krohn, B., Downing, J., Petrov, V., & Manera, A. (2019). High-resolution velocity field measurements of turbulent round free jets in uniform environments. Nuclear Technology, 205(1-2), 213-225.

151.Radon, J. (1986). On the determination of functions from their integral values along certain manifolds. IEEE transactions on medical imaging, 5(4), 170-176.

152.Rao, A. S., & Narender, K. (2014). Studies on thermophysical properties of CaO and MgO by-ray attenuation. Journal of Thermodynamics, 2014.

153.Ren, Q. Y., Pan, L. M., Zhou, W. X., Du, S. J., & Li, Z. C. (2018). Phase distribution characteristics

of bubbly flow in 5× 5 vertical rod bundles with mixing vane spacer grids. Experimental Thermal and Fluid Science, 96, 451-459.

154.Richenderfer, A., Kossolapov, A., Seong, J. H., Saccone, G., Demarly, E., Kommajosyula, R., ... & Bucci, M. (2018). Investigation of subcooled flow boiling and CHF using high-resolution diagnostics. Experimental Thermal and Fluid Science, 99, 35-58.

155.Sadatomi, M., Kano, K., Kawahara, A., & Mori, N. (2005). Void fraction and pressure drop in two-phase equilibrium flow in a vertical 2 x 3 rod bundle channel.

156.Sadatomi, M., Kawahara, A., Kano, K., & Sumi, Y. (2004). Single-and two-phase turbulent mixing rate between adjacent subchannels in a vertical 2× 3 rod array channel. International journal of multiphase flow, 30(5), 481-498.

157.Salvat, F., & Fernández-Varea, J. M. (2009). Overview of physical interaction models for photon and electron transport used in Monte Carlo codes. Metrologia, 46(2), S112.

158.Salvetti, C. (2004). The birth of nuclear energy: Fermi's pile. In Enrico Fermi (pp. 177-203). Springer, Berlin, Heidelberg.

159.Sathe, M. J., Thaker, I. H., Strand, T. E., & Joshi, J. B. (2010). Advanced PIV/LIF and shadowgraphy system to visualize flow structure in two-phase bubbly flows. Chemical Engineering Science, 65(8), 2431-2442.

160.Sawicka, B. D., Murphy, R. V., Tosello, G., Reynolds, P. W., & Romaniszyn, T. (1990). Computed tomography of radioactive objects and materials. Nuclear Instruments and Methods in Physics Research Section A: Accelerators, Spectrometers, Detectors and Associated Equipment, 299(1-3), 468-479.

161.Schlegel, J. P., Sawant, P., Paranjape, S., Ozar, B., Hibiki, T., & Ishii, M. (2009). Void fraction and flow regime in adiabatic upward two-phase flow in large diameter vertical pipes. Nuclear Engineering and Design, 239(12), 2864-2874.

162.Schleisiek, K., Aberle, J., Homann, C., Schmuck, I., Maschek, W., Rahn, A., ... & Verwimp, A. (1998). The Mol-7C in-pile local blockage experiments: main results, conclusions, and extrapolation to reactor conditions. Nuclear science and engineering, 128(2), 93-143.

163.Schmitt, S. (2015). Fast Variance Prediction for Iteratively Reconstructed CT with Applications to Tube Current Modulation (Doctoral dissertation).

164.Schulman, T. (2006). Si, CdTe and CdZnTe radiation detectors for imaging applications.

165.Sha, W. T., & Bonilla, C. F. (1965). Out-of-pile steam-fraction determination by neutron-beam attenuation. Nuclear Applications, 1(1), 69-75.

166.Shen, X., Miwa, S., Xiao, Y., Han, X., & Hibiki, T. (2019). Local measurements of upward air-water two-phase flows in a vertical 6× 6 rod bundle. Experimental and Computational Multiphase Flow, 1(3), 186-200.

167.Shirley, P., & Morley, R. K. (2008). Realistic ray tracing. AK Peters, Ltd..

168.Spartiotis, K. E., Orava, R., Schulman, T., Pyyhtia, J., Sarakinos, M. E., Sanghera, B., ... & Myers, M. (1998, July). Novel direct digital modular x-ray device and system. In Medical Imaging 1998: Physics of Medical Imaging (Vol. 3336, pp. 529-536). International Society for Optics and Photonics.

169.Spartiotis, K., Havulinna, J., Leppänen, A., Pantsar, T., Puhakka, K., Pyyhtiä, J., & Schulman, T. (2004). A CdTe real time X-ray imaging sensor and system. Nuclear Instruments and Methods in Physics Research Section A: Accelerators, Spectrometers, Detectors and Associated Equipment, 527(3), 478-486.

170.Spartiotis, K., Leppänen, A., Pantsar, T., Pyyhtiä, J., Laukka, P., Muukkonen, K., ... & Schulman, T. (2005). A photon counting CdTe gamma-and X-ray camera. Nuclear Instruments and Methods in Physics Research Section A: Accelerators, Spectrometers, Detectors and Associated Equipment, 550(1-2), 267-277.

171.Spartiotis, K., Pyyhtiä, J., & Schulman, T. (2003). Improvement of the radiation hardness of a directly converting high resolution intra-oral X-ray imaging sensor. Nuclear Instruments and Methods in Physics Research Section A: Accelerators, Spectrometers, Detectors and Associated Equipment, 513(3), 579-584.

172.Speis, T. P., Fauske, H. K., & Randles, J. (1973). UO2/Na interactions: recent in-and out-of-pile experiments in the US and their interpretation for fast reactor safety analysis (No. EUR-5309e; CONF-731126-). Atomic Energy Commission, Washington, DC (US); Argonne National Lab., Argonne, IL (US).

173.Stahl, P., & von Rohr, P. R. (2004). On the accuracy of void fraction measurements by single-beam gamma-densitometry for gas–liquid two-phase flows in pipes. Experimental Thermal and Fluid Science, 28(6), 533-544.

174. Sudharsanan, R., Karam, N. H., Halverson, W. D., Greenwald, A. C., Dixit, M., Dubeau, J., & Somerville, E. (1997). Deposition and characterization of CdZnTe thin films for gas microstrip detectors. IEEE Transactions on Nuclear Science, 44(3), 665-670.

175. Suzuki, H., Tombrello, T. A., Melcher, C. L., & Schweitzer, J. S. (1992). UV and gamma-ray excited luminescence of cerium-doped rare-earth oxyorthosilicates. Nuclear Instruments and Methods in Physics Research Section A: Accelerators, Spectrometers, Detectors and Associated Equipment, 320(1-2), 263-272.

176. Taitel, Y., Bornea, D., & Dukler, A. E. (1980). Modelling flow pattern transitions for steady upward gas-liquid flow in vertical tubes. AIChE Journal, 26(3), 345-354.

177. Takiguchi, H., Furuya, M., & Arai, T. (2018). Temperature Profile Measurement in Simulated Fuel Assembly Structure with Wire-Mesh Technology. Science and Technology of Nuclear Installations, 2018.

178. Tentner, A. M., Karahan, A., & Kang, S. H. (2020). Overview of the SAS4A Metallic Fuel Models and Extended Analysis of a Postulated Severe Accident in the Prototype Gen-IV Sodium-Cooled Fast Reactor. Nuclear Technology, 206(2), 242-254.

179. Testa, D., & Kunkle, A. (1984). The Westinghouse pressurized water reactor nuclear power plant. Pittsburgh, Pennsylvania, 15230.

180. Todreas, N. E., & Kazimi, M. S. (2012). Nuclear Systems: Thermal Hydraulic Fundamentals (Vol. 1). CRC Press.

181. Tomiyama, A., Tamai, H., Zun, I., & Hosokawa, S. (2002). Transverse migration of single bubbles in simple shear flows. Chemical Engineering Science, 57(11), 1849-1858.

182. Turtos, R. M., Gundacker, S., Pizzichemi, M., Ghezzi, A., Pauwels, K., Auffray, E., ... & Paganoni, M. (2016). Measurement of LYSO intrinsic light yield using electron excitation. IEEE Transactions on Nuclear Science, 63(2), 475-479.

183. Ullberg, C., Nilsson, J., Weber, N., Urech, M., Lindman, K., Lindqvist, L., ... & Redz, A. (2010, July). Evaluation of the performance of a novel CdTe based photon counting detector for NDT applications. In Proc. 4th Jpn.-US Symp. Emerg. NDE Capabilities (pp. 211-217).

184. Ullberg, C., Urech, M., Weber, N., Engman, A., Redz, A., & Henckel, F. (2013, March). Measurements of a dual-energy fast photon counting CdTe detector with integrated charge sharing

correction. In Medical Imaging 2013: Physics of Medical Imaging (Vol. 8668, p. 86680P). International Society for Optics and Photonics.

185. Van Aarle, W., Palenstijn, W. J., Cant, J., Janssens, E., Bleichrodt, F., Dabravolski, A., ... & Sijbers, J. (2016). Fast and flexible X-ray tomography using the ASTRA toolbox. Optics express, 24(22), 25129-25147.

186. Vassallo, P., & Keller, K. (2006). Two-phase frictional pressure drop multipliers for SUVA R-134a flowing in a rectangular duct. *International Journal of Multiphase Flow*, 32(4), 466-482.

187. Venkateswararao, P., Semiat, R., & Dukler, A. E. (1982). Flow pattern transition for gas-liquid flow in a vertical rod bundle. International Journal of Multiphase Flow, 8(5), 509-524.

188. Wagner, M., Bieberle, A., Bieberle, M., & Hampel, U. (2017). Dynamic bias error correction in gamma-ray computed tomography. Flow Measurement and Instrumentation, 53, 141-146.

189. Wagner, W., & Kretzschmar, H. J. (2008). IAPWS industrial formulation 1997 for the thermodynamic properties of water and steam. International steam tables: properties of water and steam based on the industrial formulation IAPWS-IF97, 7-150.

190. Warinner, D. K., & Saxena, S. C. (1980). Sodium flow blockage in liquid-metal fast breeder reactors: sweepout of a planar blockage. Nuclear Science and Engineering, 76(3), 361-366.

191. Williams, C. L., & Peterson Jr, A. C. (1978). Two-phase flow patterns with high-pressure water in a heated four-rod bundle. Nuclear Science and Engineering, 68(2), 155-169.

192. Wunderlich, A., & Noo, F. (2008). Image covariance and lesion detectability in direct fan-beam x-ray computed tomography. Physics in Medicine & Biology, 53(10), 2471.

193. Wunderlich, A., & Noo, F. (2008, October). Rapidly converging image covariance estimation for FBP reconstruction methods. In 2008 IEEE Nuclear Science Symposium Conference Record (pp. 5187-5190). IEEE.

194. XCOM. XCOM: Photon Cross Section Database (version 1.5). National Institute of Standards and Technology, Gaithersburg, MD. Published 2010. http://physics.nist.gov/xcom

195. Yamano, H., Fujita, S., Tobita, Y., Sato, I., & Niwa, H. (2008). Development of a three-dimensional CDA analysis code: SIMMER-IV and its first application to reactor case. Nuclear engineering and design, 238(1), 66-73.

196. Yang, X., Schlegel, J. P., Liu, Y., Paranjape, S., Hibiki, T., & Ishii, M. (2013). Experimental study

of interfacial area transport in air–water two phase flow in a scaled 8× 8 BWR rod bundle. International Journal of Multiphase Flow, 50, 16-32.

197. Ye, T. P., Pan, L. M., Ren, Q. Y., Zhou, W. X., & Zhong, T. (2019). Experimental study on distribution parameter characteristics in vertical rod bundles. International Journal of Heat and Mass Transfer, 132, 593-605.

198. Ylönen, A. T. (2013). High-resolution flow structure measurements in a rod bundle (No. INIS-CH--10383). Swiss Federal Institute of Technology.

199. Yoo, Y., Kim, K., Eom, K., & Lee, S. (2019). Finite element analysis of the mechanical behavior of a nuclear fuel assembly spacer grid. Nuclear Engineering and Design, 352, 110179.

200. Yoon, S., Mäkiharju, S. A., Fessler, J. A., & Ceccio, S. L. (2017). Image reconstruction for limited-angle electron beam X-ray computed tomography with energy-integrating detectors for multiphase flows. IEEE Transactions on Computational Imaging, 4(1), 112-124.

201. Yun, B. J., Park, G. C., Julia, J. E., & Hibiki, T. (2008). Flow structure of subcooled boiling water flow in a subchannel of 3× 3 rod bundles. Journal of nuclear science and technology, 45(5), 402-422.

202. Zboray, R., & Prasser, H. M. (2013). Optimizing the performance of cold-neutron tomography for investigating annular flows and functional spacers in fuel rod bundles. Nuclear Engineering and Design, 260, 188-203.

203. Zboray, R., & Trtik, P. (2019). In-depth analysis of high-speed, cold neutron imaging of air-water two-phase flows. Flow Measurement and Instrumentation, 66, 182-189.

204. Zhou, X. (2014). Measurement and Modeling of the Liquid-phase Turbulence in Adiabatic Air-water Two-phase Flows with a Wide Range of Void Fractions (Doctoral dissertation, The Ohio State University).

205. Zhou, Y., Hou, Y., Li, H., Sun, B., & Yang, D. (2015). Flow pattern map and multi-scale entropy analysis in 3× 3 rod bundle channel. Annals of Nuclear Energy, 80, 144-150.

206. Zuber, N., & Findlay, J. A. (1965). Average volumetric concentration in two-phase flow systems.